Multifunctional Properties of Two-Dimensional Materials, $V_xW_yMo_{1-x-y}S_{2z}Se_{2(1-z)}$: First-Principles Study

Melak Birara Dagnaw

A Dissertation Submitted to the Department of Applied Physics
College of Applied Natural Science

in Fulfillment of the Requirements for the Degree of Doctor of Philosophy in Applied Physics (**Specialization in Condensed Matter Physics**)

School of Graduate Studies
Adama Science and Technology University

January, 2026
Adama, Ethiopia

Multifunctional Properties of Two-Dimensional Materials, $V_xW_yMo_{1-x-y}S_{2z}Se_{2(1-z)}$: First-Principles Study

Melak Birara Dagnaw

Major-Supervisor: Prof. Abebe Belay Gemta (PhD)

Co-Supervisor: Dr. Kunsa Haho Habura (Assi. Prof.)

A Dissertation Submitted to the Department of Applied Physics
College of Applied Natural Science

in Fulfillment of the Requirements for the Degree of Doctor of Philosophy in Applied Physics (**Specialization in Condensed Matter Physics**)

School of Graduate Studies
Adama Science and Technology University

January, 2026
Adama, Ethiopia

DECLARATION

I hereby declare that this PhD Dissertation entitled ”**Multifunctional Properties of Two-Dimensional Materials, $V_xW_yMo_{1-x-y}S_{2z}Se_{2(1-z)}$: First-Principles Study**” is my original work. It has not been submitted for the award of any academic degree, diploma, or certificate at any other university or institution, and all sources used in this dissertation have been duly acknowledged through proper citation.

Name	Signature	Date

RECOMMENDATION

I/We, the supervisor(s) of this PhD dissertation, hereby certify that I/we have carefully read and revised the dissertation entitled ”**Multifunctional Properties of Two-Dimensional Materials, $\mathbf{V}_x\mathbf{W}_y\mathbf{Mo}_{1-x-y}\mathbf{S}_{2z}\mathbf{Se}_{2(1-z)}$: First-Principles Study**” prepared under my/our guidance by **Melak Birara Dagnaw** submitted in partial fulfillment of the requirements for the Degree of Doctor of Philosophy in Applied Physics (**Specialization in Condensed Matter Physics**). I/We therefore recommend that the dissertation be submitted to the department for further review and defense.

Major-Supervisor	Signature	Date
Co-Supervisor	Signature	Date

APPROVAL SHEET

I/We hereby certify that all recommendations of the Board of Examiners have been duly addressed and incorporated into the final version of the dissertation entitled ”**Multifunctional Properties of Two-Dimensional Materials, $\mathrm{V}_x\mathrm{W}_y\mathrm{Mo}_{1-x-y}\mathrm{S}_{2z}\mathrm{Se}_{2(1-z)}$: First-Principles Study**” by **Melak Birara Dagnaw.**

________________	________________	________________
Major-Supervisor	Signature	Date
________________	________________	________________
Co-Supervisor	Signature	Date

We, the undersigned, members of the Board of Examiners for the open defense of the dissertation submitted by **Melak Birara Dagnaw** have read and evaluated the dissertation entitled ”**Multifunctional Properties of Two-Dimensional Materials, $\mathrm{V}_x\mathrm{W}_y\mathrm{Mo}_{1-x-y}\mathrm{S}_{2z}\mathrm{Se}_{2(1-z)}$: First-Principles Study**” and examined the candidate during open defense. This certifies that the dissertation is accepted in partial fulfillment of the requirements for the Degree of Doctor of Philosophy in Applied Physics (Specialization in Condensed Matter Physics).

________________	________________	________________
Chairperson	Signature	Date
________________	________________	________________
External Examiner 1	Signature	Date
________________	________________	________________
External Examiner 2	Signature	Date
________________	________________	________________
Internal Examiner 1	Signature	Date
________________	________________	________________
Internal Examiner 2	Signature	Date

Finally, approval and acceptance of the dissertation is contingent upon submission of its final copy to the College of Postgraduate Studies (CPGS) through the candidate’s Department Graduate Council (DGC) and College Graduate Committee (CGC).

________________	________________	________________
Department Head	Signature	Date
________________	________________	________________
College Dean	Signature	Date
________________	________________	________________
College of Postgraduate Studies, Dean	Signature	Date

ACKNOWLEDGMENTS

Above all, I offer my deepest gratitude and praise to Almighty God, the source of all blessings and my steadfast protector. His divine guidance has been my constant companion, illuminating my path throughout this journey. In all my endeavors, I acknowledge His presence and trust that He will continue to guide and sustain my future pursuits. My lifelong commitment is to glorify Him for His unfailing grace.

Beyond my personal efforts, the successful completion of this dissertation owes much to the exemplary guidance and unwavering encouragement of my supervisors. Words are insufficient to convey my profound appreciation to my principal supervisor, Professor doctor Abebe Belay Gemta, whose patience, dedication, and insightful feedback have been invaluable. His generosity, steadfast support and counsel transcend expression. This work would not have come to fruition without his mentorship and encouragement. I am equally indebted to my co-supervisor, Dr. Kunsa Haho Habura, who generously devoted his precious time to provide guidance, motivation, constructive critique and invaluable suggestions throughout this endeavor.

I am sincerely grateful to the Applied Physics Department staff for their moral support, with special thanks to Dr. Fekadu Tolessa, Dr. Solomon Tiruneh, Dr. Gashaw Beyene, Dr. Mesfin Asfaw, Dr. Megersa Wodajo, Dr. Jima Assefa, Dr. Kindie Yeneayehu, and Dr. Kumneger Tadele for their role in facilitating the successful completion of my Ph.D. coursework.

My heartfelt appreciation extends to all members of the Physics Department at Injibara University, particularly to our esteemed university president, H.E. Dr. Gardachew Worku, whose unwavering support and encouragement profoundly impacted my academic journey. Furthermore, I acknowledge H.E. Mrs Tiquaded Mulu from the Department of Sport Science, for her invaluable administrative support, which ensured the smooth progress of my studies.

I am deeply grateful to Adama Science and Technology University, Injibara University, and the Ministry of Education for their material support, resources, and facilitation, including access to computational laboratories and dormitory services, which were instrumental to this research. I also extend my sincere thanks to the Ministry of Education, especially H.E. Ms. Lensa Abera, for granting access to the HPC computational account, which significantly advanced my work.

Finally, I am deeply grateful to everyone who contributed, directly or indirectly, to the successful completion of this dissertation. Your encouragement and support will always be cherished and remembered with profound appreciation.

TABLE OF CONTENTS

LIST OF TABLES

LIST OF FIGURES

ABBREVIATIONS AND ACRONYMS

CBM	Conduction Band Minima
VBM	Valance Band Maxima
DFT	Density Functional Theory
ESPRESSO	opEn Source Package for Research Electronic Structure Simulation
eV	electron Volt
KSE	Kohn Sham Equation
LDA	Local Density Approximation
PP	Pseudo Potential
NC	Norm Conserving
USPP	Ultra Soft Pseudo Potential
HK	Hohenberg Kohn
GGA	Generalized Gradient Approximation
TM	Transition Metal
MBP	Many Body Problem
EELF	Electron Energy Loss Function
TMDCs	Transition Metal Dichalcogenides
TD-DFPT	Time-Dependent Density Functional Perturbation Theory
2D	Two Dimensional
NM	Non-Metal
FETs	Field-Effect Transistors
CVD	Chemical Vapor Deposition
ALD	Atomic Layer Deposition
PVD	Physical Vapor Deposition
GW	Green’s Function
HSE06	Heyd-Scuseria-Ernzerhof 2006
Å	Angstroms
h-BN	hexagonal Boron Nitride
2H, 1T, 3R	Two Hexagonal, One Trigonal, Three Rhombohedral
LPE	Liquid Phase Exfoliation
ATAT	Alloy Theoretic Automated Toolkit
OLEDs	Organic Light Emitting Diodes
OPVs	Organic Photovoltaics
OFETs	Organic Field Effect Transistors

ABSTRACT

First principles calculations were employed to study the multifunctional properties including structural, phonon, electronic, thermal and optical of two dimensional materials, $V_xW_yMo_{1-x-y}S_{2z}Se_{2(1-z)}$ incorporating both the periodic substitutions and randomly doped structures. The structural analysis reveals that the incorporation of vanadium, sulfur and tungsten alters the bond lengths, bond angles and lattice constants of the pristine of two dimensional, hexagonal molybdenum diselenide (2H-$MoSe_2$). Phonon dispersion spectra confirmed the dynamic stability of the materials with higher frequency modes attributed to smaller atomic mass of sulfur and shorter metal-sulfur bonds. The thermodynamic results indicated substitution and/or doping raises the Helmholtz free energy at low temperatures while enhancing the entropy and specific heat capacity at high temperatures. The modifications enhance thermal performance underscoring the suitability of the substituted or doped systems for optoelectronic and thermal management applications at higher temperature. Electronic structure calculations show at higher vanadium composition, the material exhibits degenerate semiconductor behavior caused by localized 3d states, while at lower doping compositions retains its normal semiconductor properties. In contrast, all substitutions or dilute doping compositions of tungsten preserve the semiconductor character of the material due to the presence of isoelectronic behavior between tungsten and molybdenum atoms. Among all studied compositions, the $W_{0.5}Mo_{0.5}S_{1.5}Se_{0.5}$ has the smaller band-gap, and the $MoS_{0.125}Se_{1.875}$ the larger. The dielectric function is computed within the independent particle approximation and considering non-zero dipole matrix elements and energy conservation reveals a strong sensitivity of the optical response to chemical substitution. In general, the findings indicate tuning the types and composition of dopants precise control the material's properties and enhancing its suitability for infrared optoelectronic and thermal management applications at higher temperature.

KEYWORDS: *Degenerate semiconductor, TMDCs, Thermal properties, Infrared optoelectronics, Molybdenum diselenide*

1. INTRODUCTION

1.1 Background of the Study

Transition metal dichalcogenides (TMDCs) including monolayer, bilayer, few-layer are two dimensional (2D) materials represented by the general stoichiometry of TMQ_2, where TM denotes transition metals such as Molybdenum (Mo), tungsten (W), Vanadium (V) or Niobium (Nb) and Q represents chalcogen elements like Sulfur (S), Selenium (Se) or Tellurium (Te). Their distinctive layered structures combined with adjustable physicochemical properties make them favorable candidates for applications in nanoelectronics, optoelectronics, catalysis and energy related technologies (Jing et al., 2020; Muhammad, 2021; Ugeda et al., 2014). Their crystal structure consists of covalently bonded TM-Q-TM trilayers stacked vertically and held together by weak van der Waals (vdW) forces (Komsa & Krasheninnikov, 2012; Wehling et al., 2008). This layered architecture enables mechanical exfoliation down to monolayers and underpins a rich variety of electronic properties ranging from semiconducting (e.g., MoS_2, $MoSe_2$) to metallic (e.g., NbS_2) behavior (Muhammad, 2021; Yamcicier et al., 2018). While graphene remains the prototypical 2D material due to its exceptional carrier mobility, its zero bandgap limits its utility in semiconductor devices (Bhimanapati et al., 2015; Novoselov et al., 2004). In contrast, many TMDCs possess tunable bandgaps often within the visible to near infrared range making them promising candidates for nanoelectronics, optoelectronics and flexible electronics (Bernardi et al., 2017; Q. Wang & Kalantar-Zadeh, 2012; J. Yu et al., 2023). For instance, two layered hexagonal molybdenum diselenide (2H-$MoSe_2$) exhibits an indirect bandgap of $\sim$ 0.85-1.33 eV (Afrid et al., 2022; Mashmool et al., 2020), which transitions to a direct bandgap of $\sim$ 1.5 eV in the monolayer limit (Böker et al., 2001; Guguchia et al., 2018; Y. Li et al., 2022), enabling strong photoluminescence and efficient light matter interaction (Tonndorf et al., 2013). In 1923, the crystal structure of TMDCs was first determined by Linus Pauling (Jariwala et al., 2014). By the end of the 1960s, nearly 60 TMDCs had been discovered (Wilson & Yoffe, 1969), of which about 40 exhibited layered structures and displayed diverse electronic properties, including semiconducting, metallic, semimetallic, superconducting and topological insulating behavior (Q. H. Wang et al., 2012).

The weak interlayer vdW coupling not only facilitates exfoliation via techniques like liquid phase exfoliation (J. Shen et al., 2016) but also allows integration into heterostructures with other 2D materials (e.g., graphene, hexagonal boron nitride, black phosphorus) (Yamusa et al., 2022). This has spurred interest in TMDCs for applications spanning biosensing, photocatalysis, energy storage, hydrogen evolution and quantum emitters (Afrid et al., 2023;

Rhodes et al., 2019; G. Zhang & Yong-Wei, 2017). To tailor their functional properties, strategies such as strain engineering (W. Zhou et al., 2013), chemical doping (Yun et al., 2012), surface functionalization (Yue et al., 2013) and defect engineering (Hossen et al., 2024; Y. Zhao et al., 2017) have been widely explored. Notably, substitutional doping where foreign atoms replace host species offers precise control over electronic, optical and magnetic properties without disrupting the overall lattice framework (Sahoo et al., 2019; J. Tian et al., 2018). Transition metal (TM) dopants can profoundly alter the electronic and magnetic properties of 2D materials by modulating their d-electron configuration. For instance, Nb doping in MoS_2 has been shown to induce p-type conductivity (Suh et al., 2014), while other TM dopants can drive the system toward half-metallic behavior a state with 100% spin polarization at the Fermi level as demonstrated in doped TMDCs (Z. Wang et al., 2016). Additionally, TM incorporation can introduce or enhance magnetism in otherwise nonmagnetic hosts through localized d-electron states and exchange interactions, as reported in studies (Andriotis & Menon, 2014; Yun & Lee, 2014). Among TMDCs, 2H-$MoSe_2$ stands out for its thermal stability, strong light emission and compatibility with doping induced property tuning such as carrier type control via W substitution (M.-Y. Li et al., 2016) or ferromagnetic ordering via Cu doping (Champion, 1965). Despite these advances, systematic studies on the bulk/bilayer forms of $MoSe_2$ particularly regarding the combined effects of TM and chalcogen co-doping/substituting remain limited (Yamusa et al., 2022).

This study applies first-principles density functional theory (DFT) to analyze structural, vibrational, thermal, electronic and optical properties of the two-dimensional layered alloy, $V_xW_yMo_{1-x-y}S_{2z}Se_{2(1-z)}$ from solid solution to dilute doping regimes. By using vanadium and tungsten as single and combined dopants at the transition metal site, and sulfur as a replacement at the chalcogen site, this study examines changes in lattice parameters, phonon spectra, thermal properties, band structures and dielectric functions across compositions. All doped and substituted structures show dynamic stability, with dopant compositions providing effective control over key properties. These results offer a basic approach for developing layered TMDC alloys in electronic, optoelectronic and thermal management devices.

1.2 Statement of the Problem

Two-dimensional transition metal dichalcogenides (TMDCs) such as 2H-$MoSe_2$ have attracted considerable attention for nanoelectronic, optoelectronic and thermal management applications due to their tunable electronic structures and mechanically robust layered architectures (Jing et al., 2020; C. Lee & Gonze, 1995; Ugeda et al., 2014). Despite these advantages, the practical implementation of these materials based devices is limited by the presence of intrinsic and extrinsic defects which strongly influence their multifunctional properties including structural, electronic, optical, phononic and thermal (Hossen et al., 2024; Lin et al., 2016; W. Zhou et al., 2013). Furthermore, many 2D TMDCs including

2H-$MoSe_2$ exhibit the intrinsically low density of electronic states near the Fermi level characteristic of semiconductors along with relatively modest infrared optical absorption both of which can limit certain device performances (Mashmool et al., 2020). Bilayer, $V_xW_yMo_{1-x-y}S_{2z}Se_{2(1-z)}$, introduce additional complexity due to interlayer van der Waals interactions and dopant or alloy induced perturbations which modify the electronic state distribution near the band edges relative to monolayer and pristine forms. Although doping and substitution offer effective pathways to tune carrier concentrations and functional properties, the underlying charge transfer mechanisms and dopant host interactions remain insufficiently understood (Iqbal et al., 2020). Most computational studies to date have focused on monolayer and bulk systems leaving the effects of multi-element doping, co-doping strategies and interlayer coupling in $V_xW_yMo_{1-x-y}S_{2z}Se_{2(1-z)}$ largely unexplored (Fu et al., 2015; Y. Gong et al., 2014; Muhammad, 2021; Y. Wang, Shang, et al., 2016; S. Zhang et al., 2018). Consequently, a comprehensive understanding of how variations in vanadium, tungsten and/or sulfur compositions influence charge transfer, Fermi level modulation, thermal transport, van der Waals interlayer interactions and the structural stability of 2H-$MoSe_2$ without disrupting its intrinsic electronic structure is still lacking. To address this gap, we use first-principles DFT and DFT+U calculations to understand how controlled doping or substitution changes the structure, electronic behavior, vibrations, optical response and stability of bilayer $V_xW_yMo_{1-x-y}S_{2z}Se_{2(1-z)}$. This knowledge can help guide the design of next-generation 2D TMDC materials for infrared electronic, optoelectronic and thermal management devices.

1.3 Objectives

1.3.1 General Objective

The general objective of this research is to investigate the multifunctional properties of two-dimensional materials, $V_xW_yMo_{1-x-y}S_{2z}Se_{2(1-z)}$ using first principles study.

1.3.2 Specific Objectives

The specific objectives of this research include

- To assess the structural, electronic and optical properties of $V_xW_yMo_{1-x-y}S_{2z}Se_{2(1-z)}$ ($x = 0.5, y = 0, z = 0, 0.25, 0.5, 0.75$) using first-principles calculation.
- To analyze of the structural, vibrational, electronic and optical properties of $V_xW_yMo_{1-x-y}S_{2z}Se_{2(1-z)}$ ($x = 0,\ y = 0.5,\ z = 0.25, 0.5, 0.75$) via first-principles method.
- To compute structural, electronic and optical properties of $V_xW_yMo_{1-x-y}S_{2z}Se_{2(1-z)}$ ($x = 0.125, y = 0, z = 0, 0.0625, 0.125, 0.1875$) by employing first-principles approach.

- To calculate the structural, phonon, thermal, electronic and optical properties of $V_xW_yMo_{1-x-y}S_{2z}Se_{2(1-z)}$ ($x = 0,\ y = 0, 0.125,\ z = 0, 0.0625, 0.125$) based on first-principles technique.

1.4 Motivations

The rapid advancement of modern electronics, optoelectronics and energy conversion technologies demands the development of innovative functional materials with precisely tunable properties (Pike et al., 2018). 2D TMDCs have emerged as promising candidates due to their unique layered structures and versatile physical properties. However, binary and ternary TMDCs, despite extensive study, face inherent limitations in the range of achievable property tuning (Wickramaratne et al., 2014). This constraint motivates exploration into higher order alloyed systems, such as two-dimensional materials, $V_xW_yMo_{1-x-y}S_{2z}Se_{2(1-z)}$, which offer a rich compositional design space to manipulate multiple interacting cation and anion species. By exploiting this chemical complexity, it is possible to co-engineer essential material properties including electronic band structure, phonon dynamics, thermal transport and optical responses beyond what simpler systems allow. Yet, the experimental synthesis and theoretical modeling of these 2D alloys pose significant challenges, resulting in a sparse understanding of their fundamental behaviors. Monolayers are often extremely fragile and offer limited tunability, while bulk TMDCs are very thick and have a weak optical response. Bilayer TMDCs, such as 2H-$MoSe_2$, address this gap by combining atomic scale thinness suitable in nanoelectronics with sufficient stability for reliable fabrication, enabling optoelectronic devices and rich physical behavior that allow voltage tunable functionalities not possible with monolayers or bulk materials alone. This dissertation aims to fill this knowledge gap by applying first principles DFT together with advanced alloy modeling methods like ATAT to reveal how atomistic compositional changes affect multifunctional properties. The results provide foundational insights and design principles to support the targeted design and scalable synthesis of next coming TMDC based nanoelectronic and optoelectronic materials for transformative device applications.

1.5 Significance

Two-dimensional materials, $V_xW_yMo_{1-x-y}S_{2z}Se_{2(1-z)}$, offer several advantages such as tunable bandgaps, favorable thermal behavior and weak van der Waals interactions that make them promising alternatives to conventional III-V and II-VI semiconductors for infrared optoelectronics (Sedhain & Kaphle, 2017). Their low cost, ease of integration and highly adjustable electronic structures open opportunities for improved photodetectors, solar energy conversion (Aftab et al., 2022), and coming-generation microelectronic devices (Reshak & Auluck, 2003). Understanding their properties is therefore essential for advancing future technologies in optoelectronics, thermal management and energy conversion.

1.6 Delimitation

This research is limited to a computational exploration of the two-dimensional TMDCs alloy, $V_xW_yMo_{1-x-y}S_{2z}Se_{2(1-z)}$, across the compositional ranges $0 \leq x < 1$, $0 \leq y < 1$ and $0 \leq z \leq 1$. The investigation focuses solely on doping and substitution involving vanadium, tungsten and sulfur atoms either individually or in combination. No other dopants, phases or intercalated species are considered. This restriction enables a targeted analysis of how controlled variations in alloy composition and element type affect the multifunctional properties of the two-dimensional 2H-phase $MoSe_2$ TMDC framework, examined at both the unit cell and supercell configurations. The structural analysis includes lattice parameters, bond lengths and bond angles. Phonon related properties encompass phonon dispersion curves and phonon density of states. Thermal behavior is evaluated through heat capacity, Helmholtz free energy and entropy. Electronic structure investigations cover band structures, total and projected densities of states, Fermi energy and carrier effective masses. Optical properties analyzed include the refractive index, absorption coefficient, reflectivity, extinction coefficient, dielectric function components and electron energy loss spectra. All simulations are carried out using first-principles methods implemented in Quantum ESPRESSO and Phonopy, without reliance on experimental data or empirical corrections. Furthermore, external influences such as temperature, pressure, environmental exposure, as well as catalytic or chemical reactivity effects, are not included within the scope of this work.

1.7 Organization of the Dissertation

This dissertation presents first-principles study of the multifunctional properties of 2D materials, $V_xW_yMo_{1-x-y}S_{2z}Se_{2(1-z)}$. The study investigates both pristine and doped or substituted structures using unit cells and supercells, enabling an accurate representation of the compositional and structural changes introduced by different dopant types and composition at the metal and chalcogen sites. The dissertation is structured as follows: Chapter 1 introduces the research motivation, objectives and overall framework. Chapter 2 reviews key developments in 2D TMDC alloys with emphasis on their roles in optoelectronics, nanoelectronics and thermal management and outlines the theoretical background, including DFT, generalized gradient approximation (GGA), GGA+U and pseudopotentials. Chapter 3 describes the computational methods and materials, Chapter 4 presents the main results on sulfur, vanadium and tungsten doping and/or substitutions in bilayer 2H-$MoSe_2$ using first-principles calculations, and Chapter 5 summarizes the findings, compares them with literature and outlines future research directions.

2. LITERATURE REVIEW

2.1 Two-Dimensional Transition Metal Dichalcogenide Materials

Two dimensional TMDC semiconductors demonstrate distinct physical properties in their bulk and single layer forms, making them attractive for optoelectronic and quantum spin transport applications (Wickramaratne et al., 2014). These properties of monolayers are qualitatively different from those of bulk materials (Pike et al., 2018; Wickramaratne et al., 2014). Monolayer materials offer a wide range of applications, particularly in the areas of catalysis and photoelectrochemistry, due to their unique properties (J. Yu et al., 2023). The bulk electronic properties of TMDC materials exhibit strong dependence on both chemical composition and fundamental crystal symmetry (Jariwala et al., 2014; Rasmussen & Thygesen, 2015). For optoelectronic and solar energy applications (such as electronic logic devices, photovoltaic devices, and photo-detection devices (Wilson & Yoffe, 1969)), TMDC systems show exceptional promise due to their layer dependent and strain responsive band structure transitions between indirect and direct gap states (Ataca et al., 2012; Gupta et al., 2015; Yun et al., 2012). Furthermore, layered semiconductor TMDCs have garnered substantial interest due to their diverse range of unique physical and chemical properties, including high anisotropy, as well as noteworthy optical and thermoelectric characteristics (J. Yu et al., 2023). From these TMDC materials, molybdenum diselenide ($MoSe_2$) and tungsten diselenide (WSe_2) are suitable for nanoelectronic and optoelectronic applications (Afrid et al., 2023) due to their simple and easy tuning properties. These layered materials demonstrate both high charge carrier mobilities (Pike et al., 2018) and exceptional lubrication characteristics, owing to their anisotropic structure. Notably, certain compounds exhibit charge density wave (CDW) phenomena (Calandra et al., 2009; Johannes et al., 2006). Recent computational advances have established DFT as an effective tool to discover exfoliable materials with technologically relevant properties (Choudhary et al., 2017; Sofer et al., 2017).

Numerous proposed optoelectronic devices (M.-Y. Li et al., 2016; Wei et al., 2015) utilize TMDC heterostructures to combine their distinctive properties, requiring a thorough understanding of interconnected mechanical, electronic, dielectric, thermal, elastic, and acoustic properties, whether in purely 2D or semi-bulk configurations, for effective design and analysis of these 2D material systems. Researchers have increasingly studied 2D TMDCs due to their promising electronic, optical, mechanical, and thermal properties for advanced applications (Canpolat et al., 2019; Wilson & Yoffe, 1969; Yoffe, 1973). The sulfide based compounds significantly influence the physical properties of these materials due to their distinct properties (Mashmool et al., 2020). These compounds typically exist as dark, diamagnetic solids with semiconductor behavior, exhibiting complete insolubility in common solvents (Wells, 2012). Within the metal dichalcogenide family, MoS_2 and $MoSe_2$ have emerged as particularly noteworthy materials because of their exceptional optical, catalytic, electronic, and lubricating capabilities (Kim et al., 1991). The bulk form of these materials is characterized by a layered structure, where strong covalent bonds form between sulfur (or selenium) and molybdenum atoms within each layer, while the layers themselves are held together by comparatively weak vdW forces (Böker et al., 2001). Furthermore, thickness dependent studies reveal quantum confinement effects through modifications in phonon dispersion relations (C. Lee et al., 2010; Splendiani et al., 2010). Due to the tunable electrical, optical, and magnetic properties, ultrathin TMDCs could serve as a viable substitute for group III-V materials and graphene (Lin et al., 2016). However, while naturally occurring 2D TMDC monolayers represent the purest form, their inherent defects restrict their practical use. These 2D materials exhibit unique physical properties such as valley effects, excitonic fluidity, topologically protected states, and moiré physics, making them promising for coming generation nanoelectronics (Manzeli et al., 2017). While graphene is the most widely studied, its lack of a bandgap has shifted research interest toward alternative materials like TMDCs, which possess a tunable bandgap in the visible to near-infrared range, enabling exceptional properties such as electrostatic coupling, photo switching, gate tunable superconductivity, and valleytronics (Hossen et al., 2024). For example, the semiconductor $MoSe_2$ is a direct bandgap when in the single layer but an indirect bandgap when in the bulk state (Muhammad, 2021; Tyagi & Choudhary, 2022). It can have either a trigonal or hexagonal shape, with its hexagonal dimensions are $a = b = 3.32$ Å and $c = 13.54$ Å for a space group of p6$_3$/mmc-D$^4_{6h}$ (Böker et al., 2001). The bandgap of single layer or bilayer 2H-$MoSe_2$ material typically falls within the range of visible and infrared regions (Yamusa et al., 2022) and can be synthesized using top down approach of CVD method (Brixner, 1963; J. Yu et al., 2023).

In addition to the TM dopants it has been reported that non-metal (NM) elements dopants such as H, C, F, etc., (X. Zhao et al., 2017) can well tailor the bandgap of $MoSe_2$, but they can solely induce very weak ferromagnetism property which is not favorable in practical applications of spin based devices (Beiranvand, 2021). Intriguingly, the structural, electronic and optical properties of monolayer 2D TMDCs materials can be significantly influenced by co-doping of TM with NM elements, defective of chalcogens and varying the compositions (W.-b. Xu et al., 2014). The optical properties of monolayer WS_2 in co-doping of Mn-NM elements leads to the red shifts of the bandgap which is very suitable for the infrared photodetector applications (Xie & Zhang, 2017). The pure form of $MoSe_2$ is the non-magnetic semiconductor material having of unaltered form, without any intentional modulations. Up to date, this material has exhibited excellent chemical, physical and optical properties where the energy bandgap values are in the range of 1.1 eV to 1.58 eV for bilayer and monolayer structures (Haldar et al., 2015). The energy bandgap of pristine $MoSe_2$ can vary depending on the specific density functional used for calculations. For instance, the calculated bandgaps for non-defective monolayer $MoSe_2$ are 1.75 eV for hybrid HSE06, 2.41 eV for Green's function (GW), and 1.52 eV for GGA exchange-correlation density functionals (Beiranvand, 2021). Additionally, the static dielectric constant in two directions of applied external electric field ($E\|x$ and $E\|z$) are given as 8.01 and 4.51 (Beiranvand, 2021), respectively. In its bulk state the calculated energy bandgap are in the ranges of 0.80-1.09 eV (Böker et al., 2001; Muhammad, 2021), whereas the static dielectric constant in two directions of applied external electric field ($E\|x$ and $E\|z$) are given as 16.66 and 8.26 (Böker et al., 2001), respectively. The different physical behaviors of pure monolayer or bulk 2D materials ($MoSe_2$, MoS_2, WSe_2, WS_2, etc,.) can be modified using many feasible mechanisms such as defects, (impurity doping, vacancies, grain boundaries, etc.,), external strain and chemical adsorption (Haldar et al., 2015). For instance, there is a p-type conduction realization in MoS_2 when we incorporated a substitutional doping of Nb TM atom (D. Shen et al., 2022). The single Co substitutional dopant can transform from the semiconducting monolayer MoS_2 to half metallic (Loh et al., 2021). Additionally, doping of NM elements such as B, N, H, Cl and F can induce fascinating electronic and non-negligible spin polarization (Y. Zhao et al., 2017). The W mono-doping in monolayer of $MoSe_2$ switches the dominant conduction from an n-type to a p-type with enhanced PL intensity (D. Su et al., 2024). Previously in mixed 2D TMDCs compounds, there is realized that the metal and chalcogen atoms substitutional dopants to the system of $MoS_{2x}Se_{2(1-x)}$ and $Mo_xW_{1-x}Se_2$ with 0.6 dopant concentration are stable and possesses an intriguingly electronic properties (Schneemeyer & Sienko, 1980). The partial DOS reveals strong Mo-Se covalent hybridization due to overlapping and broad energy distributions.

Many recent studies have proved that mono or single doping is an effective route to alter the magnetic, electronic structures, thermoelectric, optoelectronic, etc., properties of monolayer or bulk form of $MoSe_2$ material (Suh et al., 2014). Similar to the conventional semiconductors, substitution is a key way to tune the properties of monolayer or bulk $MoSe_2$ material to enable their device applications (Y. Wang, Li, & Yi, 2016). Different experimental and theoretical studies have shown that a number of different elements can replace or substitute either TM or non-metal atoms in this material and act as n-type, p-type or isoelectronic dopants (Yun & Lee, 2014). The mono-doping and co-doping of monolayer or bulk $MoSe_2$ approach are recognized as an effective method for modulating the properties of TMDCs materials (Yue et al., 2013). Thus, either mono-doping, co-doping or chalcogen vacancies of $MoSe_2$ can change the electronic conduction properties, increase electron mobility and also to make that non magnetic to magnetic to realize specific electronic structures, optical, thermoelectric, magnetic, etc., properties (X. Li et al., 2016). In previous studies, it was observed that the various properties including stability, electronic, optical, and magnetic properties of $Mo_{1-x}W_xSe_2$ alloys and others are determined using the first principle calculation method (Afrid et al., 2022). The properly doping elements with different valence states into different cationic lattice states a well regulated charge density can be obtained which leads to optimize properties of materials. Doping causes a change in the cell parameters, induce point defects, bring lattice distortion because of the position of the atoms and the lengths of the valence bands changes resulting in variations of the structural, electronic and optical properties of 2H-$MoSe_2$ layered material. The applicability of doping to 2D TMDC materials' electronic/ionic states is to rendering them to useful for energy storage (Y. Li et al., 2022).

The heteroatoms used to dope to $MoSe_2$ can be classified into three categories like non metals (NM), TM and noble metals (S. Deng et al., 2017). Doping engineering is able to confer the pristine $MoSe_2$ numerous beneficial properties depending on the doped elements. In addition to a single dopant atoms, dual and multiple doping strategies can be used to fabricate materials with optimized performances (Y. Li et al., 2022). The most commonly NM used to dope $MoSe_2$ include S, N, O, P and B. From these types of dopants, the N doped $MoSe_2$ induced partial phase transition of the $MoSe_2$ and significantly improved the electrical conductivity, σ by decreasing its energy bandgap from 1.22 to 0.51 eV (Y. Li et al., 2022). The S doped $MoSe_2$ are useful to increase the active sites of which is crucial for its HER performances (Tan et al., 2018). Additionally, the benefits of S doped on the alkali ion storage capacity of $MoSe_2$ was confirmed by using DFT calculation (Sharma et al., 2021). Halogens like F and Cl are effective n-type dopants for $MoSe_2$. Ion implantation, a technique where ions are embedded into a material, can be used to introduce these halogens into $MoSe_2$, thereby modifying its electronic structure and optical properties (Z. Luo et al., 2022). These modifications primarily affect the semiconductor properties of $MoSe_2$, making it suitable for applications like field-effect transistors (FETs). However, more research is needed to explore the potential benefits of halogen doped $MoSe_2$ in energy related applications. TMs are frequently used to enhance the catalytic properties of $MoSe_2$. By increasing the number of active sites on the $MoSe_2$ surface, TMs can improve its catalytic performance, particularly for the HER. Theoretical and experimental studies have shown that TMs like Mn, Fe, Co, Ni and Nb can significantly enhance the HER activity of $MoSe_2$ (Vikraman et al., 2018).

2.1.1 Crystal Structure of TMDCs Materials

The atomic structure of 2D TMDCs consists of a trilayer Q-TM-Q motif, in which a plane of TM atoms is covalently bonded between two planes of Q atoms (Mak et al., 2010). Adjacent trilayers are held together by weak vdW forces (Israelachvili & Tabor, 1973), a feature that enables mechanical exfoliation into atomically thin 2D sheets similar to graphite (Coleman et al., 2011). As illustrated in Figure 1, the crystal lattice is built from vertically stacked Q-TM-Q units, with hexagonally arranged TM atoms sandwiched between upper and lower Q layers. The Bulk or bilayer TMDC crystals are formed by vdW interactions between adjacent trilayers, which are significantly weaker than the strong covalent bonds within each trilayer (Israelachvili & Tabor, 1973). The primary phases of $MoSe_2$ are the octahedral (1T) and trigonal prismatic (2H or 3R) structures, where uppercase letters denote Q atoms, lowercase letters denote TM atoms, and the numerical and lettered prefixes (1, 2, 3; T, H, R) specify distinct stacking sequences and symmetry groups (Yun et al., 2012).

Monolayer TMDCs materials typically measure 6-7 Å in thickness, with strong in-plane covalent bonds (TM-Q distances ranging from 2.4-2.6 Å) and weaker interlayer interactions mediated by vdWs forces (interlayer spacing of 3.0-3.5 Å) (Splendiani et al., 2010). Among various structural configurations, group VI TMDCs such as MoS_2 and WS_2 preferentially adopt the 2H phase, in which the TM atoms are coordinated in a trigonal prismatic geometry by surrounding chalcogen atoms (Mak et al., 2010). This specific arrangement plays a crucial role in endowing these materials with their remarkable electronic properties and structural stability. As illustrated in Figure 1, the 2H-MTQ_2 crystal structures are depicted from both side and top views. In these figures, the transition metal atoms occupy the central position, while the chalcogen atoms are situated at the top of the trigonal prismatic structure, with M representing Mo or W and X denoting S or Se (Muhammad, 2021). According to (Muhammad, 2021), the left portion of the TMQ_2 illustration depicts its bulk structure, while the right portion shows the monolayer form of the TMQ_2 materials.

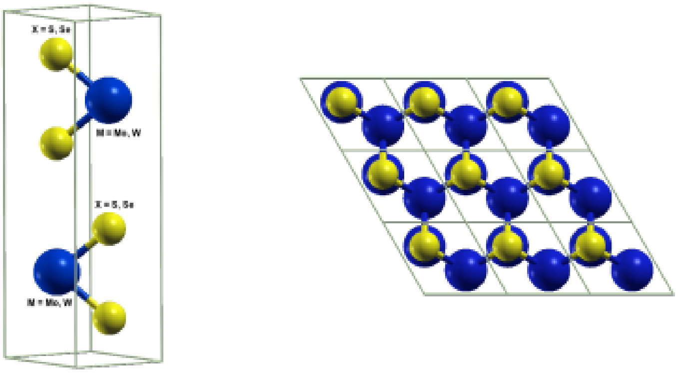

Figure 1: General crystal structures of layered 2H-TMQ_2 materials, where the left and right sides are the side and top view structures, respectively. The box represents the unit cell used in our simulations. (Muhammad, 2021)

The structural diversity of TMDCs stems from variations in the coordination geometry of the TM atoms, which is fundamentally dictated by the occupancy of their d-orbitals (Kuc et al., 2015). This atomic arrangement, together with the specific electronic configuration of the d-orbitals, plays a decisive role in determining phase stability and, consequently, the resulting electronic properties. The capacity of TMDCs to adopt multiple structural phases such as 1T, 2H, or 3R while retaining identical chemical composition underpins their remarkable versatility for a wide range of technological applications (Manzeli et al., 2017).

Beyond TMDCs, the family of naturally occurring layered materials encompasses a

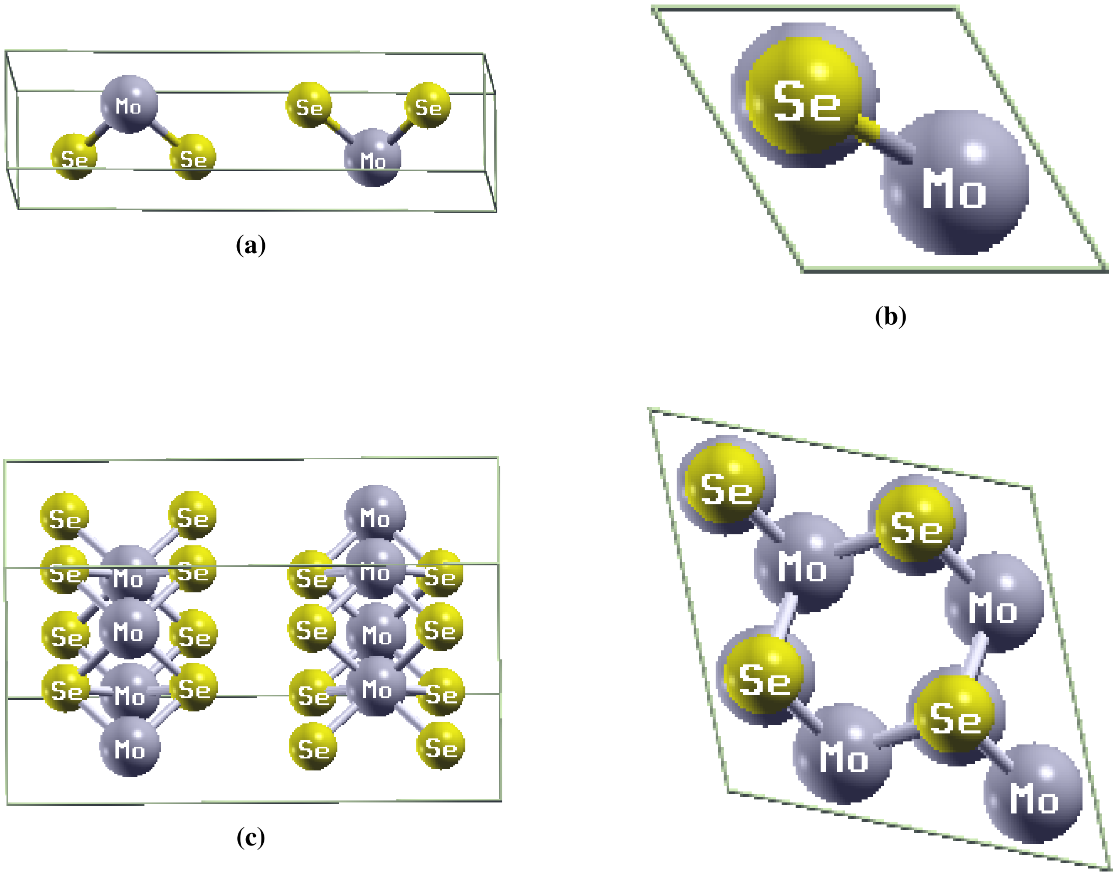

(a) (b) (c) (d)

Figure 2: Side (a, c) and top (b, d) view crystal structures of the unit cell and supercell of 2H-$MoSe_2$ layered TMDC materials, respectively.

broad spectrum of 2D crystals, including minerals, transition metal oxides, and dichalcogenides (Wilson & Yoffe, 1969). Crucially, when thinned down to monolayer or few-layer thicknesses, TMDCs exhibit properties markedly distinct from their bulk counterparts most notably in their phonon spectra, electronic band structures, and light matter interactions (X. Zhang et al., 2015). By combining different TMs (e.g., Mo, W, Nb, Ta, Ti) with various chalcogens (S, Se, Te), more than 40 distinct TMDC compounds can be synthesized, each offering unique physical and chemical characteristics (X. Zhang et al., 2015). The side and top views of bulk or bilayer TMDC materials are illustrated in Figure 2, showing both the unit cell (panels a and b) and the supercell (panels c and d) representations, which are obtained by the XCrySDen (Kokalj, 1999).

2.1.2 Bandgap Energy in TMDC Families

TMDCs display an electronic band structure that varies with the number of layers (Chaves et al., 2020). In their bulk form, materials such as $MoSe_2$, MoS_2 and WS_2 possess an indirect bandgap due to interlayer coupling, which shifts the conduction band minimum

(CBM) away from the K-point (H. Liu et al., 2014; R. Wu et al., 2019). Conversely, when reduced to a monolayer, these materials exhibit a direct bandgap at the K-point, resulting in strong light matter interactions and enhanced photoluminescence, as initially demonstrated by (Mak et al., 2010). Figure 3 illustrates various types of 2D materials along with their corresponding bandgaps. The TMDCs featured in this figure were selected for their experimental significance, and their crystal structures are depicted in perspective view (Chaves et al., 2020). Materials are organized by bandgap magnitude, aligned with the wavelength scale below. Horizontal bars beneath each structure show bandgap variation from narrower (bulk) to wider (monolayer), with standard cases in black and exceptions in red. Gray boxed materials on the left have zero or near zero bandgaps, indicating metallic or semimetallic behavior. Following the mechanical exfoliation techniques pioneered for graphene, monolayer TMDCs were isolated, exhibiting distinct structural phases (2H, 1T, 1T', 1T$_d$) (Chaves et al., 2020). Semiconducting 2H phases (e.g., MoS$_2$) possess direct bandgaps (1-2 eV) and exhibit unique valleytronic and excitonic properties, while metallic or semimetallic T phases (e.g., WTe$_2$) display topological properties (Fei et al., 2017; Kappera et al., 2014; G. Wang et al., 2018). Beyond TMDCs, the 2D materials family includes TM trichalcogenides (e.g., TiS$_3$ (Island et al., 2014)), group III-VI layered

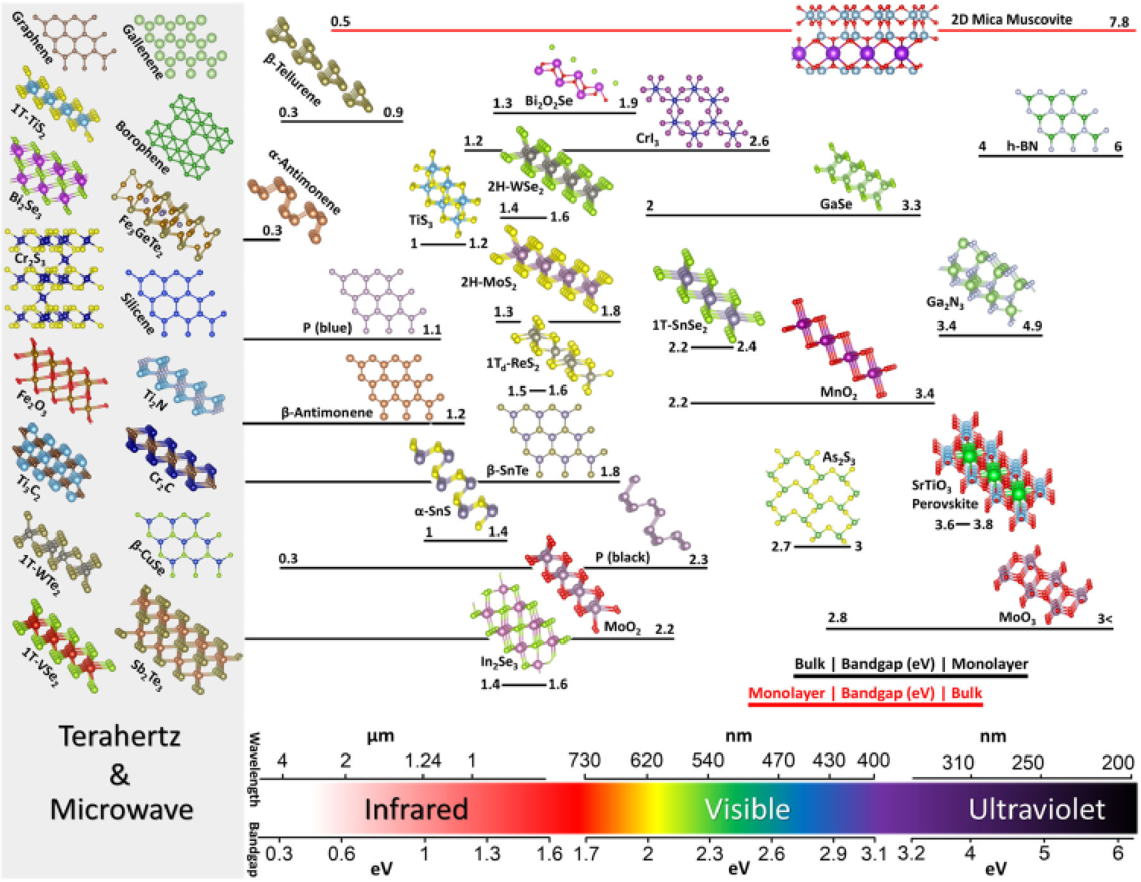

Figure 3: Selected families of 2D materials and their bandgaps.
(Chaves et al., 2020)

chalcogenides (e.g., GaSe (Lei et al., 2013)), group IV monochalcogenides (e.g., SnS (Y. L. Huang et al., 2015), GeSe (L. Li et al., 2013) and TMXenes (Anasori et al., 2023) (e.g., Ti_3C_2) ceramic like conductors with tunable stoichiometries (TM_2Q, TM_3Q_2, TM_4Q_3) (Al Balushi et al., 2016). Wide bandgap materials like h-BN (Dean et al., 2010) serve as ideal substrates, while transition metal oxides (e.g., α-MoO_3) (Ma et al., 2018) and perovskites (e.g., $SrTiO_3$) (Hodes, 2013; M. Liu et al., 2013; Lodesani et al., 2019) enable optoelectronic and photovoltaic applications. Recent additions include 2D ferromagnets (CrI_3 (B. Huang et al., 2017), Fe_3GeTe_2) (C. Gong et al., 2017), ferroelectrics (In_2Se_3) (W. Ding et al., 2017) and elemental analogs (phosphorene) (H. Liu et al., 2014), silicene (Vogt et al., 2012), borophene (R. Wu et al., 2019)), spanning metallic to insulating behavior, where their bandgap tunability from bulk to monolayer across the electromagnetic spectrum is summarized.

2.1.3 Factors Tuning the Bandgap of TMDC Materials

Modern semiconductor devices commonly employ band structure engineering via hetero-structures (Kroemer, 2001), super lattices (Esaki & Tsu, 1970), strain (M. L. Lee et al., 2005) or alloying (Ning et al., 2017) to enhance their performance. For instance, strained silicon increases hole mobility by a factor of four (Chu et al., 2009), while tailored lasers achieve lower threshold currents and precise wavelength control (Thijs et al., 1991). Multilayer hetero-structures provide enhanced charge and optical confinement in transistors (Mimura et al., 1980) and light emitting devices (Kroemer, 1963), whereas super lattices have enabled innovations such as quantum cascade lasers (Faist et al., 1994). This approach has also propelled fundamental physics forward through phenomena such as quantum tunneling (L. L. Chang & Esaki, 1992) and the fractional quantum Hall effect (Tsui et al., 1982). The drive toward atomic scale miniaturization has intensified interest in 2D materials, whose weak vdWs interlayer coupling allows for arbitrary stacking without lattice matching constraints and offers exceptional bandgap tunability (Novoselov et al., 2004). Unlike conventional quantum wells, 2D TMDC semiconductors preserve their electronic performance even at atomically thin dimensions. They also exhibit bandgap responses to external stimuli that are an order of magnitude stronger than those of bulk materials, while offering distinctive chemical tunability due to their exceptionally high surface to volume ratios (Redaelli et al., 2014).

2.1.3.1 Effects of van der Waals in Multilayer Structure

A van der Waals (vdW) multilayer is a structure composed of stacked 2D materials, where the layers are bound by weak vdW interactions instead of traditional chemical bonds, which enables unprecedented control over the resulting physical and electronic properties (Molas et al., 2017). For instance, TMDCs exhibit fundamentally distinct electronic behavior when they are stacked (Molas et al., 2017). Research reveals that their bandgap and overall band structure are highly sensitive to stacking configuration, which governs interlayer coupling (He et al., 2014). Variations in stacking order can dramatically modify crystal symmetry and electronic spectra, potentially enabling phenomena like second harmonic generation (Y. Li et al., 2013), magnetism (C. Gong et al., 2017) and superconductivity (Xi et al., 2016). In the hexagonal 2H phase of TMDCs, the layers remain only weakly coupled at any twist angle, as the momentum mismatch between neighboring layers prevents strong interlayer interactions. This absence of interlayer registry prevents coherent electron transport across layers, leaving the conduction and valence bands edge states of individual layers quantum mechanically isolated (Chaves et al., 2020). The analysis focuses on AB stacked TMDCs, the thermodynamically stable configuration in bulk systems (Chaves et al., 2020). Taking WS_2 as a representative case (see Figure 4a), bulk crystals display an indirect bandgap with their valence and/or conduction band edges located at the Γ or Q points, whereas monolayer WS_2 exhibits a direct bandgap with transitions occurring at the K points (Chaves et al., 2018, 2020). This layer dependent transition explains the strong PL and absorption features in monolayers, where direct K-point transitions (labeled A, B) dominate (Mak et al., 2010; Splendiani et al., 2010; G. Wang et al., 2018). The PL spectra reveal an additional low energy feature (I) in multilayers, stemming from indirect transitions (see Figure 4b). Experimental studies (Arora et al., 2015; Mak et al., 2010; Molas et al., 2017) demonstrate that A, B peak intensities diminish with increasing layer count due to the direct to indirect gap transition, while their energies remain nearly constant (shifting less than 100 meV) consistent with the flat band dispersion along K-H. In contrast, the I peak energy shows strong layer dependence (200-300 meV red shift from bilayer to bulk), reflecting the non parabolic valence band dispersion along Γ-A that enhances hole interlayer coupling. The band structure of bulk

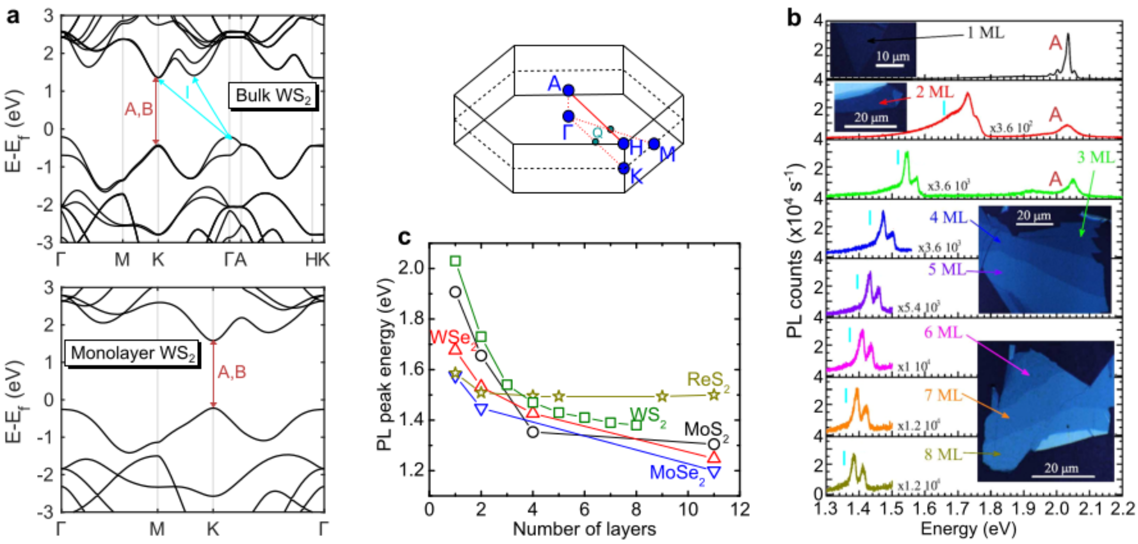

Figure 4: Layer dependent bandgap of TMDC materials.
(Chaves et al., 2020)

(top) and monolayer (bottom) of WS_2 is shown from Figure 4a. The high symmetry points are indicated on the right (above Figure 4c). Bulk TMQ_2 band structures are qualitatively similar, with the lowest energy bandgap indirect. This supports PL from indirect transitions labeled I, as well as direct transitions labeled A and B. Figure 4b shows PL spectra of WS_2 from monolayer (1ML) to 8 layers (8ML) measured at 5 K, with optical sample images inset (Molas et al., 2017). The energy of the most prominent PL peak depending on layer number for various TMDCs such as $MoSe_2$, MoS_2, WSe_2, WS_2, and ReS_2 is shown in Figure 4c. In this figure, as the number of layers increases, the PL intensity of the materials decreases significantly because thicker structures exhibit weaker optical responses. Conversely, when the number of layers decreases and the system approaches a monolayer, the PL intensity becomes much stronger. This enhancement arises from the transition to a direct bandgap and the resulting stronger optical response of the monolayer material.

2.1.3.2 Effects of Doping, Substitution and Alloying

Substitution is the process in which certain atoms within a crystal structure are replaced by other atoms that have comparable sizes and bonding behaviors (Y. Gong et al., 2014; W. Zhou et al., 2013). Although the overall crystal structure usually remains unchanged, substitution modifies the spacing between atoms and their bonding interactions, which can influence properties like mechanical strength, magnetic behavior, and thermal stability (J. Zhou et al., 2018). Alloying, on the other hand, involves mixing two or more elements to produce a material with improved mechanical, chemical or physical performance (C. Gong et al., 2017; Y. Gong et al., 2014). Depending on the elements used and their relative amounts, alloying may result in solid solutions or mixtures of different phases. In contrast to doping and substitution, alloying typically incorporates much larger quantities of additional elements and brings about substantial changes in both microstructure and overall material properties.

Doping, the intentional or unintentional addition or substitution of foreign atoms such as metals or non-metals into parent materials, modifies the hosts' electronic and crystal structures (Vinturaj et al., 2023). It effectively manipulates electronic structure and charge separation efficiency in semiconductors (Hoque & Zubair, 2022) through charge transfer between dopants and hosts, improving carrier density and mobility by modulating the Fermi level (Iqbal et al., 2020). A key benefit is the ability to tune the TMDC bandgap, increasing or decreasing it, since doped TMDCs generally outperform undoped ones due to shifts in their Fermi levels. Non metal dopants like sulfur and selenium typically substitute chalcogen sites or occupy interstitial positions, introducing mixed or localized states near the valence or conduction bands that wide the bandgap (Asadi & Nourbakhsh, 2019). Dopants can also create impurity levels within the bandgap, enabling new excitations and enhancing photogenerated carrier compositions (Ghafari & Janowitz, 2019), while potentially causing defects that lead to new optical properties (Vinturaj et al., 2023). Metal dopants including alkaline earth, transition, rare earth and post transition metals are used for bandgap engineering in TMDCs (Hoque & Zubair, 2022; Khan et al., 2022). Metal ion doping can induce defects and modify diffusion behavior, improving electron mobility and charge transport (Hoque & Zubair, 2022; Vinturaj et al., 2023) and can activate photocatalytic surfaces to enhance reaction rates and optoelectronic performance (Khalid et al., 2020; Khan et al., 2022). Overall, metal doping increases electron-hole mobility, introduces new energy states within or near the bandgap and enhances visible light absorption via red shifted edges.

Furthermore, dopant alters carrier composition while largely preserving the host's intrinsic electronic structure (Iqbal et al., 2020). Donor impurities introduce levels near the conduction band, while acceptors create states near the valence band, allowing precise control for tailored functionalities (Johannes et al., 2006). Additionally, doping involves interstitially to modify electronic, optical or magnetic properties, affecting conductivity, band structure and phase stability (Kittel, 2005; Nieminen & Ashcroft, 1981), a critical role in devices from transistors and solar cells to superconductors and catalysts (Q. H. Wang et al., 2012). Alloying modifies material composition and bulk properties through extensive elemental mixing, enabling continuous compositional tuning, whereas doping introduces controlled impurity levels to selectively engineer electronic states or carrier concentration while preserving host lattice integrity, distinguishing broad compositional modulation from discrete electronic perturbation (Togo & Tanaka, 2015; K. Zhang, 2023). Despite theoretical predictions that monolayer TMDC alloys can achieve continuously tunable bandgaps (Komsa & Krasheninnikov, 2012), issues such as structural instability, reactivity and non directional atomic bonding complicate synthesis and stability compared to bulk

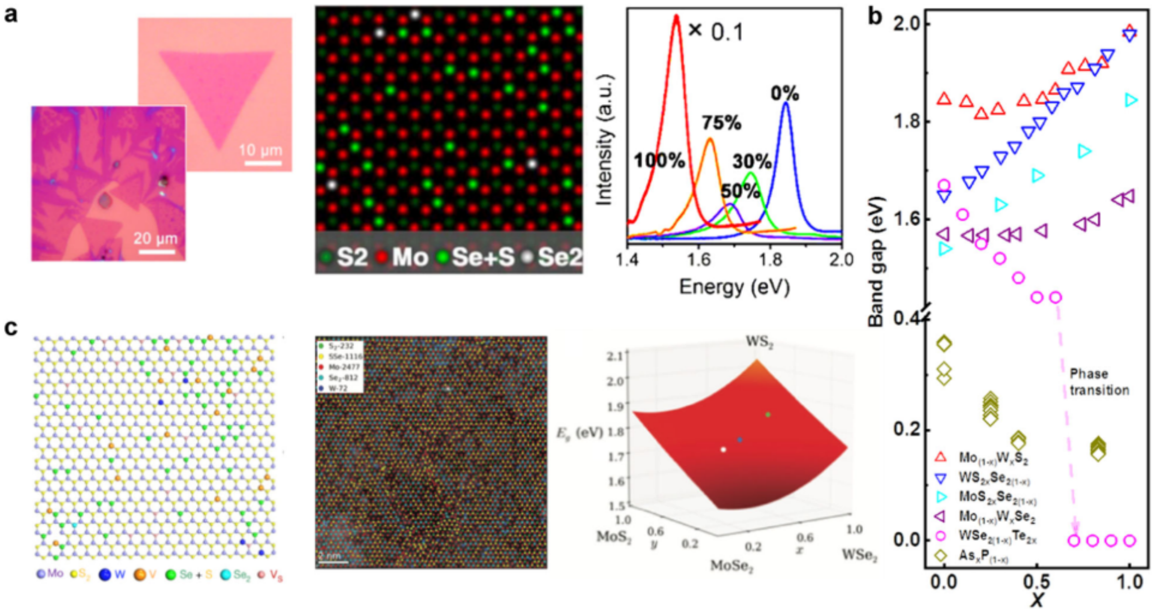

Figure 5: Bandgap tuning by alloying or doping.
(Y. Gong et al., 2014; J. Zhou et al., 2018)

counterparts.

Mechanical exfoliation produces stable, phase pure flakes but suffers from limited size and poor thickness control (Komsa & Krasheninnikov, 2012). Physical vapor deposition (PVD) enables larger films but struggles with dopant incorporation due to thermal decomposition (Feng et al., 2015). Chemical vapor deposition (CVD) has emerged as the most viable method, offering scalable growth of complex alloys from ternary (e.g., $WS_{2x}Se_{2(1-x)}$) to quinary (e.g., $V_xW_yMo_{1-x-y}S_{2z}Se_{2(1-z)}$) systems (J. Zhou et al., 2018). Monolayer TMDC alloys like $MoS_{2(1-x)}Se_{2x}$ maintain direct bandgaps with linear tuning from 1.85 eV (MoS_2) to 1.54 eV ($MoSe_2$) as Se the compositions increases, confirmed by PL and Scanning Transmission Electron Microscopy (STEM) measurements (Y. Gong et al., 2014) (Figure 5a-b). Notably, $WSe_{2(1-x)}Te_{2x}$ undergoes a semiconductor to metal transition above $x = 0.6$ due to a $2H \rightarrow 1T_d$ phase change, illustrating the pronounced electronic impact of alloying (P. Yu et al., 2017). Beyond TMDCs, black arsenic phosphorus (b-As_xP_{1-x}) alloys synthesized via CVT allow bandgap modulation from 0.3 eV to 0.15 eV for infrared applications (B. Liu et al., 2015; Z. Zhang et al., 2015). Recent advances in molten salt CVD enable the fabrication of quaternary (e.g., $Mo_xW_{1-x}S_{2y}Se_{2(1-y)}$) and quinary alloys with DFT predicted bandgaps ranging from 1.60 to 2.03 eV, confirmed by uniform elemental distributions seen in STEM (Susarla et al., 2017; J. Zhou et al., 2018) (see Figure 5c). These developments highlight the potential of alloys for tailored optoelectronics across various spectral regimes. Figure 5a presents characterization data for the composition tuned $MoS_{2(1-x)}Se_{2x}$ the alloys such as optical microscopy of high quality monolayer single crystals and continuous films with $x = 0.1$ (left); STEM image showing atomic structure of 12% Se doped MoS_2 (middle) and systematic redshift in PL emission peaks for compositions ranging from pristine MoS_2 (0% Se) to $MoSe_2$ (100% Se), demonstrating continuous bandgap tuning (Y. Gong et al., 2014). Figure 5b illustrates the correlation between composition and optical bandgap of alloys. Figure 5c shows STEM images of the quinary alloy $V_xW_yMo_{1-x-y}S_{2z}Se_{2(1-z)}$ (left), quaternary alloy $Mo_xW_{1-x}S_{2y}Se_{2(1-y)}$ (middle) and theoretical versus experimental bandgap values color coded by synthesis temperature (right) (Susarla et al., 2017; J. Zhou et al., 2018). This study shows that co-doping vanadium/tungsten at metal sites and sulfur at chalcogen sites in 2D materials enables precise bandgap tuning and synergistic enhancement of the electronic, optical and structural properties compared to the single element doping (Iqbal et al., 2020). Further, tungsten doping in molybdenum based TMDCs and the vice versa is an effective cation substitution processes to tailor their optical properties (Cadiz et al., 2017).

2.2 Multifunctional Properties of TMDC Materials

This section presents the fundamental properties of layered 2D-TMDC materials, encompassing their phonon (vibrational), thermal, electronic and optical behaviors. A comprehensive understanding of these properties is essential for optimizing the layered TMDCs in various applications, including photovoltaics, sensing technologies and nanoelectronics (Pike et al., 2018). The optical, electronic, thermal and phonon properties of these materials are fundamentally influenced by the number of atoms and layer thickness. Increasing the thickness from monolayer to bulk causes a transition from a direct to an indirect bandgap, which alters optical absorption and PL, enabling fine tuning for optoelectronic applications. On the electronic front, thicker materials present more complex defect states and interaction patterns that affect carrier localization and conductivity. Thermally, the addition of layers introduces new vibrational modes and phonon scattering channels, which tend to reduce thermal conductivity while affecting heat capacity and lattice dynamics. These phenomena arise from the anisotropic vdWs structure characteristic of TMDCs, allowing precise engineering of properties via control of thickness and doping. This tunability makes TMDCs highly adaptable for advanced electronics, photonics and energy applications (Togo & Tanaka, 2015; Q. H. Wang, 2020; K. Zhang, 2023; W. Zhao, 2015).

2.2.1 Phonon Properties

Over the past decade, first principles calculations have become central to condensed matter and materials research, particularly with the routine inclusion of phonon analysis in materials modeling (Togo & Tanaka, 2015). Phonon frequencies are obtained from the dynamical matrices derived via Fourier interpolation of interatomic force constants (IFCs) across the Brillouin zone. The finite displacement method (FDM) is widely used for this purpose (Kresse et al., 1995; Parlinski et al., 1997), while density functional perturbation theory (DFPT) offers a direct, derivative free alternative (Pavone & Baroni, 1991). Phonopy an open source code developed by the authors (Togo & Tanaka, 2015) supports both FDM and DFPT derived force constants and enables phonon dispersion, density of states and thermal property calculations (e.g., Helmholtz free energy, entropy, specific heat capacity). It has become a widely adopted tool for lattice dynamics due to its robustness and compatibility with major DFT packages. Phonon analysis provides critical insight into dynamic stability, thermal transport, mechanical response, phase transitions and electron-phonon mediated superconductivity (K. H. Habura et al., 2024; D. Wang et al., 2014). Phonon dispersion relations reveal wave vector, q dependent vibrational modes along high symmetry paths, exposing dynamic instabilities (imaginary frequencies), anharmonicity and sound velocities from acoustic branch slopes (Togo & Tanaka, 2015). The phonon density of states decomposes vibrational contributions by frequency, highlighting atomic participation and enabling prediction of heat capacity and thermal expansion (Togo & Tanaka, 2015; Y. Wang, Shang, et al., 2016). In a crystal with N total number of atoms per unit cell, there are 3 acoustic and 3(N-1) optical branches (Mirabella et al., 1994; Molina-Sanchez & Wirtz, 2011), collectively encoding the material's vibrational, thermodynamic and functional properties from thermoelectrics to quantum materials. Phonopy derived phonon data provide crucial insights into how lattice vibrations influence the electronic, thermal and optical properties of TMDCs, thereby facilitating the design and optimization of advanced materials and devices (Hinsche & Thygesen, 2017).

Symmetry classification, phonon dispersions and lattice vibrations at the Γ point

The classification of lattice vibrational modes is derived from the irreducible representations of the crystal's symmetry group, providing a framework to understand phonon behaviors in crystalline materials (X. Zhang et al., 2016). Group theory analysis reveals that the Γ point vibrations decompose into the following irreducible representations of D_{6h} symmetry (Verble & Wieting, 1970). The mathematical expression of this irreducible representation is given as follows (X. Zhang et al., 2015).

$$\Gamma = A_{1g} + 2A_{2u} + 2B_{2g} + B_{1u} + E_{1g} + 2E_{1u} + 2E_{2g} + E_{2u} \tag{2.1}$$

where A, B and E indicate the symmetry types of the irreducible representations, with A and B being 1D (non-degenerate), E being 2D (doubly degenerate), the subscripts g and u denoting symmetry (gerade) or antisymmetry (ungerade) with respect to inversion and the numbers (1 or 2) distinguishing different irreducible representations of the same symmetry type. One A_{2u} and one E_{1u} are acoustic modes, A_{1g}, E_{1g} and E_{2g} are Raman (R) active, another A_{2u} and E_{1u} are infrared (IR) active, and B_{2g}, B_{1u} and E_{2u} are optically inactive (silent). Here the modes denoted by the letter "E" are doubly degenerate in the xy plane. The breaking of translational symmetry along the z-axis in few layer TMDCs nanolayers (NL-TMQ_2) reduces their crystallographic symmetry compared to bulk materials (Ribeiro-Soares et al., 2014). For odd numbered layers (ONL-TMQ_2), the presence of a horizontal mirror plane (σh) through the TM atoms results in D_{3h} symmetry. Monolayer (1L-TMQ_2), for instance, exhibits nine Γ point vibrational modes decomposing into irreducible representations. In contrast, even numbered layers (ENL-TMQ_2) adopt D_{3d} symmetry due to inversion symmetry (i), lacking σh. For instance, bilayer (2L-TMQ_2), with six atoms per unit cell, shows 18 Γ point modes. Mathematically,

$$\Gamma = 3A_{1g} + 3A_{2u} + 3E_{1g} + 3E_{1u} \tag{2.2}$$

where each coefficient (3) indicates three such modes of each symmetry type, A_{2u} + E_{1u} are IR active and A_{1g} + E_{1g} are R active (see Figure 6a). Crucially, inversion symmetry enforces mutual exclusion of R and IR modes in bulk and ENL-TMQ_2. The atomic displacements and symmetry assignments for these modes are illustrated in Figure 6a (Ataca et al., 2011; Ribeiro-Soares et al., 2014). The points in c) are experimental data extracted from the neutron scattering measurements. The total 9N vibrational modes at the

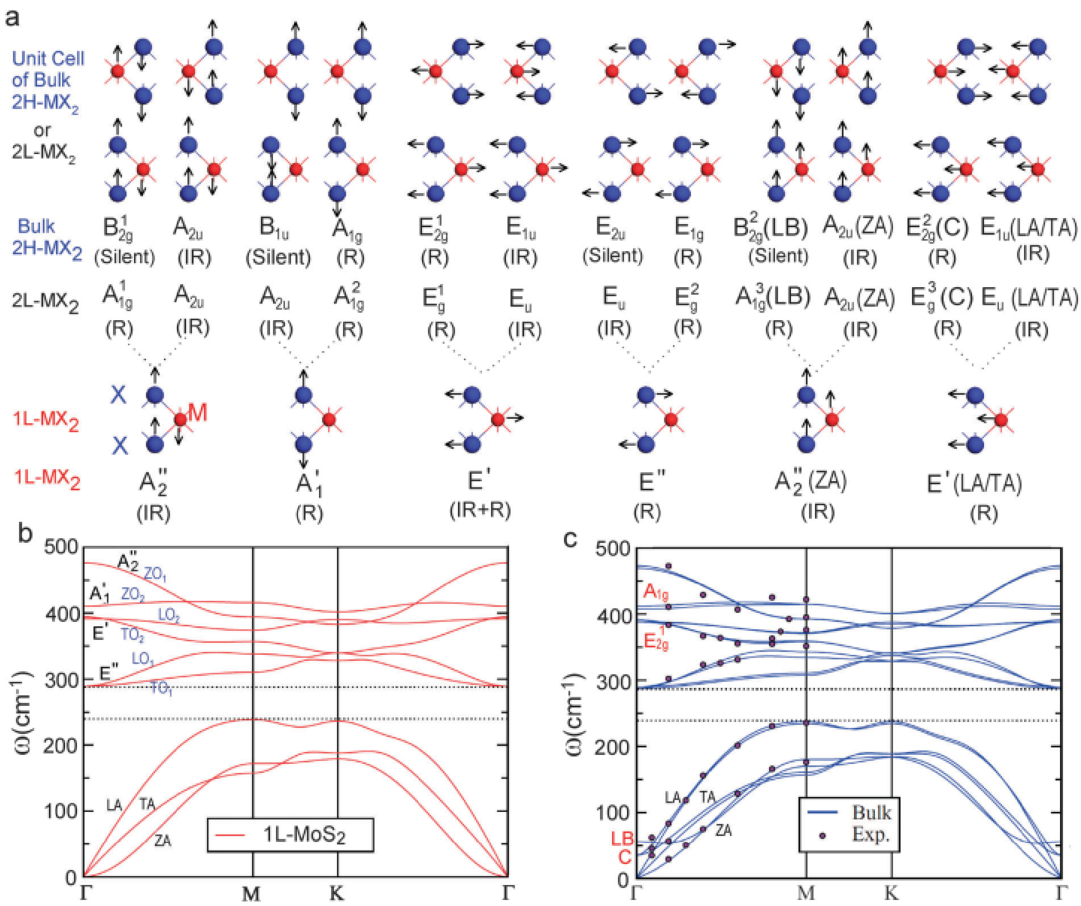

Figure 6: a) Normal displacements of each optical vibration mode for bulk TMQ$_2$, 2L-TMQ$_2$ and 1L-TMQ$_2$, b) phonon dispersion curves for 1L-TMQ$_2$, and c) calculated and experimental phonon dispersion relations for bulk TMQ$_2$.
(Molina-Sanchez & Wirtz, 2011; Wakabayashi et al., 1975)

Γ point for N layer TMQ$_2$ (NL-TMQ$_2$) systems can be classified according to their respective point group symmetries (Ribeiro-Soares et al., 2014; Y. Zhao et al., 2013). These normal modes decompose into irreducible representations that reflect the crystal's layer dependent symmetry constraints, where N represents the number of atomic layers in the material. Mathematically (Ribeiro-Soares et al., 2014), for ONL-TMQ$_2$ (D$_{3h}$) and ENL-TMQ$_2$ (D$_{3d}$), we have that

$$\Gamma_{ONL} = \frac{3N-1}{2}\left(A' + E''\right) + \frac{3N+1}{2}\left(A'' + E'\right) \tag{2.3}$$

$$\Gamma_{ENL} = \frac{3N}{2}\left(A_{1g} + E_{1g} + A_{2u} + E_{1u}\right) \tag{2.4}$$

From the group theory analysis, the 9N vibrational modes separate into three characteristic frequency regimes, including acoustic branches near the Γ-point, ultra low frequency interlayer modes and high frequency optical phonons (X. Zhang et al., 2015). Both versions maintain the core meaning while enhancing technical precision and readability. The first provides more specific frequency information, while the second emphasizes the group theory foundation.

The nine fundamental vibrational modes of monolayer TMQ_2 undergo systematic splitting when transitioning to bilayer (2L) and bulk (bilayer) configurations (Ribeiro-Soares et al., 2014). As illustrated by the dotted correlation lines in Figure 6a, each monolayer phonon branch gives rise to two corresponding modes in thicker crystals due to interlayer coupling and restored translational symmetry. This splitting pattern demonstrates the continuity of vibrational states across different layer thicknesses. In monolayer TMQ_2, the Raman active mode E' (R+IR) splits into different symmetry representations depending on the number of layers (X. Zhang et al., 2015). For instance, in bilayer TMQ_2, it separates into E_{1g} (Raman active) and E_u (infrared active), while in bulk TMQ_2, it divides into E^1_{2g} (Raman active) and E_{1u} (infrared active). The phase relationship between the displacements of the top and bottom layers distinguishes these modes of E_u and E_{1u} exhibit in phase motion, whereas E_{1g} and E^2_{2g} display out of phase motion. The numerical superscript in the mode notation (e.g., E^1_{2g} and E^2_{2g}) helps differentiate modes of the same symmetry and applies universally to other vibrational modes. For E_{1g} and E^1_{2g} in bilayer and bulk TMQ_2, the inter layer coupling between chalcogen (Q) atoms of adjacent layers increases their frequency compared to E_u and E_{1u}, a phenomenon known as Davydov splitting (Verble & Wieting, 1970). This effect also influences other modes in multilayer TMQ_2. Consequently, the frequency of E^1_{2g} in TMQ_2 is typically higher than that of E_{1u}. However, the bulk MoS_2 presents an exception, where E^1_{2g} appears slightly lower in frequency than E_{1u}, suggesting contributions from factors beyond weak inter layer interactions. Similar splitting occurs in the acoustic modes of monolayer TMQ_2. The out of plane acoustic mode A''_1 (ZA) splits into A_{1g} and A_{2u} (ZA) in bilayer TMQ_2 or B_{1g} and A_{2u} (ZA) in bulk TMQ_2. Meanwhile, the in plane acoustic mode E' (LA/TA) divides into E_{3g} and E_u in bilayer TMQ_2 or E^2_{2g} and E_{1u} (LA/TA) in bulk TMQ_2. The A_{1g}/B_{2g} and E_{3g}/E^2_{2g} modes in multilayer TMQ_2 are known as layer breathing (LB) and shear modes, respectively, describing the relative vertical and horizontal motions of adjacent Q-TM-Q layers.

The lattice dynamics of solid materials fundamentally dictate a wide array of their physical properties, encompassing electronic behavior (B. K. Chang, 2024), optical properties (Dai et al., 2023) and thermoelectric performance (Z. Chen et al., 2018). These intrinsic relationships arise because phonon interactions and vibrational modes directly influence charge carrier behavior, photon absorption/ emission processes and heat transport mechanisms in the crystalline solids. As demonstrated by recent studies (Z. Ding et al., 2015; J. Li et al., 2023), the phonon spectrum and its temperature dependence serve as critical determinants of material performance across multiple functional domains, necessitating thorough vibrational analysis for comprehensive materials characterization. TMDCs exhibit a layer dependent electronic band structure. Bulk TMDCs like $MoSe_2$,

MoS_2 and WS_2 have an indirect bandgap caused by interlayer coupling that shifts the CBM away from the K-point. In contrast, their monolayers transition to a direct bandgap at the K-point, enabling strong light matter interaction and efficient PL as first reported by (Mak et al., 2010). As the wave vector, q moves away from the Γ point, the vibrational modes exhibit dispersion, which means that their frequencies vary with, q (X. Zhang et al., 2015). Figure 6b and 6c show the calculated phonon dispersion curves for monolayer and bulk MoS_2, obtained using the DFT within the local density approximation (Molina-Sanchez & Wirtz, 2011; Wakabayashi et al., 1975). The phonon dispersion of monolayer TMQ_2 consists of three acoustic and six optical branches, corresponding to the nine vibrational modes at the Γ point (Wakabayashi et al., 1975). The three acoustic branches include the in plane longitudinal acoustic (LA), transverse acoustic (TA) and out of plane acoustic (ZA) modes (Horzum et al., 2013). Near the Γ point, the LA and TA branches exhibit linear dispersion and higher frequencies compared to the ZA mode. The diagrams show that all phonon branches maintain positive frequencies across the entire Brillouin zone, indicating the material's dynamical stability (Horzum et al., 2013). Further, the figures display the 2D polarizability of the system using a model based on the highest Raman active mode and there is atomic displacement of associated with these Raman active modes. Notably, while recent Raman spectroscopy studies by (Tongay et al., 2012) detected only a single characteristic peak of E_{2g} at 240 cm^{-1} in monolayer $MoSe_2$ where the symmetry based analysis suggests the presence of two additional Raman active modes. This discrepancy between experimental observations and theoretical predictions warrants further investigation. Experimentally, the disappearance of the E" (A_{1g} in bulk), the Raman shift around 170 cm^{-1} which is due to the inactivity of this vibration mode to normally incident light (Horzum et al., 2013).

The symmetry of $MoSe_2$ undergoes a reduction from the D_{6h} point group in its bulk form to D_{3h} in the monolayer configuration. Similar to MoS_2, the monolayer $MoSe_2$'s (Molina-Sanchez & Wirtz, 2011) fundamental lattice vibrations manifest as nine distinct phonon branches, comprising three acoustic and six optical modes. The lattice dynamics analysis reveals the following key behaviors at the Γ point including the vibrational representation decomposes as $\Gamma = A'_1 + 4E' + 2E'' + 2A''_2$. The acoustic branches exhibit distinct dispersion behaviors the in plane LA and TA modes show linear dispersion, while the out of plane ZA mode displays quadratic dispersion near $q = 0$. Close to the Γ point, the measured in plane sound velocities reach $1.5\text{x}10^3$ m/s for LA and $0.9\text{x}10^3$ m/s for TA modes (Horzum et al., 2013). Notably, the phonon dispersion of $MoSe_2$ differs from graphene in two important aspects like a clear energy separation exists between acoustic and optical modes and the A'_1 mode occupies an intermediate frequency position between the E" and E" modes, unlike in MoS_2 and WS_2, where A'_1 represents the highest frequency Raman active mode (Horzum et al., 2013).

2.2.2 Thermal Properties

The thermal properties of TMDCs materials such as layered molybdenum diselenide (2H-MoSe$_2$) as a function of temperature can be effectively tuned through the intentional incorporation of dopants and/or substitutions (Asadi & Nourbakhsh, 2019; D. Wang et al., 2014). Various findings indicate that doping profoundly alters key thermodynamic parameters, namely Helmholtz free energy (F), entropy (S) and specific heat capacity (C$_v$) (Bonilla et al., 2018; J. Li et al., 2020; D. Wang et al., 2014). The observed monotonic decrease in Helmholtz free energy with rising temperature signifies greater thermal stability and is a fundamental consequence of statistical mechanics (Asadi & Nourbakhsh, 2019). This behavior, along with entropy approaching zero at absolute zero and rising with temperature due to increased lattice vibrations, is consistent with the third law of thermodynamics. The rise in entropy is linked to the broadening of phonon modes, an effect modified by dopant induced mass and strain fluctuations within the crystal lattice. The specific heat capacity at constant volume shows a rapid low temperature increase from phonon activation and nears the classical Dulong-Petit limit (Ong et al., 2013) at elevated temperatures. Dopants such as tungsten, vanadium and sulfur alter the phonon density of states by inducing softening or hardening of vibrational modes, thereby affecting the material's thermal storage and transport properties. The capability to tailor these essential thermal properties via controlled dopant compositions underscores the significant potential of defect and alloy engineering for optimizing MoSe$_2$ in applications such as thermoelectrics, thermal management and energy conversion devices. Within the harmonic approximation, electronic contributions to the thermodynamic properties of semiconductors are regarded as negligible; therefore, only lattice vibrational effects are accounted for in these calculations. Within this framework, the Helmholtz free energy, F the constant volume specific heat, C_v and the entropy, S are determined using the following expressions (C. Lee & Gonze, 1995).

$$C_v = 3nNK_B \int_0^{\omega_L} \left(\frac{h\omega}{4\pi K_B T}\right)^2 csch^2\left[coth\frac{h\omega}{4\pi K_B T}\right] g(\omega)d\omega \tag{2.5}$$

$$S = 3nNK_B \int_0^{\omega_L} \left[\frac{h\omega}{4\pi K_B T} coth\frac{h\omega}{4\pi K_B T} - ln\left(2sinh\frac{h\omega}{4\pi K_B T}\right)\right] g(\omega)d\omega \tag{2.6}$$

$$F = 3nNK_B T \int_0^{\omega_L} ln\left(2sinh\frac{h\omega}{4\pi K_B T}\right) g(\omega)d\omega \tag{2.7}$$

where K_B denotes the Boltzmann constant, n indicates the number of active degrees of freedom per atom or per unit cell, N is the number of atoms (or modes) being counted, T is the temperature and ω_L is the maximum phonon frequency, whereas $g(\omega)d\omega$ is the the fractional number of phonon frequencies or phonon density of states in the range between ω

and $\omega + d\omega$. As evident from the equations above, the integration over the entire phonon spectrum is approximated by a summation over a finite set of phonon frequencies, determined by the size of the supercell used in the calculation. The Helmholtz free energy, constant volume specific heat and entropy are connected to the phonon frequencies (phonon density of states) via hyperbolic functions, meaning that lower frequency phonon modes contribute more significantly to these thermodynamic quantities (C. Lee & Gonze, 1995). Substitutional dopants induced lattice distortions modify free energy, heat capacity and entropy, thereby influencing the dynamic stability of the material. Meanwhile, S-Se alloying fine tunes vibrational entropy, shifting phase stability boundaries and potentially affecting thermal expansion and heat capacity (Togo & Tanaka, 2015) of the systems.

2.2.3 Electronic Properties

The electronic band structure of TMDCs exhibits significant thickness, dopant compositions, external electric field, strain, etc., dependent variations (Chaves et al., 2020; Iqbal et al., 2020; Komsa & Krasheninnikov, 2012; Lu & Yang, 2017; Molas et al., 2017; Singh et al., 2018; Sun et al., 2008). For instance, bulk TMDC such as MoS_2 possesses an indirect bandgap of 1.2 eV, which transitions to a direct bandgap of 1.8 eV in the monolayer form. This dramatic change arises from quantum confinement induced shifts in the band edge positions with reduced layer count (Manzeli et al., 2017; Singh et al., 2018). The most prominent manifestation of this phenomenon is the transition from indirect to direct bandgap behaviors in monolayer limit, as schematically shown in Figure 7 (Manzeli et al., 2017). These distinctive thickness tunable electronic properties position TMDCs as ideal candidates for optoelectronic technologies demanding exact bandgap engineering (Mak et al., 2010). The fundamental principles governing electron dynamics in crystalline solids form the theoretical foundation for explaining material properties and technological

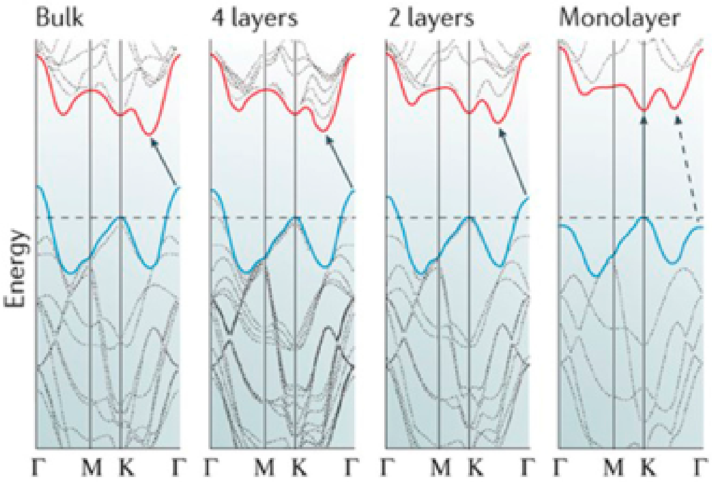

Figure 7: Thickness dependent bandgap of TMDC materials.
(Manzeli et al., 2017)

applications (Sutton, 1993). The electron theory of solids effectively explains the optical, magnetic, thermoelectric and electrical properties of materials (Hummel, 2011). This electronic theory establishes essential fundamentals for technology, forming the backbone of modern civilization such as for switching in the realm of semiconducting electronic devices (Alshammari et al., 2024). The electronic properties of materials are described by the density of states (DOS) such as partial density of states (PDOS) or total density of states (TDOS) (Brixner, 1963), band structure, effective masses of carriers and Fermi level (Iqbal et al., 2020). The electronic energy level distributions of the material and the presence of defects that can cause an alter in the position of atoms in the crystal can be described by the energy band structure of the semiconducting material (M.-Y. Li et al., 2016). In addition to the previously mentioned factors that influence the electronic properties of TMDCs, temperature and pressure (X. Zhang et al., 2015) also play a significant role in shaping these properties. Incorporating non-metal elements such as oxygen, nitrogen and phosphorus into MoS_2 can alter its electronic structure, reduce its band gap, improve its conductivity and generate active sites for catalytic reactions (H. Xu et al., 2021). The room temperature bandgaps of pristine bulk TMDC materials such as WSe_2, WS_2, $MoSe_2$ and MoS_2 materials are 0.97 eV, 0.89 eV, 0.80 eV and 0.75 eV (H.-L. Liu et al., 2020), respectively. The evolution of bandgap with thickness as well as strain in TMDCs (Chaves et al., 2020; H.-L. Liu et al., 2020; X. Zhang et al., 2015) represents a fundamental behavior of their electronic properties, allowing for adjustable optoelectronic behavior that makes these materials suitable for diverse applications including solar cells and quantum technologies. This energy shift occurs when interlayer electron hopping becomes the dominant factor over vdWs interactions, thereby modifying the relative positions of the conduction and valence bands (Pandey et al., 2020). The thickness dependent band structure evolution in Figure 7 reveals progressive shifts in valence and conduction band positions from Γ point localization (bulk) to K-Γ dispersion (few layer) configurations (Manzeli et al., 2017). This demonstrates the thickness dependent bandgap modulation property of 2D TMDCs (Hossen et al., 2024). Monolayer MoS_2 exhibits a direct bandgap of 1.8 eV that reduces to 1.2 eV in bulk form, demonstrating the indirect bandgap transition resulting from layer dependent shifts in band edge positions (Hossen et al., 2024). Additionally, the bandgap transition happens because of the quantum mechanical confinement in the z direction as well as a change in the orbital hybridization of the TM and Q atoms (Manzeli et al., 2017). Beyond modifications to lattice vibrations caused by strain, the electronic properties of monolayer $MoSe_2$ can also display unexpected alterations (Horzum et al., 2013).

Defects in semiconductors cause local structural distortions that alter the crystals' lattice periodic potential, consequently reshaping the material's band structure and electronic properties (D. Su et al., 2024). Gradual energy level transitions correlate with increased effective mass, carrier localization and quantum confinement (D. Su et al., 2024), consistent with (Y. Zhao et al., 2017) who demonstrated p-type conversion in $MoSe_2$ via isovalent nonmetal doping (C, O, Si, S, Te) while maintaining photocatalytic activity (D. Su et al., 2024). Defect and doping engineering modify the electronic structure of semiconductors by introducing mid-gap states, localizing carriers via potential fluctuations and altering chemical bonds (Y. Tian et al., 2020). Zero dimensional defects such as chalcogen vacancies in TMDCs, act as electron donors inducing n-type conductivity (Hossen et al., 2024). This is exemplified by sulfur deficient MoS_2, which clearly demonstrates n-type charge transfer behaviors as shown in Figure 8a (McDonnell et al., 2014). In contrast to sulfur deficient n-type MoS_2, sulfur rich or molybdenum deficient conditions induce p-type conductivity (see Figure 8b) (McDonnell et al., 2014). Remarkably, both carrier types can coexist within different regions of the same sample highlighting the need for precise synthesis control to achieve uniform electronic properties. Sulfur vacancies create two distinct electronic modifications including defect states near the conduction band minimum (CBM) from unsaturated Mo 4d orbitals and shallow states near the valence band maximum (VBM) due to reduced S 3p-Mo 4d orbital hybridization. Transition metal vacancies are particularly detrimental generating mid-gap states that pin the Fermi level via dangling bonds from surrounding chalcogen atoms (Santosh et al., 2014). The electronic behavior of sulfur vacancies evolves with temperature such that at elevated temperatures, localized electrons migrate to neighboring defect states, while low temperature transport occurs via variable range hopping between defect states (Qiu et al., 2013). Sulfur adatoms introduce additional complexity by forming gap states near the VBM through S 3s-Mo 4d orbital hybridization, effectively narrowing the bandgap (Santosh et al., 2014). Additionally, doping provides an effective bandgap engineering strategies (Hossen et al., 2024) for semiconductor materials. For example, in $Mo_xW_{1-x}S_2$ and $Mo_xW_{1-x}Se_2$ alloys, PL studies reveal non-linear bandgap variation due to the bowing effect as shown in Figure 8c (Y. Chen et al., 2013). Theoretical studies confirm that Nb doping induces p-type behaviors in MoS_2 (S. Wang et al., 2018), demonstrating the potential for controlled defect engineering in TMDC materials. Both theoretical (DFT) and experimental studies confirm that the rhenium (Re) as an effective n-type dopant in TMDCs (S. Wang et al., 2018) material. At low doping compositions, Re significantly enhances electrocatalytic performance by reducing the onset potential and improving hydrogen evolution reaction (HER) activity (Aliaga et al., 2019). Unlike conventional TMDCs that show pressure induced bandgap widening, ReS_2 and $ReSe_2$ exhibit anomalous bandgap narrowing under pressure suggesting unique potential for pressure sensitive optoelectronic devices (Oliva et al., 2019). One dimensional defects including grain boundaries and inversion domains dramatically alter electronic properties (Hossen et al., 2024). Sulfur line vacancies at inversion domain boundaries modify local stoichiometry, introducing bandgap states primarily through transition metal contributions (Enyashin et al., 2013). In MoS_2 heterostructures, the coexistence of semiconducting (2H) and metallic (1T) phases creates interface states that are further modulated by defects like sulfur vacancies (V_S and V_{2S}) introduce Fermi level states (especially for interface parallel

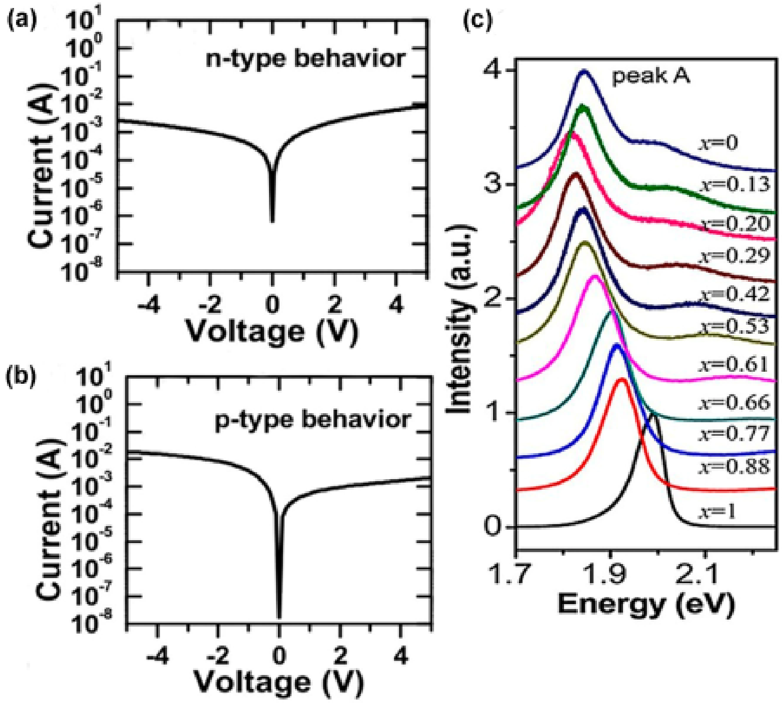

Figure 8: (a) n-type, (b) p-type behaviors and (c) bandgap variations of MoS_2.
(Y. Chen et al., 2013; McDonnell et al., 2014)

divacancies) molybdenum vacancies (V_{Mo}) and their complexes (V_{Mo+3S}, V_{Mo+6S}) generate band edge resonant states from Mo 4d orbitals to enhance carrier injection and anti site defects (e.g., $2S_{Mo}$) create mid-gap states via Mo-S hybridization with Mo vacancies having the most pronounced effect on interfacial electronic structure (Bahmani et al., 2021). Similar defect mediated effects occur in epitaxial $MoSe_2$, where selenium deficiency promotes twin grain boundary formation. Non zigzag oriented mirror twin boundaries (MTBs) in CVD grown $MoSe_2$ introduce bandgap states that locally reduce the bandgap by up to 1 eV, significantly degrading electronic quality and homogeneity (Koós et al., 2019). First principles calculations indicate these defect states increase conductivity through localized in gap charges (Lehtinen et al., 2015). Grain boundary behavior exhibits doping type dependence on atomic termination, they can display either p-type or n-type properties based on the boundary's stoichiometric configuration. This aligns with observations in Nb doped MoS_2, which demonstrates p-type transitional behavior (Y. Chen et al., 2013). This leads to the formation of locally doped regions within the material. Line defects also reduce the rotational symmetry but increase the in plane anisotropy in the quantum conductance (Ghorbani-Asl et al., 2013). The hetero interfaces between two different TMDC materials are another 1D defect that forms a p-n junction. For example, the epitaxial growth of MoS_2-WS_2 and $MoSe_2$-WSe_2 in plane lateral hetero-structures forms 1D interfaces that are p-n junctions (C. Huang et al., 2014; Terrones et al., 2013). Monolayer TMDCs interact via vdWs forces when laterally stacked, creating interfacial regions that function as 2D defects capable of modifying electronic behaviors. Notably, the reduction of multilayer TMDC systems to single layer configurations induces a fundamental band structure transition from indirect to direct bandgap behavior. For instance, the single layer of MoS_2 or WSe_2 shows direct bandgap properties, but beyond the monolayer these TMDC materials show indirect bandgap transition (M.-Y. Li et al., 2016). While DFT calculations suggest that laterally structured TMDC hetero bilayers may exhibit direct bandgap semiconducting behavior with reduced bandgap energy compared to their constituent monolayers (Terrones et al., 2013), experimental observations reveal different behaviors. Both MoS_2-WS_2 and $MoSe_2$-WSe_2 bilayer hetero-structures demonstrate indirect bandgap transitions even in their mono bilayer configurations. Despite this, these hetero-structures show superior electronic performance including enhanced rectification current, strong photovoltaic response and significantly improved short circuit current (approximately 10^3 gain) (Sahoo et al., 2019). The optoelectronic behaviors of these vdWs hetero-structures is fundamentally determined by the unique properties of constituent mono layers and their interlayer coupling distance. This precise structure property relationship makes bilayer configurations exceptionally suitable for next-generation optoelectronic devices. Practical implementations such as MoS_2-WSe_2 based tunneling diodes and photodetectors have already revealed unprecedented device functionalities. Monolayer $MoS_{2x}Se_{2(1-x)}$ can be synthesized through two primary routes like selenization of MoS_2 or sulfurization of $MoSe_2$, resulting in bandgap tunable alloys (S.-H. Su et al., 2014). The chemical vapor transport (CVT) process enables further bandgap engineering and doping modifications (M.-Y. Li et al., 2016). The effective masses of electrons and holes, (m_q^*), are crucial parameters derived from the high symmetry points within a material's electronic band structure (Afrid et al., 2023; Kassa et al., 2024). It plays a vital role in precisely forecasting how charge carriers behave in semiconductors affecting their electrical and optical properties. This, in turn has a direct effect on the functionality and development of electronic and optoelectronic devices. These values are obtained by fitting the energy momentum (E-k) relationship specifically, the VBM for holes and the CBM for electrons to a quadratic polynomial using the given equation (Kassa et al., 2024).

$$m_q^* = \hbar^2 \left(\frac{d^2E}{dk^2} \right)^{-1} \tag{2.8}$$

Here, $q = e$ or h denotes the electrons or holes, while $\hbar = 1.0551 \times 10^{-34}$ J.S, E, and k represent the reduced Planck's constant, the energy at the band extremum and the momentum space coordinate, respectively.

2.2.4 Optical Properties

The optical properties reveal how light interacts with matter and are closely related to the electronic properties of a material, especially its bandgap (Djalab et al., 2023; Vinturaj et al., 2023). This property of the material is described by the complex dielectric function, which depends on frequency (Y. Tian et al., 2020). To describe the optical properties of materials, the electron energy loss function, L(ω), extinction coefficient, k(ω), reflectivity, R(ω), optical absorption coefficient, α(ω) and refractive index, n(ω) (Aktar et al., 2024) are manually determined. Understanding of light interactions with materials those which have significant responses to incoming radiation are good candidates for the optoelectronic (Yamusa et al., 2022) and photonic (Ermolaev et al., 2020) devices applications such as photo-detectors (S. H. Yu et al., 2014), solar cells (Sangwan & Hersam, 2018) and sensors (Cho et al., 2015). Therefore, based on these parameters, the optical properties and the potential applications in solar cells and hydrogen evolution reactions can be assessed (Alshammari et al., 2024). The complex dielectric function, ε(ω) which is characterized by the real, $\varepsilon_1(\omega)$ and imaginary term, $\varepsilon_2(\omega)$ contribute essentially describing the electronic features of materials. The mathematical expression of this function is given by (D. Tian et al., 2016; J. Tian et al., 2018; Y. Tian et al., 2020),

$$\varepsilon(\omega) = \varepsilon_1(\omega) + i\varepsilon_2(\omega). \tag{2.9}$$

In Equ. 2.9, the $\varepsilon_1(\omega)$ and $\varepsilon_2(\omega)$ of the dielectric function provide how materials store and re-emit energy of electromagnetic waves (EMW) and permanent energy absorption of the system, respectively. The $\varepsilon_2(\omega)$ is also equivalent to the sum of all possible transitions between the occupied and unoccupied states (Djalab et al., 2023). The following formula is used to determine the $\varepsilon_2(\omega)$ (Ambrosch-Draxl & Sofo, 2006),

$$\varepsilon_2(\omega) = \frac{e^2\hbar}{\pi m^2\omega^2}\sum_{c,v,k}\int_{BZ}|M_{c,v}(k)|^2\delta[\omega_{c,v}(k)-\omega]d^3k, \tag{2.10}$$

Or

$$\varepsilon_2(\omega) = -\frac{2\omega P}{\pi}\int_0^\infty \frac{\varepsilon_1(\omega')\omega'}{\omega'^2-\omega^2}d\omega'. \tag{2.11}$$

In Equ. 2.11, the momentum dipole elements $M_{c,v}(k) = <u_{c,k}|u_{v,k}>$ are matrix elements for direct transitions between VB$u_{v,k}$ and CBu$_{c,k}$ states (here VB$u_{v,k}$ and CBu$_{c,k}$ represent the valence and conduction bands states at the wavevector k, respectively). The energy $\hbar\omega_{c,v}(k) = E_{c,k} - E_{v,k}$ represents the corresponding transition energy, where ω is the angular frequency of the incident photon, and e and m denote the charge and mass of the charge carriers, respectively. The $\varepsilon_1(\omega)$ is obtained using the imaginary part of dielectric using Kramers Kronig transformation (Gao et al., 2016) as:

$$\varepsilon_1(\omega) = 1 + \frac{2P}{\pi}\int_0^\infty \frac{\varepsilon_2(\omega')\omega'}{\omega'-\omega}d\omega', \tag{2.12}$$

where ω' is the resonance frequency of the material and P is the Cauchy principal value of the integral. The static real dielectric constant, $\varepsilon_1(0)$, of the system is the description of the degree of polarization and systems' binding energy ability to the charge. The higher values of $\varepsilon_1(0)$ suggest that the system has strong polarization and a better ability to bind charges (Kassa et al., 2024; Lahourpour et al., 2019; Y. Li et al., 2014; Loh et al., 2021). This results in a stronger photo-generated electric field, which optimizes the photovoltaic response of the material and beneficial for creating more efficient photodiodes, photodetectors and solar cells (Q. Wang et al., 2013). The values of the static dielectric constant indicate an increase in the rate of photo-excited carriers in the system, which is utilized to enhance the photocatalytic activity of the material. From the complex dielectric function of the system, $\varepsilon_2(\omega)$ gives degree of electrons jumping and the larger values shows the larger the probability of electrons undergoing jumping (Kassa et al., 2024; Lahourpour et al., 2019; L. Li et al., 2017; Y. Li et al., 2013). The transverse dielectric function, $\varepsilon(\omega)$ (Nourbakhsh, 2010), serves as the fundamental descriptor of a material's optical response (Mashmool et al., 2020). This $\varepsilon(\omega)$ consists of two contributions, such as intraband as well as interband transitions (Mashmool et al., 2020), which are used for metals and direct and indirect transitions (Nourbakhsh, 2010), respectively. The complex dielectric function provides critical insights into how materials interact with electromagnetic waves. Analyzing this frequency dependent optical response is essential for assessing a material's suitability for optoelectronic applications (Bhattacharjee & Chattopadhyaya, 2017). Additionally, key optical parameters related to interband transitions in semiconductors can be extracted from the real and imaginary parts of the dielectric function, supplying vital information for calculating other important optical properties such as the refractive index (Djalab et al., 2023).

The absorption coefficient, $\alpha(\omega)$ which describes the percentage of energy absorbed per unit length passing via the systems (Z. Luo et al., 2022), refractive index, n(ω), measuring of the reduction of the speed of light inside that system, R(ω), measures the proportion of light reflected from a surface relative to the incident light intensity, electron energy loss function, L(ω) expresses the loss of energy of a fast electron that crosses the material and pliantly show energy ranges corresponding to the electronic excitation of the various orbitals (Nazir et al., 2018; Yaseen et al., 2021). The optical properties of materials such as bulk or monolayer TMDC can be calculated in two electromagnetic wave polarization such as $\varepsilon_{xx}(\omega)$ and $\varepsilon_{zz}(\omega)$ which are parallel and perpendicular to the surface of the material, respectively, however it is also possible to calculate these optical properties by using the average isotropic optical properties across all systems. The following equations show the relationship between the complex dielectric function and optical parameters (Shawahni et al., 2018; Yaseen et al., 2021),

$$L(\omega) = \frac{\varepsilon_2(\omega)}{\varepsilon_1^2(\omega) + \varepsilon_2^2(\omega)}. \tag{2.13}$$

The energy loss function, $L(\omega)$, describes the energy loss experienced by fast-moving electrons as they pass through a material (Khalid et al., 2020; Shawahni et al., 2018). An electron moving through a dielectric material loses energy due to interactions with the material's electrons and atomic nuclei (Khalid et al., 2020). It is also important to understand that while L(ω) peaks can provide valuable information about electronic transitions, they are not the only factor to consider when evaluating material suitability for optoelectronic applications (Vinturaj et al., 2023).

$$\alpha(\omega)=\frac{\sqrt{2}\omega}{c}\left(\sqrt{\varepsilon_1^2(\omega)+\varepsilon_2^2(\omega)}-\varepsilon_1(\omega)\right)^{1/2} \tag{2.14}$$

The optical absorption coefficient, denoted as $\alpha(\omega)$ (see Eq. 2.14), is a frequency dependent parameter that quantifies how strongly a material absorbs electromagnetic radiation as light propagates via it. It indicates the rate at which the intensity of incident light decreases per unit distance due to electronic transitions triggered by photons of energy $\hbar\omega$. Peaks in $\alpha(\omega)$ reveal allowed optical transitions and critical points in the electronic band structure, while the onset of absorption provides insight into the material's optical bandgap. Overall, $\alpha(\omega)$ serves as a key descriptor of a material's optical response and its suitability for applications in optoelectronic and photonic devices (Kassa et al., 2024; Z. Luo et al., 2022; Vinturaj et al., 2023).

$$n(\omega)=\left(\frac{\varepsilon_1(\omega)+\sqrt{\varepsilon_1^2(\omega)+\varepsilon_2^2(\omega)}}{2}\right)^{1/2} \tag{2.15}$$

From Equ. 2.15, at the low frequency, $(\omega=0)$ the $n(\omega)$ becomes

$$n(\omega)=\sqrt{\varepsilon(\omega)} \tag{2.16}$$

and also the $R(\omega)$ can be deduced as

$$R(\omega)=\frac{(n(\omega)+1)^2+k^2(\omega)}{(n(\omega)-1)^2+k^2(\omega)} \tag{2.17}$$

where c and ω are the speed of light in vacuum and angular frequency of the incoming light, respectively. $R(\omega)$ represents the optical reflectivity of a material as a function of the angular frequency ω of incident light and it tells how much of that incoming electromagnetic radiation is reflected from the material's surface rather than being transmitted or absorbed (Z. Luo et al., 2022). A high value of $R(\omega)$ at a given frequency indicates strong reflection due to factors such as electronic transitions, plasma resonance or dielectric mismatch, while low reflectivity suggests that light at that frequency is more effectively absorbed or transmitted (Mashmool et al., 2020). Thus, $R(\omega)$ provides insight into surface optical behavior, electronic structure features and the material's suitability for applications like mirrors, coatings, optical sensors and photonic devices.

The optical absorption and emission properties of a semiconductor are closely related to its band structure (Kassa et al., 2024). A precise understanding of light matter interactions is crucial for probing the material's internal structure and behavior, which is fundamental to advancing photovoltaic (PV) cells, optoelectronic devices and infrared technologies (Kassa et al., 2024; Noman et al., 2023). In solar cells, optimizing light absorption and minimizing reflection are key to improving efficiency, necessitating the careful selection of materials with appropriate bandgaps and optical properties (M. Zhao et al., 2022). Similarly, in optoelectronic applications such as LEDs, photodetectors and lasers, precise control of light emission including color purity, sensitivity and wavelength tuning depends on a thorough understanding of these optical properties (Jing et al., 2020; Mashmool et al., 2020). The extinction coefficient $k(\omega)$, or mass attenuation coefficient indicates the extent of photon absorption or attenuation within a material during light propagation (Shawahni et al., 2018; Shrivastava et al., 2022),

$$k(\omega) = \left(\frac{\sqrt{\varepsilon_1^2(\omega) + \varepsilon_2^2(\omega)} - \varepsilon_1(\omega)}{2} \right)^{1/2} \tag{2.18}$$

$k(\omega)$ is the extinction coefficient of a material as a function of the angular frequency ω of incident light and it describes how strongly the material attenuates (absorbs and loses) electromagnetic radiation as light travels through it. It is directly related to the imaginary part of the complex refractive index, meaning that higher values of $k(\omega)$ indicate stronger absorption or damping of the light at that frequency. Because it reflects how electronic transitions, defects and band structure features interact with incoming photons, $k(\omega)$ provides important insight into a material's optical absorption behavior, penetration depth of light and overall optical response across the spectrum.

The optoelectronic performance of semiconducting TMDC, including absorption and emission is dictated by their bandgap transitions and exciton dynamics, making them highly tunable for photonic devices (Hossen et al., 2024). The electronic structure of TMDC exhibits tunable bandgap modifications through dopant incorporation, as evidenced by systematic shifts in absorption edges and excitonic features. Photoluminescence spectroscopy quantitatively confirms this bandgap disorder correlation, revealing defect induced spectral broadening and Stokes shifts characteristic of localized state formation. The vdWs heterostructures, enabled by dangling bond free interfaces, exhibit unique properties absent in individual TMDCs. For example, mechanically stacked MoS_2/WSe_2 (with monolayer bandgaps of approximately 1.87 eV and 1.64 eV, respectively) shows a redshifted PL peak at 1.50-1.56 eV (Figure 8c) due to interfacial exciton binding in the type-II band alignment (M.-Y. Li et al., 2016). Similarly, Mo vacancies in $MoSe_2$ introduce midgap states, reducing the bandgap by approximately 0.3 eV (Koós et al., 2019). The minimal lattice mismatch in vapor deposited in plane heterostructures (e.g., MoS_2/WS_2, $MoSe_2/WSe_2$) further facilitates tailored optoelectronic properties. Interface-dominated exciton recombination in TMDC heterostructures enhances light emission intensity by 50% compared to monolayers (Figure 8d) (M.-Y. Li et al., 2016), with photon energies intermediate between component bandgaps. The noncentrosymmetric structure of monolayers enables strong SHG, though polycrystalline films show grain boundary induced signal cancellation and edge termination dependent enhancement. While Bernal stacked 2H bilayers suppress SHG, stacking faults restore nonlinear response, with interlayer twist angles governing signal modulation (Figure 8e) (M.-Y. Li et al., 2016). The pressure- and temperature-independent optical anisotropy of ReQ_2 (Q = S, Se) up to 20 kbar (Oliva et al., 2019) motivates studies of additional nonlinear phenomena and doped hetero-structure engineering. Precisely determining how materials interact with light is essential for gaining insights into their internal structure and properties, which is vital for enhancing the efficiency of PV and optoelectronic devices, as well as for applications in infrared technology (Kassa et al., 2024). For solar cells (PV devices), optimizing how materials absorb and reflect light is crucial for improving their efficiency (Noman et al., 2023). This involves selecting materials with the right bandgap and light absorption properties. In other optoelectronic devices like LEDs, photodetectors, and lasers, understanding these optical properties helps engineers design components with better light emission, purer colors, higher sensitivity and the desired wavelengths of light (M. Zhao et al., 2022).

2.3 Defect on the Properties of TMDC Materials

Defects in TMDC materials arise from various factors, including missing TM or chalcogen atoms, substitutional impurities, adatoms, grain boundaries, charged defects, oxidation and vdWs hetero-epitaxial strain (Hossen et al., 2024). These imperfections are categorized as zero dimensional (0D), one dimensional (1D) or 2D based on their structure (Lin et al., 2016). They can be either intrinsic (inherent to the material) or extrinsic (introduced externally) and significantly influence the electronic, optical and magnetic properties of TMDCs (Hossen et al., 2024; Jing et al., 2020). For instance, anti-site defects in MoS_2 alter its electronic band structure by splitting d-orbital energy levels, creating triplet and singlet states within the bandgap properties that enable their use as quantum bits (Tsai et al., 2022). Similarly, chalcogen vacancies in pristine MoS_2 introduce mid-gap states that enhance photonic emission (Mitterreiter et al., 2021). In $MoTe_2$, antisite defects formed during growth modify the magnetic behavior of the material (Sahoo et al., 2019). Furthermore, chalcogen vacancies can improve electrical contact by reducing resistance at the metal-TMDC interfaces (J. Kumar & Shrivastava, 2023). Meanwhile, grain boundary interactions in TMDCs affect both electrical conductivity and optical response (Hossen et al., 2024). Although both defect free and defect engineered TMDCs have distinct applications, precise defect control is essential. Defects can be either introduced or repaired through in situ (during synthesis) or ex situ (post-synthesis) methods (Lin et al., 2016), allowing tailored modifications for specific functionalities.

Defects in 2D materials significantly influence their optical and electrical properties due to their pronounced impact at atomic scales (Jing et al., 2020; D. Su et al., 2024). First principles studies by (Shafqat et al., 2017) demonstrate that monolayer $MoSe_2$ is highly sensitive to intrinsic point defects vacancies progressively reduce the bandgap and introduce deep electronic states. Similarly, it was (Shu et al., 2017) revealed that defective $MoSe_2$ structures (including vacancies and edges) exhibit exceptional structural stability and electrocatalytic performance. Computational studies have systematically explored how defects modulate $MoSe_2$'s electronic and optical properties (D. Su et al., 2024). The (Guo et al., 2019) demonstrated that halogen passivated Se vacancies in $MoSe_2$ shift defect states from donor to acceptor levels, converting n-type to p-type behavior through controlled doping. Such strategic modifications enable tailored charge transport and enhanced electron mobility, critical for optoelectronic applications. Further (L. Zhou et al., 2021) showed that noble metal dopants (Au, Pt, Pd, Ag, Ru) significantly improve $MoSe_2$'s gas sensing performance by enhancing catalytic activity and stability. The (Cui et al., 2019) extended these insights, revealing Rh-doped $MoSe_2$'s potential for toxic gas sensing and treatment through electronic structure modulation. While these studies highlight $MoSe_2$'s versatility as a 2D material, most focus on single atom doping or isolated defects (D. Su et al., 2024). To address this gap (Y. Zhao et al., 2017) investigated NM-doped $MoSe_2$ (H, B, C, etc.), analyzing its geometric, electronic, and photocatalytic properties.

2.4 Applications of TMDC Materials

In recent years, TMDCs have attracted significant scientific interest due to their unique electronic, optical and magnetic properties, which differ from those of graphene, a zero bandgap semiconductor and h-BN, an insulating material often known as white graphene (Kandemir et al., 2016). First principles calculations have revealed that semiconducting TMDCs exhibit tunable bandgaps across the visible to near infrared spectrum, making them highly promising candidates for nanoelectronic and optoelectronic devices (Ataca et al., 2011; Tonndorf et al., 2013) where graphene lacks a usable bandgap and h-BN cannot support charge transport. The layered molybdenum diselenide (2H-$MoSe_2$), a prominent TMDC, has emerged as a highly promising material to complement or potentially replace graphene in nanoelectronic and optoelectronic applications (Ataca et al., 2012; Chhowalla et al., 2013; Tonndorf et al., 2013). It exhibits distinctive electronic and optical properties, including an intrinsic band gap (Horzum et al., 2013; Tongay et al., 2012; G. Zhang & Yong-Wei, 2017), strong PL (Onga et al., 2016) and a robust PV response (B. K. Chang, 2024). In addition, the favorable electronic and optical properties of 2H-$MoSe_2$ make it an excellent candidate for applications in field effect transistors (Onga et al., 2016), photodetectors (B. K. Chang, 2024) and solar cells (Bernardi et al., 2017; Horzum et al., 2013). Its bandgap, close to that of silicon (approximately 1.1 eV), along with its ability to reversibly switch between metallic and semiconducting phases, further positions 2H-$MoSe_2$ as a promising material for next-generation electronic devices, including flexible and transparent electronics (Duerloo et al., 2014).

Moreover, single layer and few layer TMDCs such as MoS_2 (S. Luo et al., 2015), $MoSe_2$ (Chhowalla et al., 2013), $MoTe_2$ (Chhowalla et al., 2013), WS_2 (Sahoo et al., 2019) and WSe_2 (D. Li et al., 2017), along with their hetero-structures (Tongay et al., 2014), have been successfully synthesized and extensively studied. These materials show great potential across various applications including catalysis (Chhowalla et al., 2013), energy storage (D. Wang et al., 2014), sensing technologies (Jariwala et al., 2014) and electronic devices such as field effect transistors (M. Liu et al., 2013), thermoelectrics (C. Lee et al., 2014) and logic circuits (Jariwala et al., 2014; Q. H. Wang et al., 2012).

2.5 Model Hamiltonians and Density Functional Theory

Density functional theory (DFT) is a quantum mechanical method used in physics, chemistry and materials science to obtain electronic ground state properties of many body systems based on the electron density, $n(r)$ (Kohn & Sham, 1996). In contrast, model Hamiltonians simplify the many electron problem by treating non-interacting fermions (Gori-Giorgi et al., 2006). While DFT is the established approach for quantitative electronic structure calculations of solids and molecules, its accuracy for strongly correlated systems is limited due to the lack of suitable approximations and computational techniques (Kohn & Sham, 1996). Model Hamiltonians provide simplified representations of complex physical systems that capture essential behavior while omitting unnecessary details (Dreizler & Gross, 2012). Although both methods investigate electronic properties in materials, they differ significantly in methodology, applications and underlying assumptions (Dreizler & Gross, 2012).

Hohenberg and Kohn Theorems

The foundation of the DFT method is the Hohenberg-Kohn (HK) theorem, which states that for each given electronic density, $n(r)$, there is one and only one corresponding potential (Görling, 1999). The HK theorem implies that the ground state for any system can be determined by varying the charge density until the global minimum in the energy functional is obtained. For this theorem, we have the Fundamental Pillars of DFT calculations as follows:

First Theorem of HK

The ground state energy of many body system (Sahni & Sahni, 2004) is a unique functional of the particle density. The ground state charge density can uniquely describe all the ground state properties of system. Therefore, the ground state wave function, ψ_0 (which can be determined by the DFT) minimizing the energy functional (Sahni & Sahni, 2004).

$$E[\psi] = \langle\psi|\hat{H}|\psi\rangle \tag{2.19}$$

Using $\psi_0(\rho_0)$ one can determine all properties by calculating;

$$\langle\hat{O}\rangle[\rho_0] = \langle\psi_0[\rho_0]|\hat{O}|\psi_0[\rho_0]\rangle \tag{2.20}$$

where $\hat{O}$ is an arbitrary operator, while ρ_0 is the initial charge density of states for an electron. This is in particular true for the ground state energy, $E[\rho_0]$ or the expectation value of the kinetic energy $\langle\hat{T}\rangle[\rho_0]$ or for the interaction energy of the electrons $\langle\hat{u}\rangle[\rho_0]$.

Second Theorem of HK

A universal functional for the energy $E[n]$ in terms of the density $n(r)$ can be defined and valid for any external potential, $V_{ext}(r)$. For any particular $V_{ext}(r)$, the ground state energy of the system is the global minimum value of this functional and the density that minimizes the functional is the ground state density $n_0(r)$ (Kohn & Sham, 1996).

The Local Density Approximation (LDA)

The local density approximation (LDA) is the first family of exchange correlation (*xc*) functionals (Schmidt & Kalos, 1987), which looks at the case of a homogeneous electron gas. In this system, the electron is assumed to move in uniform (homogeneous) external potential. In DFT, the electron density, $n(r)$, rather than the wave function, $\psi(r)$, serves as the fundamental variable. The mathematical expression of this approximation is given as,

$$E_{xc}^{LAD} = \int n(r)E_{xc}[n(r)]dr. \tag{2.21}$$

Hohnberg and Kohn proved that there exist a universal functional of the density called, G[ρ], such that:

$$E[\rho_r] = \int V_{ext}(r)\rho_r\rho_{r'}d^3r + \frac{1}{2}\int\frac{\rho_r\rho_{r'}}{|r-r'|} + G[\rho] \tag{2.22}$$

where the first term on the right hand side of Equ. 2.22 is the energy due to external potential while the second term is the classical coulomb energy of the electron system.

Generalized Gradient Approximation (GGA)

This approach seeks to improve the LDA by incorporating information about the density's variation (Perdew et al., 1996). These functionals enhance the LDA by accounting for both the $n(r)$ and its local gradient (Perdew, 1991). The GGA functional can be expressed as,

$$E_{xc}^{GGA}[n] = \int n(r) E_{xc}[n(r), \nabla_n] dr \tag{2.23}$$

where $E_{xc}^{GGA}[n]$ is the exchange correlation energy per particle of an electron gas as a function of density of electrons, $n(r)$, whereas ∇_n represents the gradient of the $n(r)$ in space. This method provides more accurate total energies than former. The most widely used GGA functional is the Perdew-Burke-Ernzerhof (PBE) (Perdew et al., 1996), which is employed in this study to investigate the multifunctional properties of two-dimensional TMDCs materials.

The Kohn-Sham Assumptions

The breakthrough enabling high accuracy DFT calculations today is Kohn-Sham (KS) equation (Kohn & Sham, 1996). It introduces wave mechanics into the kinetic energy functional while retaining the $n(r)$, as the central variable elsewhere. Figure 9 presents the iterative workflow used to solve the Kohn-Sham (KS) equation (Eq. 2.24). In this approach,

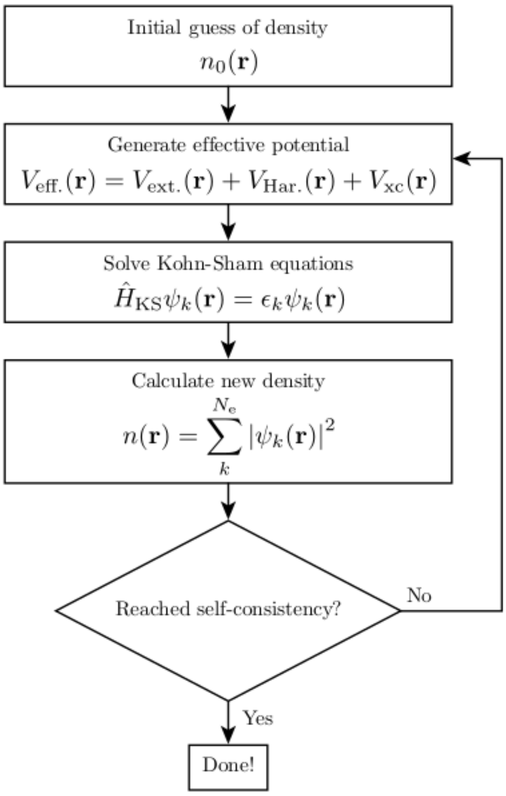

Figure 9: Self-consistence in Kohn-Sham Scheme.
(Kohn & Sham, 1996)

the original interacting n-electron system is replaced by a fictitious system of non-interacting electrons moving in an effective potential, constructed such that it reproduces the exact ground state electron density of the original system. The equation takes the form:

$$\left(-\frac{1}{2}\nabla^2+V_{eff}(r)\right)\psi(r)=E\psi(r) \tag{2.24}$$

where, $V_{eff}(r)=V_H[n]+V_{XC}[n]+V_{ext}(r)$ is the effective potential, $V_{ext}(r)$, is the potential for the interaction between electrons and atoms, $V_H(r)$, is the Hartree potential (electrostatic potential from the electron charge density) which is given by:

$$V_H[n]=\int\frac{n(r')}{|r-r'|}dr' \tag{2.25}$$

The exchange-correlation potential, $V_{XC}[n]$, which is the contribution to the single electron equation and given by:

$$V_{XC}[n]=\frac{\delta E_{XC}[n]}{\delta n(r)} \tag{2.26}$$

here $E_{XC}[n]$ is the exchange-correlation energy as a function of electron density and it can be calculated either LDA or GGA, and $\frac{\delta E_{XC}[n]}{\delta n(r)}$ is the functional derivative. Furthermore, by focusing on electron density, $n(r)$, rather than the many body wavefunction, $\psi(r)$, DFT balances computational efficiency and accuracy across diverse materials (A. Kumar et al., 2024). Among DFT software, Quantum opEn-Source Package for Research in Electronic Structure, Simulation, and Optimization (ESPRESSO) is a prominent open-source package optimized for periodic systems such as crystals, using plane wave basis sets and pseudopotentials to simulate electronic structures effectively (Giannozzi et al., 2009). Complementing this, Phonopy is widely employed alongside DFT codes to calculate phonon and vibrational properties from force constants obtained via DFT, enabling detailed analysis of lattice dynamics and thermal behavior (Togo & Tanaka, 2015).

3. Computational Methodology

This study performed first-principles Density Functional Theory (DFT) calculations using Quantum ESPRESSO (Giannozzi et al., 2009) and Phonopy (Togo & Tanaka, 2015). Electron-electron interactions were treated using the Generalized Gradient Approximation (GGA) and the GGA+U approach, employing the Perdew-Burke-Ernzerhof (PBE) exchange-correlation (xc) functional and incorporating the Hubbard U parameter (Perdew, 1991; Perdew et al., 1996, 1998). The Hubbard U values for the transition-metal atoms (Mo, V, and W) were determined using the linear-response formalism within density-functional perturbation theory (DFPT) combined with the ortho-atomic projection method, following previous first-principles studies on similar transition-metal dichalcogenide systems. The GGA+U scheme was employed to more accurately describe on-site Coulomb interactions in the localized *d* orbitals, which are typically underestimated by standard GGA, thereby improving the treatment of strongly correlated electrons in molybdenum, vanadium, and tungsten based materials. Specifically, these values have been shown to effectively correct self-interaction errors and improve the description of localized *d* electrons in these TM, leading to better agreement with experimentally measured and previously reported theoretical electronic properties. Furthermore, both GGA and GGA+U results are presented to illustrate the impact of the Hubbard correction on the electronic structure and related properties. The differences are evaluated by comparing band-gap values and densities of states, demonstrating that the GGA+U approach provides a more accurate representation of electron-correlation effects than the standard GGA method. The Alloy Theoretic Automated Toolkit (ATAT) is a robust open-source software suite for computational modeling of alloy systems (van de Walle et al., 2002). It efficiently builds cluster expansions from first-principles calculations to accurately predict alloy energetics based on atomic configurations.

Convergence tests for k-points, cutoff energy (ecut), and lattice parameters were followed by variable cell relaxation (vc-relax) using the Broyden-Fletcher-Goldfarb-Shanno (BFGS) algorithm (Pfrommer et al., 1997). After structural optimization, self-consistent field (SCF) and non-self-consistent field (NSCF) calculations with finer k-point meshes enhanced electronic structure accuracy. The post processing extracted properties of 2D 2H-$MoSe_2$ and $V_xW_yMo_{1-x-y}S_{2z}Se_{2(1-z)}$ alloys. The band structure was computed along high symmetry paths (Γ-M-K-Γ) using Monkhorst-Pack grids (Monkhorst & Pack, 1976). Atomic positions were optimized by locating stationary points on the potential energy surface with BFGS. Total energies were obtained via SCF calculations, and forces were derived using the Hellmann-Feynman theory.Atomic positions were refined until energy and forces met convergence thresholds. The density of states (DOS) and partial DOS

(PDOS) were calculated using finer k-point meshes and the tetrahedron method, processed with the dos.x utility. A 2×2×1 supercell (24 atoms) was built with the Phonopy package (Katre et al., 2015; Togo et al., 2008; Togo & Tanaka, 2015). Dopant compositions were 12.5% and 50% for vanadium and tungsten, whereas they were 6.25%, 12.5%, 18.75%, 25%, 50%, and 75% for sulfur substituting molybdenum and selenium sites.

Electron-ion interactions employed the projector augmented wave (PAW) method (Blöchl, 1990), using ultrasoft and norm-conserving pseudopotentials from Quantum ESPRESSO and the Standard Solid State Pseudopotentials (SSSP) library (Hamann et al., 1979). The PBE-GGA functional balanced computational efficiency and accuracy despite known bandgap underestimations (Y. Zhang & Yang, 1998). Hubbard U values, determined self-consistently via linear response within Density Functional Perturbation Theory (DFPT) (K. H. Habura et al., 2024; Izyumov, 1995; Timrov et al., 2018), ranged from 3.2 to 5.0 eV for vanadium, molybdenum, and tungsten, consistent with literature (Cococcioni & de Gironcoli, 2005).Initial lattice parameters were set according to experimental and theoretical data from the Inorganic Crystal Structure Database (ICSD) (Böker et al., 2001; Bronsema et al., 1986; Kam & Parkinson, 1982; Schneemeyer & Sienko, 1980; Schutte et al., 1987) and recent computational work (Z. Luo et al., 2022; Mashmool et al., 2020). Brillouin zone sampling used Monkhorst-Pack grids starting from the unit cell and supercell, progressing to meshes of 12×12×1 for SCF, 16×16×1 for band structure, and 18×18×1 for phonon calculations.

Vibrational properties, Helmholtz free energy, entropy, and specific heat capacity were calculated as a function of temperature with dopant compositions using DFPT combined with Phonopy within the harmonic approximation (Asadi & Nourbakhsh, 2019; Nourbakhsh, 2010). Phonon dispersion and phonon density of states (DOS) were calculated using DFPT for the unit cell, while phonon properties for the supercell were obtained through atomic displacements analyzed with Phonopy. The dielectric function components of the systems were calculated using time-dependent density functional theory (TDDFT) within the independent-particle approximation (Kassa et al., 2024), employing momentum matrix elements and Kramers-Kronig relations (Gao et al., 2016), with dense k-point meshes. Furthermore, structural visualization and supercell generation employed XCrySDen and VESTA. Data visualization of phonon spectra, band structures, and vibrational trends was performed using Xmgrace and Gnuplot for clear graphical presentation. Python, with libraries such as NumPy and SciPy, was employed for data processing, thermal property calculations, automation, YAML data conversion, and statistical analysis.

4. RESULTS AND DISCUSSION

4.1 Multifunctional Properties of 2D $V_xW_yMo_{1-x-y}S_{2z}Se_{2(1-z)}$ Alloys

4.1.1 Convergence Tests

The convergence tests for the pristine bilayer hexagonal molybdenum diselenide (2H-$MoSe_2$) system shown for the unit cell in Figure 10(a-c) and for the supercell in Figure 10(d-f) reveal a consistent trend across all doped variants. In these plots, the total energy decreases steadily as the cut-off energy (Fig. 10a, d), k-point density (Fig. 10b, e), and lattice constant (Fig. 10c, f) increase, plateauing once convergence is reached. This behavior underscores a key principle for modeling 2D materials: selecting an optimal cut-off energy, k-point grid, and lattice constant is essential to obtain accurate and reliable computational results without incurring excessive cost. Because 2D materials are highly sensitive to factors such as defects and interlayer interactions, achieving full convergence in energy and related parameters is critical for making trustworthy predictions of their mechanical, electronic, and optical properties. Similarly, the convergence patterns for 2D materials, $V_xW_yMo_{1-x-y}S_{2z}Se_{2(1-z)}$ of different compositions of V, W, and S can be established by following the same trends; however, this is omitted here to avoid redundancy as well as the computational costs.

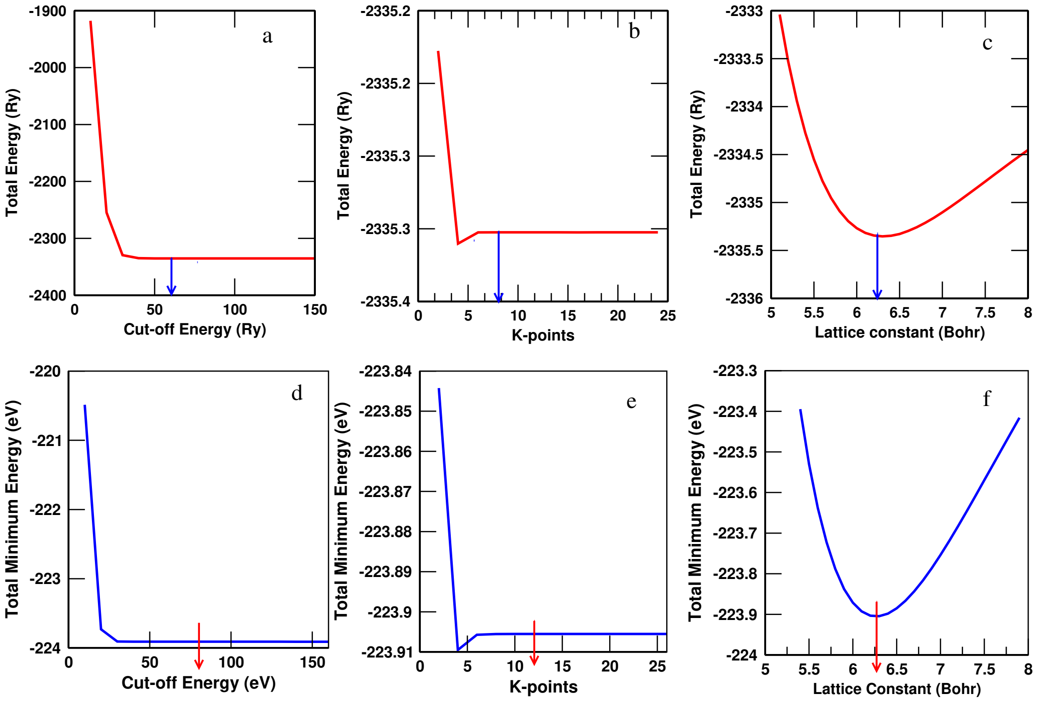

Figure 10: Convergence tests for unit cell (a-c) and supercell (d-f) of 2H-$MoSe_2$.

4.1.2 Structural Properties of $\mathbf{V_xW_yMo_{1-x-y}S_{2z}Se_{2(1-z)}}$

Structural properties including bond lengths, bond angles, and lattice constants were analyzed for the 2D alloy system $V_xW_yMo_{1-x-y}S_{2z}Se_{2(1-z)}$ across a range of dopant and alloy compositions, with particular focus on systems containing vanadium and tungsten, both with and without sulfur substitution.

4.1.2.1 Lattice Parameters of $\mathbf{V_xW_yMo_{1-x-y}S_{2z}Se_{2(1-z)}}$ ($x = 0, 0.5$, $y = 0$, $z = 0, 0.25, 0.5, 0.75$)

Figure 11(a-d) show the optimized hexagonal bilayer structures of the pristine system alongside various substituted systems. Specifically, Figure 11(a) presents the pristine structure, whereas Figure 11(b-d) display the substituted structures containing V atoms, with or without S substitution. These all optimized crystal structures were generated using the XcrysDen software (Kokalj, 1999). The diagrams show that Mo atoms occupy the center of the hexagonal lattice, while S or Se atoms are positioned at the vertices. The calculated lattice constants for the pristine system closely matches both experimental values (Böker et al., 2001) and other theoretical results (Z. Luo et al., 2022). However, some distortions are observed upon V substitution, with or without S, due to the ionic size differences between V and Mo, which is approximately 0.15 Å (J. Deng et al., 2022). The calculated equilibrium lattice constants ($a = b \neq c$), bond lengths (Å), and bond angles ($\alpha = \beta \neq \gamma$) of $V_xW_yMo_{1-x-y}S_{2z}Se_{2(1-z)}$ obtained using XcrysDen software (Kokalj, 1999) are summarized in Table 1. These determined lattice parameters including lattice constants,

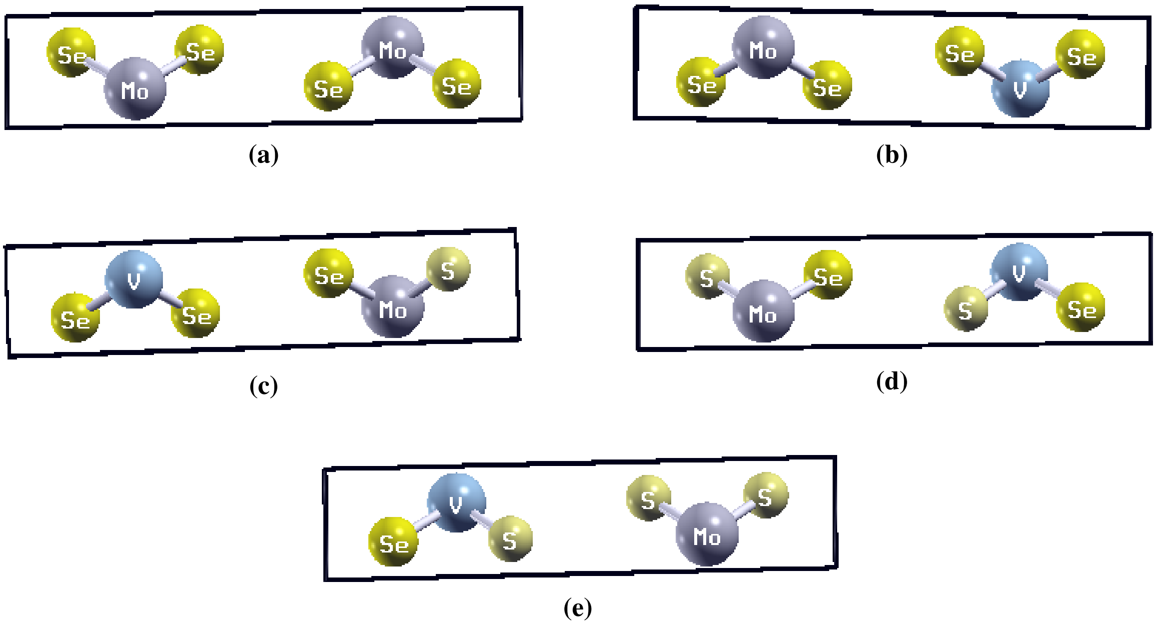

(a) (b) (c) (d) (e)

Figure 11: Unit cell crystal structures for (a) pristine, (b) 50%-V, (c) 50%-V with 25%-S, (d) 50%-V with 50%-S and (e) 50%-V with 75%-S substituted $V_xW_yMo_{1-x-y}S_{2z}Se_{2(1-z)}$ alloys.

bond angles, and bond lengths for both pure and V substituted configurations (with or without S substitution) closely match those of the bilayer pristine systems and previously reported data (Afrid et al., 2023). Additionally, the calculated structural properties of the pure and V-doped systems show good agreement with other theoretical and experimental results (Asadi & Nourbakhsh, 2019; Böker et al., 2001). The atomic radius of the chalcogen increases from S to Se; consequently, the lattice parameters change with varying S composition in a manner that does not strictly follow Vegard's law (Denton & Ashcroft, 1991). Deviations from the linear trend arise from local structural distortions, dopant-induced charge transfer, and modifications in bonding environments. These factors can produce non-linear lattice behavior, emphasizing the need for first-principles calculations to reliably determine the structural properties of these materials. Furthermore, the table indicates that geometric features in both pure and substituted systems are affected by the incorporation of foreign atoms (dopants) (Lin et al., 2020). The shorter bond length between V and Se (V-Se) compared to Mo and Se (Mo-Se) is attributed to V having one fewer valence electron in its d-subshell than Mo (Hoque & Zubair, 2022). Additionally, the Mo-S bond length is shorter than Mo-Se because S atoms are smaller than Se atoms.

Table 1: Optimized lattice parameters of $V_xW_yMo_{1-x-y}S_{2z}Se_{2(1-z)}$ alloys with experimental and theoretical values.

Structure	a(b) (Å)	c/a	BA (°)	BL (Å)
$V_xW_yMo_{1-x-y}S_{2z}Se_{2(1-z)}$				
$x = y = z = 0$	3.30	4.03	Se-Mo-Se = 81	Mo–Se = 2.51
Exp'l	3.29 (Böker et al., 2001)			3.93 (Muhammad, 2021)
Others	3.33 (Z. Luo et al., 2022)			
$x = 0.5, y = 0, z = 0$	3.31	4.00	Mo-V-Se = 78	V-Se = 2.51
$x = 0.5, y = 0, z = 0.25$	3.24	4.02	Mo-V-Se = 77	V-1S = 2.45
$x = 0.5, y = 0, z = 0.5$	3.26	4.06	Mo-V-Se = 76	V-2S = 2.50
$x = 0.5, y = 0, z = 0.75$	3.21	4.04	Mo-V-Se = 75	V-3S = 2.49

4.1.2.2 Lattice Parameters of $V_xW_yMo_{1-x-y}S_{2z}Se_{2(1-z)}$ ($x = 0$, $y = 0, 0.5$, $z = 0, 0.25, 0.5, 0.75$)

The energy minimized structures of 2H-$MoSe_2$ and $V_xW_yMo_{1-x-y}S_{2z}Se_{2(1-z)}$ alloy compositions, visualized using the XCrySDen software (Kokalj, 1999), are illustrated in Figure 12(a-d). These figures present the atomic configurations of a) the pristine 2H-$MoSe_2$ unit cell and three co-substituted variants such as b) $W_{0.5}Mo_{0.5}S_{0.5}Se_{1.5}$, c) $W_{0.5}Mo_{0.5}S_1Se_1$ and d) $W_{0.5}Mo_{0.5}S_{1.5}Se_{0.5}$ alloys.

The comparison of lattice parameters which are obtained from the present calculations, experimental measurements and previously reported using first principles studies are exhibited from Table 2. The current findings are in good agreement with the GGA

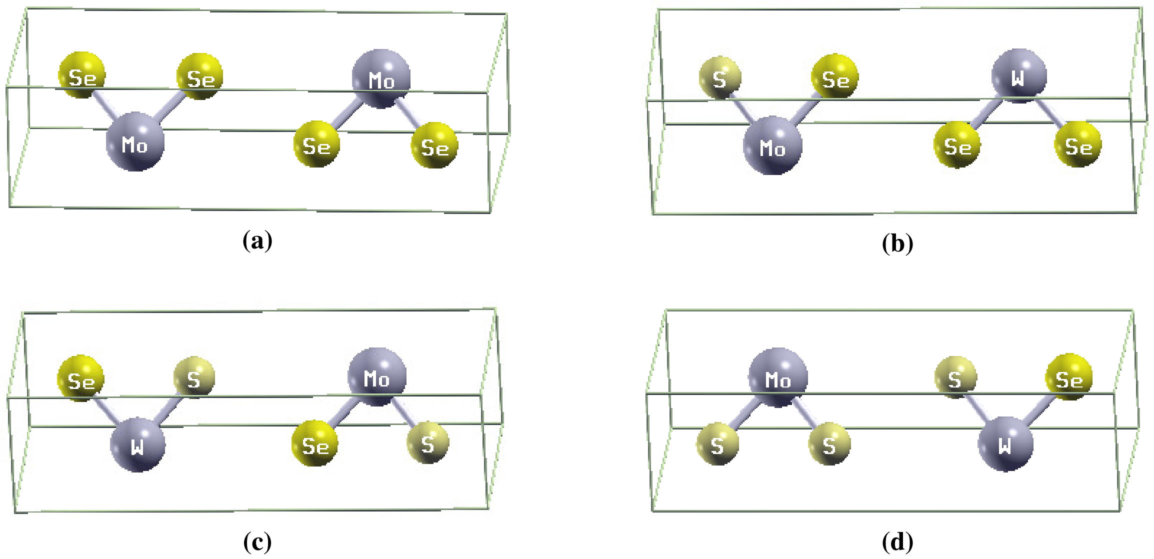

(a) **(b)**

(c) **(d)**

Figure 12: Optimized crystal structures for a 1 × 1 × 1 unit cell of (a) pure, (b) mono-W with monosulfide, (c) mono-W with disulfide, and (d) mono-W with trisulfide $V_xW_yMo_{1-x-y}S_{2z}Se_{2(1-z)}$ alloys.

Table 2: Optimized lattice parameters for $V_xW_yMo_{1-x-y}S_{2z}Se_{2(1-z)}$ alloys obtained from the current calculation and other theoretical as well as experimental reported values.

Composition	***a* (Å)**	***c* (Å)**	**BA (°)**	**BL (Å)**
$x = y = z = 0$	3.30	13.30	Se-Mo-Se = 81.2	Mo-Se = 2.51
Exp'l	3.30 (Böker et al., 2001)			3.93 (Muhammad, 2021)
Other	3.34 (Mashmool et al., 2020)	13.32 (Wickramaratne et al., 2014)	81	2.51 2.54 (Afrid et al., 2023)
$x = 0, y = 0.5, z = 0.25$	3.28	13.27	Se-Mo-Se = 79.6 Se-W-S = 81.2 S-Mo-Se = 82.6	Mo-Se = 2.51 W-Se = 3.27 Mo-S = 2.41 W-Se = 2.51
$x = 0, y = 0.5, z = 0.5$	3.25	13.15	S-W-Se = 80.2 Se-W-Se = 80.0	W-S = 2.40 W-Se = 2.51 Mo-Se = 2.51 Mo-S = 2.39
$x = 0, y = 0.5, z = 0.75$	3.28	12.97	S-Mo-S = 78.8 Se-W-Se = 79.7	W-S = 2.42 W-Se = 2.50 Mo-S = 2.44

calculations reported in Ref. (Asadi & Nourbakhsh, 2019; Mashmool et al., 2020) and lie within the usual range of DFT deviations from experimental measurements. In this table, the observed contraction in the lattice constants is attributed due to the smaller ionic size of S^{2-} (1.84 Å) substituted in Se^{2-} (1.98 Å) (Asadi & Nourbakhsh, 2019), and stability from W^{4+} (0.80 Å) replacing Mo^{4+} (0.79 Å) (K. H. Habura et al., 2024). Furthermore, as the chalcogen ionic radius increases from S to Se, the lattice parameters of $V_xW_yMo_{1-x-y}S_{2z}Se_{2(1-z)}$ alloys vary with increasing S composition,x, in a manner that deviates from Vegard's law (Asadi & Nourbakhsh, 2019). The Pauli dimensionless electronegativity (EN) values (Hall, 1978) for the constituent elements follow the trend Mo (2.16) < W (2.36) < Se (2.55) < S (2.58) (Rudnev et al., 2017), reflecting increasing electron affinity across the chalcogen series and transition metal components.

4.1.2.3 Lattice Parameters of $\mathbf{V_xW_yMo_{1-x-y}S_{2z}Se_{2(1-z)}}$ ($x = 0$, $y = 0, 0.125$, $z = 0, 0.0625, 0.125$)

Figure 13(a-d) show the energy optimized supercell (SC) structures of the undoped unit cell of 2H-$MoSe_2$ and doped $V_xW_yMo_{1-x-y}S_{2z}Se_{2(1-z)}$ systems, as visualized with the XCrySDen software (Kokalj, 1999). These figures exhibit the atomic arrangements of a) the pristine 2H-$MoSe_2$ and S with or without W doped variants such as b) $MoS_{0.125}Se_{1.875}$, c) $W_{0.125}Mo_{0.875}S_{0.125}Se_{1.875}$ and d) $W_{0.125}Mo_{0.875}S_{0.25}Se_{1.75}$ materials. These crystal structures correspond to the pristine a), monosulfide b), W-monosulfide c) and W-disulfide d) doped systems, respectively. Furthermore, the side view representations show that each structure was fully geometry optimized in the simulations to ensure equilibrium configurations.

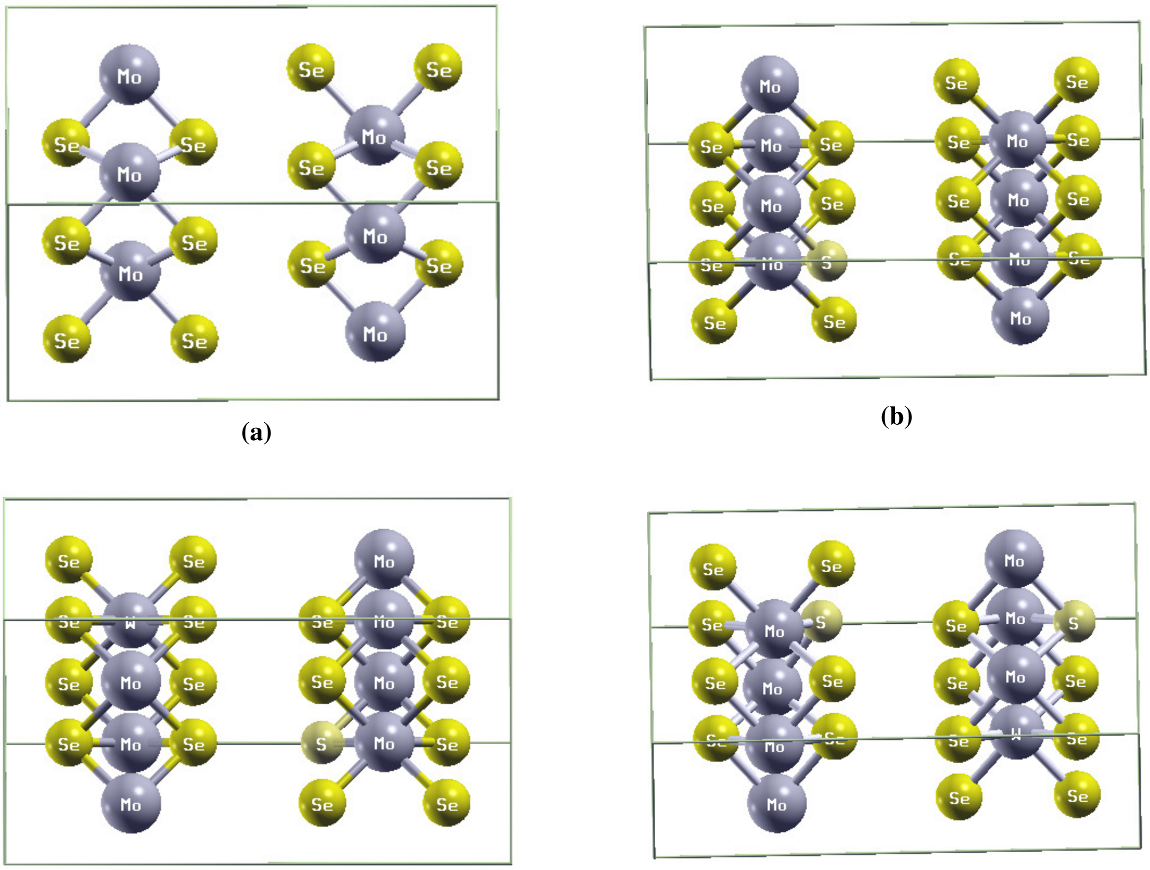

(a)

(b)

(c)

(d)

Figure 13: Optimized crystal structures of a 2 × 2 × 1 supercell for (a) undoped, (b) monosulfide, (c) mono-W with monosulfide, and (d) mono-W with disulfide $V_xW_yMo_{1-x-y}S_{2z}Se_{2(1-z)}$ alloys.

Table 3 provides a comparison of the lattice parameters obtained from the present calculations, experimental measurements, and previously reported first principles studies. The current findings are in good agreement with the GGA calculations reported in Ref. (Asadi & Nourbakhsh, 2019; Mashmool et al., 2020) and lie within the usual range of DFT

Table 3: Optimized lattice parameters, bond angles and bond lengths for $V_xW_yMo_{1-x-y}S_{2z}Se_{2(1-z)}$ alloys from the present work, compared with experimental and theoretical literature.

Composition	a (Å)	c (Å)	Bond Angles (°)	Bond Lengths (Å)
$x = y = z = 0$ ($MoSe_2$)	3.134	13.06	Se-Mo-Se: 86	Mo-Se: 2.53
Experiment	3.29[a]			Mo-Se: 3.93[b]
Previous theory	3.34[c]	13.31-13.32[d]	81	2.51-2.54[e]
$x = y = 0,\ z = 0.0625$	3.295	13.805	Se-Mo-Se: 83 S-Mo-Se: 81	Mo-Se: 2.53 Mo-S: 2.40
$x = 0,\ y = 0.125,\ z = 0.0625$	3.293	13.605	S-W-Se: 81 Se-W-Se: 81	W-S: 2.41 W-Se: 2.50 Mo-Se: 2.51 Mo-S: 2.50
$x = 0,\ y = 0.125,\ z = 0.125$	3.170	13.284	S-Mo-S: 80 Se-W-Se: 80	W-Se: 2.49 Mo-S: 2.50

[a](Schutte et al., 1987), [b](Muhammad, 2021), [c](Mashmool et al., 2020), [d](Wickramaratne et al., 2014), [e](Afrid et al., 2023).

deviations from experimental measurements. In this table, the observed contraction in the lattice constants is attributed to the smaller ionic size of S^{2-} (1.84 Å) doped in Se^{2-} (1.98 Å) (Asadi & Nourbakhsh, 2019), and stability from W^{4+} (0.80 Å) replacing Mo^{4+} (0.79 Å) (K. H. Habura et al., 2024). Furthermore, as the chalcogen atomic radius increases from S to Se (in the periodic table), the computed lattice parameters of the $V_xW_yMo_{1-x-y}S_{2z}Se_{2(1-z)}$ materials exhibit an almost linear decrease with rising S composition (y), in disagreement with Vegard's law (Asadi & Nourbakhsh, 2019). The deviation from Vegard's law is slightly more pronounced for the in plane lattice parameter a, while the out of plane parameter c shows only a negligible deviation and can be considered to follow the ideal mixing behavior. This difference arises from the nature of the bonding, specifically whether it is covalent or governed by vdWs interactions. The Pauli electronegativity (EN) values of the constituent elements follow the order Mo (2.16) < W (2.36) < Se (2.55) < S (2.58) (Hall, 1978; Rudnev et al., 2017), indicating a progressive increase in electron affinity across both the TMs and the chalcogen series. This growing EN difference suggests a stronger polar interaction between the atoms, likely leading to enhanced atomic attraction and the formation of more robust covalent bonds. The calculated Mo-Se bond length of 2.53 Å in pristine 2H-$MoSe_2$ shows consistency with established experimental and other theoretical values reported in prior studies (Hilaire et al., 2020; C.-Y. Li et al., 2019). Moreover, this table presents the bond lengths and angles across the $V_xW_yMo_{1-x-y}S_{2z}Se_{2(1-z)}$ series, revealing composition dependent structural trends with varying chalcogen content ($y = 0, 0.125; z = 0.0625, 0.125$). The W-disulfide co-doped system exhibits the most reduced bond angles, primarily attributed to Se's lower EN relative to S (Rudnev et al., 2017). Notably, all compositions exhibited consistent and expected trends in bond lengths and bond angles, in close agreement with previous theoretical studies

(Afrid et al., 2023; Gan et al., 2014), where differences in ionic size were found to directly influence bond angle distortions. A detailed summary of the changes in essential structural parameters with varying S content in the $V_xW_yMo_{1-x-y}S_{2z}Se_{2(1-z)}$ system is presented in Table 3. These results show good agreement with the previous reported theoretical values (Asadi & Nourbakhsh, 2019; Lin et al., 2020). Moreover, as shown in the table, W-Se bonds are shorter than Mo-Se bonds in the crystal structure, which can be attributed to W having a lower number of valence electrons in the d-subshell compared to Mo, leading to stronger orbital contraction (Hoque & Zubair, 2022). In contrast, Mo-S bonds are shorter than Mo-Se bonds due to S's smaller atomic radius, allowing for a closer and more compact bonding interaction with the metal atom (Gibbs et al., 2017; K. Habura et al., 2023).

4.1.2.4 Lattice Parameters of $V_xW_yMo_{1-x-y}S_{2z}Se_{2(1-z)}$ ($x = 0.125$, $y = 0$, $z = 0.0625, 0.125, 0.1875$)

Figure 14(a-d) illustrates the optimized supercell structures of $V_xW_yMo_{1-x-y}S_{2z}Se_{2(1-z)}$ systems for $x = 0.125, y = 0, z = 0$, $x = 0.125, y = 0, z = 0.0625$, $x = 0.125, y = 0, z = 0.125$ and $x = 0.125, y = 0, z = 0.1875$ compositions visualized using the XCrySDen software (Kokalj, 1999). These figures indicate that the atomic configurations of vanadium containing systems with and without sulfur dopant compositions, (a) $V_{0.125}Mo_{0.875}Se_2$, b) $V_{0.125}Mo_{0.875}S_{0.125}Se_{1.875}$, c) $V_{0.125}Mo_{0.875}S_{0.25}Se_{1.75}$ and d) $V_{0.125}Mo_{0.875}S_{0.375}Se_{1.625}$), materials.

Table 4: Optimized lattice parameters for $V_xW_yMo_{1-x-y}S_{2z}Se_{2(1-z)}$ alloys obtained from the present calculation and experimental as well as other theoretical studies.

Composition	a **(Å)**	c **(Å)**	**Bond Angles (BA, °)**	**Bond Lengths (BL, Å)**
$x = 0.125, y = z = 0$	3.13	13.05	Se-V-Se = 84	V-Se = 2.50
$x = 0.125, y = 0, z = 0.0625$	3.12	13.04	Se-V-Se = 86	V-Se = 2.44; Mo-S = 2.35
$x = 0.125, y = 0, z = 0.125$	3.11	13.05	Se-V-Se = 83; Se-Mo-S = 80.6	Mo-S = 2.4; V-Se = 2.5; Mo-Se = 2.53
$x = 0.125, y = 0, z = 0.1825$	3.285	13.78	Se-V-Se = 83; Se-Mo-Se = 82	V-Se = 2.5; Mo-S = 2.41

Comparison of lattice parameters (bond lengths, bond angles and lattice constants) corresponding to different dopant compositions of vanadium and sulfur atoms is presented in Table 4 . The present results show good consistency with the GGA based calculations reported in Ref. (Asadi & Nourbakhsh, 2019; Mashmool et al., 2020) and fall within the typical range of DFT deviations observed relative to experimental data. In this table, the observed contraction in the lattice constants is attributed to the smaller ionic size of S^{2-} (1.84 Å) doped in Se^{2-} (1.98 Å) (Asadi & Nourbakhsh, 2019), and stability from V^{3+} (0.80 Å) replacing Mo^{4+} (0.79 Å) (K. H. Habura et al., 2024). Moreover, as the chalcogen atomic radius decreases from Se to S in the periodic table, the calculated lattice parameters of the $V_xW_yMo_{1-x-y}S_{2z}Se_{2(1-z)}$ compounds show an almost linear reduction with increasing sulfur compositions (z), which is not consistent with Vegard's law (Asadi &

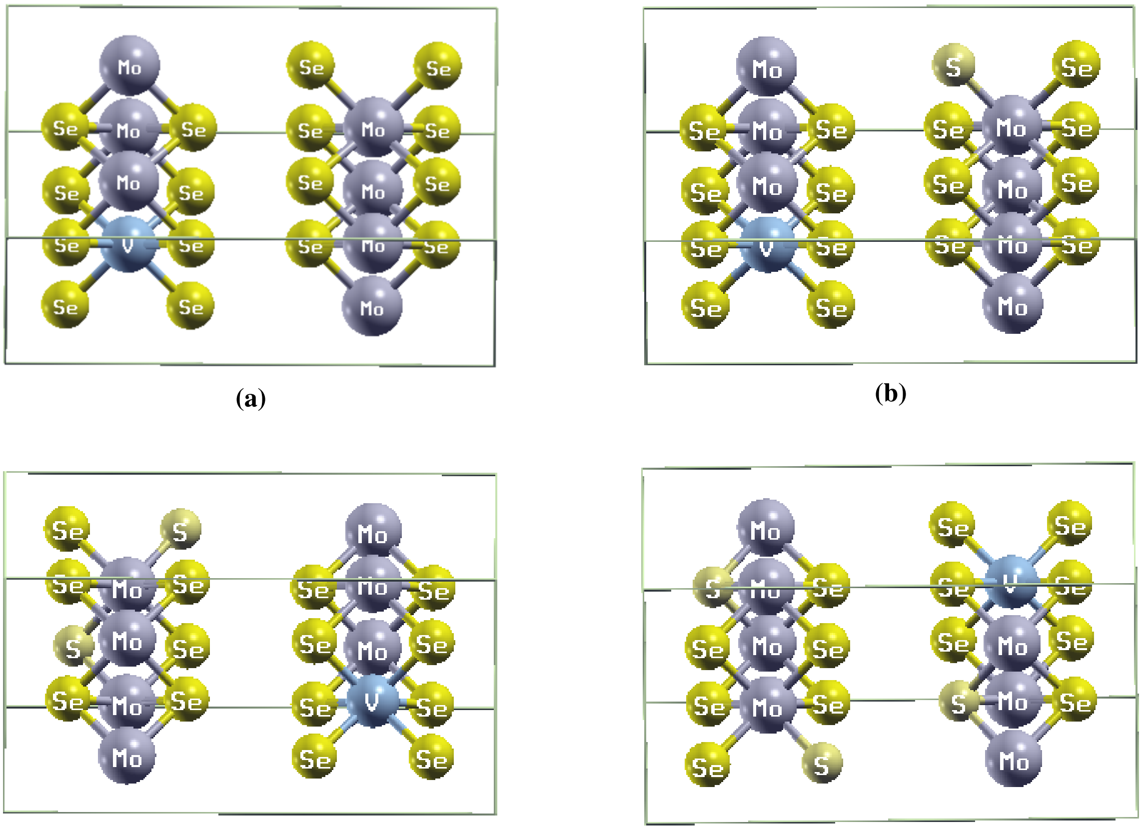

(a) **(b)**

(c) **(d)**

Figure 14: Supercell crystal structures of (a) mono-V, (b) mono-V with monosulfide, (c) mono-V with disulfide, and (d) mono-V with trisulfide for $V_xW_yMo_{1-x-y}S_{2z}Se_{2(1-z)}$ alloys.

Nourbakhsh, 2019). The deviation from Vegard's law is slightly more pronounced for the in plane lattice parameter a, while the out of plane parameter c shows only a negligible deviation and can be considered to follow the ideal mixing behavior. This difference arises from the nature of the bonding, specifically whether it is covalent or governed by vdWs interactions. The Pauli EN values of the constituent elements follow the order of V (1.63) $<$Mo (2.16) $<$ Se (2.55) $<$ S (2.58) (Hall, 1978; Rudnev et al., 2017), indicating a progressive increase in electron affinity across both the TMs and the chalcogen series. This growing EN difference suggests a stronger polar interaction between the atoms, likely leading to enhanced atomic attraction and the formation of more robust covalent bonds. Moreover, this table presents the bond lengths and angles across the $V_xW_yMo_{1-x-y}S_{2z}Se_{2(1-z)}$ series, revealing composition dependent structural trends with varying chalcogen compositions ($x = 0, 0.125; z = 0.0625, 0.125, 0.1875$). Notably, all compositions illustrated consistent and expected trends in bond lengths and bond angles, in close agreement with previous theoretical studies (Afrid et al., 2023; Gan et al., 2014; Rudnev et al., 2017), where differences in ionic size were found to directly influence bond angle distortions. A detailed summary of the changes in essential structural parameters with varying S dopant compositions in the $V_xW_yMo_{1-x-y}S_{2z}Se_{2(1-z)}$ system is presented in

Table 4. These results show good agreement with the previous reported theoretical values (Asadi & Nourbakhsh, 2019; Lin et al., 2020). Moreover, as shown in the table, V-Se bonds are shorter than Mo-Se bonds in the crystal structure, which can be attributed to V having a lower number of valence electrons in the d-subshell compared to Mo, leading to stronger orbital contraction (Hoque & Zubair, 2022). In contrast, Mo-S bonds are shorter than Mo-Se bonds due to S's smaller atomic radius, allowing for a closer and more compact bonding interaction with the metal atom (Gibbs et al., 2017; K. Habura et al., 2023).

4.1.3 Phonon and Thermal Properties of $V_xW_yMo_{1-x-y}S_{2z}Se_{2(1-z)}$

This section discusses phonon properties including dispersion relations, phonon density of states (PhDOS) and thermodynamical properties (Helmholtz free energy, entropy and specific heat capacity) of layered $V_xW_yMo_{1-x-y}S_{2z}Se_{2(1-z)}$ alloys focusing on various substitutional compositions and types. These lattice vibration properties significantly influence the thermal and dynamic stability of the materials (Molina-Sanchez & Wirtz, 2011). Phonon dispersion relations describe atomic vibrations within the crystal lattice and are crucial for understanding and tuning thermal conductivity and related properties (Wakabayashi et al., 1975). Additionally, thermal properties provide insights into thermodynamic behavior of the alloys across different compositions and temperatures, impacting their stability and functional performance.

4.1.3.1 Phonon Properties of $V_xW_yMo_{1-x-y}S_{2z}Se_{2(1-z)}$ ($x = 0, 0.5$, $y = 0$, $z = 0, 0.25, 0.5$)

Figure 15 presents the phonon dispersion relations of 2H-$MoSe_2$, $V_{0.5}Mo_{0.5}Se_2$, $V_{0.5}Mo_{0.5}S_{0.5}Se_{1.5}$ and $V_{0.5}Mo_{0.5}S_1Se_1$ materials. Dynamic stability of these systems is confirmed by the absence of imaginary frequencies throughout the Brillouin Zone. Our calculations for dopant compositions of $x = 0.5$, $z = 0$; $x = 0.5, z = 0.25$ and $x = 0.5$, $z = 0.5$ indicate that $V_xMo_{1-x}S_{2y}Se_{2(1-y)}$ alloys remain dynamically stable across these compositions. The case of $x = 0.5$, $z = 0.75$ is expected to follow the same trend and was not explicitly computed. The phonon dispersion relations as a function of wavevector, $\omega(q)$ in Figure 15(a-d) illustrate the relationship between phonon frequency (cm^{-1}) and $\omega(q)$, revealing their vibrational properties. Specifically, Figure 15b, 15c and 15d show that increased overlap between acoustic and optical modes at low frequencies in $V_{0.5}Mo_{0.5}Se_2$, $V_{0.5}Mo_{0.5}S_{0.5}Se_{1.5}$ and $V_{0.5}Mo_{0.5}S_1Se_1$, respectively, enhances anharmonicity, reducing thermal conductivity (Bejo et al., 2025). Figure 15a shows phonon bandgaps between 193-217 cm^{-1} and 230-264 cm^{-1}, which hinder phonon transport and lead to lower thermal conductivity (Aktar et al., 2024). The acoustic and optical branches appear clearly separated, with acoustic modes at lower frequencies and optical modes at higher frequencies (Molina-Sanchez & Wirtz, 2011). The phonon spectra along the high symmetry

Γ-M-K-Γ path further demonstrate the structural stability and lattice dynamics of $V_xMo_{1-x}S_{2z}Se_{2(1-z)}$ alloys. Increasing S content shifts phonon frequencies upward (up to ≈ 400 cm^{-1}), reflecting stronger bonds and enhanced stiffness. No negative frequencies are observed, confirming the absence of soft modes or phase transitions (Togo & Tanaka, 2015). The growing complexity of the phonon band structure, with additional branches and mode crossings, suggests greater atomic diversity and possible strain effects in the mixed alloys. Overall, these results confirm that $V_xMo_{1-x}S_{2z}Se_{2(1-z)}$ maintains structural integrity while offering tunable vibrational properties, making them promising for thermoelectric, optoelectronic and nanomechanical applications leveraging phonon engineering (Z. Chen et al., 2018). The phonon band structure of $V_xMo_{1-x}S_{2z}Se_{2(1-z)}$ systems exhibits between 193 and 217 cm^{-1}, indicating a frequency range with negligible vibrational states. The high frequency optical branches (>230 cm^{-1}) are relatively flat, suggesting localized vibrations likely involving lighter S atoms behavior that would manifest as sharp peaks in the phonon density of states (PhDOS). Although the full PhDOS was not computed, the dispersion reveals distinct frequency regimes dominated by specific atomic motions, implying a non-uniform distribution of vibrational states across the spectrum.

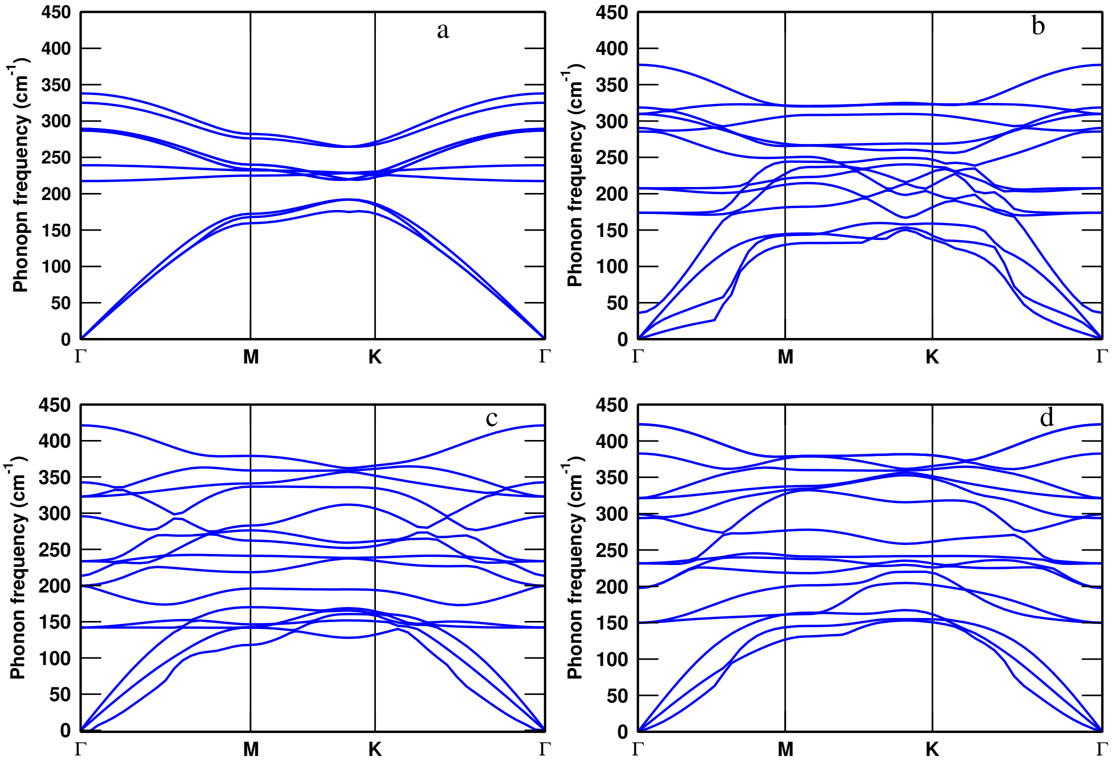

Figure 15: Phonon dispersion relation for pristine a), mono-V b), mono-V with mono-S c), and mono-V with di-S substituted d) of $V_xMo_{1-x}S_{2z}Se_{2(1-z)}$ alloys.

4.1.3.2 Phonon Properties of $V_xW_yMo_{1-x-y}S_{2z}Se_{2(1-z)}$ ($x = 0$, $y = 0.5$, $z = 0, 0.25, 0.5, 0.75$)

Figure 16(a-d) illustrates the phonon dispersion curves of how distortions caused by W or Mo and S or Se substitutional compositions that influence the lattice vibrations and bond lengths, which is evident from the changes in phonon band structures and shifts in vibrational modes. The changes in phonon frequencies signify variations in bond strength or atomic masses; typically, heavier atoms (W, Mo, Se) lead to smaller vibrational frequencies, while shorter bond lengths or smaller atomic mass (S) cause primarily contribute to the high frequency optical modes (Aktar et al., 2024). In Figure 16a, as 50 % of W is substituted in the place of Mo, the phonon frequencies remain below 350 cm^{-1}. This is due to W's greater average atomic mass relative to Mo. Moreover, the atomic vibrations do not exceed 350 cm^{-1} due to the relatively higher atomic masses of W, Mo and Se in the $W_{0.5}Mo_{0.5}Se_2$ alloy compositions. As shown, there are no atomic vibrations between 192 and 218 cm^{-1} of frequency ranges. Acoustic and optical modes interact more often if there is no phonon bandgap, while the presence of phonon bandgap decreases their interaction which leads to lower thermal conductivity, κ_l (Aktar et al., 2024). Figure 16b displays the phonon dispersion relation of $W_{0.5}Mo_{0.5}S_{0.5}Se_{1.5}$ alloy composition. As observed, the vibrations of atoms is above 400 cm^{-1} compared to Figure 16a. This is because S possess a smaller atomic mass than Se. Additionally, the bond length of Mo-S is shorter relative to Mo-Se and W-Se. In this

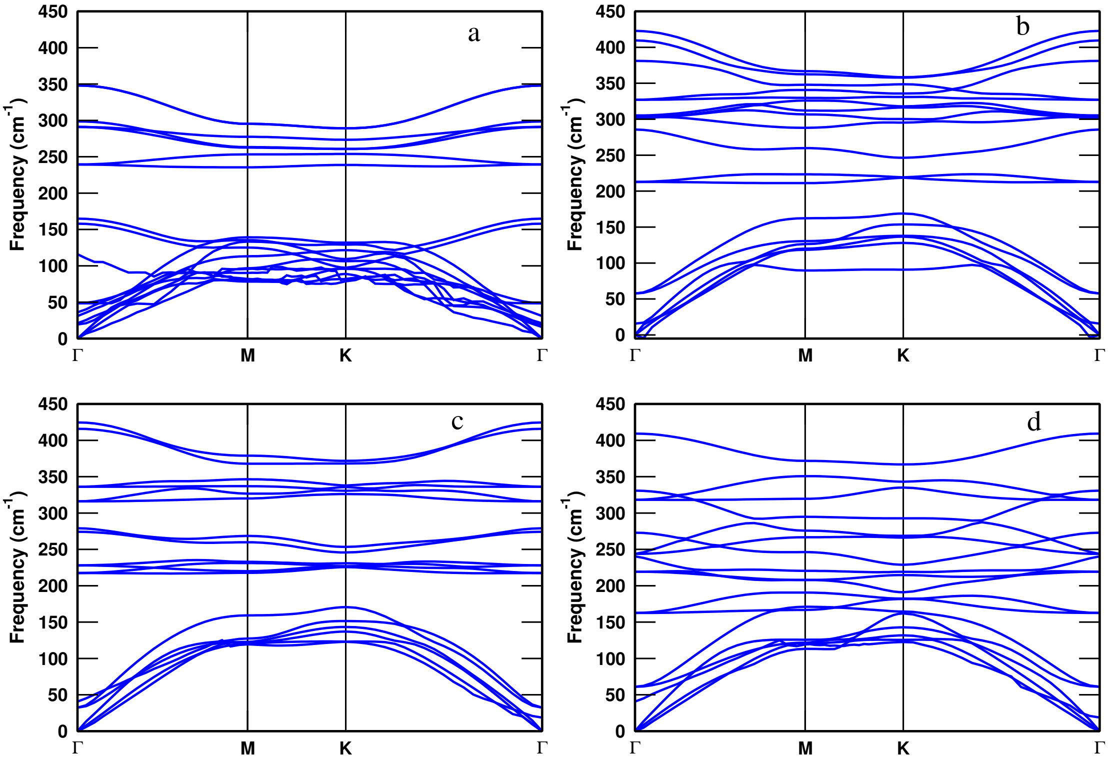

Figure 16: Phonon dispersion relation for mono-W a), mono-W with mono-sulfide b), mono-W with di-sulfide c) and mono-W with tri-sulfide substituted d) $W_yMo_{1-y}S_{2z}Se_{2(1-z)}$ alloys.

figure, no atomic vibrations occur within the frequency range of 235-285 cm^{-1}. The phonon dispersion for $W_{0.5}Mo_{0.5}S_1Se_1$ is illustrated in Figure 16c. Similar to Figure 16b, the atomic vibrations exceed above 400 cm^{-1} as compared to Figure 16a, due the shorter bond length and smaller atomic mass of S. In this diagram, no atomic vibrations are occurred in the frequency range of 127-167 cm^{-1}, 267-313 cm^{-1} and 337-353 cm^{-1}. Further, Figure 16d depicts the phonon dispersion for $W_{0.5}Mo_{0.5}S_{1.5}Se_{0.5}$ system as a function of $q(\omega)$. Figure 17(a-d) displays the PhDOS for pristine 2H-MoSe$_2$, $W_{0.5}Mo_{0.5}Se_2$, $W_{0.5}Mo_{0.5}S_{0.5}Se_{1.5}$ and $W_{0.5}Mo_{0.5}S_1Se_1$ systems illustrating the distribution frequencies of phonons and offering a detailed overview of their vibrational spectra. The distinctive structure observed in the phonon spectrum as shown in Figure 17a, 17b, 17c and 17d is a direct consequence of the varying atomic masses of Mo, Se, W and S in the material. The PhDOS for 2H-MoSe$_2$ system (see Figure 17a) reveals that the low frequency vibrations are predominated by the heavier Mo atoms, while the lighter Se atoms contribute significantly to the higher frequency regions which agrees with the ICSD and other previously reports (Schneemeyer & Sienko, 1980; X. Zhang et al., 2015). Moreover, in this figure, the peak of PhDOS is approximately 0.25 states cm^{-1} indicating the distribution of quantized lattice vibration energies within the system. The three major peaks are displayed at 160 cm^{-1}, 228 cm^{-1} and 279 cm^{-1} where each correspond to the distinct vibrational modes with the strongest peak reaching close to 0.25 states/cm^{-1}. Between 160 cm^{-1} and 192 cm^{-1} frequencies ranges, the PhDOS

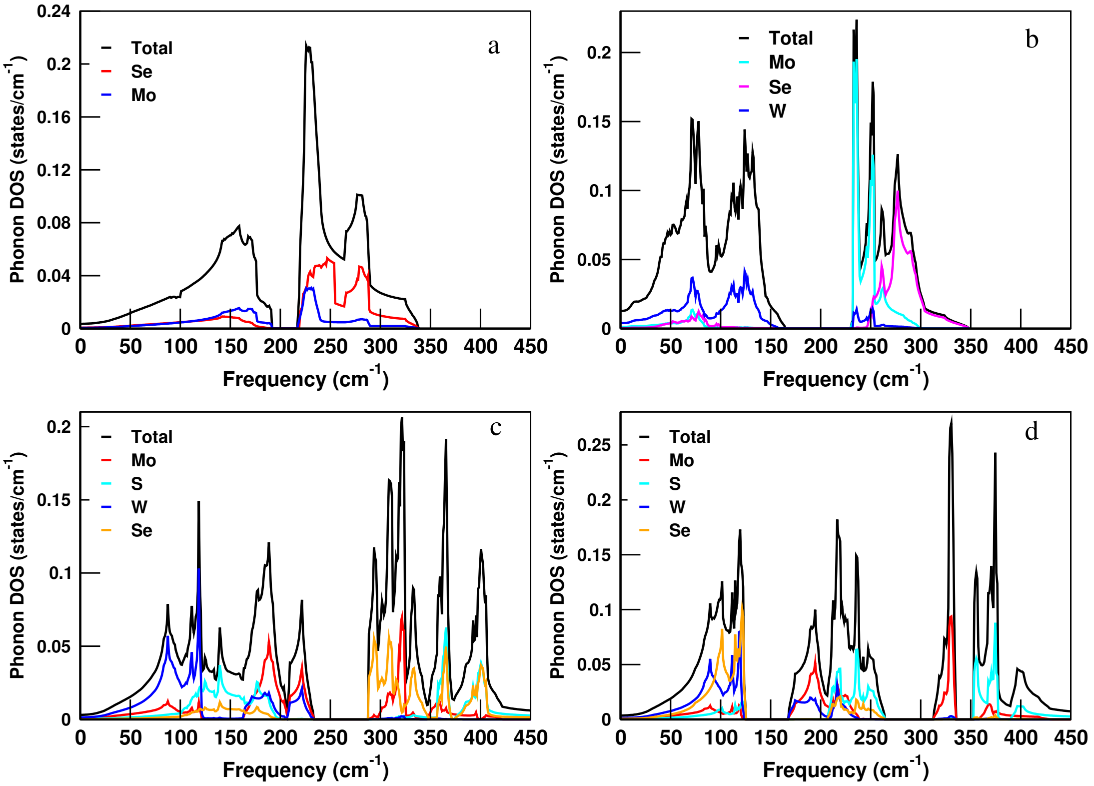

Figure 17: Phonon DOS for prestine a), mono-W b), mono-W with mono-sulfide c), and mono-W with di-sulfide substituted d) of $W_yMo_{1-y}S_{2z}Se_{2(1-z)}$ alloys.

exhibits a noticeable reduction presenting a decreased availability of vibrational states in this frequency range then it increases from 218 to 228 cm^{-1} and it decreases from 228 to 340 cm^{-1}. Furthermore, a well defined phonon bandgap of 26 cm^{-1} appears between 192 cm^{-1} and 218 cm^{-1} frequencies representing a complete absence of phonon modes. Analysis of the PhDOS in only one W-substituted system (see Figure 17b) shows a distinct atomic contributions to different vibrational modes, the acoustic branches are primarily governed by Mo atom followed by W and Se atomic vibrations (Banu S et al., 2023), while the optical branches show stronger participation from Se atomic virations followed by Mo and W atoms. And also the defined phonon bandgap of 63 cm^{-1} appears between 168 cm^{-1} and 231 cm^{-1} frequency ranges exhibits the absence of atomic vibrations. In the figure, the six various peaks (three of them from 72-125 cm^{-1} and other three are from 237-278 cm^{-1}) frequency ranges are observed which line up with particular vibrational modes of the material. The largest peak among these one reaches a PhDOS of about 0.22 cm^{-1} which exhibits that a reduction in the peak of PhDOS relative to the pristine system's largest peak value. The subsequent peaks exhibit a gradual increase in state density across two distinct frequency regimes like a higher energy range (253-278 cm^{-1}) and a lower energy range (72-125 cm^{-1}). This frequency upshift aligns with the previous studies of analogous systems demonstrating the S composition dependent redistribution of vibrational energy within the material (Banu S et al., 2023). There is also a higher PhDOS for the acoustic regions than the optical branch. The PhDOS for $W_{0.5}Mo_{0.5}S_{0.5}Se_{1.5}$ system (see Figure 17c) is presented by the nine distinct main peaks. These peaks appear in the 88-223 cm^{-1} and 295-402 cm^{-1} frequency ranges. In this diagram, the first main four peaks are in optical branches, whereas the remaining five main peaks are in the acoustic branches indicating that more PhDOS are found in the acoustic branch than the optical branch. In the optical branch, the first, second, third and fourth peaks appear at 88, 120, 189 and 223 cm^{-1}, respectively, where the first peak corresponds to the lowest frequency vibrational modes. The second peak exhibits a greater PhDOS compared to the subsequent peaks reflecting its slightly higher intensity in the vibrational spectrum. The acoustic branch of the phonon frequency displays five distinct peaks located at progressively higher frequencies of 295 cm^{-1} (first peak), 309 cm^{-1} (second), 324 cm^{-1} (third), 367 cm^{-1} (fourth) and 402 cm^{-1} (fifth). The maximum PhDOS shows a significant decrease with the primary peak intensity reduced to approximately 0.21 states cm^{-1} compare to the pristine and the only one W-substituted systems. The well defined phonon bandgap of 52 cm^{-1} appears between 235 cm^{-1} and 287 cm^{-1} frequency ranges which indicates the lack of atomic vibrations. Additionally, the acoustic phonon modes of the system are more predominantly by the S atomic vibrations followed by Mo and W yet the contribution of Se is negligible, whereas the optical branch is more dominanted by the Mo atomic vibrations followed by the Se, W and S atoms. In a similar manner, Figure 17d presents the PhDOS plotted versus phonon frequency revealing nine main distinct peaks. The first three peaks appear from 90-121 cm^{-1} frequency ranges, while the remaining six peaks are between 195-

237 cm^{-1}, at 332 cm^{-1} and 357-375 cm^{-1}. This diagram shows three well defined phonon bandgaps located between 127 cm^{-1}-167 cm^{-1}, 267-313 cm^{-1} and 337 cm^{-1}-353 cm^{-1}, respectively. The highest PhDOS value of 0.27 states cm^{-1} occurs at 332 cm^{-1} clearly indicates an increase in phonon density with higher S substitution composition compared to the pure and other substituted materials. In this diagram, the acoustic phonons primarily arise from vibrations of Mo atoms, whereas the optical phonon branch is mainly dominated by W atoms followed by the contributions from S and Se atoms. These all modifications arise from atomic mass contrasts (W/Mo:183.84/95.95 amu; S/Se: 32.06/78.96 amu) that redistribute vibrational spectra while enhancing phonon scattering in gapless regions (0-168 cm^{-1} and 231-348 cm^{-1} for only mono-W substituted system, 0-235 cm^{-1} and 287-475 cm^{-1} for mono-W with mono-sulfide substituted systems and 0-127 cm^{-1}, 167-267 cm^{-1}, 313-337 cm^{-1} and 353-400 cm^{-1} for mono-W with di-sulfide substituted systems) significantly improves the thermoelectric efficiency via reduced thermal conductivity, κ_l (Aktar et al., 2024; Yan et al., 2018). The vibrational spectrum exhibits distinct atomic contributions across different frequency regimes, Mo/W atomic vibrations dominate the low frequency region (Banu S et al., 2023), while Se/S related phonon modes prevail at intermediate frequencies. The high frequency range is primarily governed by the lighter Se/S atoms which generate elevated vibrational frequencies due to their reduced mass. The figures show that the higher phonon frequencies are mainly due to the lighter mass of the S atom compared to other atoms, which directly leads to an increase in the Debye temperature, Θ_D (Herbstein, 1961), since Θ_D corresponds to the highest frequency or energy of lattice vibrations within the material. Furthermore, as the temperature nears and exceeds this elevated Θ_D, a greater number of phonon modes become thermally excited which causes the heat capacity to approach the classical Dulong-Petit limit (Ong et al., 2013), that is a constant value per atom (3nR). Consequently, higher vibrational frequencies and the associated rise in the Θ_D imply that greater thermal energy (i.e., higher temperatures) is necessary to fully excite all phonon modes thereby shifting the temperature range over which the heat capacity transitions from low values at low temperatures to a constant maximum at high temperatures (Ong et al., 2013).

4.1.3.3 Phonon Properties of $V_xW_yMo_{1-x-y}S_{2z}Se_{2(1-z)}$ ($x = 0$, $y = 0, 0.125$, $z = 0, 0.0625, 0.125$

Figure 18(a-d) presents the phonon dispersions of the $W_yMo_{1-y}S_{2z}Se_{2(1-z)}$ ($y = 0, 0.125$, $z = 0, 0.0625, 0.125$) systems along the high symmetry points (Γ-M-K-Γ). In the plots, the vertical axis shows the phonon frequencies (in cm^{-1}) represent the vibrational energies of atomic modes, while the horizontal axis exhibits the k-points (high symmetry points). Imaginary modes appear as negative frequencies and indicate structural instabilities or potential phase transitions (Afrid et al., 2023; Sadasivam et al., 2015; Yamusa et al., 2022).

The lack of such modes means that the systems retain their crystal structure without spontaneous distortions at absolute zero temperature. As observed, the absence of imaginary frequencies across the entire Brillouin zone confirms the dynamic stability of all the studied materials. Phonon band structure curves of supercell (shown in Figure 18(a-d) exhibits how distortions caused by W/Mo and S/Se dopants influence lattice vibrations and bond lengths which is evident from the changes in phonon band structures and shifts in vibrational modes. The changes in phonon frequencies signify variations in bond strength or atomic mass and the percent of the compositions of atoms; typically, heavier atoms like W, Mo or Se lead to lower vibrational frequencies in the higher frequency regimes, while shorter bond lengths or lighter atoms like S cause primarily contribute to the high frequency optical modes (Aktar et al., 2024). Figure 18a shows the phonon band structure of bilayer pristine of 2H-$MoSe_2$ system. In this diagram, the phonon frequencies reach to appropriately 377.82 cm^{-1} which is closely matching earlier findings reported by (Horzum et al., 2013; Togo & Tanaka, 2015). As illustrated, no atomic vibrations occur in the frequency range of 160.28 to 346.13 cm^{-1}). In the absence of such a gap, acoustic and optical phonon modes interact more frequently, whereas the existence of a gap reduces their coupling, resulting in diminished thermoelectric performance (Aktar et al., 2024). Figure 18b presents the phonon dispersion relation of $MoS_{0.125}Se_{1.875}$ monosulfide system. As observed, atomic vibrations are absent above 336.05 cm^{-1}, in contrast to those seen in Figure 18a. The decrease in atomic vibrations in 2H-$MoSe_2$ upon substituting Se atoms

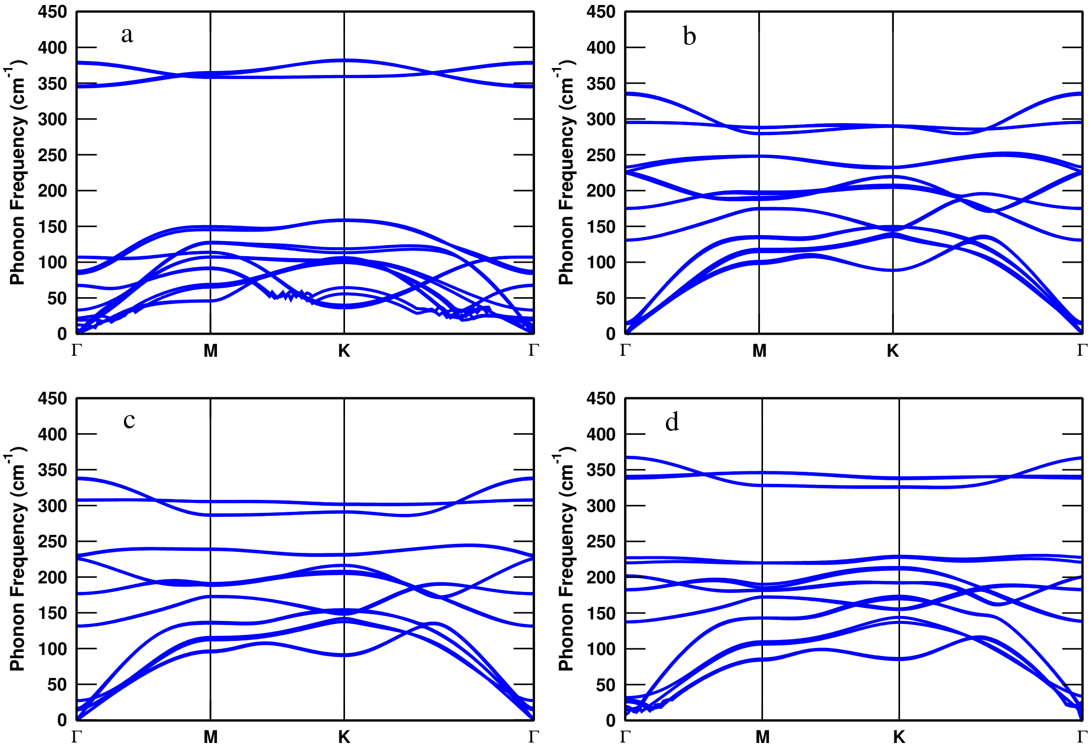

Figure 18: Phonon dispersion relations for pristine a), mono-sulfide b), mono-W with mono-sulfide c) and mono-W with di-sulfide d) doped of $W_yMo_{1-y}S_{2z}Se_{2(1-z)}$.

with S atoms is primarily attributed to the lower atomic mass, small dopant composition of S and stronger bonding of S. These factors modify the local vibrational modes and phonon dispersion, resulting in suppressed vibrational amplitudes and altered lattice dynamics in the doped system. In this figure, there are no atomic vibrations observed in the frequency range of 232.93 to 295.26 cm^{-1}. The phonon dispersion for $W_{0.125}Mo_{0.875}S_{0.125}Se_{1.875}$ is illustrated in Figure 18c. Similar to Figure 18b, the atomic vibrations not exceed above 338.38 cm^{-1} as compared to Figure 18a, due the stronger bonding of S and lower atomic mass. In this diagram, atomic vibrations are absent in the frequency range of 307.47 to 230.51 cm^{-1}. Moreover, Figure 18d depicts the phonon dispersion for $W_{0.125}Mo_{0.875}S_{0.25}Se_{1.75}$ co-doped system. In this plot, no atomic vibrations are shown in the frequency ranges of 227.22 to 342.94 cm^{-1} due to the low composition of S atoms, which have a lighter atomic mass than Se. As a result, atomic vibrations are suppressed in this range and only occur upto 367.62 cm^{-1}.

Figure 19(a-d) illustrate the PhDOS of 2H-$MoSe_2$, $MoS_{0.125}Se_{1.875}$, $W_{0.125}Mo_{0.875}S_{0.125}Se_{1.875}$ and $W_{0.125}Mo_{0.875}S_{0.25}Se_{1.75}$ systems which show the distribution of phonon frequencies and offer a detailed overview of their vibrational spectra. The distinctive structure observed in the phonon spectrum, as indicated in Figure 19a, 19b, 19c and 19d, is a direct consequence of the varying atomic masses as well as the percent composition of Mo, W, Se and S elements within the material. The PhDOS for 2H-$MoSe_2$

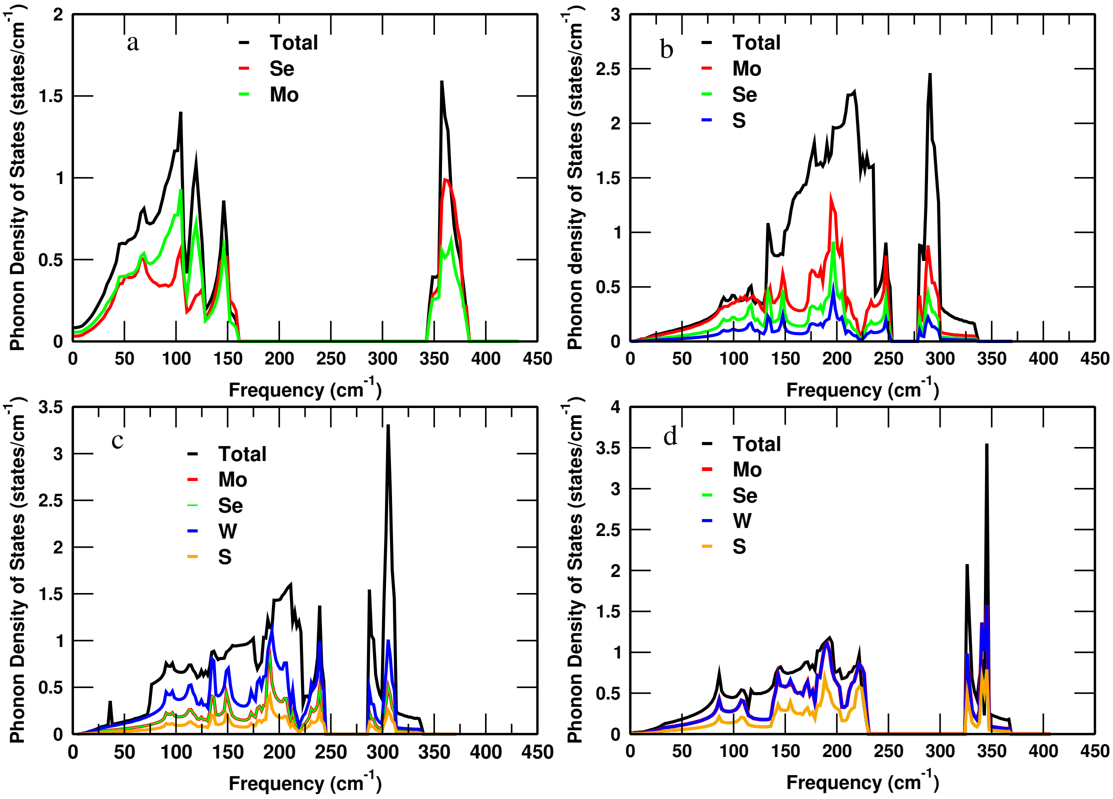

Figure 19: Phonon DOS for a) pure, b) mono-sulfide, c) mono-W with mono-sulfide and d) mono-W with di-sulfide substituted of $W_xMo_{1-x}S_{2z}Se_{2(1-z)}$ alloys.

system (shown in Figure 19a) reveals that the low frequency vibrational modes are mainly attributed to the heavier Mo atoms, while the smaller Se atoms predominantly contribute to the higher frequency modes in the higher frequency regime. This behavior is agreed with earlier reports (Afrid et al., 2022; Horzum et al., 2013; Kandemir et al., 2016). Furthermore, the observation is consistent with structural data from the ICSD and corroborates findings from prior theoretical and experimental studies (Banu S et al., 2023; Schneemeyer & Sienko, 1980; X. Zhang et al., 2015). This distinction gives rise to two distinct regions in the partial phonon density of states (PhDOS), each primarily governed by the vibrational characteristics of a specific atomic species. The PhDOS exhibits a prominent peak of approximately 1.60 states/cm^{-1} at a frequency of 358.64 cm^{-1}, reflecting the distribution of quantized lattice vibrational energies in the system. This value is higher than our previously reported result for the unit cell, owing to the larger number of atoms in the supercell; however, it does not alter the underlying physics of the system. The optical phonon branch shows three different peaks at the frequencies of 106, 121.065 and 146.02 cm^{-1} each correspond to specific vibrational modes with the peak 1.4, 1.3 and 0.8 states/cm^{-1}, respectively. In the range between 160.28 to 346.13 cm^{-1}, the PhDOS significantly declines indicating a scarcity of vibrational states. The highest phonon vibrational intensity is occurred in the acoustic phonon branches which is approximately 1.60 states/cm^{-1} at the frequency of 358.64 cm^{-1}. The PhDOS of the monosulfide dilute doped system, $MoS_{0.125}Se_{1.875}$ (Figure 19b), reveals distinct contributions from different atomic species across the vibrational spectrum. Both the acoustic and optical branches are predominantly governed by Mo atoms, with smaller contributions from Se and S atoms consistent with their respective atomic masses (Banu S et al., 2023). While Mo and Se atoms dominate the vibrational modes of the system, the contribution from S atoms is weak, reflecting their very low doping concentration. In this plot, the vibrational activity in the optical branch is more pronounced compared to that in the acoustic branch. A phonon bandgap of 24 cm^{-1} is observed between 255 cm-1 and 279 cm^{-1} signifying the absence of atomic vibrations in this frequency range. This gap is smaller than our and other previously reported values of the unit cell for bilayer 2H-$MoSe_2$ which can be attributed to the use of a supercell in our system increases the vibrations of atoms. The five distinct peaks appeared in the frequency ranges of 134.66 cm^{-1} (1.14 states/cm^{-1}), 179 cm^{-1} (1.85 states/cm^{-1}), 191.07 cm^{-1} (1.86 states/cm^{-1}). 218.19 cm^{-1} (2.30 states/cm^{-1}), and 291.95 cm^{-1} (2.46 states/cm^{-1}). These peaks correspond to particular vibrational modes within the material. Among these, the highest peak reaches a PhDOS/cm^{-1} signifying an increase in peak intensity compared to the maximum peak in the pristine material. Additionally, there is a gradual rise in state density across the two separate frequency ranges, a lower energy region between 255 and 279 cm^{-1} and a higher energy region from 8.401 THz to 9.051 THz. This upward shift in frequency is consistent with earlier studies on similar systems highlighting a redistribution of vibrational energy that depends on the

S-W compositions within the material (Banu S et al., 2023). The PhDOS of $W_{0.125}Mo_{0.875}S_{0.125}Se_{1.875}$ quaternary co-oped system (presented in Figure 19c) is indicated by four prominent peaks which are distributed within the frequency ranges of 212.2 to 240.4 cm^{-1} and 287.04 to 306.57 cm^{-1}. In the plot, the first two primary peaks are located at 212.2 cm^{-1} (1.63 states/cm^{-1}) and 240.4 cm^{-1} (1.37 states/cm^{-1}), while the remaining peaks appear in the higher frequency of the system which are 287.04 cm^{-1} (1.56 states/cm^{-1}) and 306.57 cm^{-1} (3.32 states/cm^{-1}). Additionally, the observed overlap in atomic vibrational contributions suggests that, for the low S and W dopant concentrations, the lattice dynamics remain primarily controlled by the host Mo-Se framework, with dopant atoms contributing through vibrational hybridization. Moreover, although the S atom has a smaller atomic mass than the other constituent atoms, its vibrational contribution remains in the lower frequency range due to its low dopant concentration and the resulting weak influence on the overall lattice dynamics. On the other hand, the influence of the W atom is more pronounced than that of the other atoms, which can be attributed to its heavier atomic mass. Similarly, Figure 19d displays the PhDOS of the mono-W with disufide co-doped systems as a function of phonon frequency showing seven clearly separated major peaks. The first five peaks which are located the lower frequency regimes of 85.84 cm^{-1} (0.83 states/cm^{-1}), 145.5 cm^{-1} (0.84 states/cm^{-1}), 172.62 cm^{-1} (0.92 states/cm^{-1}), 193.24 cm^{-1} (1.21 states/cm^{-1}), and 222.54 cm^{-1} (1.01 states/cm^{-1}), while the remaining two are situated in the higher frequency regimes of 327.75 cm^{-1} (2.09 states/cm^{-1}), and 346.19 cm^{-1} (3.55 states/cm^{-1}). The plot also reveals a well defined phonon bandgap of between 233.37 to 323.4 cm^{-1} indicates the absence of vibrational modes in this frequency ranges. The maximum PhDOS value reaches to 3.55 states/cm^{-1} at 346.2 cm^{-1} clearly shows an enhancement in phonon density with increasing S dopant composition compared to the pristine and other doped systems. The phonon bandgap located within the optical branches suggests modified optical phonon dynamics arising from dopant induced mass and bonding contrasts. While this feature has a limited direct impact on lattice thermal conductivity, it is relevant for applications involving electron-phonon interactions, optical responses, and phonon engineering at high frequencies. The vibrational spectrum reveals distinct differences in atomic contributions and dopant concentrations across the frequency range. Phonon modes associated with Mo and W atoms primarily dominate the low frequency region, whereas those related to Se and S atoms are more prominent at intermediate frequencies, consistent with earlier reports (Banu S et al., 2023), but in our case the lattice vibrations modes of the system also depends on the dopant concentrations of the atoms. In the high frequency region, vibrations are largely influenced by the lighter atomic masses of Se and S, as their lower masses lead to higher vibrational frequencies, whereas heavier atoms contribute predominantly at lower frequencies. This effect directly contributes to an increase in the Debye temperature, Θ_D (Herbstein, 1961) which is associated with the maximum frequency or energy of lattice vibrations in the material. Moreover, as the temperature approaches and surpasses the increased Θ_D, more phonon modes are thermally activated leads to the heat capacity, (C_v) toward the classical Dulong-Petit limit (Ong et al., 2013) which represents a constant C_v per atom (Togo & Tanaka, 2015). As a result, the higher vibrational frequencies and the corresponding increase in Θ_D indicates that more thermal energy (i.e., higher temperatures) is required to fully excite all vibrational modes. This shifts the temperature range over which the C_v evolves from low values at low temperatures to its maximum constant value at elevated temperatures.

4.1.3.4 Thermodynamical Quantities of $V_xW_yMo_{1-x-y}S_{2z}Se_{2(1-z)}$ ($x = 0$, $y = 0, 0.125$, $z = 0, 0.0625, 0.125$)

Figure 20 presents the calculated thermodynamical quantities (F(T), $C_v(T)$ and S(T)) of $W_yMo_{1-y}S_{2z}Se_{2(1-z)}$ alloys over the temperature range of 0 K-1000 K and in various compositions of S, V and W substances. Figure 20a shows the thermal properties of unperturbed 2H-MoSe$_2$ system as a function of temperature, $T(K)$. At absolute zero, the entropy is vanished consistent with the findings reported by (C. Lee & Gonze, 1995) indicates that the atoms are in their equilibrium positions without vibrational disorder. Starting from 0 JK^{-1}mol^{-1} at 0 K, the entropy gradually increases to about 317.64 JK^{-1}mol^{-1} in 1000 K. This trend aligns with typical solid behavior where rising

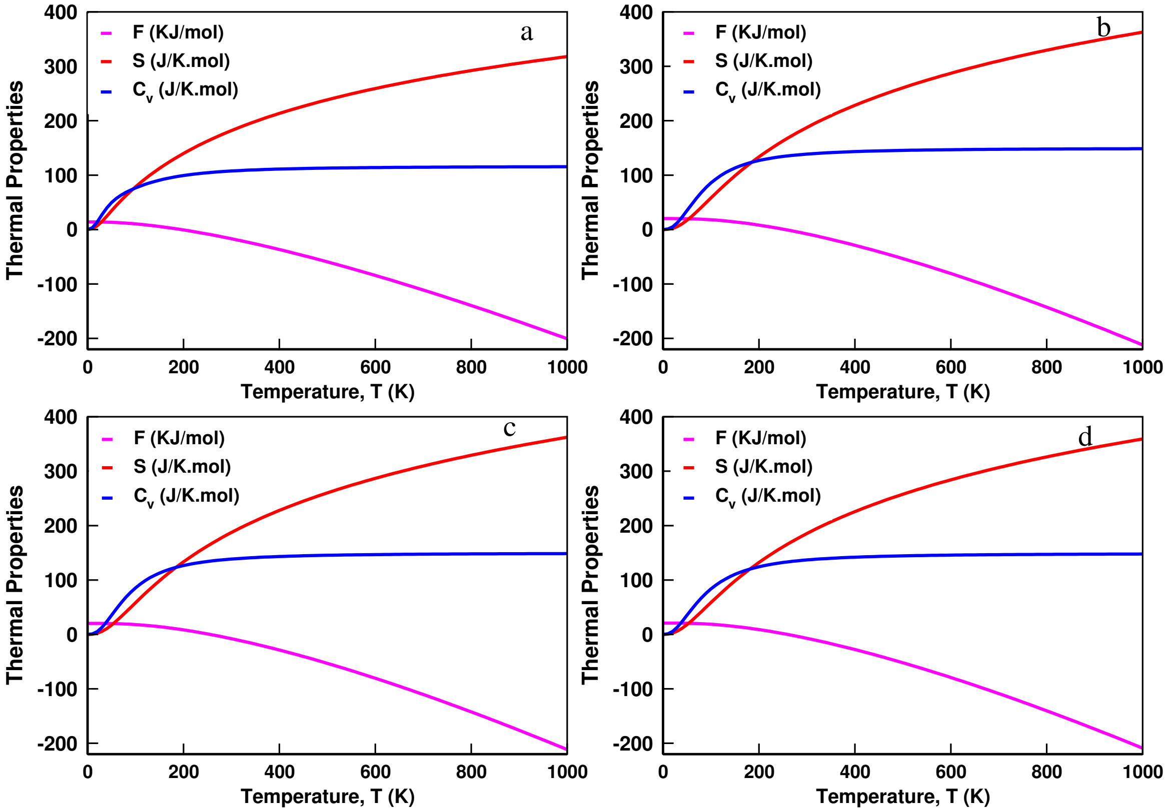

Figure 20: Thermodynamically quantifies for $W_yMo_{1-y}S_{2z}Se_{2(1-z)}$ alloys as a function of temperature with different dopant compositions.

temperature leads to greater disorder due to increased atomic vibrations and a larger number of possible configurations (C. Lee & Gonze, 1995). As temperature reaches 1000 K, the entropy elevates owing to intensified atomic vibrations and thermal disorder culminating near 317.64 $JK^{-1}mol^{-1}$. In the figure, the temperature dependence of the C_v is also depicted. At 0 K, it is zero which consists with the previous result determined by (C. Lee & Gonze, 1995) as expected since no phonon modes are excited at this temperature. It increases with rising temperature and reaches a value of 114.401 $JK^{-1}mol^{-1}$ at around 527.761 K. Beyond this point, this thermal property saturates and remains nearly steady approximately from 527.761 K up to 1000 K, which is approached to the classical Dulong-Petit limit (Ong et al., 2013). The Helmholtz free energy is highest at 0 K, (14.1067 $KJmol^{-1}$) which shows the system's maximum energy and absence of thermal fluctuations (C. Lee & Gonze, 1995). As temperature increases, it decreases and becomes increasingly negative that reaches to its most negative value (-200.637 $KJmol^{-1}$) at the highest temperature due to the growing contribution of the entropy term -TS to the free energy.

Figure 20b displays the thermal properties as a function of temperature for $W_yMo_{1-y}S_{2z}Se_{2(1-z)}$ alloys with compositions set of $y = 0$ and $z = 0.0625$. In the plot, similar to Figure 20a, the entropy as a function of temperature is zero at absolute zero temperature and it is minimum due to the absence of the disturbances of atoms in this temperature. As the temperature rises to 1000 K, the entropy gradually increases and reaches a maximum value of 362.71 $JK^{-1}mol^{-1}$ which is higher than the pure system at the same high temperature value. This enhancement is attributed to the incorporation of sulfur dopant atoms which introduce greater vibrational disturbances in the lattice (C. Lee & Gonze, 1995). Furthermore, the C_v of the mono-sulfide doped 2H-$MoSe_2$ system is zero at absolute zero temperature that consists with the behavior of the pure system (see Figure 20a) and other previously finding (C. Lee & Gonze, 1995). This shows that the incorporation of foreign atoms through doping does not affect the heat capacity (C_v) at absolute zero in agreement with (C. Lee & Gonze, 1995). This thermal property rises with temperature reaches a value of 594.28 $JK^{-1}mol^{-1}$ beyond which it plateaus and remains constant. The temperature dependence of the Helmholtz free energy for this doped system has also been determined. As shown in the plot, the Helmholtz free energy is 21.2705 $kJmol^{-1}$ at 3.05717 K which is higher compared to the undoped material (see Figure 20a). The minimum F(T) occurs at 1000 K reaching approximately -212.007 $kJmol^{-1}$ which is lower (more negative) than that of the pure system.

The F(T), S(T) and C_v(T) for $y = 0.125$ and $z = 0.0625$ compositions of $W_xMo_{1-x}S_{2z}Se_{2(1-z)}$ system is illustrated in Figure 20c. In this diagram, both S(T) and C_v(T) are vanished at absolute zero temperature which is similar to Figures 20a and 20b. The S(T) steadily rises from 0 K-1000 K and reaches a value of around 362.33645 $JKmol^{-1}$ at highest temperature. This maximum S(T = 1000K) is lower than that of the mono-sulfide doped system but higher than that of the pure material, which is attributed to the presence of the heaviest element W among Mo, Se and S of the study. Due to its greater atomic mass of W substance, it reduces the lattice vibrations and atomic disorder more than lighter atoms which results in a moderate increase of the S(T). The C_v(T) at absolute zero remains zero which is consistent with the property of both the pure and mono-sulfide doped materials. The F(T) gradually increases with temperature from 0 K-810 K and remains stable beyond that point. Its maximum value of 20.2282 kJmol^{-1} occurs at absolute zero. Following this peak, the F(T) steadily decreases, reaching -211.600 kJmol^{-1} at 1000 K which is lower than the pure system but higher than the mono-sulfide doped material. As temperature rises, the F(T) decreases gradually due to increasing S(T) and intensified atomic vibrations. Its minimum value reaches approximately -209.005 kJmol^{-1} at high temperature which is lower than that of the pristine material but higher than other doped variants. For a fixed temperature, F(T) raises with higher compositions of sulfur and tungsten elements implying that the average phonon frequencies also rise as these dopants compositions increase.

In Figure 20(a-d), at low temperatures the C_v follows the T^3 power law consistent with the Debye model (Herbstein, 1961) which shows that the atoms of the systems depict the quantum behaviors and this arises because of at sufficiently low temperatures, the C_v(T) is dominated by the acoustic phonon modes. At high temperature, the results in all figures of Figure 20 demonstrates that the C_v(T) approaches to the classical Dulong-Petit limit (Ong et al., 2013), C_v(T = 1000K) = 3nR, where n is the number of atoms per mole of the unit cell crystal material and R is the gas constant which is ~8.314 JK^{-1}mol^{-1}. Furthermore, at a fixed temperature, both the S(T) and C_v(T) of layered $W_yMo_{1-y}S_{2z}Se_{2(1-z)}$ materials decrease with increasing sulfur and tungsten dopant compositions. As temperature rises, the contribution from atomic vibrations to the PhDOS becomes more pronounced leading to a rapid increase in S(T). Understanding the temperature dependent thermal properties of these doped systems requires analyzing their phonon derived F(T) (to identify stable phases and doping induced transitions), S(T) (to quantify disorder from atomic substitution) and C_v(T) (to evaluate thermal storage and dissipation) collectively guiding the optimization of TMDCs structural and functional properties for reliable device performance under diverse thermal conditions (Togo & Tanaka, 2015; K. Zhang, 2023). Table 5 shows that in

Table 5: Helmholtz free energy (kJmol^{-1}), entropy (Jmol^{-1}K^{-1}) and heat capacity, (Jmol^{-1}K^{-1}) of $W_yMo_{1-y}S_{2z}Se_{2(1-z)}$ alloys for T = 0K and T = 1000 K.

Composition	**F(0K)**	**F(1000K)**	**S(0K)**	**S(1000K)**	**C_v(0K)**	**C_v(1000 K)**	**Θ_D (K)**
2H-$MoSe_2$	14.02	-200.64	0	317.64	0	115.47	221
$MoS_{0.125}Se_{1.875}$	20.15	-212.00	0	362.71	0	148.60	337
$W_{0.125}Mo_{0.875}S_{0.125}Se_{1.875}$	20.28	-211.60	0	362.34	0	148.59	336
$W_{0.125}Mo_{0.875}S_{0.25}Se_{1.75}$	20.84	-209.01	0	359.17	0	147.80	335

agreement with the third law of thermodynamics, S(T) and C_v(T) are canceled at 0K for all compositions (e.g., S(T = 0 K) = 0 and C_v(T = 0 K) = 0. The increased S(T) and C_v(T) of $W_yMo_{1-y}S_{2z}Se_{2(1-z)}$ materials at 1000K relative to pure 2H-$MoSe_2$ arise from configurational and vibrational disorder introduced by compositional alloying. The increased thermodynamic stability evidenced by more negative values of the F(T) demonstrates superior dynamic resilience at high temperatures. The negligible differences between the two alloyed systems indicate that their properties are effectively invariant to minor compositional fluctuations. For all compositions, F(T) decreases rapidly with rising temperature indicating the enhanced stability at this temperature; while doped systems have somewhat higher F(T) at 0 K (showing slightly less stability initially) where their F(T) values at 1000K are similar, settling around -200 kJmol^{-1}. The S(T) grows with temperature and is greater for the doped samples pointing to increased disorder and C_v(T) also rises at high temperature especially with W substitution demonstrating that doping increases both C_v(T) and S(T) ultimately affecting the thermodynamic stability and properties of the systems. In the table, the F(T) is maximum at T = 0 K, where F(T = 0 K) = U_0(T = 0 K) and thermal fluctuations vanished. As the temperature T(K) increases, F(T) decreases monotonically due to the growing entropic contributions (-TS). The results further indicate that, at room temperature (T = 300 K), the F(T) of the 2H-$MoSe_2$, $MoS_{0.125}Se_{1.875}$, $W_{0.125}Mo_{0.875}S_{0.125}Se_{1.875}$ and $W_{0.125}Mo_{0.875}S_{0.25}Se_{1.75}$ are -16.85 kJmol^{-1}, -7.97 kJmol^{-1}, -7.81 kJmol^{-1} and -7.12 kJmol^{-1}, respectively which shows that each and every doped systems are thermodynamically less stable than the undoped material due to the presence of the high vibrations of atoms in the case of doping. For these materials, the S(T) and C_v(T) of the pristine system are 181.98 Jmol^{-1}K^{-1} and 107.64 Jmol^{-1}K^{-1}. In comparison, $MoS_{0.125}Se_{1.875}$ exhibits S(T) = 187.68 Jmol^{-1}K^{-1} and C_v (T) = 138.70 Jmol^{-1}K^{-1}, while $W_{0.125}Mo_{0.875}S_{0.125}Se_{1.875}$ shows S(T) = 187.39 Jmol^{-1}K^{-1} and C_v(T) = 138.52 Jmol^{-1}K^{-1}. For $W_{0.125}Mo_{0.875}S_{0.25}Se_{1.75}$, the corresponding values are S(T) = 185.52 Jmol^{-1}K^{-1} and C_v(T) = 136.90 Jmol^{-1}K^{-1}. This table also shows that replacing some atoms with sulfur and tungsten makes the crystal structure of 2H-$MoSe_2$ stiffer and softer as evidenced by the steady rise in Θ_D. The increased stiffness of the doped systems leads to a better heat conduction, greater mechanical strength and improved interactions between electrons and atomic vibrations making these materials well favorable for coming-generation nanoelectronics, efficient thermal management and tunable IR optoelectronic devices (Herbstein, 1961).

4.1.4 Electronic Properties of $V_xW_yMo_{1-x-y}S_{2z}Se_{2(1-z)}$

This section presents the electronic properties of 2D materials, $V_xW_yMo_{1-x-y}S_{2z}Se_{2(1-z)}$ including the electronic band structure, density of states (DOS) and effective masses. These properties mainly arise from the interaction between the d orbitals of TMs and the p orbitals of chalcogen atoms. The materials exhibit tunable semiconducting behavior, where variations in dopant compositions and its types enable modulation of the electronic bandgap and electrical conductivity (Iqbal et al., 2020). This adaptability allows transitions between conventional semiconductor and degenerate semiconductor states underscoring their favorability for IR electronic and optoelectronic applications.

4.1.4.1 Electronic Band Structure and Density of State of $V_xW_yMo_{1-x-y}S_{2z}Se_{2(1-z)}$ ($x = 0, 0.5$, $y = 0$, $z = 0, 0.25, 0.5, 0.75$)

Figure 21 presents the electronic band structure, total density of states (TDOS) and projected density of states (PDOS) for pure 2H-$MoSe_2$ material. In all figures, the Fermi level (set at 0 eV) is indicated by dashed horizontal and vertical lines. As shown in Figure 21(a-d), the fundamental bandgap denoted by black arrows is the energy difference between the conduction band minimum (CBM) and the valence band maximum (VBM) of the system. As shown, the 4d localized orbital states of Mo atom are the main source of the electronic band and DOS clustered above the Fermi energy which is in a good agreement with reported by (Sedhain & Kaphle, 2017). In accordance with the computational findings published by (T.-m. Wu et al., 2016), the VBM is situated at the Γ high symmetry point, while CBM is situated between the K-Γ high symmetry points which exhibits that prestine 2H-$MoSe_2$

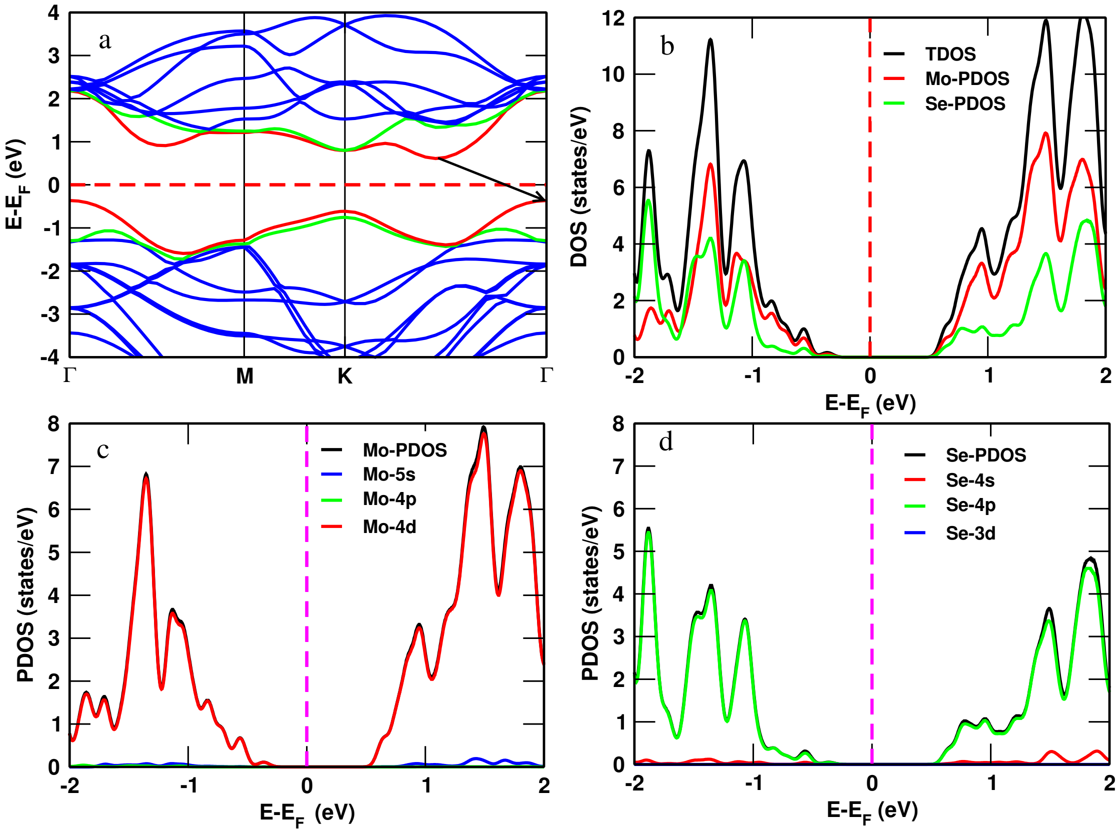

Figure 21: Electronic band structure a) and TDOS b) PDOS (c, d) for pure 2H-$MoSe_2$ using GGA approximation.

system is an indirect bandgap material (Böker et al., 2001). The band groups below the Fermi energy for the pure system are separated from these bands by a bandgap of 0.9759 eV that is consistent with the ICSD parameters and other previous results (Z. Luo et al., 2022; Y. Tian et al., 2020) which demonstrates the precision of the analysis. In Figure 21(b-d), the compositions of electron density in the vicinity of the Fermi level are low which restricts the material's electrical conductivity and carrier mobility. The TDOS which is the sum of the Mo PDOS and Se PDOS atoms is illustrated in Figure 21b. The Mo PDOS compromises the conduction band (CB) and valence band (VB) energy levels more than the Se PDOS. This shows that in pristine 2H-MoSe$_2$, both the CB and VB energy levels are predominantly derived from Mo atoms rather than Se atoms as the Se PDOS lies farther from the Fermi level compared to the Mo PDOS which suggests that Mo atom determines the electrical and other properties of 2H-MoSe$_2$ crystal material more than Se atom. In Figure 21c, the VB and CB are more composed of Mo 4d localized atomic orbitals, whereas in Figure 21d, the CB and VB are more composed of Se 4p delocalized atomic orbitals with minimal contributions from other atomic orbitals. Generally speaking, it can be claimed that both CBM and VBM energy levels of pure material are composed of Mo 4d localized and Se 3p delocalized states, which is in good agreement with the data reported by (Banu S et al., 2023; Böker et al., 2001). The density of electrons between approximately 0.3657 eV in the VB and 0.6107 eV in the CB are empty which indicates that a fully forbidden region of the electron states. Furthermore, the band structure reveals that both the VBM and CBM exhibit weakly parabolic dispersions suggesting that high effective masses of carriers and consequently lower electrical conductivity and reduced carrier mobility. The determined bandgap is lower than the experimentally measured value of approximately 1.1 eV for pristine 2H-MoSe$_2$ shows that the calculations likely due to the well known limitations of standard DFT functionals underestimate the true bandgap (Muhammad, 2021) due to the lack of appropriate approximations and computational techniques (Kohn & Sham, 1996). Figure 22(a-h) presents the band structure, PDOS and TDOS of V$_x$Mo$_{1-x}$S$_{2z}$Se$_{2(1-z)}$ alloys for $x = 0.5$ and $z = 0, 0.25, 0.5, 0.75$ dopant compositions. The band structure and DOS of V$_{0.5}$Mo$_{0.5}$Se$_2$ system is depicted in Figure 22a and b, respectively. In Figure 22a, the VBM is located at the Γ high sysmmetry point, while CBM is at the K high symmetry point which is different from its undoped system. This figure shows that the Fermi level lies within the VB rather than inside the bandgap indicating that the material is transformed into a p-type degenerate semiconductor due to its asymmetric band structure and creations of electronic states within the energy bandgap. For more, the density of electrons is empty $\sim$ 0.8471 to 0.5214 eV. This exhibits that a minimum of 0.3257 eV energy is required to promote electrons from the VB to the CB across it. To further elucidate the nature of chemical bonding in V$_{0.5}$Mo$_{0.5}$Se$_2$, the TDOS and PDOS is calculated. Figure 22b reveals that the VB is more composed of V PDOS localized atomic orbitals, whereas the CB is primarily composed of Mo 4d and Se PDOS localized atomic orbitals. Based on the DOS plots,

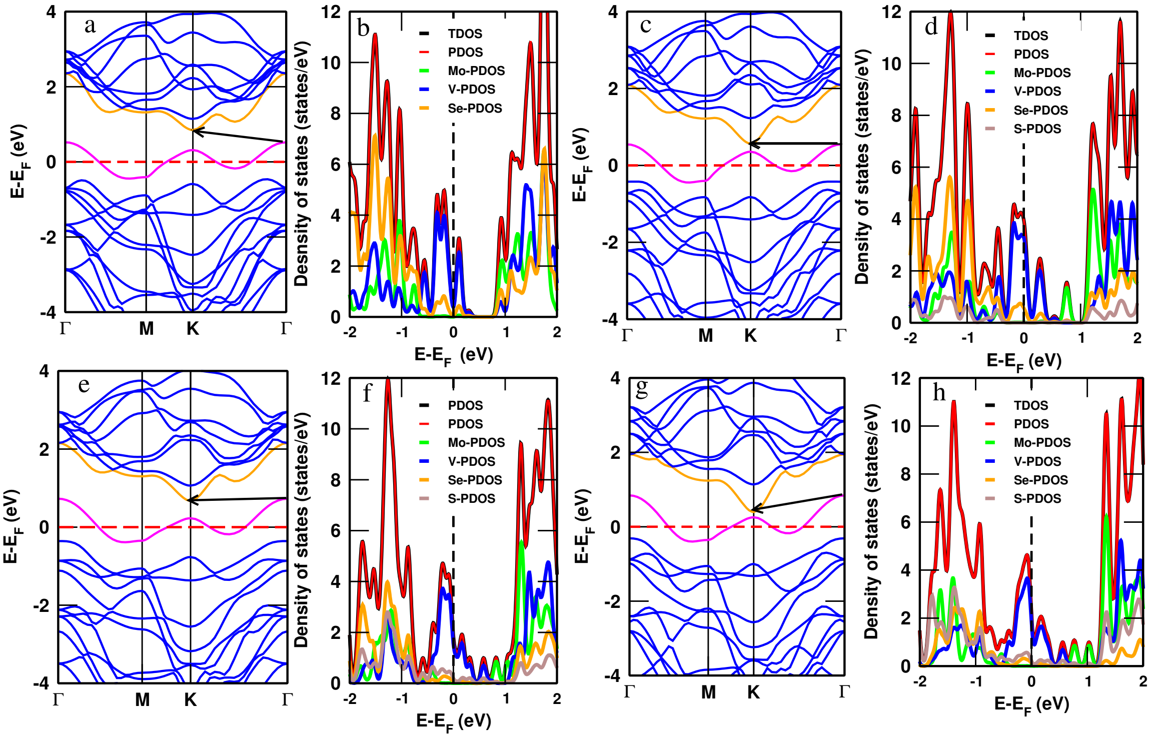

Figure 22: Electronic band structure and TDOS/PDOS of $V_xMo_{1-x}S_{2z}Se_{2(1-z)}$ alloys for mono-V (a, b), mono-V with mono-sulfide (c, d), mono-V with di-sufide (e, f) and mon-V with tri-sulfide (g, h) using the GGA approximation.

a sharp peak at the Fermi level suggests structural instability, while a deep valley in this diagram at Fermi level indicates structural stability which agrees with reported by (Nasir et al., 2017). Additionally, the VB exhibits a significantly higher density of states than the CB, depicting a greater composition of electrons near the Fermi level in the VB than CB. Figure 22c and d exhibit the electronic band structure and DOS of $V_{0.5}Mo_{0.5}S_{0.5}Se_{1.5}$, respectively. As seen, the VBM is located at the Γ high symmetry point, whereas the CBM is located at K high symmetry sites which is similar in Figure 22a and b. Both the VB and CB energy eigenvalues are becoming closer to each other at the K high symmetry point and there is also high band asymmetry and more degenerate semiconductor properties as compared to $V_{0.5}Mo_{0.5}Se_2$ system. In these figures, a negligible forbidden energy bandgap of 0.0212 eV effectively approximate a zero bandgap prohibits electron flow only minimally. This shows that the $V_{0.5}Mo_{0.5}S_{0.5}Se_{1.5}$ system exhibits stronger degenerate semiconductor property than the $V_{0.5}Mo_{0.5}Se_2$ system. The TDOS/ PDOS of $V_{0.5}Mo_{0.5}S_1Se_1$ system is displayed in Figure 22d. In this figure, the CBM and VBM are more composed of the Mo PDOS with the Se PDOS orbitals with high electron density at the CB regions compared to VB regions. Figure 22e and f illustrate the electronic band structure and DOS of $V_{0.5}Mo_{0.5}S_1Se_1$ system, respectively. As seen in Figure 22e, the VBM and CBM are located at the Γ and K high sysmmetry points, like other substituted systems and it is indirect bandgap behavior. In Figure 22f, the TDOS/ PDOS for same system is displayed. In these plots, there is very small but discernible bandgap (0.0048 eV) along the Fermi level intersecting the

DOS. This suggests that while the V substituted composition remains fixed, increasing the S substitutional composition leads to enhanced degenerate semiconductor behavior compared to a mono V with mono-sulfide substituted systems due to the higher EN of S (Rudnev et al., 2017). Additionally, the energy levels of both the VB and CB near the Fermi level are predominantly derived from Mo projected localized atomic orbitals indicating that the electronic properties of V substituted 2H-MoSe$_2$ are primarily governed by Mo orbitals rather than those of S, V or Se; however, in this figure, while the VBM and CBM are still largely dominated by Mo PDOS, the contributions from Mo and S near the Fermi level are notably smaller than those from V and Se substances. Figure 22g and 22h illustrate

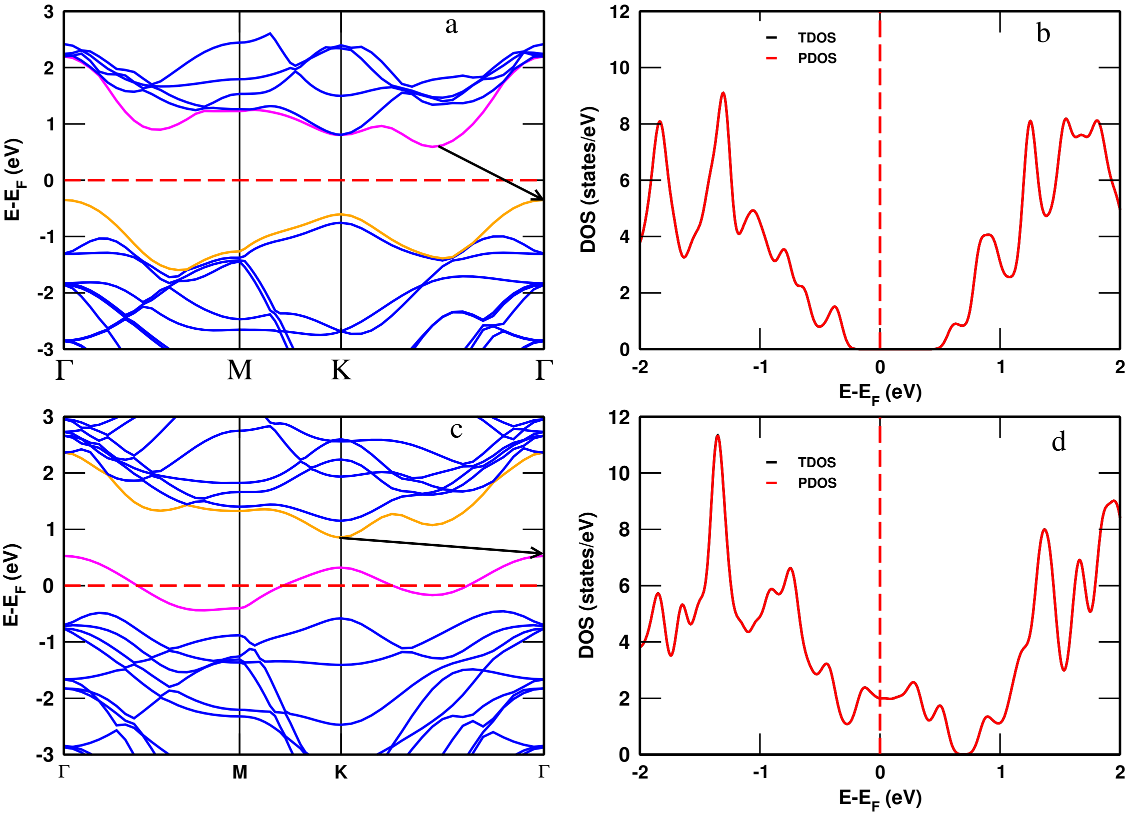

Figure 23: Electronic band structure and TDOS/PDOS of V$_x$Mo$_{1-x}$S$_{2z}$Se$_{2(1-z)}$ for unsubstituted (a, b) and mono-V substituted (c, d) systems using the GGA+U approach.

the band structure and DOS of the V$_{0.5}$Mo$_{0.5}$S$_{1.75}$Se$_{0.5}$ system, respectively. In the band structure, the CBM lies very close to the Fermi level, while the VBM is shifted farther away indicating that an extremely narrow bandgap behavior. As observed in other V substituted systems with or without S substitutional compositions, the VBM and CBM are located at the Γ and K high symmetry points, respectively. Moreover, at the K high symmetry point, the CBM and portions of the VB move progressively closer together resulting in a reduced electronic bandgap and enhanced degenerate semiconductor behavior compared to other substituted systems due to the narrowing energy separation between the VBM and CBM. Figure 22h indicates that near to the Fermi level the contribution of Mo PDOS, Se PDOS and S PDOS atomic orbitals is small compared to the contribution of V PDOS localized atomic orbitals which is similar to mono V with or without mono-sulfide, di-sufide and tri-sulfide substituted 2H-MoSe$_2$ systems. Particularly, in the mono V (50%) system co-substituted with S at compositions corresponding to mono, di, and tri-sulfide compositions (S = 0%, 25%, 50%, 75%), the computed bandgap is extremely small, indicating a transition from semiconductor to degenerate semiconductor behavior due to the strong perturbative effect of V and S substitutional compositions compared to the pristine 2H-MoSe$_2$. This bandgap collapse leads to significant overlap between VB and CB enabling intraband transitions, enhanced electron-hole pair generation, high electrical conductivity and potential electronic phase transitions. As shown in all panels of Figure 22, substitutional composition of V with or without S induces a phase transition from semiconductor to degenerate semiconductor characteristics and become the material more suitable for supercapacitor applications than the unsubstituted system due to its enhanced electrical conductivity and carrier composition. Figure 23a and 23b of the $x = z = 0$ and $x = 0.5, z = 0$ substitutional compositions represent the band structure and DOS for pure 2H-MoSe$_2$ applying the GGA+U approach which shows that its energy bandgap is improved compared to the GGA approach. Figure 23c and 23d, the band structures and DOS of the V substituted 2H-MoSe$_2$ system reveal that the GGA+U method yields a distinctly different (and more accurate) energy bandgap than standard GGA, underscoring its superiority for modeling d block elements like V. Furthermore, both the GGA and GGA+U methods predict degenerate semiconductor behavior for V substituted systems with or without S while the GGA+U results exhibit broader band dispersion and DOS features compared to GGA. Table 6 depicts the bandgap of the 2H-MoSe$_2$ and its V substituted systems with or without S where the observed modifications arise primarily from impurity states introduced by substituting, the p-type property that shifts the Fermi level and defect induced changes in the electronic structure. Collectively, these effects substantially alter the intrinsic semiconductor properties of 2H-MoSe$_2$, which is an n-type character. Furthermore, the GGA+U calculations of the electronic band structure and DOS reveal that the pristine system remains semiconductor, while the V with or without S substituted variants exhibit degenerate semiconductor behavior.

Table 6: Calculated bandgap (eV) of layered materials, $V_xMo_{1-x}S_{2z}Se_{2(1-z)}$ compared with experimental and other theoretical findings using the GGA and GGA+U approaches.

Composition	GGA	GGA+U	Experimental	Other Theoretical
$x = z = 0$	0.9759	1.1564	1.09 (Muhammad, 2021) 0.85, 1.33 (Wen et al., 2017)	0.95 (Mashmool et al., 2020) 0.80 (C. Lee et al., 2014)
$x = 0,\ z = 1$	0.7473	1.2716	1.23 (Böker et al., 2001)	0.89 (Ahmad & Mukherjee, 2014) 0.70 (Markov et al., 2019) 0.78 (Mashmool et al., 2020)
$x = 0.5,\ z = 0$	0.3257	1.0462		
$x = 0.5,\ z = 0.25$	0.0212			
$x = 0.5,\ z = 0.5$	0.0126			
$x = 0.5,\ z = 0.75$	0.0048			

4.1.4.2 Electronic Band Structure, Density of States and Effective Masses of $V_xW_yMo_{1-x-y}S_{2z}Se_{2(1-z)}$ ($x = 0$, $y = 0, 0.5$, $z = 0, 0.25, 0.5, 0.75$)

Figure 24(a-d) illustrates the electronic band structure of layered material, $W_yMo_{1-y}S_{2z}Se_{2(1-z)}$ for the dopant compositions of $y = 0, 0.5$ and $z = 0, 0.25, 0.5, 0.75$ which is calculated using the GGA functional. In each plot, the Fermi level is indicated by a horizontal dashed line and the energy bandgap marked by downward red arrows is defined as the energy difference between the VBM and the CBM (Sadasivam et al., 2015). Figure 24a depicts the electronic band structure of the 2H-$MoSe_2$ system showing the VBM at the Γ high symmetry point, whereas the CBM is located between the Γ and K high symmetry paths with an energy range of -4 to 4 eV consistent with the previous result (Böker et al., 2001). The diagram confirms that the material exhibits an indirect bandgap of 0.9764 eV in agreement with previous theoretical studies (Böker et al., 2001; Mashmool et al., 2020; Sedhain & Kaphle, 2017). This bandgap value makes the system well suitable for optoelectronic applications in the near infrared spectral regions (Jing et al., 2020). Figure 24b illustrates the electronic band structure of $W_{0.5}Mo_{0.5}S_{0.5}Se_{1.5}$ compositions. The plot reveals an indirect bandgap with the CBM located at the K point, whereas the VBM located at the Γ point. The bandgap narrows to 0.8134 eV that is attributed to the Fermi level shift caused by substitutional composition of W and S compared to the pristine material. As illustrated, the electron density distributions exhibit more distinct separations than to the

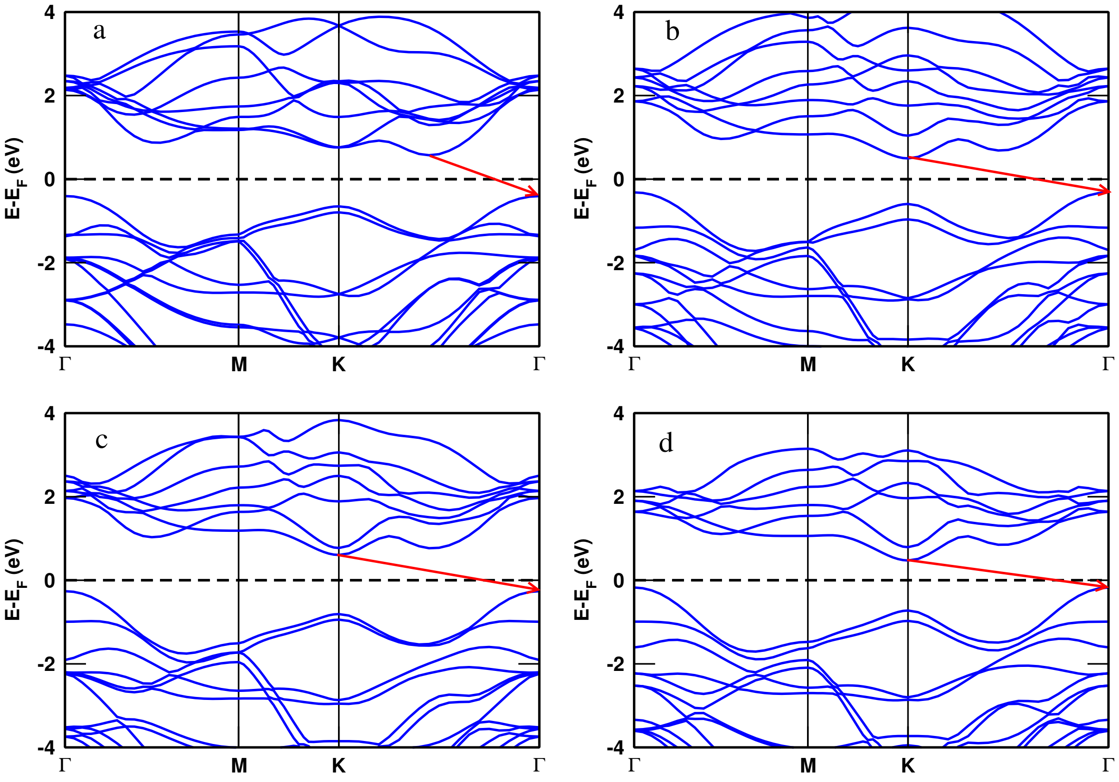

Figure 24: Electronic band structure for a) pure, b) mono-W with mono-sulfide, c) mono-W with di-sulfide and d) mono-W with tri-sulfide of $W_yMo_{1-y}S_{2z}Se_{2(1-z)}$ using the GGA approximation.

pristine system. Figure 24c presents the electronic band structure of the $W_{0.5}Mo_{0.5}S_1Se_1$ compositions. Compared to the $W_{0.5}Mo_{0.5}S_{0.5}Se_{1.5}$ system, the VBM lies closer to the Fermi level showing the influence of higher S composition which also enhances the clarity of electron distribution relative to Figures 24a and 24b with electron density extending down to the Fermi level. As a result, this system exhibits an indirect bandgap value of 0.868 eV with both the VBM and CBM located nearer to the Fermi level than in other configurations. Figure 24d depicts the electronic band structure of the $W_{0.5}Mo_{0.5}S_{1.5}Se_{0.5}$ material. In this material, both the VBM and CBM lie exceptionally close to the Fermi level and the electron distribution near and above the Fermi level is more pronounced than in all other the W-S co-substitutional composition systems. This configuration exhibits an ultra-narrow indirect bandgap of 0.6462 eV which is the smallest value among all the W with or without S substitutional compositions studied layered material.

Figure 25(a-d) demonstrates the significant impact of the GGA+U functional on the electronic band structures of unperturbed 2H-$MoSe_2$ and the W-S co-substitutional compositions notably improves the bandgap compared to standard GGA results. The calculations further reveal a downward shift of the Fermi level upon inclusion of the Hubbard U correction in agreement with previous studies (K. H. Habura et al., 2024). As shown in Figure 25a, the GGA+U calculated bandgap of 2H-$MoSe_2$ is ~1.2 eV in good

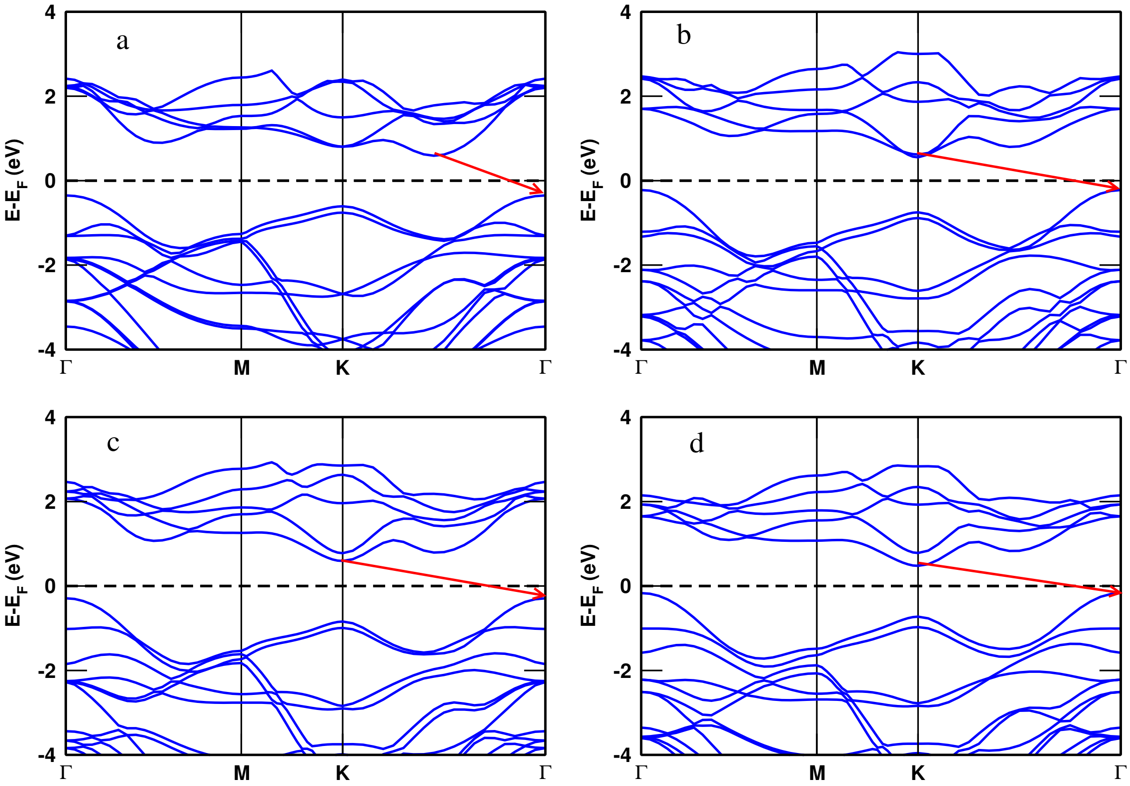

Figure 25: Electron band structure for a) unsubstituted, b) mono-W with mono-sulfide, c) mono-W with di-sulfide and d) mono-W with tri-sulfide substitutional compositions in $W_yMo_{1-y}S_{2z}Se_{2(1-z)}$ systems using the GGA+U approximation.

agreement with previously reported values (Mashmool et al., 2020; Schneemeyer & Sienko, 1980). This finding confirms the typical bandgap widening effect caused by the inclusion of the U correction (K. H. Habura et al., 2024) which is improved by 0.22 eV as compared to the GGA result. In this figure, the VBM is located at the Γ high symmetry point, while the CBM lies along the Γ-K paths consistent with the indirect bandgap nature observed in the electronic band structure of Figure 25a and previously reported values (Afrid et al., 2022, 2023; Yamusa et al., 2022). The plot further gives more densely packed electron states above the Fermi level and a reduction in electron distribution spread compared to the GGA result. The electronic band structure for the W-S co-substitutional composition systems ($W_{0.5}Mo_{0.5}S_{0.5}Se_{1.5}$, $W_{0.5}Mo_{0.5}S_1Se_1$ and $W_{0.5}Mo_{0.5}S_{1.5}Se_{0.5}$) are illustrated in Figure 25b, 25c and 25d, respectively. The electronic band structure of the mono-W with mono-sulfide co-substitutional composition system as displayed in Figure 25b reveals an indirect bandgap of 0.826 eV when the U correction is included which optimizeds the bandgap of the system by 0.0126 eV relative to the GGA approach. In agreement with the GGA findings, the U correction causes the VBM to shift upward and the CBM to shift downward. Furthermore, the electron distributions both above and below the Fermi level appear clearer and more distinct compared to the pure layered material. Figure 25c presents the electronic band structure of the mono-W with di-sulfide co-substitutional composition system. The CBM remains at the Γ point while the CBM resides at the K point confirming the persistence of indirect bandgap behaviors. The calculated bandgap including U corrections is 0.8843 eV which is larger than the GGA value by 0.0163 eV. Moreover, for the system with 50% of W and 75% of S co-substitutional composition system (see Figure 25d), the VBM is at Γ and CBM at K align with those of other substituted configurations, yielding the GGA+U corrected bandgap of the system as 0.6647 eV which is improved by 0.0185 eV of the GGA result. The electron distributions in both bands are notably sharper than in lower substitutional composition cases (Figure 24b and 24c) indicating reduced orbital hybridization. These findings show the significant role of the Hubbard U correction in accurately capturing bandgap properties in materials containing TMs (d-block) elements (Izyumov, 1995). Figure 26 displays the TDOS for the $W_yMo_{1-y}S_{2z}Se_{2(1-z)}$ systems with the substitutional compositions of $y = 0, 0.5$ and $z = 0, 0.25, 0.5, 0.75$. The DOS is analyzed over the energy range from -3 to 3 eV. For the 2H-$MoSe_2$ (see Figure 26a), a symmetric DOS profile is observed mainly dominated by Mo 4d and Se 4p orbitals which is consistent with the previous studies (Afrid et al., 2023; Yamusa et al., 2022). The contributions fromthe other orbitals such as Mo 5s, Mo 4p and Se 4s are minimal aligning with previous theoretical findings (Afrid et al., 2022, 2023; Yamusa et al., 2022). The absence of band crossings at the Fermi level further confirms the conventional semiconductor nature of the material (Y. Tian et al., 2020; Yamusa et al., 2022). The plot also shows low electron density near the Fermi level which limits the electrical conductivity and carrier mobility (C. Lee et al., 2014) of the system. As a result, the Mo atoms have a more significant

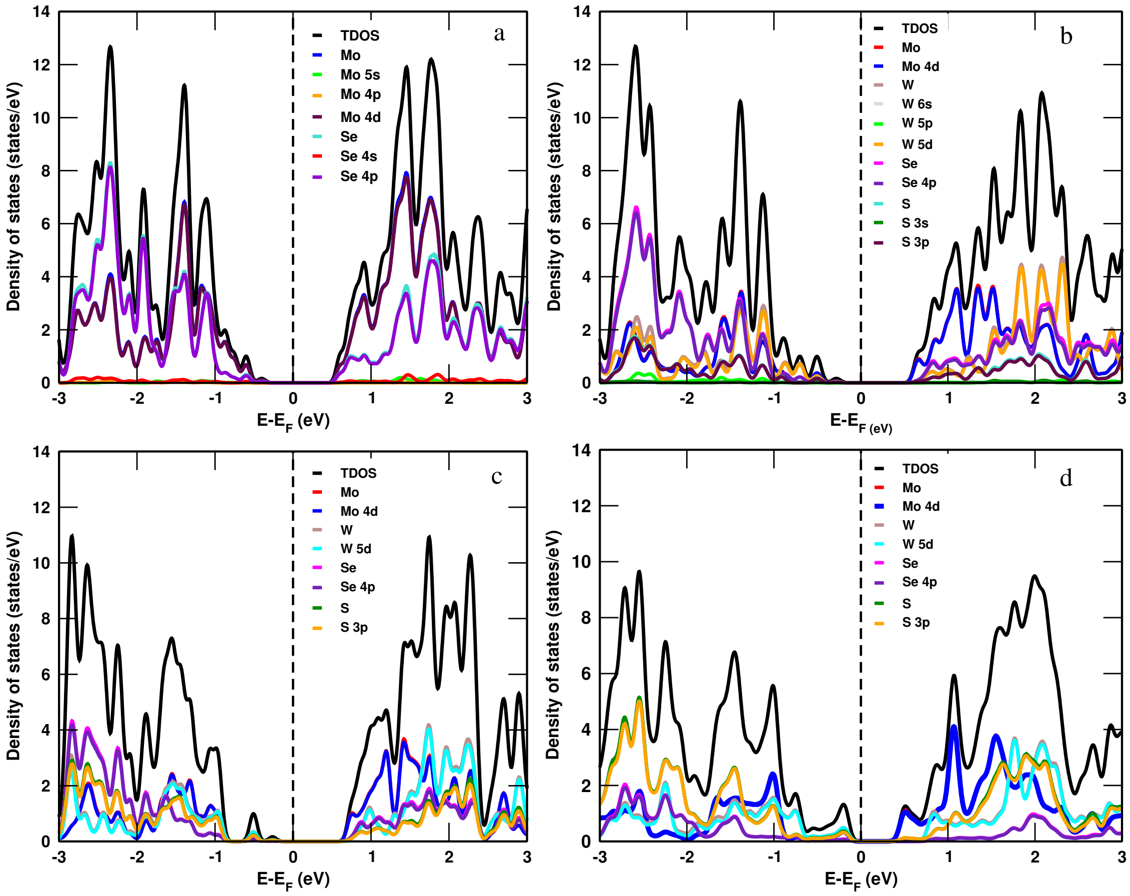

Figure 26: Density of states for a) unsubstituted, b) mono-W with mono-sulfide, c) mono-W with di-sulfide and d) mono-W with tri-sulfide substitutional composition in $W_yMo_{1-y}S_{2z}Se_{2(1-z)}$ using the GGA approximation.

influence than Se atoms on the electrical and functional properties of the 2H-$MoSe_2$ (Afrid et al., 2022; Yamusa et al., 2022). In the figure, the TDOS reaches a peak value of ~12.66 states/eV at -2.34 eV within the VB and consistent with the previous reported by (Yamusa et al., 2022). Four distinct peaks are evident in both the VB and CB. Specifically, the two peaks appear in the VB region at -2.66 eV (12.66 states/eV) and -1.4 eV (11.32 states/eV), while the remaining two are found in the CB at 1.77 eV (12.22 states/eV) and 1.47 eV (11.92 states/eV). Since enhancing conductivity fundamentally requires increasing the DOS at the Fermi level via controlled charge carriers (S. Kumar & Schwingenschlogl, 2015), we apply targeted substitutional compositions strategies to modify the electronic structure accordingly. Figure 26b depicts the TDOS for the $W_{0.5}Mo_{0.5}S_{0.5}Se_{1.5}$ system. The CB is mainly influenced by the Mo 4d and Se 4p orbitals with secondary contributions from the W 5d and S 3p states, whereas the VB is more dominanted by the Mo 4d and W 5d states followed by the S 3p and Se 4p orbitals. In contrast, orbitals such as the W 6s, W 5p and S 3s show a negligible effect on the CB and VB compared to the dominant atomic orbitals which is consistent with previous research (Sedhain & Kaphle, 2017; Yamusa et al., 2022). In the diagram, TMs (such as Mo and W) consistently exhibit greater contributions to the electronic structure compared to the chalcogen atoms (like Se and S) (Afrid et al., 2023; Sedhain & Kaphle, 2017). Additionally, the VB exhibits a prominent TDOS peak (12.74 states/eV) at -2.58 eV, while new electronic states appear close to 0 eV concurrent with a minor Fermi level depression. The Fermi level also shifts towadr to the VB as the S Substitutional composition is applied with a fixed W substitutional composition which exhibits that the system approaches to the p-type semiconductor material (Kang et al., 2013). The PDOS for $W_{0.5}Mo_{0.5}S_1Se_1$ system is illustrated in Figure 26c. In this diagram, the CB is primarily composed of the Mo 4d states with notable contributions from the Se 4p, W 5d and S 3p orbitals. Conversely, the VB is mainly governed by the S 3p states followed by the W 5d, Mo 4d, and Se 4p contributions (Sedhain & Kaphle, 2017) similar to Figure 22b, the contributions of the W 6s, W 5p and S 3p atomic orbitals are minimal. Additional peak is created near to the Fermi level compared to the unsubstituted and one-W with one-S co-substitutional composition systems (see Figure 26a and 26b, respectively). This shows that the density of electrons near to the Fermi level is higher as the S dopant composition is increased (Kang et al., 2013). The TDOS peak value of 10.97 states/eV occurred at -2.84 and 10.94 states/eV at 1.76 eV energy within the VB and CB, respectively. Similarly, Figure 26d presents the PDOS of the $W_{0.5}Mo_{0.5}S_{1.5}Se_{0.5}$ system

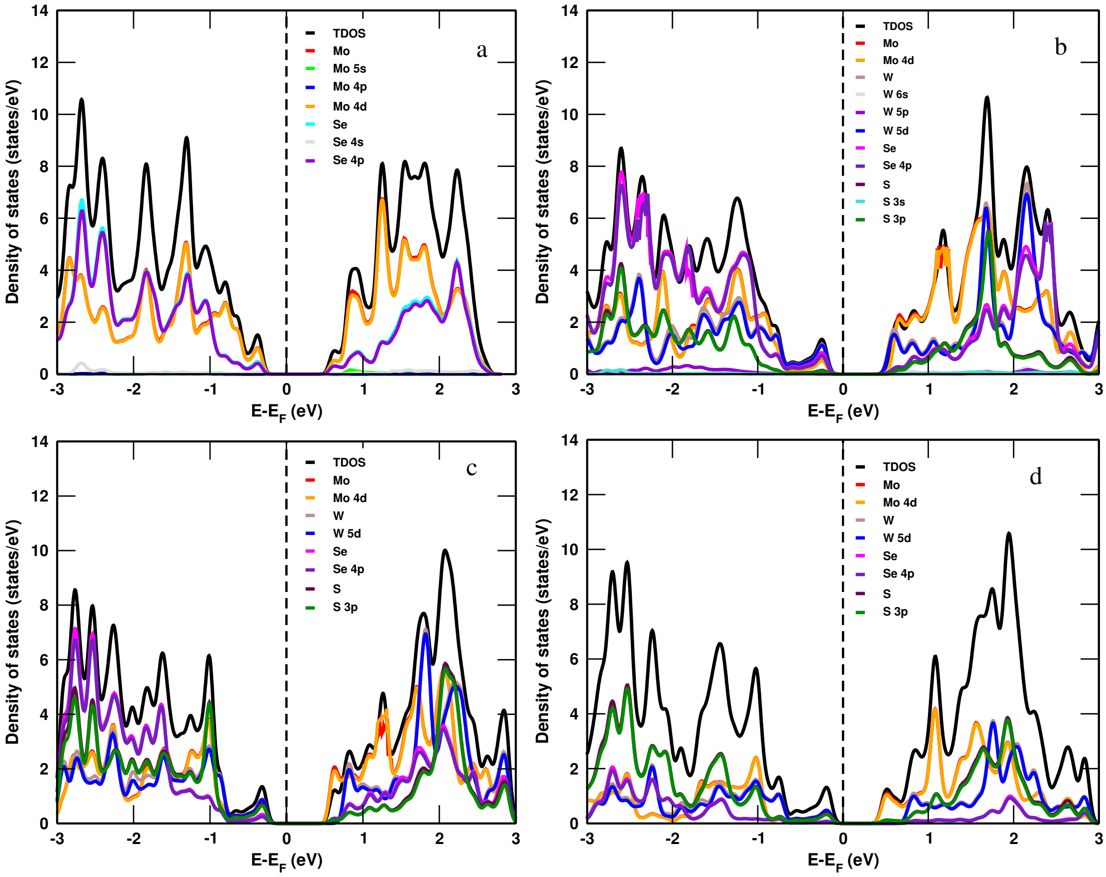

Figure 27: Density of states for a) pure, b) mono-W with mono-sulfide, c) mono-W with di-sulfide and d) mono-W with tri-sulfide substitutional compositions of $W_yMo_{1-y}S_{2z}Se_{2(1-z)}$ using the GGA approximation.

where the Fermi level is positioned closer to the VB and the electron density near this energy level is higher compared to both the other S-substitutional composition systems and the unsubstituted material. In this plot, the CB is mainly comprised of the Mo 4d and S 3p orbitals with the W 5d making fewer contribution and Se 4p contributing even less. Conversely, the VB is predominantly characterized by the W 5d and S 3p orbitals with lower contributions from the Se 4p and Mo 4d states. The higher impacts of the S atomic orbitals on the VB is due to its elevated compositions. With increasing the S composition, the collective electronic contributions of the S and W atoms become more significant in both the VB and CB. Additionally, the TDOS exhibits peak values of 9.67 states/eV at -2.54 eV in the VB and 9.50 states/eV at 2.01 eV in the CB. As expected, TMs exhibited stronger band contributions than chalcogen elements (Afrid et al., 2023; Asadi & Nourbakhsh, 2019; Dumcenco et al., 2010). These results demonstrate excellent consistency between the DOS analysis and the atomic orbital projected electronic band structure calculations. Figure 27 shows the PDOS computed with the GGA+U functional for the unsubstituted 2H-MoSe$_2$ and W-S co-substitutional composition variants in the energy range of -3 to 3 eV. As shown in Figure 27a, the VB and CB of the pure system are mainly dominated by the Mo 4d orbitals with the Se 4p orbitals contributing to a lesser extent which agrees with the GGA calculated results (see Figure 26a) (Afrid et al., 2022, 2023). The main distinction lies in the broader bandgap induced by the inclusion of U corrections (K. H. Habura et al., 2024). Consistent with the GGA findings, the Mo 5s, Mo 4p and Se 4s orbitals contribute only minimally to the electronic properties. The system exhibits a TDOS peak of 10.59 states/eV at -2.66 eV within the VB which is lower than the value obtained from the GGA calculations (see Figure 26a). The energy range between -0.5628 and 0.5917 eV shows empty of electron states indicating a forbidden gap with no available electron states consistent with the electronic structure calculations (see Figure 25a). Figure 27b shows the PDOS analysis of the W$_{0.5}$Mo$_{0.5}$S$_{0.5}$Se$_{1.5}$ substitutional system where the Fermi level moves toward the to the VB. In this plot, the CB is mainly dominated by the W 5d orbitals followed the Mo 4d, Se 4p and S 3p states, while the VB is primary composed of the W 5d followed the Se 4p, Mo 4d and S 3p atomic orbitals. The impact of the W 6s, W 5p and S 3s orbitals are minimal for both the CB and VB. The system shows a maximum TDOS peak of 10.71 states/eV at 1.70 eV which is lower than the value obtained from the corresponding GGA calculation (see Figure 26b). Additionally, the energy range between -0.2735 and 0.5525 eV exhibits no density of states indicating a forbidden gap with no available electron states. Figure 27c illustrates the PDOS of the W$_{0.5}$Mo$_{0.5}$S$_1$Se$_1$ material where the Fermi level is shifted toward the VB region indicating p-type semiconductor behavior. The energy range between -0.2919 and 0.5924 eV shows no density of states revealing a forbidden gap consistent with the electronic structure calculations (see Figure 25c). The TDOS reaches a maximum peak of 10.01 states/eV at 2.09 eV in the CB which is lower than the corresponding GGA value. The CB is primarily dominated by the Mo 4d orbitals followed by the contributions of the W 5d, Se 4p and S 3p states, whereas the VB is more composed of the W 5d followed the Mo 4d, S 3p and Se 4p states. Figure 27d presents the PDOS for the 2H-MoSe$_2$ which is the simultaneously substitution of one W with three S atoms showing a highest peak of 10.59 states/eV at 1.97 eV. In this figure, the CB mainly consists of the Mo 4d orbitals, followed the W 5d and S 3p, where the contribution of the Se 4p states is smaller compare to others. The VB is predominantly composed of the W 5d orbitals, succeeded by the S 3p, Se 4p and Mo 4d orbitals, but the contribution of the Se 4p orbit is small. In this system, the Fermi level lies closer to the VB compared to other S co-substitutional materials suggesting enhanced electrical conductivity. The energy bandgap between -0.1873 and 0.4774 eV contains no states confirming a bandgap consistent with the electronic structure results. All calculated DOS profiles from both the GGA and GGA+U functionals exhibit sharp features behaviors of the Van Hove singularities (Van Hove, 1953) which arise at band extrema. Furthermore, within the GGA approximation increasing the S composition leads to a reduction in the prominent density of states peaks in both the VB and CB. However, this pattern is not observed when using the GGA+U approximation. The U parameter affects the density of states by altering the energy levels and electron localization particularly in correlated orbitals resulting in shifts and possible splitting of DOS features that provide a more accurate representation of the material's true electronic structure (K. H. Habura et al., 2023, 2024).

Table 7: Calculated effective masses of electrons (m_e^*) and holes (m_h^*) in $W_yMo_{1-y}S_{2z}Se_{2(1-z)}$ with varying substitutional compositions.

	GGA		**GGA+U**	
Material	m_e^*/m_0	m_h^*/m_0	m_e^*/m_0	m_h^*/m_0
2H-MoSe$_2$	0.40	0.45	0.41	0.50
Others	0.47(Afrid et al., 2023)	0.53(Afrid et al., 2023)		
$W_{0.5}Mo_{0.5}S_{0.5}Se_{1.5}$	0.33	0.36	0.37	0.39
$W_{0.5}Mo_{0.5}S_1Se_1$	0.30	0.34	0.36	0.38
$W_{0.5}Mo_{0.5}S_{1.5}Se_{0.5}$	0.25	0.27	0.30	0.34

The effective masses of charge carriers in $W_yMo_{1-y}S_{2z}Se_{2(1-z)}$ systems were calculated using both the GGA and GGA+U functionals with the corresponding values summarized in Table 7. The differences observed between the GGA and GGA+U results shows the improved description of localized d electron states provided by the U correction. For reference, the m_e^* of the pristine 2H-MoSe$_2$ is approximately equal to 0.47m$_0$, where m$_0$ represents the free electron rest mass (Afrid et al., 2023). The calculated effective masses of the unsubstituted system (Table 7) are consistent with the previously reported results, which shows that this material is intrinsically n-type due to Se vacancies that act as donor defects (Afrid et al., 2022, 2023). The effective masses of charge carriers, m_q^* in these systems are generally larger when computed using the GGA+U functional compared to standard GGA because the inclusion of U improves the values of the m_q^*, which mitigates self interaction errors and more accurately captures electron correlation effects in the d orbitals (K. H. Habura et al., 2024). Consequently, electronic states become more localized the band curvature near edges decreases, leading to less dispersive bands and thus greater effective masses (since effective mass is inversely proportional to band curvature of the systems (Afrid et al., 2023; Kassa et al., 2024)). The extent of this effect is influenced by the substitutional composition as changes in the W-Mo ratio and S-Se composition alter the d electron correlations and the overall band structures. As a result, the GGA+U calculations generally predict larger m_q^* compared to standard GGA which has a notable impact on carrier mobility and the electronic behavior of these materials (Afrid et al., 2022; Yamusa et al., 2022). Despite this, both computational functional reveal consistent trends demonstrating that electronic properties can be finely tuned via compositional design. This tunability shows the potential of TMDC alloys for advanced IR optoelectronic applications. The table generally illustrates how varying the substitutional composition through alloying affects the m_q^* of charge carriers where the smaller m_q^* are associated with enhanced carrier mobility and the vice versa.

4.1.4.3 Electronic Band Structures, Density of States and Effective Masses of $\mathbf{V}_x\mathbf{W}_y\mathbf{Mo}_{1-x-y}\mathbf{S}_{2z}\mathbf{Se}_{2(1-z)}$ ($x = 0$, $y = 0, 0.125$, $z = 0, 0.0625, 0.125$)

Figure 28 shows the electronic dispersion relations of the supercell form of pristine 2H-$MoSe_2$ and its S with or without W doped variants using the GGA functional along the Γ-M-K-Γ high symmetry points. In each panel, the Fermi level is marked by a red horizontal dashed line and the energy gap indicated by downward black arrows in Figure 28(a-d) is defined as the energy difference between the highest point of the VB and the lowest point of the CB (Afrid et al., 2023; Sadasivam et al., 2015). Figure 28a displays the enegry band structure of the pristine 2H-$MoSe_2$ with the VBM located at the K point and the CBM situated along the M-K high symmetry paths shown within an energy range of -2 to 2 eV. The graph confirms an indirect bandgap of 0.9251 eV which is consistent with earlier theoretical findings (Böker et al., 2001; Mashmool et al., 2020; Sedhain & Kaphle, 2017). The value of this energy gap proffers the system is suitable for optoelectronic applications (Afrid et al., 2022, 2023; Jing et al., 2020; Yamusa et al., 2022). Furthermore, the concentrations of the density of electrons distribution in both the VB and CB are more higher compared to those of the pristine system as reported in (Afrid et al., 2023; Yamusa et al., 2022). In the supercell, there is a shift of the positions of both the VBM and CBM, which is due to the folding of the Brillouin zone that causes the band structure to fold as compared to the unit cell (Afrid et al., 2022; Yamusa et al., 2022). Figure 28b presents the electronic energy band of $MoS_{0.125}Se_{1.875}$ ternary composition, revealing an indirect bandgap. In the plot, the CBM is situated along the M-K high symmetry path, whereas the VBM is located at the Γ point. The

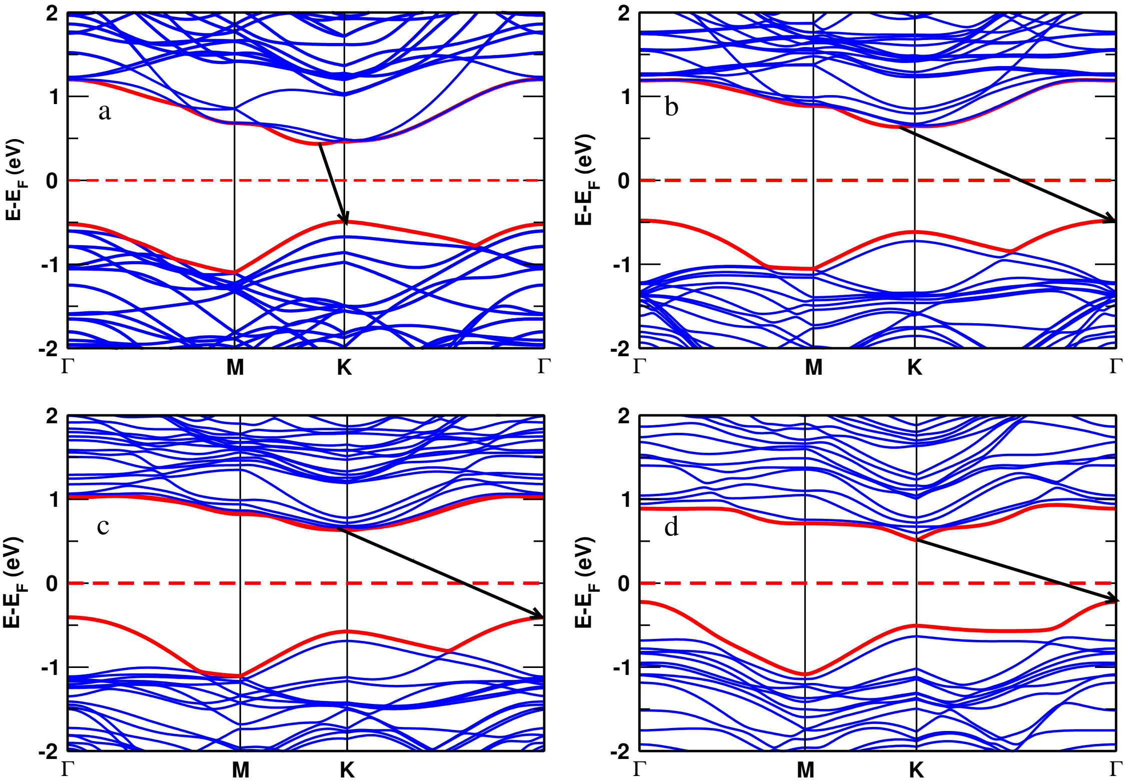

Figure 28: Electronic band diagrams of a) undoped, b) mono-sulfide, c) mono-W with mono-sulfide, and d) mono-W with di-sulfide of $W_yMo_{1-y}S_{2z}Se_{2(1-z)}$ using the GGA approximation.

energy gap of this material is $\sim$ 1.12 eV, widening that can be attributed to a shift in the Fermi level induced by mono-sulfide doping relative to the undoped material. Figure 28c shows the electronic band diagram of the $W_{0.125}Mo_{0.875}S_{0.125}Se_{1.875}$ composition. Compared to $MoS_{0.125}Se_{1.875}$ (as indicated in Figure 28b), the VBM is positioned at the Γ high symmetry point, whereas the CBM located at the M-K high symmetry points. As a result, this system displays 1.0421 eV indirect bandgap representing a slight increase compared to the pure system. The electronic band diagram of the $W_{0.125}Mo_{0.875}S_{0.25}Se_{1.75}$ quaternary material is displayed in Figure 28d. In this diagram, both the VBM and CBM are located very close to the Fermi level. Compared to all other S with or without W doped 2H-$MoSe_2$ systems, this material exhibits a more pronounced electron distribution near and above the Fermi level. It has an exceptionally narrow indirect bandgap of 0.7323 eV which is the smallest among all the studied configurations.

Figure 29(a-c) illustrates the significant impact of the GGA+U functional on the electronic energy bands of the pristine 2H-$MoSe_2$ and the mono-W with mono-sulfide, di-sulfide and tri-sulfide doped systems. The computational results show a downward shift of the Fermi level upon inclusion of the U correction that consists with findings reported in earlier studies (K. H. Habura et al., 2024; Yamusa et al., 2022). As shown in Figure 29a, the calculated bandgap of pristine 2H-$MoSe_2$ using the GGA+U functional is approximately 1.2 eV which aligns well with the previously reported values (Mashmool et al., 2020;

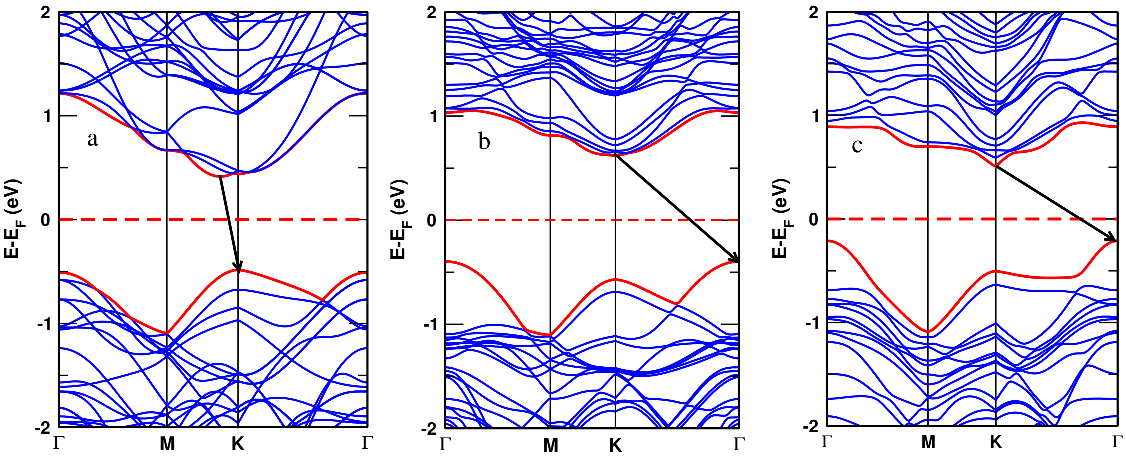

Figure 29: Electronic energy bands of a) undoped, b) mono-sulfide with mono-W and c) di-sufide with mono-W doped of $W_yMo_{1-y}S_{2z}Se_{2(1-z)}$ using the GGA+U approximation.

Schneemeyer & Sienko, 1980; Yamusa et al., 2022). This finding confirms the typical bandgap widening effect caused by the inclusion of the U correction (K. H. Habura et al., 2024), which is improved by 0.2384 eV compared to the GGA result. In this figure, the VBM is located at the Γ point, while the CBM lies along the M-K paths consistent with the indirect bandgap nature observed in the electronic energy bands of Figure 29a and other reported values (Afrid et al., 2023; Yamusa et al., 2022). The plot further shows a higher concentrations of the electron states above the Fermi level and a reduced spatial spread in electron distribution compared to the results obtained with the standard GGA functional. The electronic band structure for mono-W with S doped systems like $W_{0.125}Mo_{0.875}S_{0.125}Se_{1.875}$ and $W_{0.125}Mo_{0.875}S_{0.25}Se_{1.75}$ are illustrated in Figures 29b and 29c, respectively. Specifically, the electronic band diagram of one W with one S doped material reveals an indirect bandgap value of appropriately 1.1051 eV when the U correction is included, that optimizes the energy gap by 0.063 eV compared to the GGA value as seen in Figure 28c. In agreement with the GGA findings calculated by (Afrid et al., 2023; Yamusa et al., 2022), the U correction causes the VBM to shift upward and the CBM to shift downward. Furthermore, the electron distributions of both above and below the Fermi level appear clearer and more distinct compared to the pristine system. Figure 29c presents the electronic band structure of the mono-W with di-sulfide doped systems of 2H-$MoSe_2$. The VBM stays at the Γ point, while the CBM is located at the K point confirming that the material retains its indirect bandgap property. The bandgap value is 0.74678 eV representing an increase of 0.01448 eV compared to the GGA result as shown in Figure 28d. Furthermore, the electron distributions in both the VB and CB are more sharply defined compared to those in lower doping cases (see Figure 29b and 29c) indicating a reduction in orbital state hybridization. These computational findings demonstrate that the inclusion of the U correction notably alters the bandgap properties in materials containing TM (d-block) elements (Izyumov, 1995). In both GGA and GGA+U calculations, the pristine system exhibits a CBM located between the M and K high symmetry points with the VBM positioned near the K point. Upon doping with S and W atoms, the VBM shifts to the Γ high symmetry point, while the CBM stays between the M and K points, consistent with the behavior observed in the undoped system.

Figure 30 shows the PDOS of $W_yMo_{1-y}S_{2z}Se_{2(1-z)}$ materials in the substitutional compositions of $y = z = 0$, $y = 0, z = 0.0625$, $y = 0.125, z = 0.0625$ and $y = z = 0.125$ resolved into individual contributions from Mo, W, S and Se atoms over the energy range of -3 to 3 eV. For undoped 2H-$MoSe_2$ (see Figure 30a), a symmetric TDOS profile is observed mainly dominated by Mo 4d and Se 4p orbitals which is consistent with the previous studies (Afrid et al., 2023; Yamusa et al., 2022). The contributions Mo 5s, Mo 4p and Se 4s orbitals are minimal aligning with previous theoretical findings (Afrid et al., 2022, 2023). The absence of band crossing at the Fermi level further confirms the semiconductor nature of the material (Afrid et al., 2022, 2023; Y. Tian et al., 2020). The plot also presents the low electron density near the Fermi level that confines the electrical conductivity and carrier mobility of the system (C. Lee et al., 2014). As a result, the Mo atoms have a more significant influence than the Se on the electrical and functional properties of 2H-$MoSe_2$ (Afrid et al., 2022; Yamusa et al., 2022). In this figure, the PDOS peaks at 42.6429 states/eV at the energy of 2.1832 eV with the CB which is higher than the values previously

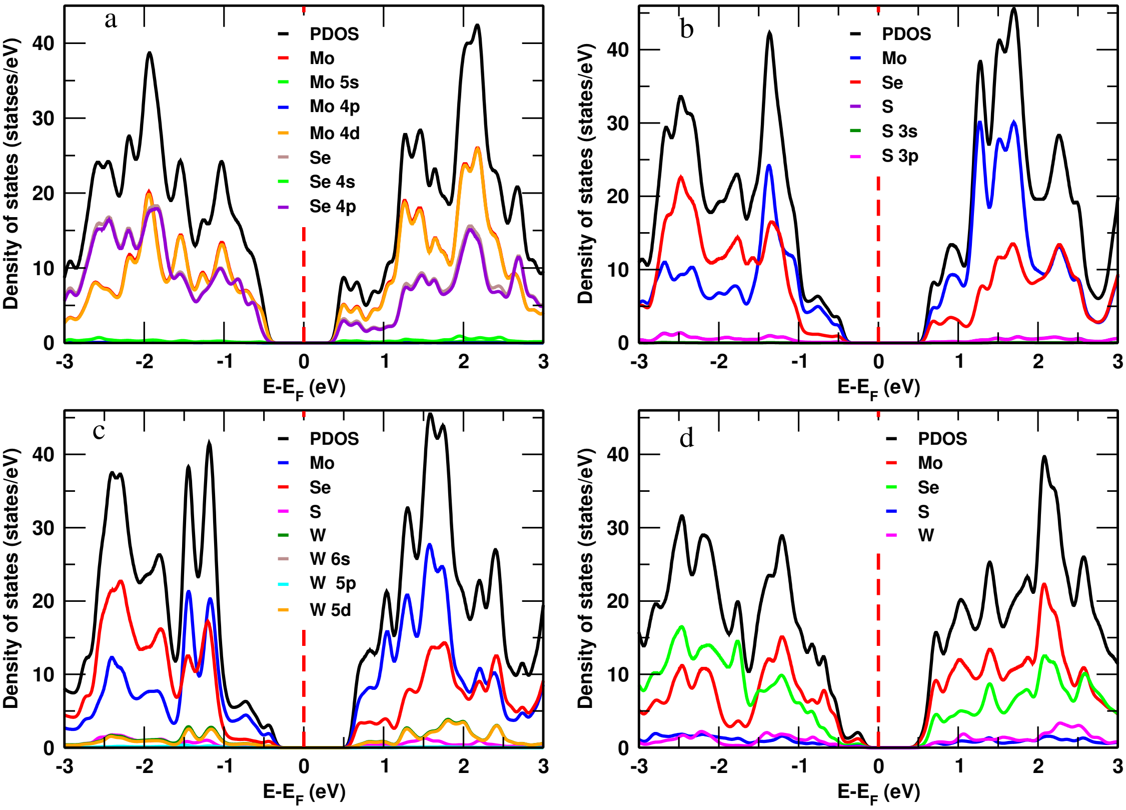

Figure 30: Density of states for a) undoped, b) mono-W with mono-sulfide, and c) W-mono with di-sulfide of $W_yMo_{1-y}S_{2z}Se_{2(1-z)}$ using the GGA approximation.

reported in the literature for the unit cell of same material (Afrid et al., 2022, 2023). Two different peaks are evident in both the VB and CB. Specifically, one peak appears in the VB region at -1.93255 eV (38.6565 states/eV), while the other peak is found in the CB at 2.1832 eV (42.6565 states/eV). Since enhancing the conductivity of the material fundamentally requires increasing the TDOS at the Fermi level via controlled charge carriers (S. Kumar & Schwingenschlogl, 2015). Figure 30b depicts the PDOS for the $MoS_{0.125}Se_{1.875}$ mono-sulfide doped system. Both the CB as well as VB are mainly influenced by the Mo 4d orbital with secondary contributions of the Se 4p orbital. On the other hand, orbital like the S 3s has a negligible effect on the these bands compared to the dominant atomic orbitals that is consistent with the previous research (Sedhain & Kaphle, 2017; Yamusa et al., 2022). In this diagram, TM (Mo) consistently exhibits the greater contributions to the electronic energy band than to the chalcogen atoms (Se and S) (Afrid et al., 2023; Sedhain & Kaphle, 2017). Additionally, the CB shows a significant PDOS peak of 45.7165 states/eV at 1.7047 eV and new electronic states emerge near 0 eV accompanied by a slight downward shift in the Fermi level, where the Fermi level moves closer to the VB upon mono-sulfide doping indicating to a p-type semiconductor behavior (Kang et al., 2013). The PDOS for $W_{0.125}Mo_{0.875}S_{0.125}Se_{1.875}$ system is illustrated in Figure 30c. In this diagram, the CB and VB are predominantly formed by the Mo 4d states with smaller contributions from the Se 4p, W 5d and S 3p orbitals consistent with earlier reports (Sedhain & Kaphle, 2017). Similar to Figure 30b, the contributions from the W 6s, W 5p and S 3p atomic orbitals are negligible. In this diagram, additional peak appears near the Fermi level compared to the pristine and mono-sulfide doped materials (see Figures 30a and 30b, respectively), shows an increased electron density in that region when sulfur and tungsten were incorporated into the system (Kang et al., 2013). The highest peak of PDOS (45.6392 states/eV) occurs at 1.5985 eV in the CB region. Similarly, Figure 30d displays the PDOS for the quaternary $W_{0.125}Mo_{0.875}S_{0.25}Se_{1.75}$ system, where the Fermi level is shifted closer to the VB and the electron density near this level is enhanced compared to both the pristine material and other perturbed systems. In this case, the CB and VB are primarily composed of the Mo 4d and Se 4p orbitals with smaller contributions from the W 5d orbitals and minimal involvement of the S 3p orbitals. The dominant contribution of sulfur and molybdenum atomic orbitals to these bands is attributed to their higher compositions. Furthermore, in the CB, the maximum PDOS reaches a peak of 39.7926 states/eV at 2.0953 eV. As anticipated, TM orbitals exhibit stronger contributions to the band structure compared to the chalcogens (Afrid et al., 2023; Asadi & Nourbakhsh, 2019; Dumcenco et al., 2010). These findings show strong agreement between the density of states analysis and the electronic structure diagrams calculations projected onto atomic orbitals. Figure 31 presents the computed PDOS plots using the GGA+U functional for pristine 2H-$MoSe_2$ and its W-S doped variants over the energy range of -3 to 3 eV. As shown in Figure 31a, the VB and CB of the pure system are predominantly derived from the

Mo 4d and Se 4p orbitals which agrees with the GGA results presented in Figure 30a. In agreement with the GGA results, the electronic properties are only slightly influenced by the Mo 5s, Mo 4p and Se 4s orbitals. The system shows a TDOS peak of 44.0934 states/eV at 2.1882 eV in the CB which exceeds the value obtained from earlier GGA+U calculations of the unit cell for the same material. The energy range from -0.4841 to 0.6794 eV is devoid of electron states revealing that a forbidden gap with no accessible states that agrees with the electronic band diagram calculations (see Figure 29a). The GGA+U functional tends to localize electron density more strongly around the correlated atomic sites compared to standard GGA often reducing delocalization and covalent character in bonds which can result in lower electron density in hybridized regions. As shown in the PDOS analysis of Figure 31b, the $W_{0.125}Mo_{0.875}S_{0.125}Se_{1.875}$ system, the Fermi level shifts toward the VB. In this system, the CB and VB are primarily governed by the Mo 4d and Se 4p orbitals with smaller contributions of the W 5d and S 3p states. The contributions of the W 6s, W 5p and S 3s orbitals to both the CB and VB are negligible. The system exhibits a maximum PDOS peak of 46.6281 states/eV at 1.5583 eV which is lower compared to the value reported in the previous GGA+U calculation for the same system. Furthermore, the energy range from -0.3963 to 0.7088 eV shows empty DOS signifying a forbidden gap where no electron states are available. Figure 31c shows the PDOS of the $W_{0.125}Mo_{0.875}S_{0.25}Se_{1.75}$ system, indicating a greater shift of the Fermi level toward the VB which suggests a p-type semiconductor character. The energy range of -0.23028 to 0.5165 eV exhibits no electron states, indicating a energy gap that aligns with the electronic band structure calculations (see Figure 29c). The PDOS achieves a maximum peak of 37.9607 states/eV at 2.10104 eV in the CB, which is lower than the corresponding GGA+U value. The CB and VB are primarily derived from the Mo 4d and Se 4p orbitals with additional contributions of the W 5d and S 3p states. All computed DOS profiles obtained using both GGA and GGA+U functionals exhibit sharp features behaviors of Van Hove singularities (Van Hove, 1953) which arise at band extrema and saddle points in the Brillouin zone where the electronic group velocity approaches zero.

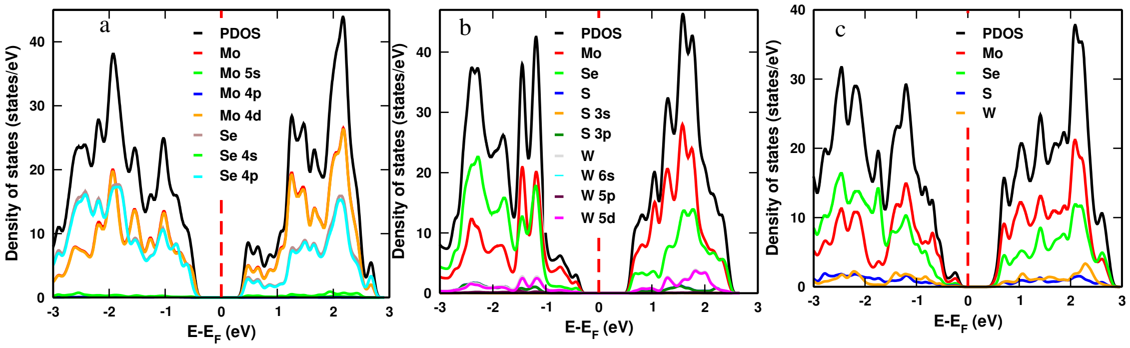

Figure 31: Density of states for a) undoped b) mono-W with mono-sulfide and c) mono-W with di-sulfide doped $W_yMo_{1-y}S_{2z}Se_{2(1-z)}$ using the GGA+U approximation.

Under the GGA approximation, higher sulfur dopant concentrations result in a suppression of the dominant DOS peaks in both the VB and CB. This behavior is not observed when the GGA+U functional is used. The inclusion of the U parameter significantly alters the DOS by shifting energy levels and enhancing electron localization particularly in strongly correlated orbitals (Mo 4d and W 5d). This can lead to noticeable shifts or even splitting of the DOS features offering a more refined and physically accurate representation of the material's electronic structure. Using the band extrema from the electronic band structures, the effective masses of charge carriers in $W_yMo_{1-y}S_{2z}Se_{2(1-z)}$ were computed with both GGA and GGA+U functionals, as summarized in Table 8. These materials are expected to exhibit p-type behavior, as the hole effective mass (m_h) is larger than the electron effective mass (m_e), as well as the Fermi level is shifted to the VBM, in agreement with previous findings (Afrid et al., 2022, 2023). We further examined the variation in the effective masses of charge carriers across various dopant compositions in $W_yMo_{1-y}S_{2z}Se_{2(1-z)}$ systems. Since the curvature of the CBM and VBM which directly determines the effective masses is sensitive to dopant compositions, the m_q^* of both electrons and holes in these doped systems (Table 8) are correspondingly influenced. In general, the values obtained with the GGA+U functional are larger than those calculated using the standard GGA. This increase stems from the inclusion the U correction in the GGA+U which reduces the self interaction errors and provides a more accurate description of electron correlation effects in the d orbitals (K. H. Habura et al., 2024). As a result, electronic states become more localized and the curvature of the energy bands near the band edges is reduced leading to flatter and less dispersive bands. Because the m_q^* is inversely proportional to band curvature (Afrid et al., 2023; Kassa et al., 2024), that diminished curvature translates into an increase in it. The extent of this effect is strongly dependent on dopant compositions including varying the W-Mo ratio and the S-Se compositions alters the d electron correlations and consequently reshapes the overall band structure. Consequently, the GGA+U calculations consistently yield higher the m_q^* compared to the standard GGA which has a pronounced impact on carrier mobility and the broader electronic response of these materials. Despite these quantitative differences, both functionals exhibit consistent qualitative trends underscoring that the electronic properties of these systems can be

Table 8: Calculated effective masses in $W_yMo_{1-y}S_{2z}Se_{2(1-z)}$ with varying dopant compositions.

Material	**GGA**		**GGA+U**	
	m_e^*/m_0	m_h^*/m_0	m_e^*/m_0	m_h^*/m_0
2H-$MoSe_2$	0.479	0.642	0.484	0.669
Others (Literature)	0.47(Afrid et al., 2023) 0.40	0.53(Afrid et al., 2023) 0.45	0.41	0.50
$MoS_{0.125}Se_{1.875}$	0.664	1.312		
$W_{0.125}Mo_{0.875}S_{0.125}Se_{1.875}$	0.786	1.022	0.887	1.029
$W_{0.125}Mo_{0.875}S_{0.25}Se_{1.75}$	0.113	0.488	0.117	0.583

precisely engineered via compositional tuning. This tunability positions doped 2D bilayer 2H-MoSe$_2$ as promising candidates for next-generation IR optoelectronic devices. As shown in the table, even subtle doping induced changes in chemical composition significantly influence the charge carrier effective mass m$_q^*$. Lower values of m$_q^*$ generally correlate with higher carrier mobility a key parameter for high performance electronic and optoelectronic applications.

4.1.4.4 Electronic Band Structures and Density of States of $\mathbf{V_xW_yMo_{1-x-y}S_{2z}Se_{2(1-z)}}$ $\mathbf{(x = 0.125, y = 0, z = 0, 0.0625, 0.125, 0.1875)}$

Energy band diagram of $V_xMo_{1-x}S_{2z}Se_{2(1-z)}$ for $x = 0.125$ and $z = 0, 0.0625, 0.125, 0.1875$ dopant compositions is depicted in Figure 32 using the GGA functional along the Γ-M-K-Γ high symmetry points. In each panel, the Fermi level is marked by the red horizontal dashed lines and the energy bandgap indicated by upward black arrows in Figure 32(a-d) is defined as the energy difference between the highest point of the VB and the lowest point of the CB (Sadasivam et al., 2015). Figure 32a presents the electronic band structure of the $V_{0.125}Mo_{0.875}Se_2$ composition that reveals an indirect bandgap property. The CBM is situated along the M-K high symmetry paths, whereas the VBM is at the Γ point. The bandgap in this ternary system increases to 0.8071 eV which is larger than the bandgap previously calculated for the 0.5 vanadium substituted unit cell of 2H-MoSe$_2$ as seen from Figure 22a. Compared to the system with higher vanadium substitutional composition, the supercell with low vanadium doping remains semiconducting, whereas the former exhibits semimetallic or degenerate semiconductor behavior due to the high vanadium dopant composition (see Figure 22a). Figure 32b exhibits the electronic band structure of the $V_{0.125}Mo_{0.875}S_{0.125}Se_{1.875}$ composition co-doped with one vanadium and one sulfur atom atoms. Compared to Figure 32a, the bandgap increases to 0.8219 eV due to the presence of the sulfur atom and this value is larger than the bandgap previously calculated for the same substitutional atoms in the unit cell (see Figure 22c). Similar to others, this system displays an indirect bandgap behavior representing a slight increase compared to the mono-V doped system. The electronic band structure of the quaternary compound $V_{0.125}Mo_{0.875}S_{0.25}Se_{1.75}$ is displayed in Figure 32c. In the plot, the VBM is positioned very close to the Fermi level compared to other compositions. Among all V doped or vanadium with sulfur co-doped systems analyzed this composition shows a more significant electron density in the Fermi level. It features a wider indirect bandgap of 0.877 eV which is the largest value observed among all previously studied of mono-V with di-sufide substituted to the unit cell configurations as exhibited in Figure 22e. The electronic band structure of the $V_{0.125}Mo_{0.875}S_{0.375}Se_{1.625}$ composition is presented in Figure 32d. In the figure, the VBM is located at the Γ point, while the CBM lies at the K point. The calculated bandgap for this system is 0.9022 eV which is the largest value among all configurations shown in Figure 32(a-c) and exceeds those reported in our previous and other studies which is shown from Figure 22g.

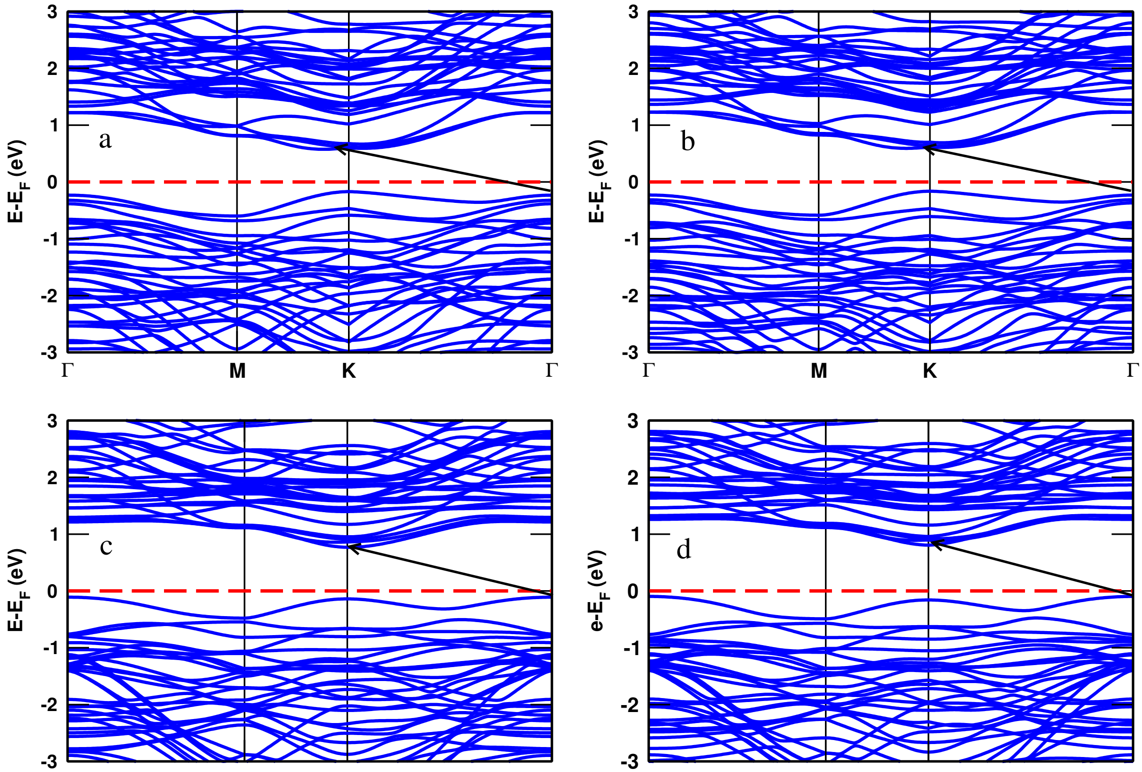

Figure 32: Electronic band diagrams for a) mono-V, b) mono-V with mono-S, c) mono-V with di-S and d) mono-V with tri-S doped of $V_xMo_{1-x}S_{2z}Se_{2(1-z)}$ using the GGA approximation.

Figure 33(a-d) illustrates the notable influence of the GGA+U method on the electronic band diagram and the Fermi level position of $V_xMo_{1-x}S_{2z}Se_{2(1-z)}$ systems. The computational findings reveal a downward shift of the Fermi level upon inclusion of the U correction in agreement with the previous research (Afrid et al., 2022, 2023; K. H. Habura et al., 2024). Figure 33a shows the electronic bandgap of the mono-V doped of supercell 2H-$MoSe_2$ using the GGA+U method which is 0.8066 eV. This value is in good agreement with the previously reported results (Mashmool et al., 2020; Schneemeyer & Sienko, 1980) and is slightly higher than the bandgap computed for the same V substitution in the pristine unit cell of this material as observed from Figures 23c and 32a. This finding confirms the typical bandgap widening effect resulting from the inclusion of the U correction (K. H. Habura et al., 2024), is equivalent to the GGA result. In the figure, the VBM is located at the Γ point, while the CBM appears along the M-K path consistent with the indirect bandgap behavior observed in the electronic band structure (Afrid et al., 2023). The plot further shows a higher composition of electron states above the Fermi level and a reduced spatial spread in electron distribution compared to the results obtained with the standard GGA method. The electronic band structures for V with S co-doped quaternary systems ($V_{0.125}Mo_{0.875}S_{0.125}Se_{1.875}$, $V_{0.125}Mo_{0.875}S_{0.25}Se_{1.75}$ and

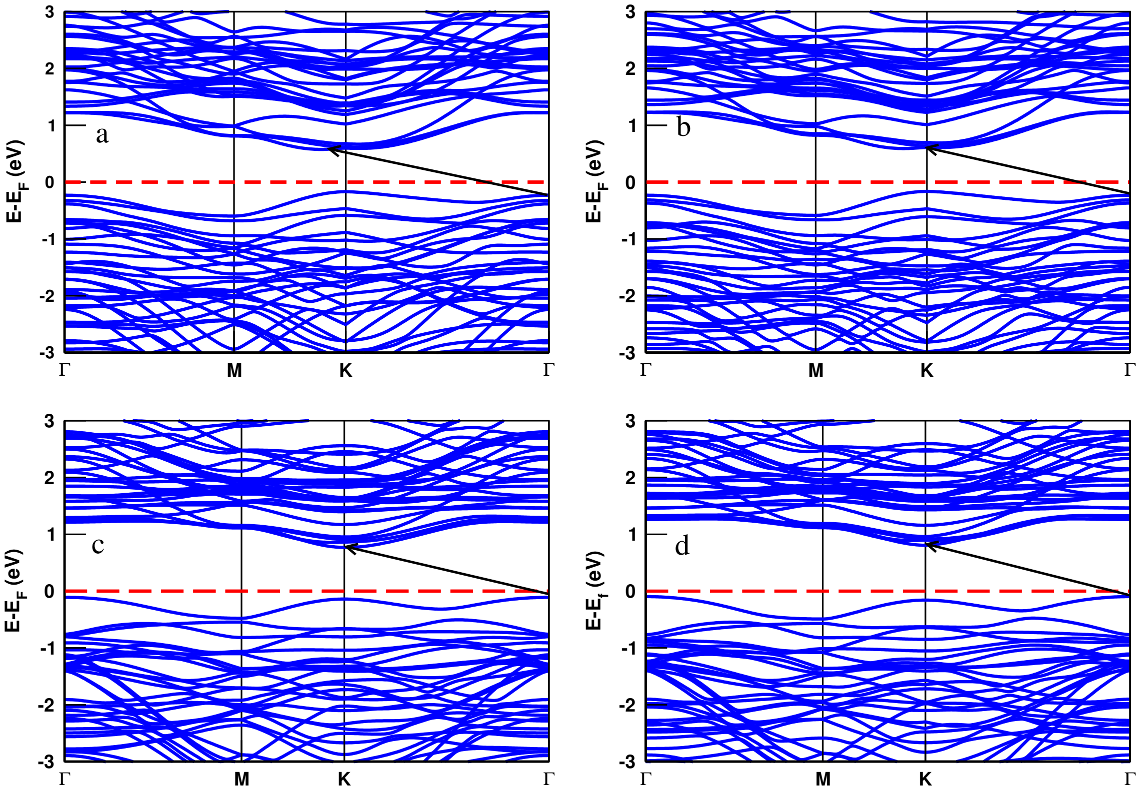

Figure 33: Electronic band structures for a) mono-V, b) mono-S with mono-V, c) di-S with mono-V and d) mono-V with tri-S doped of $V_xMo_{1-x}S_{2z}Se_{2(1-z)}$ using the GGA+U approximation.

$V_{0.125}Mo_{0.875}S_{0.375}Se_{1.625}$) are illustrated in Figures 33b, 33c and 33d, respectively. In Figure 33b, the indirect bandgap is calculated as 0.8219 eV after applying the U correction. This value matches the bandgap obtained with the GGA+U approximation in Figure 33a, since the U correction has minimal effect on p block elements and low dopant composition of vanadium. However, it is improved compared to the GGA approach as shown in Figure 32a. The computed indirect bandgap of the mono-V with di-sulfide co-doping system is 0.877 eV as shown in Figure 33c which matches the energy bandgap calculated in Figure 32c. This value also agrees with the GGA result indicating that the U correction has a negligible effect on the p block elements and low dopant composition of V in this case. Similarly, Figure 33d indicates the mono-V with tri-sulfur co-doping system where the calculated indirect bandgap is approximately 0.9022 eV that corresponds to the GGA result computed in Figure 32d.

Figure 34 shows the PDOS for the $V_xMo_{1-x}S_{2z}Se_{2(1-z)}$ layered systems with dopant compositions of $x = 0.125$, $z = 0$; $x = 0.125$, $z = 0.0625$, $x = 0.125$, $z = 0.125$ and $x = 0.125$, $z = 0.1875$, resolved into individual contributions from the Mo, V, S and Se atoms. It is analyzed within the energy range of -3 to 3 eV. Figure 34a shows the PDOS for the $V_{0.125}Mo_{0.875}Se_2$ mono-V doped system. Both the CB and VB are predominantly influenced by the Mo 4d and Se 4p atomic orbitals with a minor contributions from the V 3d. This differs from the 2H-$MoSe_2$ unit cell substituted with a 50% of vanadium (refer Figure 22b). In contrast, orbitals such as the Se 4s, 3d; Mo 5s and V 4s have a negligible effect on the CB and VB compared to the dominant atomic orbitals consistent with the previous research (Sedhain & Kaphle, 2017; Yamusa et al., 2022). In this diagram, TM (Mo) and chalcogen atom (Se) consistently exhibit greater contributions to the electronic band structure (Afrid et al., 2023; Sedhain & Kaphle, 2017) compared to the V atom. Additionally, the CB exhibits a prominent PDOS peak of 40.61 states/eV at 2.15 eV and there is no crossing of the Fermi level by the impurity bands. This indicates that the system is fundamentally different from the mono-V with mono-sulfide co-substituted system in the unit cell (again refer in Figure 22b). In this case, the low doping composition of the mono-V with mono-sulfide co-doped system behaves as a semiconductor or non-degenerate semiconductor material, unlike the system shown in Figure 22b. Figure 34b illustrates the PDOS for the $V_{0.125}Mo_{0.875}S_{0.125}Se_{1.875}$ system. In the plot, the CB is primarily dominated by the Mo 4d and Se 4p atomic orbitals with a minimal contributions from the V 3d and S 3p. Meanwhile, the VB is mainly influenced by the Mo 4d and Se 4p atomic orbitals, also with minor contributions from the V 3d and S 3p. On the other hand, the CB exhibits a prominent PDOS peak of 38.83 states/eV at 2.08 eV and there is no crossing of the Fermi level by the impurity bands. This indicates that the system is fundamentally different from the mono-Vwith di-sulfide co-substituted system in the unit cell,(refer in Figure 22d). The PDOS of the $V_{0.125}Mo_{0.875}S_{0.25}Se_{1.75}$ system is displayed in Figure 34c. In the figure, the contribution of the S 3p atomic orbital is minimal,

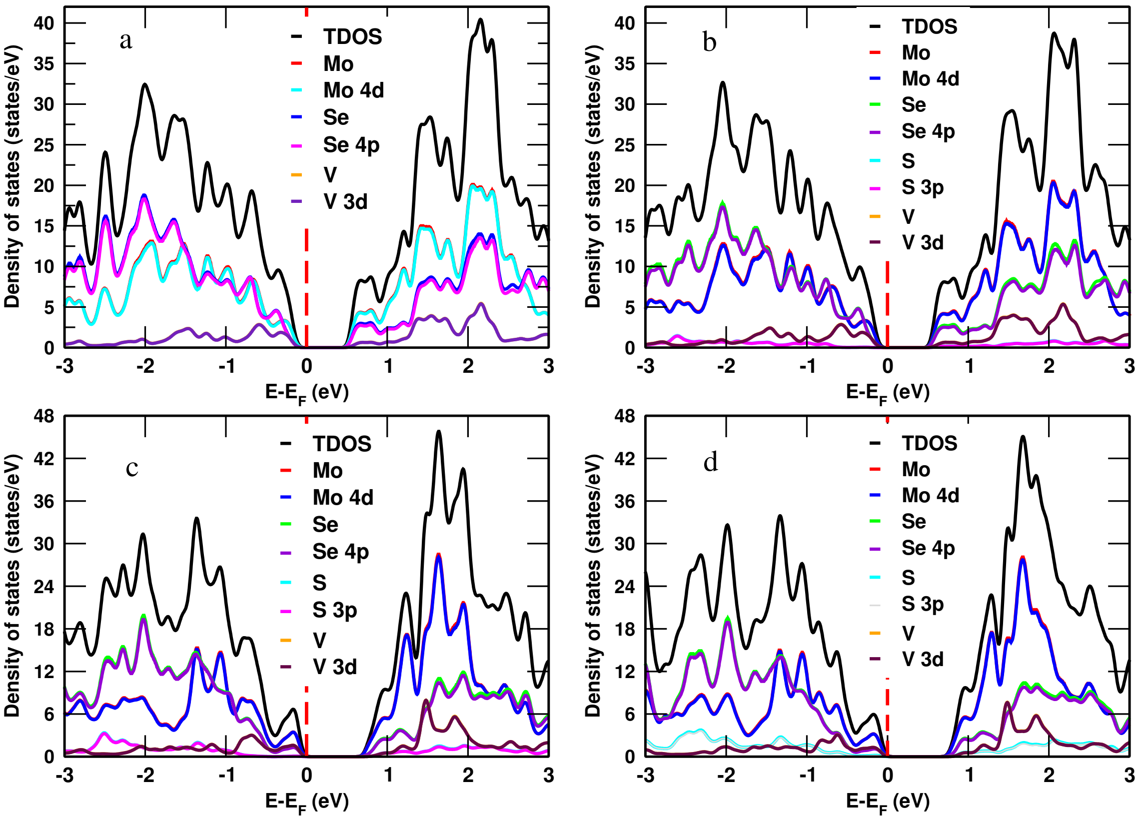

Figure 34: Density of states for a) mono-V, b) mono-S with mono-V, c) di-S with mono-V and d) mono-V with tri-S doped of $V_xMo_{1-x}S_{2z}Se_{2(1-z)}$ using the GGA approximation.

while the Mo 4d and Se 4p orbitals dominate, followed by the V 3d orbital in both the CB and VB. Furthermore, the CB displays a prominent PDOS peak of 45.96 states/eV at 1.65 eV with no crossing of the Fermi level by impurity bands. This indicates that the system is fundamentally different from the mono-V with di-sulfide co-substituted system in the unit cell (as shown in Figure 22f), where the Fermi level lies much closer to the VB. Figure 34d shows the PDOS for the system of the $V_{0.125}Mo_{0.875}S_{0.375}Se_{1.625}$. In this diagram, as in others, the contribution of the S 3p orbitals to both the VB and CB is minimal, while the Mo 4d and Se 4p orbitals dominate followed by the V 3d. Additionally, the CB displays a prominent PDOS peak of 45.22 states/eV at 1.69 eV with no crossing of the Fermi level by impurity bands. This indicates that the system is fundamentally different from the mono-V with tri-sulfide co-substituted system in the unit cell(as shown in Figure 22h).

Figure 35 shows the PDOS and atomic orbital contributions for the layered $V_xMo_{1-x}S_{2z}Se_{2(1-z)}$ systems with dopant compositions of $x = 0.125$ and z values of 0.0625, 0.125 and 0.1875. The contributions from the Mo, V, S and Se atoms are individually resolved using the GGA+U approximation. This detailed analysis reveals how varying the chalcogenide composition impacts the electronic structure with the Mo 4d and Se 4p orbitals dominating the VB and CB accompanied by varying minor contributions from the V 3d and S 3p orbitals depending on the Se/S ratios. The GGA+U method accounts for electron correlation effects localized mainly in the V 3d orbitals that yields an accurate depiction of the doped system's electronic behavior across these layered alloy compositions (Hoque & Zubair, 2022). The CB exhibits a prominent PDOS peak of 40.39 states/eV at 2.17 eV and there is no crossing of the Fermi level by the impurity bands. This indicates that the system is fundamentally different from the mono-V with mono-sulfide co-substituted system in the unit cell (as shown in Figure 23d) but equivalent to the GGA result as seen from Figure 34a. Figure 35a displays the PDOS of the $V_{0.125}Mo_00.875Se_2$ system. In this plot, both the CB and VB energy bands are predominantly composed of the Mo 4d and Se 4p atomic orbitals with smaller contributions of the V 3d. A prominent peak is observed at 2.15 eV in the CB region corresponding to 40.38 states/eV. The PDOS for the $V_{0.125}Mo_{0.875}S_{0.125}Se_{1.875}$ is illustrated in Figure 35b, where its CB and VB are more composed of the Mo 4d, Se 4p and V 3d with less contributions of the S 3p. The main peak is observed at 2.10 eV in the CB region corresponding to 38.66 states/eV. The PDOS for the $V_{0.125}Mo_{0.875}S_{0.25}Se_{1.75}$ is illustrated in Figure 35c, where its CB and VB are more composed of the Mo 4d, Se 4p and V 3d with less contributions of the S 3p. The major peak is observed at 1.65 eV in the CB region, corresponding to 48.96 states/eV. The PDOS for the $V_{0.125}Mo_{0.875}S_{0.375}Se_{1.625}$ is illustrated in Figure 35d, where its CB and CB are more composed of the Mo 4d, Se 4p and V 3d with less contributions of the S 3p. At 1.69 eV in the CB region the main peak is observed that corresponds to 45.22 states/eV. At a V doping composition of 0.125 in bilayer 2H-$MoSe_2$, the similarity between GGA and GGA+U results primarily arises because the electron correlation effects targeted by the U correction

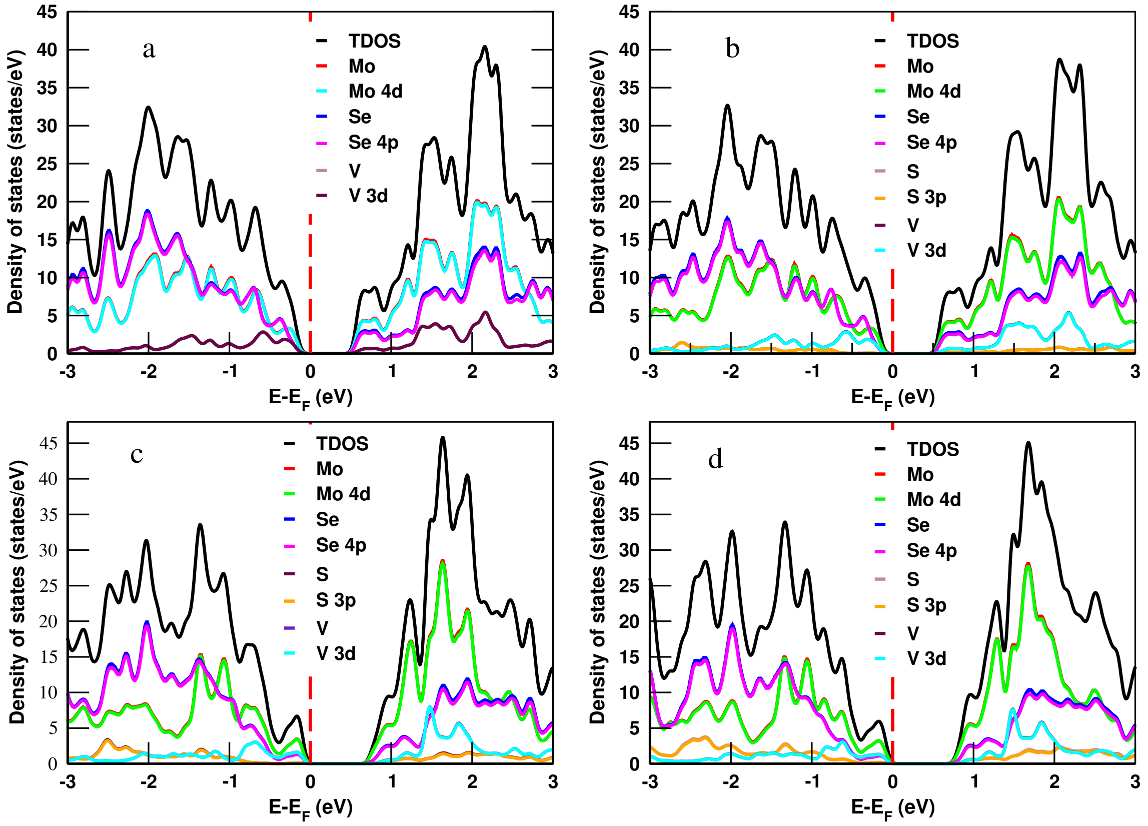

Figure 35: Density of states for a) mono-V, b) mono-S with mono-V, c) di-S with mono-V and d) mono-V with tri-S doped of $V_xMo_{1-x}S_{2z}Se_{2(1-z)}$ using the GGA+U approximation.

are not strongly pronounced at this moderate doping level. Vanadium atoms substitute molybdenum sites, but the overall electronic structure remains dominated by Mo 4d and Se 4p orbitals, with only modest contributions from the V 3d states. The U correction mainly affects strongly localized d electrons which causes the significant changes in the electronic structure at higher doping compositions or in systems with stronger electron correlation and localization.

At the dopant composition of 12.5%, the localization of the V 3d electrons is insufficient to cause major differences between GGA and GGA+U results. While U shifts and splits d states to better account for on site Coulomb interactions in this system the states remain relatively delocalized, resulting in similar bandgap and electronic structures predicted by both methods. This behavior aligns with recent studies on V-doped transition metal dichalcogenides, showing that low to moderate doping compositions produce only minor band structure changes with U corrections. The dominant role of the host lattice orbitals and relatively weak correlation changes in dopant states mean GGA+U and GGA yield comparable results. Only at higher doping or in strongly localized electron systems would GGA+U produce significantly different electronic structures compared to the GGA (Sukanya et al., 2025). Therefore, in our bilayer 2H-$MoSe_2$ system with 0.125 vanadium dopant comparison, the near equivalence of the GGA and GGA+U results is expected. The standard GGA suffices to accurately describe the electronic properties at this dopant composition. Adjusting U values or considering many body effects could be explored if stronger correlation effects are suspected, but at this doping level, the observed similarity is typical. Hence, the GGA and GGA+U calculations for 0.125 V-doped bilayer 2H-$MoSe_2$ are almost the equivalent because the correlation effects targeted by U are not pronounced enough at this dopant composition to significantly alter the electronic structure.

4.1.5 Optical Properties of $V_xW_yMo_{1-x-y}S_{2z}Se_{2(1-z)}$

In this section, we analyzed how dopant and/or substitutional compositions and its types influence the optical properties of 2D materials, $V_xW_yMo_{1-x-y}S_{2z}Se_{2(1-z)}$ with $x = 0, 0.125, 0.5$, $y = 0, 0.125, 0.5$ and $z = 0, 0.0625, 0.125, 0.1875, 0.25, 0.5, 0.75$. For each compositions, the calculated frequency dependent complex dielectric function, $\varepsilon(\omega)$, consisting of real and imaginary parts (Afrid et al., 2022). The optical behaviors of these alloys is described by the $\varepsilon(\omega)$ which includes the $\varepsilon_1(\omega)$ and $\varepsilon_2(\omega)$ components. This function governs how the material interacts with electromagnetic waves, affecting light propagation in bilayer 2H-$MoSe_2$ (Ghosh et al., 2013) and its substituted variants. Understanding the $\varepsilon(\omega)$ enables prediction of the material's electromagnetic response which is main to assessing its favorable for optoelectronic and other electronic applications (Bhattacharjee & Chattopadhyaya, 2017).

4.1.5.1 Dielectric Constants of $V_xW_yMo_{1-x-y}S_{2z}Se_{2(1-z)}$ ($x = 0, 0.5$, $y = 0$, $z = 0, 0.25, 0.5, 0.75$)

The $\varepsilon_1(\omega)$ and $\varepsilon_2(\omega)$ components of the dielectric function for pure, mono-V and mono-V with S substituted bilayer 2H-$MoSe_2$ are illustrated in Figure 36a and b, respectively. In Figure 36a, the static dielectric constant, $\varepsilon_1(0)$ which is the real dielectric function at zero frequency is observed to be higher for the substituted systems than for the unsubstituted system. This figure demonstrates that the $\varepsilon_1(0)$ increases with rising substitutional compositions, with co-substituted systems showing higher values than the mono-V substituted system. Notably, the $\varepsilon_1(0)$ value for the system with V (0.5) and S (0.25) compositions ($V_{0.5}Mo_{0.5}S_{0.5}Se_{1.5}$) reaches to 27.593455 atomic units, the highest among both the unsubstituted and other substituted systems as presented in Table 9. The $\varepsilon_1(0)$ values for the substituted systems surpass those of the pure material as reported by the previous studies (Asadi & Nourbakhsh, 2019; Lahourpour et al., 2019; Y. Li et al., 2014; Z. Luo et al., 2022). The low value of $\varepsilon_1(0)$ corresponds to the relatively large bandgaps observed in these materials (Lahourpour et al., 2019). As seen, the peak values of the $\varepsilon_1(\omega)$ for the $V_{0.5}Mo_{0.5}Se_2$, $V_{0.5}Mo_{0.5}S_{0.5}Se_{1.5}$ and $V_{0.5}Mo_{0.5}S_{1.5}Se_{0.5}$ substituted systems lie in the infrared region, whereas those of unsubstituted and $V_{0.5}Mo_{0.5}S_1Se_1$ systems lie in the visible region. A positive correlation exists between photon energy and the $\varepsilon_1(\omega)$, with

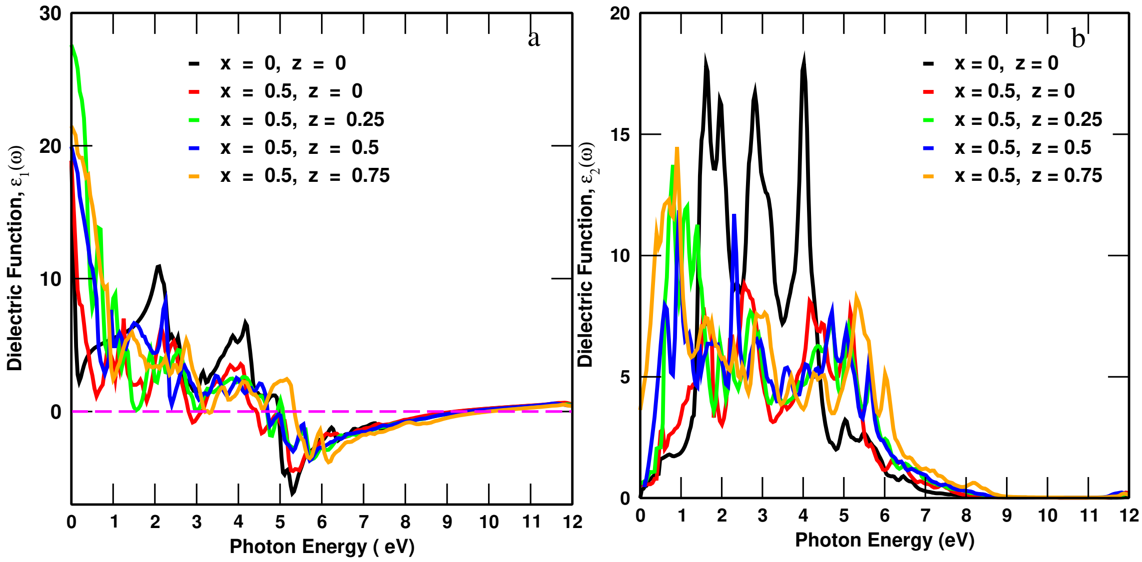

Figure 36: Real a) and Imaginary b) dielectric Spectra for unsubstituted and V with or without S substituted of $V_xMo_{1-x}S_{2z}Se_{2(1-z)}$.

increasing photon energy leading to a decrease in this value for all studied materials. A significant portion of the materials under investigation displays negative values for the $\varepsilon_1(\omega)$ in the energy range of 2.86-3.11 eV and 4.45-9.17 eV of the mono-V substituted and 4.71-9.47 eV for all other V with S-substituted systems. Beyond these specified energy ranges, the materials undergo minimal changes in their dielectric function values and approaches to zero. This indicates that photons with energies outside this range can pass via the materials without significant absorption (C.-H. Yang & Chang, 2022). The negative values of the $\varepsilon_1(\omega)$ observed across different regions for all systems indicate the primarily indicates the plasmonic or metallic response (Lahourpour et al., 2019) which suggests a lack of optical transparency. The most significant response to incident light is observed in parallel radiation for favorable application in the optical industry or solar cell technologies (Blaha et al., 2001; Flöry et al., 2015; X. Li & Zhu, 2015). The values of the $\varepsilon_1(\omega)$ become zero several times due to the Plasmon oscillations requiring a peak in the energy loss spectrum for confirmation. In Figure 36a, certain regions exhibit high dielectric constant values; they demonstrate lower absorption levels. A higher $\varepsilon_1(0)$ suggests stronger polarization and a greater ability to bind charges. The incorporation of the V with S substitution in all systems significantly improves their dielectric properties, resulting in higher values. This enhancement reflects a strong polarization response within the material. The enhanced polarization intensifies the photogenerated electric field playing a crucial role in improving the material's PV efficiency. These enhancements are particularly advantageous for increasing the performance of optoelectronic devices such as photodiodes, photodetectors and solar cells (Blaha et al., 2001; Flöry et al., 2015; X. Li & Zhu, 2015). Furthermore, the $\varepsilon_1(0)$ of the V substituted systems regardless of S presence are higher than those of unsubstituted materials suggests that the V substitution enhances the mobility of photoexcited charge carriers within the material.

The crucial factor in assessing how well 2D materials absorb light is related to the $\varepsilon_2(\omega)$ (M. Zhao et al., 2016). The $\varepsilon_2(\omega)$ component of the dielectric function as depicted in Figure 36b, quantifies the energy dissipation within the material. While an ideal dielectric exhibits a zero value for $\varepsilon_2(\omega)$, any increase in this parameter corresponds to either ohmic loss (C.-H. Yang & Chang, 2022) or absorptive effects (Shrivastava et al., 2022). In this figure, the pristine (un-substituted) system shows almost zero initial dissipation energy, whereas systems with the V substituting regardless of the S substitution exhibit measurable non-zero values. The dissipation photon energy for the pure system lies between approximately 1 and 8 eV, while for the substituted systems, it extends from 0 to 9 eV, indicating a clear deviation from the unsubstituted case. This behavior suggests that the substituted systems have weaker initial absorption compared to the pristine material, with a general reduction in absorption intensity across all substituted configurations. This reduction is attributed to a shift in electronic behavior from semiconductor in the pure system to degenerate behaviors in the V substituted systems. The plots of the $\varepsilon_2(\omega)$ for unsubstituted system displays four main peaks indicating stronger interband transitions compared to all V substituted systems (with or without S substitutional compositions). Upon substitutions in the 2H-$MoSe_2$ system, the number of peaks decreases that reflects a reduction in interband transitions. However, this also suggests an increase in intraband transitions. The maximum values of the $\varepsilon_2(\omega)$ were observed in $V_{0.5}Mo_{0.5}S_{1.5}Se_{0.5}$ system, which is approximately 14.48 at 0.91 eV, which indicates that its absorption is better compared to other substituted systems but small compared to the pure one. Additionally, the appearance of peaks in the $\varepsilon_2(\omega)$ indicates a reduction in the exciton binding energy to a level that supports sustained absorption processes (Tyagi & Choudhary, 2022) as well as the interband transition properties of materials (Lahourpour et al., 2019). In the $\varepsilon_2(\omega)$ signal, the peaks represent that the binding energy of excitons in the system has decreased to a level that permits ongoing light absorption. Some structures show a blue shift where their absorption peaks shift towards higher energies. Others show a red shift where their absorption peaks shift towards lower energies. The $\varepsilon_2(\omega)$ of $V_{0.5}$ $Mo_{0.5}Se_2$, $V_{0.5}Mo_{0.5}S_{0.5}Se_{1.5}$, $V_{0.5}Mo_{0.5}S_1Se_1$ and $V_{0.5}$ $Mo_{0.5}S_{1.5}Se_{0.5}$ systems exhibit peaks within the energy range of 0.42 to 6 eV. This suggests a significant optical conductivity in these energy intervals. The $V_{0.5}Mo_{0.5}S_{1.5}Se_{0.5}$ system exhibits the highest likelihood of electron transitions and the greatest number of electrons participating in these transitions close to the Fermi energy level. In the plots of the $\varepsilon_2(\omega)$, $V_{0.5}Mo_{0.5}$ $S_{0.5}Se_{1.5}$ and $V_{0.5}Mo_{0.5}$ S_1Se_1 systems show lower energy levels at the peak appearance. This indicates that a smaller amount of energy is needed for electrons to transition from the VB to the CB. As a result, it suggests that the mono-V with di-sufide co-substituted system is more likely to experience electron transitions compared to others. There is also normal dispersion for the $\varepsilon_1(\omega)$ and anomalous dispersion for the $\varepsilon_2(\omega)$ across all substitutional behaviors. This indicates that the $\varepsilon_1(\omega)$ experiences no absorption, while

$\varepsilon_2(\omega)$ does. The refractive index for each proposed structures derived from the

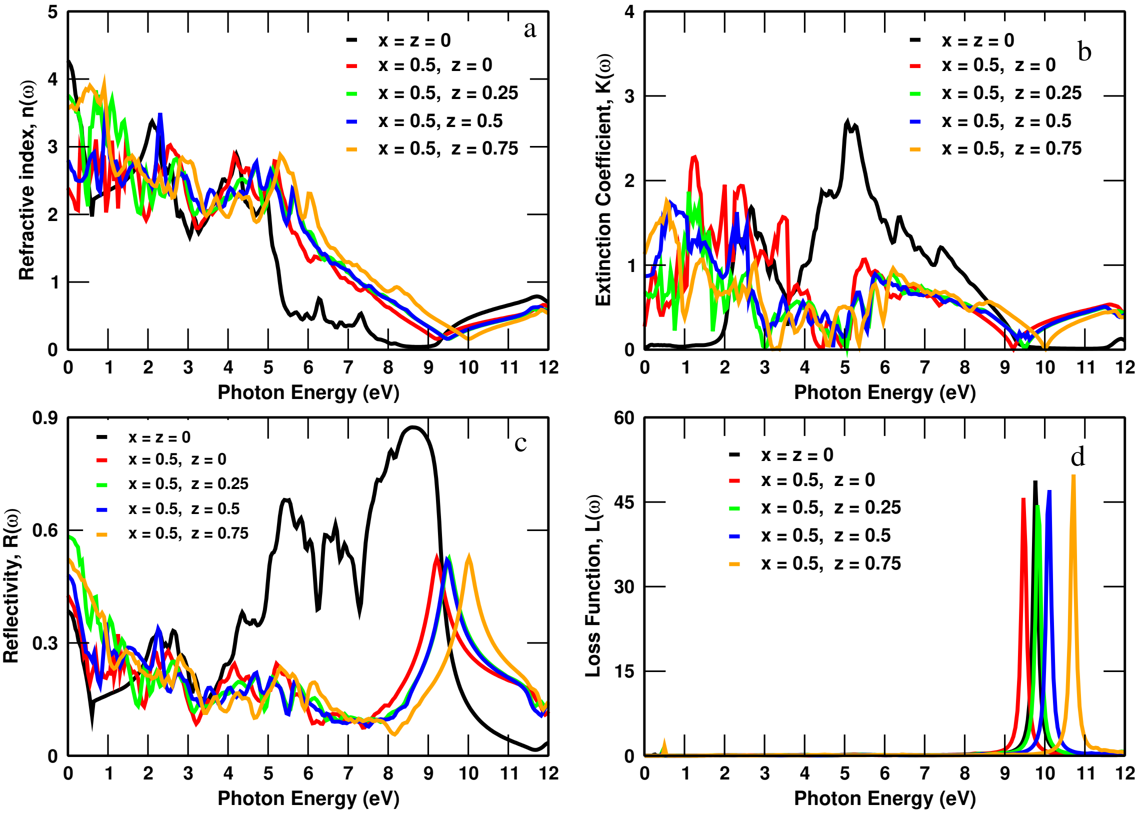

Figure 37: Refractive index a), Extinction coefficient b), Reflectivity c) and Loss function d) of prestine and V with or without S substituted $V_xMo_{1-x}S_{2z}Se_{2(1-z)}$.

corresponding complex dielectric functions and plotted in Figure 37a characterizes the phase velocity of an electromagnetic wave propagating through the material (Shawahni et al., 2018). There is a strong correlation between the peak values of $n(\omega)$, dielectric constant and absorption coefficient, $\alpha(\omega)$. In this figure, the maximum points of the $n(\omega)$ curve correspond to the maximum points of the dielectric curve. Regions of high $n(\omega)$ exhibit increased light absorption as a result of prolonged light residence time; conversely, regions with low $n(\omega)$ experience reduced absorption. Systems characterized by a high $n(\omega)$ exhibit prolonged light retention due to enhanced photon absorption probabilities (Tyagi & Choudhary, 2022). The $n(\omega)$ for all substituted systems is higher in the lower energy regions due to the reduction of their energy bandgap compared to the pure system. The $n(\omega)$ peaks for the $V_{0.5}Mo_{0.5}Se_2$ system occurs at 0.7, 1.12, 1.47, 2.24, 2.57, 4.18 and 5.20 eV; for $V_{0.5}$ $Mo_{0.5}S_{0.5}$ The Se_1 system has peaks at 0.74, 1.12, 1.44, 1.98, 2.73, 4.69, and 4.14 eV; for $V_{0.5}$ $Mo_{0.5}S_1Se_1$ systems are at 0.66, 0.96, 1.79, 2.30, 4.74, 5.06, and 5.63 eV; for $V_{0.5}Mo_{0.5}S_{1.5}Se_{0.5}$ located at 0.62, 0.94, 1.64, 2.90, 4.33, 5.35, and 6.04 eV. The $n(\omega)$ of the unsubstituted 2H-$MoSe_2$ decreases upon substitution of V irrespective of the presence of S. This is due to the degenerate semiconductor behaviors of all V with or without S substituted systems compared to pristine systems. Furthermore, the peaks of the $n(\omega)$ for the pristine material are located in the visible range, but when it is substituted by V or S, the main peaks shift to infrared regions. In Figure 37b, the k(ω) as a function of photon energy is depicted for pure, V with or without S substituted systems. As seen, there is variation in the values of k(ω) as the substitutional composition is varied. For the unsubstituted 2H-$MoSe_2$ system, only the k(ω) shows above ∼1.2 eV due to the wider bandgap which is responsible only to UV light. In contrast, the V substituted with or without the S have higher k(ω) than the unsubstituted system in the lower energy regions, allowing them to absorb visible light. For all V substituted systems, the k(ω) exhibited lower values compared to the pure material. This shows that the absorption of the substituted systems decreased. An inverse relationship exists between photon energy and extinction coefficient with increasing photon energy leading to decreasing the k(ω) values (Shawahni et al., 2018). There is a semimetallic behavior where the values of the n(0) and k(0) are higher and positive and the presence of peaks in both the n(ω) and k(ω) spectra suggests the occurrence of intraband transitions (Shawahni et al., 2018). The maximum values of k(ω) in $V_xMo_{1-x}S_{2z}Se_{2(1-z)}$, for $x = 0.5$, $z = 0, 0.25, 0.5$ and 0.75 were 2.27 (1.24 eV), 1.970 (1.104 eV), 1.75 (0.669 eV) and 1.764 (0.552 eV), respectively. As illustrated in the figure, the values k(0) for all V substituted systems are higher and positive compared to the pristine 2H-$MoSe_2$ system which represents the degenerate semiconductor behaviors of these substituted materials. The main peaks of the k(ω) for the pure system are located in the visible and UV light regions but when it is substituted, the values are shifted towards the infrared regions which can be used for infrared applications.

The computed R(ω) of pure and V with or without S substituted systems is shown in Figure 37c. In this figure, the R(ω) for a single V with or without S substituted $V_xMo_{1-x}S_{2z}Se_{2(1-z)}$ materials is illustrated. The main peaks in the R(ω) curves were observed in the energy range of 9.2 to 10.0 eV. It is decreased beyond this energy range. In the energy range of 0 to 7.5 eV, there is a decrease in R(ω) which exhibits that the amount of electromagnetic radiation on the surface of the material has fewer reflection properties. In the case of energy ranges 7.5 to 10.15 eV, the reflection of light is high, and this indicates that the amount of electromagnetic radiation on this material is small. The maxima of the R(ω) of $V_xMo_{1-x}S_{2z}Se_{2(1-z)}$, ($x = 0.5; z = 0, 0.25, 0.5$ and 0.75) systems are situated at 9.24, 9.47, 9.56 and 10 eV, respectively. The R(ω) peaks are the result of interband transitions from valence to the conduction band (Khan et al., 2022). These peaks of all substituted materials have initially increased and then decreased eventually plateauing at higher energies and have a good comparison as reported by (Khan et al., 2022; Ko et al., 2016; Liang, 1971; S. Y. Wang et al., 2014). This indicates that the R(ω) of pure 2H-$MoSe_2$ as reported by (Mashmool et al., 2020) has decreased when it was substituted either by V or S due their reduced energy bandgaps. In this figure, the R(ω) for all substituted systems is higher in the lower energy regions because of their eliminated energy bandgaps while for the pure system, its R(ω) is higher in the higher energy regions due to its wider energy bandgaps. Similarly, the R(0) of these substituted systems are improved compared to the pristine system reported by (Mashmool et al., 2020). This is because of the notable reduction in the energy bandgap that results from the substitution of the V with or without S which indicates their potential for high R(ω) coating (D. Tian et al., 2016). Figure 37d depicts the L(ω) of $V_xMo_{1-x}S_{2z}Se_{2(1-z)}$ systems for $(x = 0, 0.5; z = 0, 0.25, 0.5$ and 0.75 substitutional compositions. In the L(ω) spectra, the main peaks represent plasma energy as the oscillatory response of the delocalized valence electrons due to the plasma excitation. This excitation is induced by the inelastic scattering between the atomic electrons in materials and an electron beam. The excitation occurs when the speed of the electron beam is higher than the Fermi velocity (Egerton, 2008). The L(ω) peak values for 2H-$MoSe_2$, $V_{0.5}Mo_{0.5}Se_2$, $V_{0.5}Mo_{0.5}S_{0.5}Se_{1.5}$, $V_{0.5}Mo_{0.5}S_1Se_1$ and $V_{0.5}$ $Mo_{0.5}S_{1.5}Se_{0.5}$ systems are 48.8375 at 9.81834 eV, 45.43 at 9.52 eV, 44.29 at 9.88 eV, 46.81 at 10.24 eV and 49.67 at 10.86 eV, respectively. This demonstrates that the $V_{0.5}Mo_{0.5}S_{1.5}Se_{0.5}$ system exhibits the highest plasma resonance which is associated with the collective fluctuations of the electrons in the VB compared to other systems. This phenomenon shows how the electron density oscillates collectively leading to resonant behavior in the optical properties of the material. All peaks in the Lω) indicate the presence of plasmonic states. The major peaks in it represent the plasma resonance of the electrons collective fluctuations in the VB and the rest peaks in this energy loss function are associated with the interband transitions and excitons (Narimani & Nourbakhsh, 2016). The prominent peaks of the L(ω) spectrum act as markers of plasma resonance, electronic transitions and the material's overall properties making them crucial for analyzing and understanding the properties of different materials (Mashmool et al., 2020). Furthermore, with the exception of the V with a three S substituted system, the plasma resonance associated with collective electron fluctuations in the VB is reduced compared to the pure system. Table 9 presents the general expressions for the calculated static constants, which include the real dielectric function, refractive index, extinction coefficient and reflectivity at zero frequency. In this table, it is observed that the static dielectric constant for the unsubstituted system has small values compared to its substituted materials. This indicates that the substituted systems have better external electric field interactions and also there is stronger polarization for these systems than for the pure material. Additionally, more electrical energy was stored in the substituted systems compared to its pure system. When we compare the static real dielectric constants for one V

Table 9: Calculated and other previously reported values of static dielectric constants of $V_xMo_{1-x}S_{2z}Se_{2(1-z)}$.

Materials	$\varepsilon_1(0)$	$n(0)$	$k(0)$	$R(0)$
2H-$MoSe_2$	18.24	4.27	0.005	0.49
Others	16.66 (Lahourpour et al., 2019; Z. Luo et al., 2022)	5.49 (Rassay et al., 2016)	0 (Rassay et al., 2016)	0.526 (Rassay et al., 2016)
$V_{0.5}Mo_{0.5}Se_2$	18.87	3.39	0.275	0.43
$V_{0.5}Mo_{0.5}S_{0.5}Se_{1.5}$	27.60	3.76	0.686	0.584
$V_{0.5}Mo_{0.5}S_1Se_1$	19.95	2.80	0.869	0.481
$V_{0.5}Mo_{0.5}S_{1.5}Se_{0.5}$	21.49	3.57	1.131	0.523

substituted with or without S atoms, there is the highest $\varepsilon_1(0)$ for one V with one S co-substituted system rather than other V substituted systems. When examining the real refractive index values at zero frequency, the unsubstituted system exhibits a higher refractive index compared to the V substituted systems whether they contain S or not. This suggests that the V substituted systems have lower polarization properties in comparison to the pure system. Additionally, the small values of k(0) represents the semiconductor properties of the systems but when it becomes higher, the system becomes more metallic which agrees previously reported by (Shawahni et al., 2018). The k(0) of $V_{0.50}Mo_{0.50}S_{1.5}Se_{0.50}$ system is the highest due to its the most degenerate behavior compared to other substituted systems. There is also variations of the R(0) when the S compositions are varied with fixed V atom composition. The n(0) of all systems are displayed from Table 9 which shows that all substituted systems support the reflection edge shift towards the infrared light compared to the pure system.

4.1.5.2 Dielectric Constants of $V_xW_yMo_{1-x-y}S_{2z}Se_{2(1-z)}$ ($x = 0$, $y = 0, 0.5$, $z = 0, 0.25, 0.5, 0.75$))

Figure 38(a-f) displays the $\varepsilon_1(\omega)$ and $\varepsilon_2(\omega)$ along with other optical constants for 2H-$MoSe_2$ and $W_{0.5}Mo_{0.5}S_{2z}Se_{2(1-z)}$ materials, plotted as a function of photon energy over the 0-12 eV range. In the plot, Figure 38a (black curve) displays the $\varepsilon_2(\omega)$ of pure

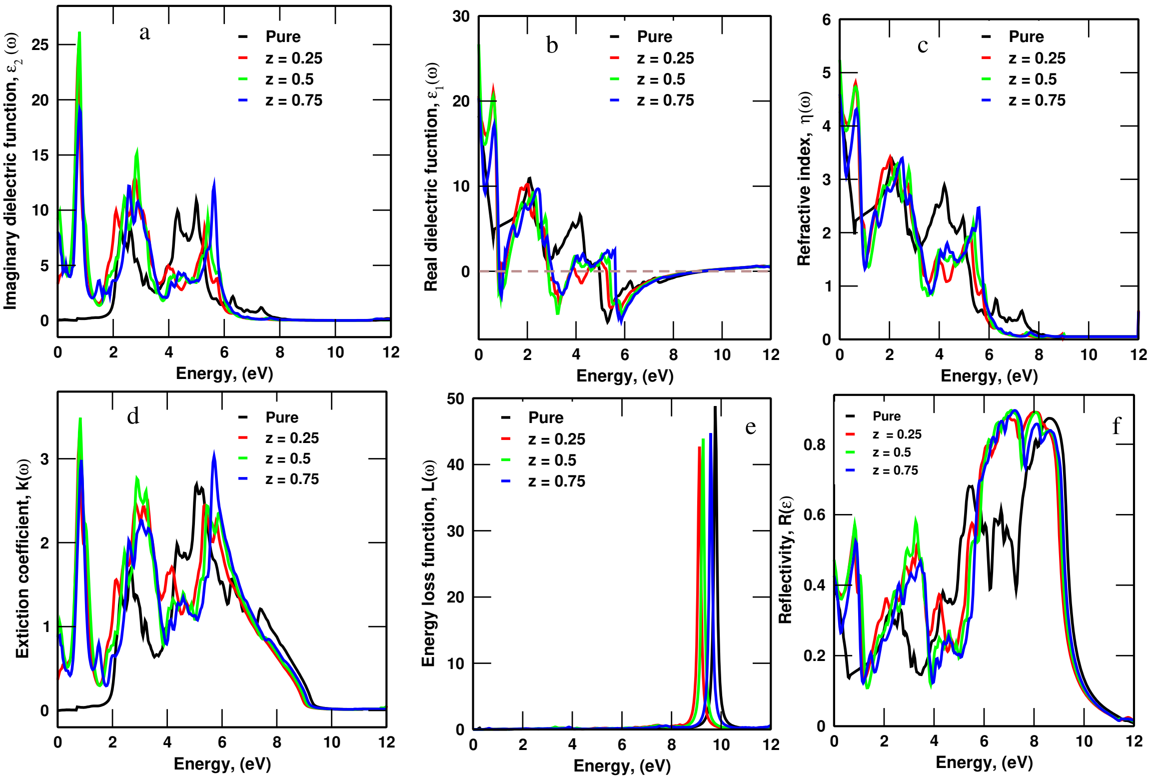

Figure 38: Imaginary a), Real b), Refractive index c), Extinction coefficient d), Loss function e) and Reflectivity f) of $W_{0.5}Mo_{0.5}S_{2z}Se_{2(1-z)}$.

2H-$MoSe_2$ which illustrates absorption energy. As shown, this system exhibits an optical absorption onset approximately 1.2 eV displaying no absorption below this energy threshold a finding that agrees with the prior reported results (Mashmool et al., 2020; Vinturaj et al., 2023). Additionally, the system demonstrates the energy loss between 1.2-7.76 eV energy ranges, with transparency occurring above this upper threshold. In the diagram, an ideal dielectric has occurred when the $\varepsilon_2(\omega) = 0$, meaning no electromagnetic energy dissipation or absorption (C.-H. Yang & Chang, 2022). Further, the rise in the $\varepsilon_2(\omega)$ indicates that the presence of the light absorption effects (Shrivastava et al., 2022) of the material. There are also some peaks in $\varepsilon_2(\omega)$ of the material in the energy range 2.28-5.08 eV, indicating the less optical conductivity compared to the W with S simultaneous substitutions. Moreover, this system shows negligible absorption from 0-1.2 eV and above 7.76 eV which is consistent with the previous results (Afrid et al., 2023; Mashmool et al., 2020). The dominant optical transitions are observed in visible and ultraviolet ranges, featuring a maximum peak intensity of 11.4866 atomic units at 5.04 eV.

Energy dissipation is observed across the 0-6.44 eV range in systems where W and S are co-substituted confirming non-ideal dielectric properties. These systems demonstrate the improved absorption behaviors due to bandgap narrowing and intensified the $\varepsilon_2(\omega)$ peaks, showing a marked difference from the unsubstituted material. The figure provides that the W substituted systems with different compositions of S exhibit absorption shifting toward mid and near infrared wavelengths along with enhanced peak intensities suggesting higher optical conductivity compared to the pristine sample. The incorporation of these elements into 2H-$MoSe_2$ results in more pronounced characteristic peaks, suggesting enhanced interband transition activity. The increased intensity and spectral shift of the $\varepsilon_2(\omega)$ features originate from high optical transition probabilities resulting from band structure flattening near Brillouin zone critical points. The modified d-p orbital hybridization alters the oscillator strengths and peak positions, while substitutions induce free carriers (Nolen et al., 2020), bandgap reduction (Afrid et al., 2023), IR-active modes (Gasiorowski et al., 2013) and enhanced screening (X. Yang et al., 2025) collectively redshifting the $\varepsilon_2(\omega)$ peaks into the infrared regime. As shown by the cyan trace in Figure 38a, the $W_{0.5}Mo_{0.5}S_1Se_1$ alloy composition displays the most pronounced interband transitions among all the W-S configurations with significantly enhanced spectral features relative to other S composition systems. The appearance of distinct peaks in the $\varepsilon_2(\omega)$ spectra indicates a significant decrease in the exciton binding energy that facilitates the persistent light matter interaction (Tyagi & Choudhary, 2022) and characteristic interband electronic transitions inherent to the material's electronic structure (Lahourpour et al., 2019). The absorption spectrum reveals that the $W_{0.5}Mo_{0.5}S_1Se_1$ exhibits maximal electromagnetic energy absorption with an onset of 0.88 eV and a dominant infrared peak at 26.49 atomic units surpassing both the pristine material and substituted systems in intensity. The peaks reveal key absorption features, showing transition energies between electronic states and the material's electronic structure. They mark strong light matter interactions, directly probing band structure and optical properties (Petrik, 2014). As seen, the $\varepsilon_2(\omega)$ enhancement and low energy shift directly correlate with the system's decreasing bandgap. Figure 38a (red curve) displays the imaginary dielectric function of $W_{0.5}Mo_{0.5}S_{0.5}Se_{1.5}$, showing that its major peaks appear at lower energy ranges. Some peaks are also present in the higher energy regions with energy dissipation beginning at 0.8 eV. The highest peak for this material reaches 25.57 atomic units, which shifts to the infrared electromagnetic wave regions due to its small energy bandgap compared to the pristine material. Similarly, the imaginary dielectric function of the $W_{0.5}Mo_{0.5}S_{1.5}Se_{0.5}$ system is represented by the blue curve (see Figure 38a). The highest S composition leads to the weakest optical absorption with a peak value of 19.14 a.u. at an infrared (IR) onset of 0.7 eV, resulting from significant modifications in electronic structure and optical transitions. In this system, interband transitions exhibit intermediate intensity situated between those of the pristine and other substituted compositions reflecting a markedly reduced bandgap induced by the higher S compositions relative to the Se. While all alloyed compositions with a fixed W composition display tunable optical responses varying S compositions, the $W_{0.5}Mo_{0.5}S_1Se_1$ system stands out by exhibiting the strongest infrared absorption among the studied alloys. Figure 38b displays the $\varepsilon_1(\omega)$ indicating its spectral variation for both pristine 2H-$MoSe_2$ and the W-S co-substituted systems. In this figure, the $\varepsilon_1(0)$ of the unsubstituted material is 18.25 a.u. aligning with the previous findings (Afrid et al., 2023; Mashmool et al., 2020). The maximum values of the real dielectric function for all systems are found in the 0 to 5.34 eV range, indicating optimal transparency there. Moreover, the shifting and increasing of the peaks of the $\varepsilon_1(\omega)$ exhibits the reduction of the energy bandgap as well as changes in the electronic polarizability of the systems (see Figure 38b). The spectra of all substituted systems exhibit multiple zero crossings near zero frequency in this plot, demonstrating the growing of electronic structure complexity with increasing theS compositions (Mashmool et al., 2020). Dielectric analysis reveals a clear energy dependent patterns among the systems such as in all substituted materials, the $\varepsilon_1(\omega)$ is negative in three energy intervals (0.82-1.0 eV, 2.9-3.89 eV and 5.38-8.7 eV), while in the pristine system, negative values only appear at higher energies (5.02-8.7 eV) due to its less electronic structure complexity behavior compared to the substituted systems. For the energies of photon outside these areas, the real dielectric function approaches zero signifying negligible absorption and nearly full light transmission (C.-H. Yang & Chang, 2022). The negative $\varepsilon_1(\omega)$ values signal regions of no light transmission, indicating an absence of optical transparency (Lahourpour et al., 2019). The strongest photoresponse is observed under parallel (in-plane) light incidence highlighting the favorability of these materials for optoelectronic and PV applications (X. Li & Zhu, 2015). The W-S co-substituted systems exhibit significantly enhanced static dielectric constants, indicative of stronger charge polarization, more robust photogenerated electric fields and improved carrier mobility compared to the pristine material. These favorable properties directly contribute to the higher PV efficiency and underscore their promise as active components in photodetectors and photodiodes (Afrid et al., 2022, 2023).

The high frequency dielectric constants of the 2H-MoSe$_2$ and W$_{0.5}$Mo$_{0.5}$S$_{2z}$Se$_{2(1-z)}$ alloy compositions are calculated and presented in Table 10. In the calculated results of the pure compound, the $\varepsilon_1(0) = \varepsilon_{averaged}(0) = 18.25$, intraplane direction is acceptable agreement with the results (Afrid et al., 2023; Asadi & Nourbakhsh, 2019). In the table, the pristine 2H-MoSe$_2$ system has the lowest high frequency dielectric constants due to its relatively wider bandgap property compared to the substituted systems. This is also attributed to the difference in EN between Se and S (Asadi & Nourbakhsh, 2019) atoms and also the reduced polarization of the electron cloud in the pure system compared to the alloyed compositions. Additionally, the intrinsic material shows the lowest $\varepsilon_1(0)$ compared to the substituted variants, suggesting weaker polarization and reduced interaction with electric fields of this material (Afrid et al., 2023). In particular, the 1W-2S co-substituted sample exhibits the highest $\varepsilon_1(0)$, signifying superior dielectric screening relative to other substituted materials. Across all the W-S co-substituted systems, the n(0) values are consistently higher than in the pristine case, reflecting increased polarization and a red shifted (infrared) reflection edge. The R(0) also varies with the S composition and these increased the n(0) values in alloyed materials confirm their enhanced optical response as supported by the previous research (Afrid et al., 2023; Shawahni et al., 2018). Furthermore, the $\varepsilon_1(0)$ is greater in the alloyed configurations than in the unsubstituted system. The Penn model (Penn, 1962) relating an inverse dependence between bandgap and the real part of the dielectric function remains applicable to both pristine and alloyed composition systems. For the W$_{0.5}$Mo$_{0.5}$S$_{0.5}$Se$_{1.5}$, W$_{0.5}$Mo$_{0.5}$S$_1$Se$_1$ and W$_{0.5}$Mo$_{0.5}$S$_{1.5}$Se$_{0.5}$ composition alloys, the peak of the $\varepsilon_1(0)$ values occur in the infrared electromagnetic waves, whereas for the pristine system the peak lies in the visible region consistent with the earlier results (Afrid et al., 2022, 2023; Mashmool et al., 2020). Figure 38c presents the computed n(ω) for the pristine and W-S systems. The pure material (black curve) shows a distinct maximum of 3.42 a.u. at 2.14 eV, decreasing at higher energies and vanishing above 8 eV as absorption diminishes (Afrid et al., 2023; Mashmool et al., 2020). Additionally, the higher value of the n(ω) shows the prolonged light retention due to the enhanced photon absorption probabilities (Tyagi & Choudhary, 2022). As seen, the n(ω) of all W-S co-substituted systems is increased in the lower energy regions due to their reduced bandgaps compared to

Table 10: Calculated and previously reported values of the static dielectric constants for W$_{0.5}$Mo$_{0.5}$S$_{2z}$Se$_{2(1-z)}$.

Material	$\varepsilon_1(0)$	$n(0)$	$k(0)$	$R(0)$
2H-MoSe$_2$	18.25	4.27	0	0.485
Others	16.7 (Z. Luo et al., 2022; Mashmool et al., 2020) 18.24 (Yamusa et al., 2022)	4.27 (Yamusa et al., 2022)	0.005 (Afrid et al., 2023)	0.49 (Afrid et al., 2023)
W$_{0.5}$Mo$_{0.5}$S$_{0.5}$Se$_{1.5}$	20.58	4.55	0.46	0.41
W$_{0.5}$Mo$_{0.5}$S$_1$Se$_1$	26.67	5.24	0.87	0.48
W$_{0.5}$Mo$_{0.5}$S$_{1.5}$Se$_{0.5}$	20.34	4.60	0.88	0.43

the unsubstituted material. Specifically, the n(ω) peaks of $W_{0.5}Mo_{0.5}S_{0.5}Se_{1.5}$ occur at 4.88 (0.65 eV), 3.48 (2.02 eV), 2.94 (2.74 eV), and 1.94 (5.24 eV) atomic units; for $W_{0.5}Mo_{0.5}S_1Se_1$ at 4.75 (0.65 eV), 3.32 (2.43 eV), 3.23 (2.79 eV), and 2.25 (5.38 eV); and for $W_{0.5}Mo_{0.5}S_{1.5}Se_{0.5}$ at 4.35 (0.69 eV), 3.42 (2.54 eV) and 2.52 (5.62 eV) atomic units. For the unsubstituted system, the peaks of the n(ω) are 3.42 (2.14 eV), 2.94 (4.24 eV) and 2.31 (4.98 eV) atomic units which is consistent with the previous result (Afrid et al., 2023; Yamusa et al., 2022). These peak analysis reveals that the W-S co-substitutions boost infrared absorption over the pristine materials via bandgap narrowing effects. Moreover, the peaks of the n(ω) for the pristine system lie within the visible spectrum (Afrid et al., 2022, 2023), whereas the substitution of W with S causes these main peaks to shift into the infrared region. The n(ω) peaks align spectrally with absorption maxima, as both derive from the dielectric response enhancements where delayed photon propagation (high $n(\omega)$) strengthens light matter coupling and energy dissipation (Tyagi & Choudhary, 2022). Materials with high n(ω) retain light longer, increasing the likelihood of photon absorption which is critical for optoelectronic applications (Afrid et al., 2022, 2023; Yamusa et al., 2022). Bandgap narrowing in co-substituted systems boosts their infrared refractive index, n(ω) above undoped levels. In Figure 38d, the k(ω) as a function of photon energy is depicted for the pure and W-S co-substituted systems.

The results reveal noticeable changes, the $k(\omega)$ values with varying S compositions. The figure reveals that the pristine 2H-$MoSe_2$ absorbs above 1.2 eV aligning with its energy bandgap and visible range optical response. In comparison, the W-S substituted systems demonstrate enhanced the k(ω) values in lower energy ranges which indicates the improved infrared light absorption capabilities that is consistent with the previous results (Afrid et al., 2023; Yamusa et al., 2022). Additionally, the absorption of this system ranges approximately from 1.2 eV to 9.41 eV that is almost similar to Figure 38a. A peak value of 2.7 at 5.11 eV marks the absorption threshold in the system. The maximum peak values of the k(ω) in the $W_{0.5}Mo_{0.5}S_{2z}Se_{2(1-z)}$ materials, where $z = 0.25, 0.5, 0.75$ compositions are 3.11 (at 5.76 eV and 2.98 at 0.89 eV); 2.8 (2.84 eV and 3.51 at 0.77 eV), respectively. As shown, all the W-S co-substituted systems exhibit higher and positive of the k(0) values indicating their narrowed bandgap semiconductor properties. For the unsubstituted system, the primary peaks of the k(ω) appear in the visible ranges, which is consistent with the previous results (Afrid et al., 2022, 2023; Mashmool et al., 2020; Yamusa et al., 2022). Substitution redshifts spectral peaks into the infrared through the bandgap reduction that enhances the infrared performance via intensified interband transitions compared to the pristine materials. At a fixed W compositions, but with increasing the S compositions, the k(ω) which correlates strongly with improved the α(ω) (Afrid et al., 2022, 2023; Bejo et al., 2025). Moreover, the $k(\omega)$ values for the pristine system are zero below 1.2 eV and above 9.36 eV, while for the W-S co-substituted materials, they are zero above 9.24 eV, indicating a lack of absorption in these energy ranges. The W-S co-substituted systems demonstrate significantly stronger absorption peaks than the unsubstituted material, resulting from both intensified interband transitions and bandgap narrowing. Spectral analysis reveals progressively lower absorption onsets at 0.80 eV ($W_{0.5}Mo_{0.5}S_{0.5}Se_{1.5}$), 0.88 eV ($W_{0.5}Mo_{0.5}S_1Se_1$), and 0.70 eV ($W_{0.5}Mo_{0.5}S_{1.5}Se_{0.5}$), directly correlating with increasing sulfur content. Figure 38e depicts the L(ω) for the $W_{0.5}Mo_{0.5}S_{2z}Se_{2(1-z)}$ alloys where $z = 0.25, 0.5, 0.75$ compositions. In the L(ω) spectra, the main peaks represent plasma energy as the oscillatory response of the delocalized valence electrons due to the plasma excitation (Narimani & Nourbakhsh, 2016). The excitation occurs when the speed of the electron beam is higher than the Fermi velocity (Egerton, 2008). As shown, the L(ω) peak value for 2H-$MoSe_2$ system is 48.83 at 9.81 eV, which is consistent with the previous results (Afrid et al., 2022, 2023; Mashmool et al., 2020), whereas for the $W_{0.5}Mo_{0.5}S_{0.5}Se_{1.5}$, $W_{0.5}Mo_{0.5}S_1Se_1$ and $W_{0.5}$ $Mo_{0.5}S_{1.5}Se_{0.5}$ systems, the L(ω) are 42.79 at 9.18 eV, 43.96 at 9.27 eV, and 44.80 at 9.63 eV, respectively. From these systems, the $W_{0.5}Mo_{0.5}S_{1.5}Se_{0.5}$ material exhibits the highest plasma resonance, which is associated with the collective fluctuations of electrons in the valence band compared to other substituted materials. In the plot, the reduced L(ω) peak intensities in co-substituted systems reflect lowered plasma resonance relative to pure material. While principal peaks represent valence electron plasmons, remaining spectral features stem from interband transitions and excitonic interactions (Narimani & Nourbakhsh, 2016). The prominent peaks in the L(ω) spectrum act as markers of plasma resonance, electronic transitions and the material's overall properties, making them crucial for analyzing and understanding the properties of materials (Mashmool et al., 2020). The incorporating of substitutions typically causes the L(ω) peaks to shift toward lower energies (redshift), indicating electronic changes such as increased interband transition likelihood, bandgap narrowing and modified plasmonic response features (Kuball et al., 1994). Figure 38f presents the calculated $R(\omega)$ for the pristine and $W_{0.5}Mo_{0.5}S_{2x}Se_{2(1-x)}$ materials with compositions ($x = 0.25, 0.5$, and 0.75). In this plot, the $R(\omega)$ for the unsubstituted system rises from 3.5 to 8.4 eV before declining at higher energies, in agreement the with previous studies (Afrid et al., 2022, 2023; Mashmool et al., 2020). This material reaches a peak reflectivity of 0.874 at 8.60 eV. The peak of the $R(\omega)$ for the $W_{0.5}Mo_{0.5}S_{0.5}Se_{1.5}$, $W_{0.5}Mo_{0.5}S_1Se_1$, and $W_{0.5}Mo_{0.5}S_{1.5}Se_{0.5}$ substituted systems exhibit higher maxima of 0.892 (8.00 eV), 0.893 (8.07 eV) and 0.896 (7.25 eV), respectively. This enhancement under W-S co-substituted suggests bandgap narrowing due to the increased S compositions. The $R(\omega)$ peaks of the substituted systems coincides with static values of 0.41-0.48 (see Table 10). As observed, both substituted and pristine systems experience a decline in $R(\omega)$ up to 12 eV; however, the unsubstituted 2H-$MoSe_2$ exhibits a higher static $R(\omega)$ overall.

4.1.5.3 Dielectric Constants of $\mathbf{V}_x\mathbf{W}_y\mathbf{Mo}_{1-x-y}\mathbf{S}_{2z}\mathbf{Se}_{2(1-z)}$ ($x = 0$, $y = 0, 0.125$, $z = 0, 0.0625, 0.125$)

Figure 39(a-d) display the $\varepsilon_1(\omega)$ and $\varepsilon_2(\omega)$ along with other optical constants for supercell of 2H-$MoSe_2$ and the $W_yMo_{1-y}S_{2z}Se_{2(1-z)}$ alloyed systems as a function of photon energy, spanning the range from 0 to 12 eV. In these plots, Figure 39a (black curve) shows the $\varepsilon_2(\omega)$ of undoped 2H-$MoSe_2$, representing its energy absorption (loss) behaviors. As depicted, the material shows an onset of optical absorption at around 1.1635 eV, with no absorption occurring below this threshold consistent with previously reported findings (Afrid et al., 2023; Mashmool et al., 2020; Vinturaj et al., 2023; Yamusa et al., 2022). Furthermore, the system exhibits energy loss within the 1.1635-7.72 eV range, while becoming transparent above this upper limit, which is consistent with the previous finding (Afrid et al., 2022, 2023; Yamusa et al., 2022). In this context, ideal dielectric behavior is defined by $\varepsilon_2(0)$, which signifies no absorption, dissipation or loss of electromagnetic energy (Afrid et al., 2022, 2023; C.-H. Yang & Chang, 2022) of the systems. As seen in the data, an increase in $\varepsilon_2(\omega)$ reflects the material's light absorption properties (Afrid et al., 2023; Shrivastava et al., 2022). The $\varepsilon_2(\omega)$ spectrum of the material exhibits several peaks within the energy range of 1.9906-4.11144 eV, suggesting relatively lower optical conductivity compared to W-S doped systems. Additionally, the material shows negligible absorption below 1.1635

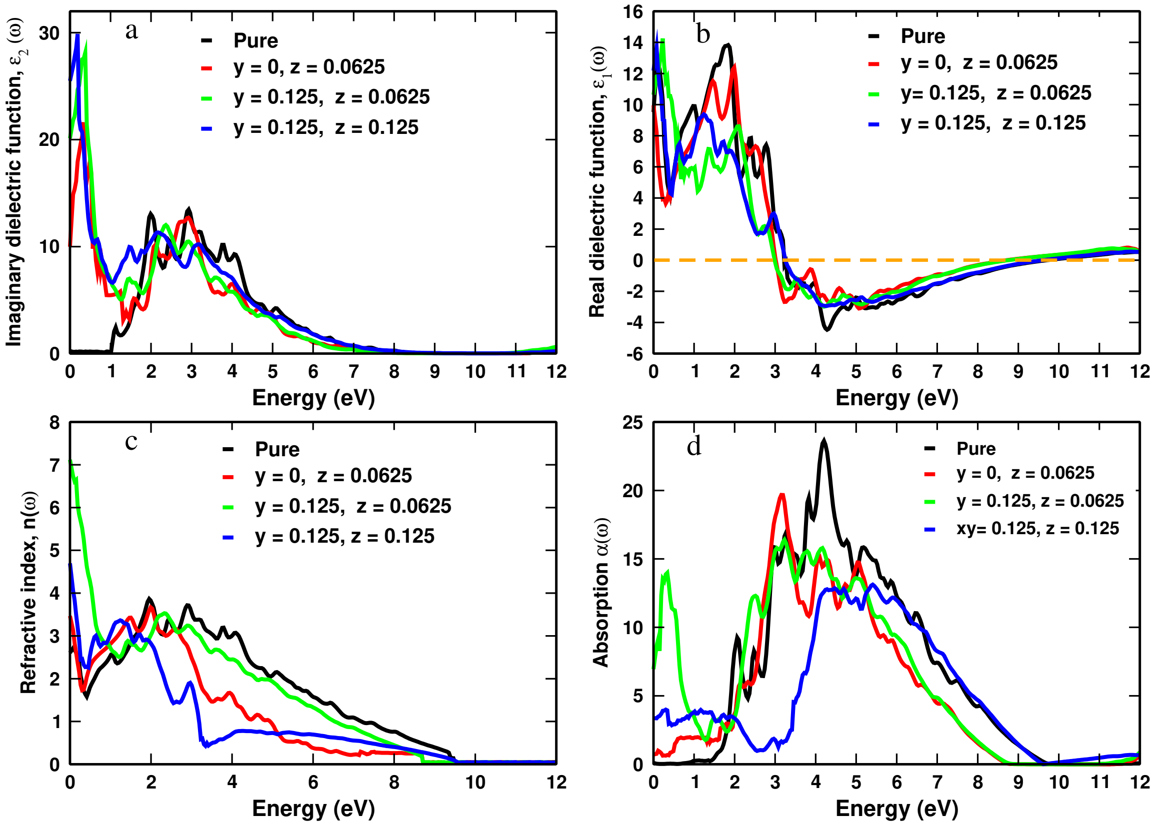

Figure 39: Imaginary dielectric function a), real dielectric function b), refractive index c) and absorption spectrum d) of $W_yMo_{1-y}S_{2z}Se_{2(1-z)}$ alloys.

eV and above 7.72 eV, which aligns well with earlier findings (Afrid et al., 2023; Mashmool et al., 2020; Yamusa et al., 2022). The primary optical transitions occur in the visible and ultraviolet regions, with a maximum peak intensity of 13.5619 atomic units observed at 2.9184 eV, a value in close agreement with previous reports (Afrid et al., 2022, 2023; Yamusa et al., 2022). Energy dissipation occurs in the 0-4.00 eV range in W and S-doped materials, reflecting deviations from ideal dielectric behavior. These doped systems demonstrate stronger light absorption due to narrower bandgaps and more prominent features in the imaginary part of the dielectric function, $\varepsilon_2(\omega)$, which distinctly differentiates their optical behaviors from the undoped material. The figure indicates that S doped systems whether co-doped with W or at different S compositions exhibit a redshift of absorption into the mid and near infrared range accompanied by heightened peak intensities, signaling enhanced optical conductivity compared to the pristine counterpart. Incorporating these elements into the 2H-$MoSe_2$ supercell results in more pronounced characteristic peaks, signifying enhanced interband transitions relative to the doped unit cell, as documented in (Afrid et al., 2023; Yamusa et al., 2022). The enhanced intensity and spectral shift in the $\varepsilon_2(\omega)$ features arise from higher optical transition probabilities, which are caused by the flattening of the band structure near critical points in the Brillouin zone. Changes in p-d orbital hybridization modify oscillator strengths and shift peak positions, while elemental substitutions introduce free carriers (Nolen et al., 2020), reduce the bandgap (Afrid et al., 2022, 2023; Yamusa et al., 2022), activate infrared-active modes (Gasiorowski et al., 2013) and enhance electronic screening (X. Yang et al., 2025), all of which together cause a redshift of the $\varepsilon_2(\omega)$ peaks into the infrared region. As shown by the blue curve in Figure 39a, the $W_{0.125}Mo_{0.875}S_{0.25}Se_{1.75}$ disulfide system, when doped with a single W atom, demonstrates the most intense interband transitions compared to all other doped configurations. This is attributed to its smallest bandgap, which leads to significantly enhanced spectral features relative to other doped variants. The presence of well-defined peaks in the $\varepsilon_2(\omega)$ spectra indicates a notable reduction in exciton binding energy, promoting sustained light matter coupling (Tyagi & Choudhary, 2022) and reflects the characteristic interband electronic transitions arising from the material's intrinsic electronic structure (Lahourpour et al., 2019). The dissipation energy spectrum shows that the $W_{0.125}Mo_{0.875}S_{0.25}Se_{1.75}$ has the highest electromagnetic energy absorption (loss), with an absorption onset at 0.74 eV and a strong infrared peak reaching 30.00 atomic units, exceeding both the pristine material and other doped variants in peak intensity. The peaks exhibit important dissipation properties, indicating the energy differences between electronic states and reflecting the material's underlying electronic structure. They indicate strong light matter interactions in the infrared range, offering direct information about the material's band structure and optical properties (Petrik, 2014), while also exhibiting reduced energy dissipation at higher energies. As observed, the increase in $\varepsilon_2(\omega)$ and its shift to lower energies are directly linked to the reduction in the system's bandgap (Afrid et al., 2022; Yamusa et al., 2022). Figure 39a (red curve) shows the imaginary part of the dielectric function for the monosulfide doped $MoS_{0.125}Se_{1.875}$ system, indicating that its primary energy dissipation peaks are located in the lower energy region. Some peaks are also present in the higher energy regions, with energy loss beginning approximately between 1.83 eV to 2.95 eV. The highest peak for this material reaches 21.697 atomic units (0.342 eV), which shifts to the infrared electromagnetic wave regions due to its small enegry bandgap compared to the pristine system. Similarly, the imaginary dielectric function for the $W_{0.125}Mo_{0.875}S_{0.125}Se_{1.875}$ system is represented by the green curve (see Figure 39a). In this curve, the highest peak reaches 29.338 atomic units (0.432 eV), which is lower than that of the disulfide doped system with two W atoms but higher compared to both the pure system and the monosulfide-doped system. Figure 39b shows the $\varepsilon_1(\omega)$ which illustrates its spectral behavior for pristine 2H-$MoSe_2$ as well as for systems doped with S with and without W. In this figure, the $\varepsilon_1(0)$ of the undoped material is 9.545 a.u., which is consistent with earlier reported results (Afrid et al., 2022, 2023; Mashmool et al., 2020; Yamusa et al., 2022). The peak values of the real part of the dielectric function for both pristine and doped materials occur within the 0 to 2.900 eV range, suggesting maximum transparency in this energy region. Furthermore, the shift and enhancement of the peaks in $\varepsilon_1(\omega)$ for these systems indicate a reduction in the energy bandgap and alterations in the electronic polarizability, as evident from Figure 39b. The spectra of all systems display irregular zero crossings near zero frequency, suggesting a simplified electronic structure, consistent with findings reported by (Afrid et al., 2022; Yamusa et al., 2022) compared to the unit cell of the same material. In all doped and pristine materials, the $\varepsilon_1(\omega)$ becomes negative within two specific energy ranges. For the disulfide system co-doped with a single W atom and the pure system, this occurs between 0.3258-10 eV, while for the monosulfide-doped and the monosulfide-doped system with a single W atom, the negative region spans 3.034-10 eV. For photon energies beyond these ranges, the real part of the dielectric function tends toward zero, indicating minimal absorption and almost complete transmission of light (C.-H. Yang & Chang, 2022). Negative values of the $\varepsilon_1(\omega)$ indicate regions where light transmission is blocked, reflecting a lack of optical transparency (Lahourpour et al., 2019). The highest photoresponse is achieved when light is incident in parallel, suggesting that these materials hold great potential for use in optoelectronic and PV devices (X. Li & Zhu, 2015). Systems doped with S, in the presence or absence of W show increased static dielectric constants, indicating greater charge polarization, enhanced photogenerated electric fields and better carrier mobility compared to the undoped material. These properties enhance PV performance, positioning the materials as strong candidates for use in photodetectors and photodiodes (Afrid et al., 2022, 2023; Yamusa et al., 2022). The primary peaks for all systems appear within the energy range of 0.112 to 2.092 eV. Figure 39c shows the calculated $n(\omega)$ for both the pristine system and those doped with S, with or without W. The pristine material (black curve) exhibits a clear peak of 3.900 a.u. at

1.969 eV, which decreases at higher energies and vanishes above 9.48 eV as absorption declines, consistent with previous findings (Mashmool et al., 2020). Moreover, the elevated values of $n(\omega)$ indicate extended light confinement resulting from increased photon absorption likelihood (Tyagi & Choudhary, 2022). As observed, the $n(\omega)$ for all doped systems is enhanced in the low energy region, attributed to their reduced bandgaps relative to the undoped material. Specifically, the $n(\omega)$ peaks for pristine 2H-$MoSe_2$ are observed at 3.9 (1.942 eV), 3.048 (2.43 eV), 3.78 (2.92 eV), 3.22 (3.79 eV), and 3.099 (4.084 eV). For $MoS_{0.125}Se_{1.875}$, the peaks occur at 3.5 (1.48 eV), 3.69 (1.996 eV), 3.254 (2.393 eV) and 1.713 (3.976 eV) atomic units, which are consistent with the previous findings (Afrid et al., 2023; Yamusa et al., 2022). In the case of the $W_{0.125}Mo_{0.875}S_{0.125}Se_{1.875}$, peaks are found at 2.946 (1.427 eV), 3.562 (2.349 eV) and 3.285 (2.945 eV). For $W_{0.125}Mo_{0.875}S_{0.25}Se_{1.75}$, the peaks appear at 3.038 (0.667 eV), 3.408 (1.237 eV), 3.31 (1.752 eV) and 1.929 (2.972 eV) atomic units. The analysis of the peaks shows that light doping enhances infrared absorption compared to the pristine material, primarily due to a reduced bandgap, especially when contrasted with alloyed systems in the unit cell of the same material. Additionally, the primary $n(\omega)$ peaks of the undoped system lie within the visible spectrum (Afrid et al., 2022, 2023; Yamusa et al., 2022), whereas S doping, with or without W incorporation, shifts these main peaks into the infrared range. The peaks in the $n(\omega)$ coincide spectrally with the absorption maxima, as both arise from enhanced dielectric response, where slower photon propagation (indicated by high $n(\omega)$) intensifies light matter interaction and energy loss (Tyagi & Choudhary, 2022). Materials exhibiting higher $n(\omega)$ values confine light for longer durations, thereby increasing the probability of photon absorption key for efficient optoelectronic devices (Afrid et al., 2023). In the co-doped systems, bandgap reduction leads to an increased infrared $n(\omega)$ compared to the undoped material. Figure 39d presents the absorption spectrum, $\alpha(\omega)$ analysis for both pristine and S doped 2H-$MoSe_2$ with or without W incorporation. The results indicate distinct optical behaviors depending on the type and concentration of dopants. The absorption onset for the pristine material is observed at 1.46795 eV, in agreement with earlier reports (Mashmool et al., 2020; Yamusa et al., 2022). From this threshold, the $\alpha(\omega)$ increases, peaks at 23.9373 when the photon energy reaches 4.23422 eV, and subsequently decreases beyond 10 eV. This behavior indicates that the undoped system primarily absorbs in the ultraviolet and visible regions of the electromagnetic spectrum. The absorption onset for the monosulfide-doped 2H-$MoSe_2$ system (shown by the red curve in Figure 39d) is observed at 1.1152 eV, with the $\alpha(\omega)$ increasing to a peak value of 19.7969 at 3.20365 eV, reflecting a redshift to lower energies relative to the pristine material. The absorption then gradually decreases from 3.20365 eV onward, continuing until approximately 8.63 eV. In contrast, in the ultraviolet and visible spectral regions, the absorption onset for the $W_{0.125}Mo_{0.875}S_{0.125}Se_{1.875}$ co-doped system (see green curve in Figure 39d) starts at 1.305 eV, increases to a peak value of 16.62 at 3.256 eV and then decreases gradually up to 8.63

eV. The absorption onset for the $W_{0.125}Mo_{0.875}S_{0.25}Se_{1.75}$ co-doped system begins at approximately 0.74 eV, then decreases until 2.688 eV, followed by an increase reaching a value of 13.15 at 5.455 eV, after which it declines again up to 9.60 eV.

Figure 40a shows the energy loss function, $L(\omega)$, for the 2H-$MoSe_2$ and $W_yMo_{1-y}S_{2z}Se_{2(1-z)}$ systems. In the $L(\omega)$ spectra, the primary peaks correspond to plasma energy, arising from the oscillatory response of delocalized valence electrons under plasma excitation (Narimani & Nourbakhsh, 2016). Excitation takes place when the electron beam's velocity exceeds the Fermi velocity (Egerton, 2008). As shown, the L(ω) peak for the pristine 2H-$MoSe_2$ occurs at 9.75 eV with a value of 37.63, in agreement with earlier reported results (Afrid et al., 2023; Mashmool et al., 2020; Yamusa et al., 2022). In comparison, the doped systems including $MoS_{0.125}Se_{1.875}$, $W_{0.125}Mo_{0.875}S_{0.125}Se_{1.875}$ and $W_{0.125}Mo_{0.875}S_{0.25}Se_{1.75}$ exhibit L(ω) peaks of 21.28 at 8.79 eV, 30.28 at 8.76 eV and 25.34 at 9.61 eV, respectively. Among these, the $W_{0.125}Mo_{0.875}S_{0.125}Se_{1.875}$ co-doped material shows the strongest plasma resonance, corresponding to enhanced collective oscillations of valence band electrons relative to the other doped materials. In the plot, the decreased peak intensities of the $L(\omega)$ in the doped systems indicate weaker plasma resonance compared to the pristine material. While the main peaks correspond to plasmons of valence electrons, the additional spectral features arise from interband transitions and excitonic effects (Narimani & Nourbakhsh, 2016). The prominent peaks in the $L(\omega)$ spectrum serve as indicators of plasma resonance, electronic excitations and the material's intrinsic properties, playing a key role in the analysis and interpretation of material properties (Mashmool et al., 2020). The incorporation of dopants generally leads to a redshift in the $L(\omega)$ peaks, which reflects electronic modifications such as enhanced probability of interband transitions, reduced bandgap and altered plasmonic behavior (Afrid et al., 2023; Kuball et al., 1994; Yamusa et al., 2022). Figure 40b shows the computed $R(\omega)$ for $W_yMo_{1-y}S_{2z}Se_{2(1-z)}$ materials with the following compositions: ($y = 0, z = 0; y = 0, z = 0.0625; y = 0.125, z = 0.0625$, and $y = 0.125, z = 0.125$). In this

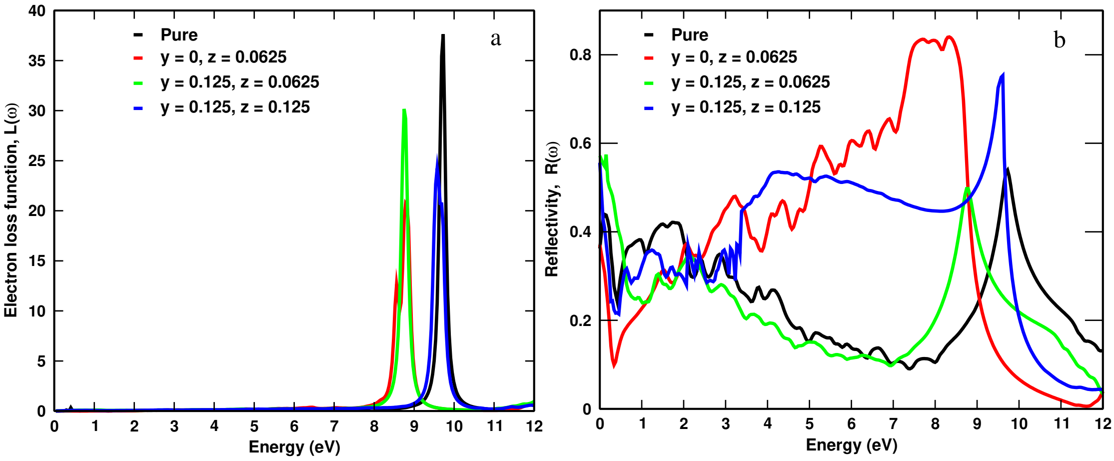

Figure 40: Electron loss function a) and reflectivity b) of $W_yMo_{1-y}S_{2z}Se_{2(1-z)}$.

plot, the $R(\omega)$ for the undoped system rises from 0.55 to 9.75 eV before declining at higher energies, in agreement the with previous studies (Afrid et al., 2022, 2023; Mashmool et al., 2020; Yamusa et al., 2022). The $R(\omega)$ peaks for the ternary and quaternary doped systems $\mathrm{MoS_{0.125}Se_{1.875}}$, $\mathrm{W_{0.125}Mo_{0.875}S_{0.125}Se_{1.875}}$ and $\mathrm{W_{0.125}Mo_{0.875}S_{0.25}Se_{1.75}}$ reach maximum values of 0.84 at 8.36 eV, 0.50 at 8.8 eV and 0.76 at 9.64 eV, respectively. This improvement in S doped systems, with or without W, indicates a reduction in bandgap caused by higher sulfur content (Afrid et al., 2022, 2023; Yamusa et al., 2022). The reflectivity peaks of the doped systems correspond to static values ranging from 0.37 to 0.57 (see Table 11). As observed, both doped and undoped systems experience a decline in reflectivity up to 12 eV; however, the unsubstituted 2H-$\mathrm{MoSe_2}$ exhibits a lower static reflectivity overall due to its relative wider bandgap compared to the doped materials. The high frequency dielectric constants for pristine 2H-$\mathrm{MoSe_2}$ and the doped $\mathrm{W_yMo_{1-y}S_{2z}Se_{2(1-z)}}$ materials are calculated and listed in Table 11. For the pure 2H-$\mathrm{MoSe_2}$ compound, the calculated static dielectric constant is $\varepsilon_1(0) = \varepsilon_{\text{averaged}}(0) = 10.08$, which shows reasonable agreement with previously reported results (Mashmool et al., 2020). This table indicates that the pristine 2H-$\mathrm{MoSe_2}$ system exhibits the lowest high frequency dielectric constant, owing to its relatively larger bandgap in comparison to the doped systems (Afrid et al., 2022, 2023; Yamusa et al., 2022). This behavior is also linked to the EN difference between Se and S (Asadi & Nourbakhsh, 2019), as well as the weaker electron cloud polarization in the pure material relative to the doped counterparts. Table 11 summarizes the calculated static optical properties such as the $\varepsilon_1(0)$, $n(0)$, $\alpha(0)$ and $R(0)$ of both undoped as well as doped materials. As shown in the table, the pure material shows the lowest $\varepsilon_1(0)$ value relative to the doped variants, indicating weaker polarization and a diminished response to electric fields (Afrid et al., 2022, 2023). Notably, the $\mathrm{W_{0.125}Mo_{0.875}S_{0.25}Se_{1.75}}$ system indicates the highest $\varepsilon_1(0)$ value, indicating enhanced dielectric screening compared to other doped variants. In all S doped systems, with or without W, the $n(0)$ values are consistently greater than those of the pristine material, indicating enhanced polarization and a redshifted reflection edge into the infrared region (Afrid et al., 2022; Yamusa et al., 2022). The static $R(0)$ changes with S concentration and the increased the $n(0)$ values in the doped materials confirm their improved optical response, consistent with findings from prior studies (Shawahni et al., 2018; Yamusa et al., 2022). Moreover, the static absorption spectrum at zero frequency, $\alpha(0)$, is higher in the doped systems compared to the undoped material.

Table 11: Calculated and other previously reported values of static dielectric constants for $\mathrm{W_yMo_{1-y}S_{2z}Se_{2(1-z)}}$ alloys.

Material	$\varepsilon_1(0)$	$n(0)$	$\alpha(0)$	$R(0)$
2H-$\mathrm{MoSe_2}$	9.52	2.60	0	0.36
Others (Literature)	10.08 (Mashmool et al., 2020) 8.19 (Yamusa et al., 2022)	4.27 (Yamusa et al., 2022)	0 (Afrid et al., 2023) 0 (Afrid et al., 2022)	0.25 (Mashmool et al., 2020) 0.49 (Afrid et al., 2023)
$\mathrm{MoS_{0.125}Se_{1.875}}$	9.52	3.47	0.71	0.37
$\mathrm{W_{0.125}Mo_{0.875}S_{0.125}Se_{1.875}}$	10.63	7.12	6.94	0.57
$\mathrm{W_{0.125}Mo_{0.875}S_{0.25}Se_{1.75}}$	12.19	4.70	3.37	0.56

The Penn model (Penn, 1962), which describes an inverse relationship between the bandgap and the real part of the dielectric function, is still valid for both the pristine material and the S doped systems, with or without W incorporation.

4.1.5.4 Dielectric Constants of $V_xW_yMo_{1-x-y}S_{2z}Se_{2(1-z)}$ ($x = 0.125$, $y = 0$, $z = 0, 0.0625, 0.125, 0.1875$)

Figure 41(a-d) presents the real and imaginary parts of the dielectric function along with other optical constants for supercell 2H-MoSe$_2$ doped with mono-vanadium, mono-vanadium with mono-sulfide, mono-vanadium with di-sulfide, and mono-vanadium with tri-sulfide systems as functions of photon energy. In particular, Figure 41a, 41b, 41c and 41d show the imaginary dielectric function $\varepsilon_2(\omega)$ for $V_{0.125}Mo_{0.875}Se_2$, $V_{0.125}Mo_{0.875}S_{0.125}Se_{1.875}$, $V_{0.125}Mo_{0.875}S_{0.25}Se_{1.75}$ and $V_{0.125}Mo_{0.875}S_{0.375}Se_{1.625}$ systems, respectively. In these materials, the absorption onset for the $V_{0.125}Mo_{0.875}Se_2$ starts around 0.802761 eV, which closely corresponds to its calculated energy bandgap. Below this threshold photon energy, no significant absorption occurs, indicating the system's semiconducting nature. This behavior aligns well with typical optical responses in vanadium doped MoSe$_2$ reported in first principles studies, where the absorption edge

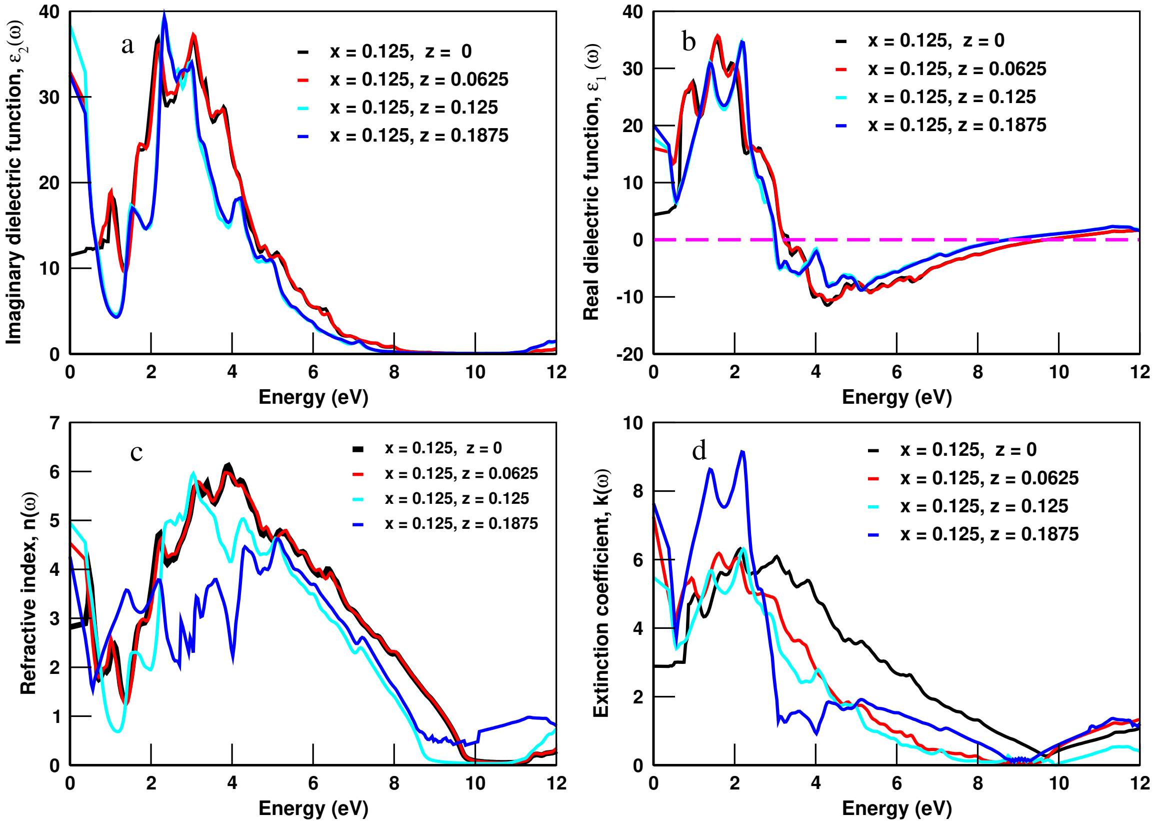

Figure 41: Dielectric functions (a, b), refractive index c) and extinction coefficient d) for $V_xMo_{1-x}S_{2z}Se_{2(1-z)}$.

aligns closely with the electronic bandgap, confirming consistent electronic and optical property descriptions for these doped layered materials (Y. Zhao et al., 2021). In this figure, the vanadium-doped systems without sulfur exhibit lower initial dissipation energy compared to those co-doped with sulfur, indicating a weaker absorption onset and reduced energy loss. The dissipation energy for all doped systems spans approximately 0 to 8 eV. The plots of $\varepsilon_2(\omega)$ for all mono-vanadium and mono-vanadium with monosulfide, disulfide and trisulfide doped systems displays three prominent peaks. Additionally, the peaks for the $V_{0.125}Mo_{0.875}Se_2$ and $V_{0.125}Mo_{0.875}S_{0.125}Se_{1.875}$ systems nearly overlap due to their similar energy bandgap behavior, and likewise the peaks for $V_{0.125}Mo_{0.875}S_{0.25}Se_{1.75}$ and $V_{0.125}Mo_{0.875}S_{0.375}Se_{1.625}$ overlap because their bandgaps are very close. The maximum peak intensities for these materials occur in the photon energy range of 2.16 to 3.08 eV. The vanadium doped systems, both with and without sulfur, show non-zero dissipation values differing from the pristine system (see Figure 36b and 39a), which displays almost zero initial dissipation. The presence of sulfur in the co-doped systems leads to higher dissipation energies, reflecting stronger absorption and more pronounced interband transitions as opposed to the vanadium only doped system, which exhibits reduced absorption and fewer interband transitions. The real part of the dielectric function for the mono-vanadium with and without monosulfide, disufide and trisulfide doped systems is shown in Figure 41b. The mono-vanadium doped systems including $V_{0.125}Mo_{0.875}Se_2$ and $V_{0.125}Mo_{0.875}S_{0.125}Se_{1.875}$, $V_{0.125}Mo_{0.875}S_{0.25}Se_{1.75}$ and $V_{0.125}Mo_{0.875}S_{0.375}Se_{1.625}$ exhibit prominent, nearly overlapping peaks. This similarity arises from their closely matched bandgaps: the first two share nearly identical energy gaps, as do the latter two. In all plots, the real part of the dielectric function does not cross zero at multiple photon energies unlike the unit cell 2H-$MoSe_2$ is substituted in vanadium with or without sulfur (see Figure 36a) due to the low dopant compositions. The system exhibits a relatively simple electronic structure, as our model involves only dilute substitution of vanadium, with or without sulfur in the host supercell. The static real dielectric constants for $V_{0.125}Mo_{0.875}Se_2$, $V_{0.125}Mo_{0.875}S_{0.125}Se_{1.875}$, $V_{0.125}Mo_{0.875}S_{0.25}Se_{1.75}$, and $V_{0.125}Mo_{0.875}S_{0.375}Se_{1.625}$ are 4.37, 16.03, 17.76, and 20.11 atomic units, respectively. These values exceed those of the unit cell substituted only with the mono-vanadium (with or without sulfur) as shown in Figure 36a, reflecting the semiconductor character of the doped systems versus the degenerate-semiconductor behavior of the substituted unit cell. In Figure 41b, the static dielectric constant, i.e., the real part of the dielectric function at zero energy, $\varepsilon_1(0)$, is smaller for the mono-vanadium doped system than for the mono-vanadium systems co-doped with sulfur in the forms of monosulfide, disulfide and trisulfide. The plot indicates that $\varepsilon_1(0)$ increases as the sulfur dopant composition rises while the vanadium composition remains fixed. Specifically, the $\varepsilon_1(0)$ value for the $V_{0.125}Mo_{0.875}S_{0.375}Se_{1.625}$ substitutional system (vanadium 12.5% with sulfur 18.75%) reaches 20.11 atomic units, the highest among all mono-vanadium with or without sulfur doped configurations. The peak positions of $\varepsilon_1(\omega)$ for the doped systems $V_{0.125}Mo_{0.875}Se_2$, $V_{0.125}Mo_{0.875}S_{0.125}Se_{1.875}$, $V_{0.125}Mo_{0.875}S_{0.25}Se_{1.75}$, and $V_{0.125}Mo_{0.875}S_{0.375}Se_{1.625}$ lie in the visible region. A positive correlation exists between photon energy and the $\varepsilon_1(\omega)$, with increasing photon energy leading to a decrease in this value for all studied materials. A significant portion of the materials under investigation displays negative values for the $\varepsilon_1(\omega)$ in the energy range of 3.29-9.58 eV and 3.04-8.95 eV for one vanadium with/without monosulfide substitutions and for other vanadium with sulfur-substituted systems, respectively. Beyond these specified energy ranges, the materials undergo minimal changes in their dielectric function values and approach zero. This indicates that photons with energies outside this range can pass through the materials without significant absorption (C.-H. Yang & Chang, 2022). The negative values of $\varepsilon_1(\omega)$ observed across different regions for all systems indicate the primarily indicates the plasmonic or metallic response (Lahourpour et al., 2019), which suggests a lack of optical transparency. The absence of optical transparency in regions where $\varepsilon_1(\omega)$ is negative, along with the sign changes in $\varepsilon_1(\omega)$, reflects instability in the optical response. The most significant response to incident light is observed in parallel radiation for potential application in the optical industry or solar cell technologies (Blaha et al., 2001; Flöry et al., 2015; X. Li & Zhu, 2015). In Figure 41a certain regions exhibit high dielectric constant values, indicating relatively low absorption in those regions. A higher $\varepsilon_1(\omega)$ suggests stronger polarization and a greater ability to bind charges. The incorporation of sulfur substitutional dopants with vanadium across all systems substantially enhances dielectric properties, yielding higher $\varepsilon_1(\omega)$ values. This enhancement reflects a robust polarization response within the material. Such increased polarization strengthens the photogenerated electric field, which is beneficial for improving photovoltaic performance. Consequently, these doped systems show higher static dielectric constants than the intrinsic (undoped) materials, indicating improved mobility and/or screening of photoexcited carriers.

Figure 41c illustrates the refractive index, n(ω) of $V_xMo_{1-x}S_{2z}Se_{2(1-z)}$ alloys, which specifies the phase velocity of an electromagnetic wave within a medium (Shawahni et al., 2018). In this figure, the maximum points of the n(ω) curve correspond to the maximum points of the dielectric curve. The n(ω) peaks for $V_{0.125}Mo_{0.875}Se_2$ system occurs at 0.48, 1.1, 2.24, 3.40, 3.90, and 4.25 eV; for $V_{0.125}Mo_{0.875}S_{0.125}Se_{1.875}$ system has peaks at 1.05, 2.29, 3.19, 3.89, and 5.33 eV; for $V_{0.125}Mo_{0.875}S_{0.25}Se_{1.75}$ systems are at 1.62, 3.05, 4.25, and 5.11 eV; for $V_{0.125}Mo_{0.875}S_{0.375}Se_{1.625}$ located at 1.43, 2.21, 2.76, 3.14, 3.60, 4.36, and 5.14 eV. In Figure 37a showing 2H-$MoSe_2$ with heavy substitution of vanadium, with or without sulfur exhibits the n(ω) peaks in the visible region. Upon modest doping with vanadium or sulfur at low compositions, these peaks shift toward the ultraviolet, i.e., a blue shift. The extinction coefficients, k(ω) for $V_xMo_{1-x}S_{2z}Se_{2(1-z)}$ alloys with various dopant compositions of sulfur but with fixed vanadium is displayed in Figure 41d. As shown, there is a variation in the values of k(ω) when the dopant compositions were varied. For the

$V_{0.125}Mo_{0.875}Se_2$ system, the extinction coefficient k(ω) appears only above 0.80706 eV; below this photon energy, there is no absorption or extinction due to the material's wider bandgap. This means absorption occurs only in the ultraviolet and visible light ranges, above the threshold photon energy. In comparison to the mono-vanadium doped system, those co-doped with vanadium and monosulfide, disulfide or trisulfide exhibit higher extinction coefficient k(ω) values in the lower energy range, enabling absorption of visible light. For all vanadium with sulfur substituted systems, the extinction coefficient k(ω) remains lower than that of the mono-vanadium doped material. Additionally, an inverse correlation is observed between photon energy and k(ω), where increasing photon energy results in decreasing extinction coefficient values (Shawahni et al., 2018). The maximum values of k(ω) in $V_xMo_{1-x}S_{2z}Se_{2(1-z)}$, for $x = 12.5\%$, $z = 6.25\%$, $z = 12.5\%$ and $z = 18.75\%$ were 6.34 (2.20 eV), 6.22 (1.60 eV), 6.34 (2.23 eV) and 9.19 (2.20 eV), respectively. As illustrated in the figure, the values, k(0), for all vanadium with monosulfide, disulfide and trisulfide substituted systems are higher and positive compared to the mono-vanadium doped system. The main peaks of the k(ω) for the $V_{0.125}Mo_{0.875}S_{0.375}Se_{1.625}$ system are located in the visible light regions, but for the $V_{0.125}Mo_{0.875}Se_2$, $V_{0.125}Mo_{0.875}S_{0.125}Se_{1.875}$ and $V_{0.125}Mo_{0.875}S_{0.25}Se_{1.75}$, the values are shifted towards the UV regions, which can be used for UV based PV applications. Additionally, the presence of peaks in both the n(ω) and k(ω) spectra suggests the occurrence of intraband transitions (Shawahni et al., 2018). In the figure, the k(ω) for $x = 0.125$ and $z = 0.1875$ of $V_xMo_{1-x}S_{2z}Se_{2(1-z)}$ exhibits sharp peaks and highest intensities compared to the other doped variants. Figure 42a presents the calculated reflectivity, R(ω), for $V_{0.125}Mo_{0.875}Se_2$, $V_{0.125}Mo_{0.875}S_{0.125}Se_{1.875}$, $V_{0.125}Mo_{0.875}S_{0.25}Se_{1.75}$ and $V_{0.125}Mo_{0.875}S_{0.375}Se_{1.625}$ systems. In this plot, the R(ω) for the $V_{0.125}Mo_{0.875}Se_2$ system rises from 2.22 to 9.67 eV before declining at higher energies, in agreement the with previous studies (Mashmool et al., 2020). This material reaches a peak reflectivity of 0.73 at 3.93 eV. Moreover, the peaks of R(ω) for

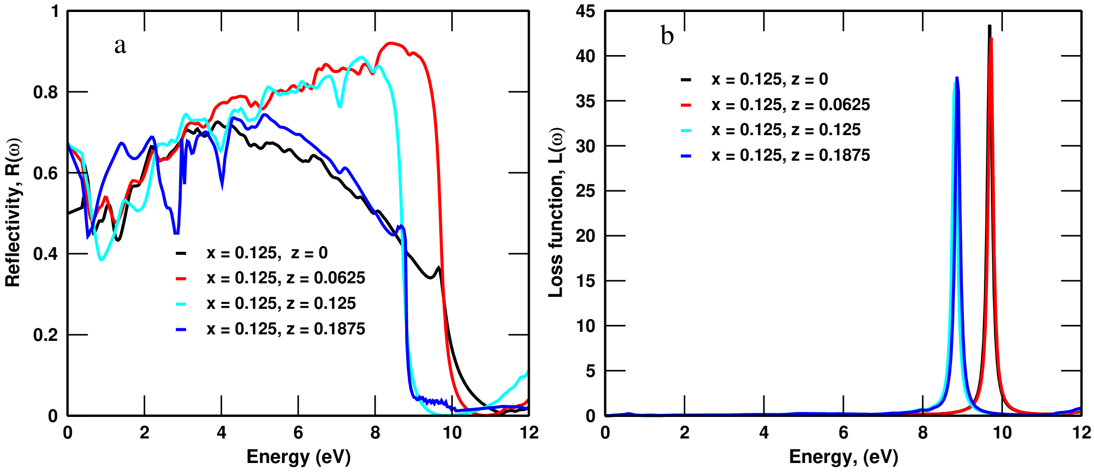

Figure 42: Electron loss function a) and reflectivity b) for $V_xMo_{1-x}S_{2z}Se_{2(1-z)}$ alloys.

$V_{0.125}Mo_{0.875}S_{0.125}Se_{1.875}$, $V_{0.125}Mo_{0.875}S_{0.25}Se_{1.75}$, and $V_{0.125}Mo_{0.875}S_{0.375}Se_{1.625}$ systems exhibit higher maxima of 0.92 (8.43 eV), 0.90 (7.67 eV), and 0.75 (5.13 eV), respectively. As observed, all doped systems experience a decline in R(ω) up to 10 eV. Figure 42b depicts the L(ω) $V_{0.125}Mo_{0.875}Se_2$, $V_{0.125}Mo_{0.875}S_{0.125}Se_{1.875}$, $V_{0.125}Mo_{0.875}S_{0.25}Se_{1.75}$, and $V_{0.125}Mo_{0.875}S_{0.375}Se_{1.625}$ systems. In the L(ω) spectra, the main peaks represent plasma energy as the oscillatory response of the delocalized valence electrons due to the plasma excitation (Narimani & Nourbakhsh, 2016). The excitation occurs when the speed of the electron beam is higher than the Fermi velocity (Egerton, 2008). As shown, the L(ω) peak value for $V_{0.125}Mo_{0.875}Se_2$ system is approximately 43.39 at 9.73 eV, whereas for $V_{0.125}Mo_{0.875}S_{0.125}Se_{1.875}$, $V_{0.125}Mo_{0.875}S_{0.25}Se_{1.75}$, and $V_{0.125}Mo_{0.875}S_{0.375}Se_{1.625}$ systems, the L(ω) are 42.00 at 9.76 eV, 37.13 at 8.79 eV and 37.69 at 8.88 eV, respectively. From these systems, $V_{0.125}Mo_{0.875}Se_2$ layered material exhibits the highest plasma resonance, which is associated with the collective fluctuations of electrons in the valence band compared to other doped materials. In the plot, the reduced L(ω) peak intensities in co-doped systems reflect lowered plasma resonance relative to vanadium mono-doped material. While principal peaks represent valence electron plasmons, remaining spectral features stem from interband transitions and excitonic interactions (Narimani & Nourbakhsh, 2016). The prominent peaks in L(ω) spectrum act as markers of plasma resonance, electronic transitions and the material's overall properties, making them crucial for analyzing and understanding the properties of materials (Mashmool et al., 2020). The incorporating of co-dopants typically causes the L(ω) peaks to shift toward lower energies (redshift), indicating electronic changes such as increased interband transition likelihood and modified plasmonic response features (Kuball et al., 1994).

5. CONCLUSIONS AND OUTLOOKS

5.1 CONCLUSIONS

The structural parameters of layered materials $V_xW_yMo_{1-x-y}S_{2z}Se_{2(1-z)}$ are significantly affected by the types and compositions of vanadium, tungsten and sulfur dopants, which in turn play a crucial role in determining their electronic, optical, thermal and vibrational properties. Comparative studies of these dopants in both solid solution and dilute doping regimes reveal that composition and dopant type strongly control the materials' multifunctional behaviors. With the highest Debye temperature ($\Theta_D = 337$K) among the investigated systems, mono-sulfide doping exhibits the most favorable thermal performance for high-temperature thermal management applications. High vanadium concentrations, either alone or combined with sulfur, introduce impurity states within the bandgap, leading to degenerate semiconducting behavior, whereas low vanadium concentrations preserve conventional semiconducting characteristics. Tungsten doping, with or without sulfur, consistently maintains typical semiconductor behavior. Vanadium and tungsten effectively tailor bandgaps, enhance carrier mobility, introduce band-edge states, and increase infrared absorption, while sulfur primarily broadens the bandgap and fine-tunes electronic and optical properties. These modifications including co-doping preserve dynamic stability, enable controlled transitions between degenerate and non-degenerate states, and influence phonon behavior and thermal transport, providing a robust design framework for 2D TMDC-based optoelectronic and thermal devices.

5.2 OUTLOOKS

In the context of optoelectronic, electronic and thermal management applications, the investigation of layered materials, $V_xW_yMo_{1-x-y}S_{2z}Se_{2(1-z)}$ spanning compositions with $x = 0, 0.5$, $y = 0, 0.125, 0.5$ and $z = 0, 0.0625, 0.125, 0.1875, 0.25, 0.5, 0.75$ have revealed remarkable tunability across their multifunctional properties. Building on these insights, the following recommendations are proposed to deepen the fundamental understanding of these materials and to accelerate their integration into practical technologies including infrared photodetectors, adaptive nanoelectronics, anti-reflective or tunable optical coatings and high performance thermal management systems.

- Future research should focus on examining the thermoelectric properties $V_xW_yMo_{1-x-y}S_{2z}Se_{2(1-z)}$ alloys due to their structural and electronic tunability. The efficiency of these materials in converting waste heat into electrical energy will be evaluated by analyzing key parameters like the Seebeck coefficient, electrical and thermal conductivities. This investigation is crucial for enhancing their potential applications in thermal management and power generation systems, contributing to sustainable energy solutions.

- Experimental synthesis and validation: While structural and dynamic stability had been predicted computationally, experimental synthesis is essential to confirm these findings. The practical viability of these materials will be established by synthesizing them under a range of pressure and temperature conditions with various dopant compositions.

List of Publications

A. Articles Published in a Reputable Journals

During this work, the publications are:

- Melak Birara Dagnaw; Abebe Belay Gemta; Kunsa Haho Habura; Fekadu Tolessa Maremi, Dereje Gelanu Dadi; Tesfaye Feyisa Hurisa; Gemechis Mathewos Fite; Manza Zityab Kasiab: **Structural, phonon, electronic and optical properties of $V_xW_yMo_{1-x-y}S_{2y}Se_{2(1-z)}$, ($x = 50\%$, $y = 0\%$ and $z = 0\%, 25\%, 50\%, 75\%$) using first principle calculations: AIP Advances 15, 055219 (2025)**
- Melak Birara Dagnaw, Abebe Belay Gemta, Kunsa Haho Habura, Fekadu Tolessa Maremi, Gashaw Beyene Kassahun, Desta Regasa Golja, Dereje Gelanu Dadi and Tesfaye Feyisa Hurisa: **Computing structural, vibrational, electronic and optical properties of $V_xW_yMo_{1-x-y}S_{2z}Se_{2(1-z)}$, ($x = 0\%, y = 50\%$ and $z = 25\%, 50\%, 75\%$) using Ab initio calculations: Mater. Res. Express 12 (2025) 086301**
- Melak Birara Dagnaw, Abebe Belay Gemta, Kunsa Haho Habura, Gashaw Beyene Kassahun, Umer Sherefedin Yasin, Gezehagn Assefa Desalegn: **Ab initio calculations of structural, phonon, thermal, electronic and optical properties of $V_xW_yMo_{1-x-y}S_{2z}Se_{2(1-z)}$, ($x = 0\%$, $y = 0\%, 25\%$ and $z = 6.25\%, 12.5\%$): AIP Advances 15, 115110 (2025)**

B. Manuscript Under Review:

- Melak Birara Dagnaw, Abebe Belay Gemta, Kunsa Haho Habura, Solomon Tiruneh Dibaba, Gashaw Beyene Kassahun, Fekadu Tolessa Maremi, Umer Sherefedin Yasin, Gezehagn Assefa Desalegn: **First principles calculations of structural, phonon, electronic and optical properties of $V_xW_yMo_{1-x-y}S_{2z}Se_{2(1-z)}$, ($x = 0\%, 12.5\%, y = 0\%$ and $z = 6.25\%, 12.5\%, 18.75\%$): Results in Physics**

C. Manuscript Under Preparation:

- Melak Birara Dagnaw, Abebe Belay Gemta, Kunsa Haho Habura, Solomon Tiruneh Dibaba, Gashaw Beyene Kassahun, Umer Sherefedin Yasin, Gezehagn Assefa Desalegn, Tadesse Bekele: **Influence of Tungsten and Vanadium Co-Doping on the Structural, Vibrational, Thermal, Magnetic and Optical Properties of Bilayer $MoSe_2$: A First-Principles Study**

D. List of Conference Participations:

- Certificate of Participation awarded for attending the 15th Annual Conference of the Ethiopian Physical Society, held at Wolkite University from February 26 to 27, 2021.
- Certificate of online participation in the training titled ”Workshop on Classical and Quantum Machine Learning for Condensed Matter Physics,” held online from 19 to 21 June 2024, Rome, Italy.
- Certificate of Participation awarded for attending the 18th Annual Conference of the Ethiopian Physical Society, held at Addis Ababa University from February 16 to 17, 2024.

REFERENCES

Afrid, S. M. T.-S., Utsha, S. G., & Zubair, A. (2022). Ab initio study on stability, electronic and optical properties of monolayer $Mo_{1-x}W_xSe_2$ alloys. In *2022 ieee international conference of electron devices society kolkata chapter (edkcon)* (pp. 319-324).

Afrid, S. M. T.-S., Utsha, S. G., & Zubair, A. (2023). First-principles study on tunable optoelectronic properties of monolayer $Mo_{1-x}W_xSe_2$ alloys and defect engineered electronic properties of $Mo_{1-x}W_xSe_2$ alloys. *Physica Scripta*, *98*(10), 104002.

Aftab, S., Iqbal, M. Z., Haider, Z., Iqbal, M. W., Nazir, G., & Shehzad, M. A. (2022). Bulk photovoltaic effect in 2D materials for solar-power harvesting. *Advanced Optical Materials*, *10*(23), 2201288.

Ahmad, S., & Mukherjee, S. (2014). A comparative study of electronic properties of bulk mos2 and its monolayer using dft technique: application of mechanical strain on MoS_2 monolayer. *Graphene*, *3*(04), 52.

Aktar, M., Liton, M., Sarker, M., Rahman, M., & Khan, M. (2024). Dft insights into mechanical, vibrational, electronic, and optical properties of bulk WSe_2 dichalcogenide. *Journal of Electronic Materials*, *53*(7), 3733-3745.

Al Balushi, Z. Y., Wang, K., Ghosh, R. K., Vilá, R. A., Eichfeld, S. M., Caldwell, J. D., ... Stone, G. (2016). Two-dimensional gallium nitride realized via graphene encapsulation. *Nature materials*, *15*(11), 1166-1171.

Aliaga, J., Vera, P., Araya, J., Ballesteros, L., Urzúa, J., Farías, M., ... Benavente, E. (2019). Electrochemical hydrogen evolution over hydrothermally synthesized Re-doped MoS_2 flower like microspheres. *Molecules*, *24*(24), 4631.

Alshammari, A., Alshehri, H., Barakat, F., & Laref, A. (2024). Density functional theory investigations of optoelectronic characteristics of MoS_2, MoS_2, and $MoSSe_2$ monolayers. *Journal of Applied Spectroscopy*, *91*(3), 605-612.

Ambrosch-Draxl, C., & Sofo, J. O. (2006). Linear optical properties of solids within the full potential linearized augmented planewave method. *Computer physics communications*, *175*(1), 1-14.

Anasori, B., Lukatskaya, M. R., & Gogotsi, Y. (2023). 2D metal carbides and nitrides (MXenes) for energy storage. In *Mxenes* (pp. 677-722). Jenny Stanford Publishing.

Andriotis, A. N., & Menon, M. (2014). Tunable magnetic properties of transition metal doped MoS_2. *Physical Review B*, *90*(12), 125304.

Arora, A., Nogajewski, K., Molas, M., Koperski, M., & Potemski, M. (2015). Exciton band structure in layered $MoSe_2$: from a monolayer to the bulk limit. *Nanoscale*, *7*(48), 20769-20775.

Asadi, Y., & Nourbakhsh, Z. (2019). Structural, electronic, mechanical, thermodynamic, and linear and nonlinear optical properties of MoS_2, $MoSe_2$ and their $Mo_{2x}Se_{2(1-x)}$ alloys: Ab initio calculations. *Journal of Electronic Materials*, *48*, 7977-7990.

Ataca, C., Sahin, H., & Ciraci, S. (2012). Stable, single layer MX_2 transition metal oxides and dichalcogenides in a honeycomb like structure. *The Journal of Physical Chemistry C*, *116*(16), 8983-8999.

Ataca, C., Topsakal, M., Akturk, E., & Ciraci, S. (2011). A comparative study of lattice dynamics of three and two-dimensional MoS_2. *The Journal of Physical Chemistry C*, *115*(33), 16354-16361.

Bahmani, M., Ghorbani-Asl, M., & Frauenheim, T. (2021). Effect of interfacial defects on the electronic properties of MoS_2 based lateral T-H heterophase junctions. *RSC advances*, *11*(60), 37995-38002.

Banu S, L., Veerapandy, V., Fjellvåg, H., & Vajeeston, P. (2023). First-principles insights into the relative stability, physical properties, and chemical properties of $MoSe_2$. *ACS omega*, *8*(15), 13799-13812.

Beiranvand, R. (2021). Theoretical investigation of electronic and optical properties of 2d transition metal dichalcogenides MoX_2 (X = S, Se, Te) from first-principles. *Physica E: Low dimensional Systems and Nanostructures*, *126*, 114416.

Bejo, A. B., Shura, M. W., Tadele, K., Afrassa, M. A., & Maremi, F. T. (2025). Structural, electronic, mechanical, optical and magnetic properties of RhNbZ (Z= Li, Si, As) half heusler compounds: a first-principles study. *Materials Research Express*, *12*(1), 016510.

Bernardi, M., Ataca, C., Palummo, M., & Grossman, J. C. (2017). Optical and electronic properties of two dimensional layered materials. *Nanophotonics*, *6*(2), 479-493.

Bhattacharjee, R., & Chattopadhyaya, S. (2017). Effects of barium (ba) doping on structural, electronic and optical properties of binary strontium chalcogenide semiconductor compounds-a theoretical investigation using dft based FP-LAPW approach. *Materials Chemistry and Physics*, *199*, 295-312.

Bhimanapati, G., Lin, Z., Meunier, V., Jung, Y., Cha, J., Das, S., … Cooper, V. (2015). Acs nano 2015, 9, 11509-11539; b) s. li, s. wang, d. *M. Tang, W. Zhao, H. Xu, L. Chu, Y. Bando, D. Golberg, G. Eda, Appl. Mater. Today*, *1*, 60.

Blaha, P., Schwarz, K., Madsen, G. K., Kvasnicka, D., & Luitz, J. (2001). wien2k. *An augmented plane wave+local orbitals program for calculating crystal properties*, *60*(1).

Blöchl, P. E. (1990). Generalized separable potentials for electronic-structure calculations. *Physical Review B*, *41*(8), 5414.

Böker, T., Severin, R., Müller, A., Janowitz, C., Manzke, R., Voß, D., … Pollmann, J. (2001). Band structure of MoS_2, $MoSe_2$, and α- $MoTe_2$: Angle resolved photoelectron spectroscopy and ab initio calculations. *Physical Review B*, *64*(23), 235305.

Bonilla, M., Kolekar, S., Ma, Y., Diaz, H. C., Kalappattil, V., Das, R., … Batzill, M. (2018). Strong room temperature ferromagnetism in VSe_2 monolayers on van der Waals substrates. *Nature nanotechnology*, *13*(4), 289-293.

Brixner, L. (1963). X-ray study and thermoelectric properties of the $W_xTa_{1-x}Se_2$ system. *Journal of The Electrochemical Society*, *110*(4), 289.

Bronsema, K. D., De Boer, J., & Jellinek, F. (1986). On the structure of molybdenum diselenide and disulfide. *Zeitschrift für anorganische und allgemeine Chemie*, *540*(9-10), 15-17.

Cadiz, F., Courtade, E., Robert, C., Wang, G., Shen, Y., Cai, H., … Lagarde, D. (2017). Excitonic linewidth approaching the homogeneous limit in MoS_2 based van der Waals heterostructures. *Physical Review X*, *7*(2), 021026.

Calandra, M., Mazin, I., & Mauri, F. (2009). Effect of dimensionality on the charge density wave in few-layer 2H-$NbSe_2$. *Physical Review B Condensed Matter and Materials Physics*, *80*(24), 241108.

Canpolat, M., Kürkçü, C., Yamçıçıer, Ç., & Merdan, Z. (2019). Structural and electronic properties of biof with two dimensional layered structure under high pressure: Ab initio study. *Solid State Communications*, *288*, 33-37.

Champion, J. (1965). Some properties of (Mo, W) $(Se, Te)_2$. *British Journal of Applied Physics*, *16*(7), 1035.

Chang, B. K. (2024). *Electron-phonon interactions and charge transport in organic crystals and transition metal oxides from first-principles calculations*. California Institute of Technology.

Chang, L. L., & Esaki, L. (1992). Semiconductor quantum heterostructures. *Physics today*, *45*(10), 36-43.

Chaves, A., Azadani, J., Özçelik, V. O., Grassi, R., & Low, T. (2018). Electrical control of excitons in van der Waals heterostructures with type-II band alignment. *Physical Review B*, *98*(12), 121302.

Chaves, A., Azadani, J. G., Alsalman, H., Da Costa, D., Frisenda, R., Chaves, A., … Zhou, J. (2020). Bandgap engineering of two dimensional semiconductor materials. *npj 2D Materials and Applications*, *4*(1), 29.

Chen, Y., Xi, J., Dumcenco, D. O., Liu, Z., Suenaga, K., Wang, D., … Xie, L. (2013). Tunable band gap photoluminescence from atomically thin transition metal dichalcogenide alloys. *Acs Nano*, *7*(5), 4610-4616.

Chen, Z., Zhang, X., & Pei, Y. (2018). Manipulation of phonon transport in thermoelectrics. *Advanced Materials*, *30*(17), 1705617.

Chhowalla, M., Shin, H. S., Eda, G., Li, L.-J., Loh, K. P., & Zhang, H. (2013). The chemistry of two dimensional layered transition metal dichalcogenide nanosheets. *Nature chemistry*, *5*(4), 263-275.

Cho, B., Yoon, J., Lim, S. K., Kim, A. R., Kim, D.-H., Park, S.-G., … Lee, B. H. (2015). Chemical sensing of 2D graphene/MoS_2 heterostructure device. *ACS applied materials & interfaces*, *7*(30), 16775-16780.

Choudhary, K., Kalish, I., Beams, R., & Tavazza, F. (2017). High throughput identification and characterization of two dimensional materials using density functional theory. *Scientific reports*, *7*(1), 5179.

Chu, M., Sun, Y., Aghoram, U., & Thompson, S. E. (2009). Strain: A solution for higher carrier mobility in nanoscale MOSFETs. *Annual Review of Materials Research*, *39*(1), 203-229.

Cococcioni, M., & de Gironcoli, S. (2005). Linear response approach to the calculation of the effective interaction parameters in the LDA+U method. *Physical Review B*, *71*(3), 035105.

Coleman, J. N., Lotya, M., O'Neill, A., Bergin, S. D., King, P. J., Khan, U., … Smith, R. J. (2011). Two dimensional nanosheets produced by liquid exfoliation of layered materials. *Science*, *331*(6017), 568-571.

Cui, H., Zhang, G., Zhang, X., & Tang, J. (2019). Rh doped $MoSe_2$ as a toxic gas scavenger: A first-principles study. *Nanoscale Advances*, *1*(2), 772-780.

Dai, Y., Qi, P., Tao, G., Yao, G., Shi, B., Liu, Z., … Dang, Z. (2023). Phonon assisted upconversion in twisted two dimensional semiconductors. *Light: Science & Applications*, *12*(1), 6.

Dean, C. R., Young, A. F., Meric, I., Lee, C., Wang, L., Sorgenfrei, S., … Shepard, K. L. (2010). Boron nitride substrates for high quality graphene electronics. *Nature nanotechnology*, *5*(10), 722-726.

Deng, J., Zhou, Z., Chen, J., Cheng, Z., Liu, J., & Wang, Z. (2022). Vanadium doped molybdenum diselenide atomic layers with room temperature ferromagnetism. *ChemPhysChem*, *23*(16), e202200162.

Deng, S., Zhong, Y., Zeng, Y., Wang, Y., Yao, Z., Yang, F., … Xia, X. (2017). Directional construction of vertical nitrogen doped 1T-2H $MoSe_2$/graphene shell/core nanoflake arrays for efficient hydrogen evolution reaction. *Advanced materials*, *29*(21), 1700748.

Denton, A. R., & Ashcroft, N. W. (1991). Vegard's law. *Physical review A*, *43*(6), 3161.

Ding, W., Zhu, J., Wang, Z., Gao, Y., Xiao, D., Gu, Y., … Zhu, W. (2017). Prediction of intrinsic two dimensional ferroelectrics in In_2Se_3 and other III2-VI3 van der Waals materials. *Nature communications*, *8*(1), 14956.

Ding, Z., Pei, Q.-X., Jiang, J.-W., & Zhang, Y.-W. (2015). Manipulating the thermal conductivity of monolayer MoS_2 via lattice defect and strain engineering. *The Journal of Physical Chemistry C*, *119*(28), 16358-16365.

Djalab, Y., Moussa, R., Maache, M., Rouf, S. A., Abdiche, A., Khenata, R., & Soyalp, F. (2023). Theoretical investigations of structural, electronic, optical and elastic properties of wurtzite $ZnO_{1-x}Se_{1-x}$ ternary alloys using first principle method. *Journal of Materials Research*, *38*(3), 799-813.

Dreizler, R. M., & Gross, E. K. (2012). *Density functional theory: an approach to the quantum many body problem.* Springer Science & Business Media.

Duerloo, K.-A. N., Li, Y., & Reed, E. J. (2014). Structural phase transitions in two dimensional Mo and W dichalcogenide monolayers. *Nature communications*, *5*(1), 4214.

Dumcenco, D., Chen, K. Y., Wang, Y., Huang, Y.-S., & Tiong, K.-K. (2010). Raman study of 2H-$Mo_{1-x}W_xS_2$ layered mixed crystals. *Journal of Alloys and Compounds*, *506*(2), 940-943.

Egerton, R. F. (2008). Electron energy-loss spectroscopy in the tem. *Reports on Progress in Physics*, *72*(1), 016502.

Enyashin, A. N., Bar-Sadan, M., Houben, L., & Seifert, G. (2013). Line defects in molybdenum disulfide layers. *The Journal of Physical Chemistry C*, *117*(20), 10842-10848.

Ermolaev, G. A., Stebunov, Y. V., Vyshnevyy, A. A., Tatarkin, D. E., Yakubovsky, D. I., Novikov, S. M., … Arsenin, A. V. (2020). Broadband optical properties of monolayer and bulk MoS_2. *npj 2D Materials and Applications*, *4*(1), 21.

Esaki, L., & Tsu, R. (1970). Superlattice and negative differential conductivity in semiconductors. *IBM Journal of Research and Development*, *14*(1), 61-65.

Faist, J., Capasso, F., Sivco, D. L., Sirtori, C., Hutchinson, A. L., & Cho, A. Y. (1994). Quantum cascade laser. *Science*, *264*(5158), 553-556.

Fei, Z., Palomaki, T., Wu, S., Zhao, W., Cai, X., Sun, B., … Cobden, D. H. (2017). Edge conduction in monolayer WSe_2. *Nature Physics*, *13*(7), 677-682.

Feng, Q., Mao, N., Wu, J., Xu, H., Wang, C., Zhang, J., & Xie, L. (2015). Growth of $MoS_{2(1-x)}Se_{2x}$ (x= 0.41-1.00) monolayer alloys with controlled morphology by physical vapor deposition. *ACS nano*, *9*(7), 7450-7455.

Flöry, N., Jain, A., Bharadwaj, P., Parzefall, M., Taniguchi, T., Watanabe, K., & Novotny, L. (2015). A WSe_2/$MoSe_2$ heterostructure photovoltaic device. *Applied Physics Letters*, *107*(12).

Fu, Q., Yang, L., Wang, W., Han, A., Huang, J., Du, P., … Xiang, B. (2015). Synthesis and enhanced electrochemical catalytic performance of monolayer $WS_{2(1-x)}Se_{2x}$ with a tunable band gap. *Advanced Materials*, *27*(32), 4732-4738.

Gan, L.-Y., Zhang, Q., Zhao, Y.-J., Cheng, Y., & Schwingenschlögl, U. (2014). Order-disorder phase transitions in the two-dimensional semiconducting transition metal dichalcogenide alloys $Mo_{1-x}W_xX_2$ (X = S, Se, and Te). *Scientific reports*, *4*(1), 6691.

Gao, J., Kim, Y. D., Liang, L., Idrobo, J. C., Chow, P., Tan, J., … Lu, T.-M. (2016). Transition-metal substitution doping in synthetic atomically thin semiconductors. *Advanced materials*, *28*(44).

Gasiorowski, J., Hingerl, K., Menon, R., Plach, T., Neugebauer, H., Wiesauer, K., … Sariciftci, N. S. (2013). Dielectric function of undoped and doped poly [2-methoxy-5-(3, 7-dimethyloctyloxy)-1, 4-phenylene-vinylene] by ellipsometry in a wide spectral range. *The journal of physical chemistry C*, *117*(42), 22010-22016.

Ghafari, A., & Janowitz, C. (2019). Electronic and thermoelectric properties of ZrS_xSe_{2-x}. *Computational Materials Science*, *169*, 109109.

Ghorbani-Asl, M., Enyashin, A. N., Kuc, A., Seifert, G., & Heine, T. (2013). Defect-induced conductivity anisotropy in MoS_2 monolayers. *Physical Review B*, *88*(24), 245440.

Ghosh, C., Sarkar, D., Mitra, M., & Chattopadhyay, K. (2013). Equibiaxial strain: tunable electronic structure and optical properties of bulk and monolayer $MoSe_2$. *Journal of Physics d: applied physics*, *46*(39), 395304.

Giannozzi, P., Baroni, S., Bonini, N., Calandra, M., Car, R., Cavazzoni, C., … Dabo, I. (2009). Quantum espresso: a modular and open-source software project for quantumsimulations of materials. *Journal of physics: Condensed matter*, *21*(39), 395502.

Gibbs, G., Ross, N., & Cox, D. (2017). Sulfide bonded atomic radii. *Physics and Chemistry of Minerals*, *44*, 561-566.

Gong, C., Li, L., Li, Z., Ji, H., Stern, A., Xia, Y., … Wang, Y. (2017). Discovery of intrinsic ferromagnetism in two-dimensional van der Waals crystals. *Nature*, *546*(7657), 265-269.

Gong, Y., Liu, Z., Lupini, A. R., Shi, G., Lin, J., Najmaei, S., … You, G. (2014). Band gap engineering and layer-by-layer mapping of selenium-doped molybdenum disulfide. *Nano letters*, *14*(2), 442-449.

Gori-Giorgi, P., Toulouse, J., & Savin, A. (2006). Model hamiltonians in density functional theory. *arXiv preprint cond-mat/0605174*.

Görling, A. (1999). Density-functional theory beyond the hohenberg-kohn theorem. *Physical Review A*, *59*(5), 3359.

Guguchia, Z., Kerelsky, A., Edelberg, D., Banerjee, S., von Rohr, F., Scullion, D., … Shermadini, Z. (2018). Magnetism in semiconducting molybdenum dichalcogenides. *Science advances*, *4*(12), eaat3672.

Guo, Y., Ji, Y., Dong, H., Wang, L., & Li, Y. (2019). Electronic and optical properties of defective electronic $MoSe_2$ repaired by halogen atoms from first-principles study. *AIP Advances*, *9*(2).

Gupta, A., Sakthivel, T., & Seal, S. (2015). Recent development in 2D materials beyond graphene. *Progress in Materials Science*, *73*, 44-126.

Habura, K., Afrassa, M., & Hone, F. (2023). Comparative analysis of the electronic structure and magnetic properties of $Zn_{1-x}TM_xSe$ (TM = Fe, V) using LDA and LDA+U approximations. *Computational Condensed Matter*, *35*, e00799.

Habura, K. H., Afrassa, M. A., & Hone, F. G. (2023). Density functional theory study of $Zn_{1-x}Se_2$ and Fe_xSe): Electronic structure, phonon, and magnetic properties. *AIP Advances*, *13*(3).

Habura, K. H., Afrassa, M. A., & Hone, F. G. (2024). Computational study on the structural, electronic, lattice vibration, and magnetism in $Zn_{1-x}Fe_xSe_yTe_{1-y}$ quaternary materials. *AIP Advances*, *14*(1).

Haldar, S., Vovusha, H., Yadav, M. K., Eriksson, O., & Sanyal, B. (2015). Systematic study of structural, electronic, and optical properties of atomic scale defects in the two dimensional transition metal dichalcogenides MX_2 (M = Mo, W; X = S, Se, Te). *Physical Review B*, *92*(23), 235408.

Hall, M. B. (1978). Valence shell electron pair repulsions and the pauli exclusion principle. *Journal of the American Chemical Society*, *100*(20), 6333-6338.

Hamann, D., Schlüter, M., & Chiang, C. (1979). Norm-conserving pseudopotentials. *Physical review letters*, *43*(20), 1494.

He, J., Hummer, K., & Franchini, C. (2014). Stacking effects on the electronic and optical properties of bilayer transition metal dichalcogenides MoS_2, $MoSe_2$, WS_2, and WSe_2. *Physical Review B*, *89*(7), 075409.

Herbstein, F. (1961). Methods of measuring debye temperatures and comparison of results for some cubic crystals. *Advances in Physics*, *10*(40), 313-355.

Hilaire, P., Millet, C., Loredo, J., Antón, C., Harouri, A., Lemaître, A., … Senellart, P. (2020). Deterministic assembly of a charged-quantum-dot-micropillar cavity device. *Physical Review B*, *102*(19), 195402.

Hinsche, N. F., & Thygesen, K. S. (2017). Electron-phonon interaction and transport properties of metallic bulk and monolayer transition metal dichalcogenide TaS_2. *2D Materials*, *5*(1), 015009.

Hodes, G. (2013). Perovskite-based solar cells. *Science*, *342*(6156), 317-318.

Hoque, K. S., & Zubair, A. (2022). First-principles study of induced magnetism in tungsten vanadium selenide alloys for spintronic applications. *ACS omega*, *7*(41), 36184-36194.

Horzum, S., Sahin, H., Cahangirov, S., Cudazzo, P., Rubio, A., Serin, T., & Peeters, F. (2013). Phonon softening and direct to indirect band gap crossover in strained single-layer $MoSe_2$. *Physical Review B-Condensed Matter and Materials Physics*, *87*(12), 125415.

Hossen, M. F., Shendokar, S., & Aravamudhan, S. (2024). Defects and defect engineering of two-dimensional transition metal dichalcogenide (2D TMDC) materials. *Nanomaterials*, *14*(5), 410.

Huang, B., Clark, G., Navarro-Moratalla, E., Klein, D. R., Cheng, R., Seyler, K. L., … Cobden, D. H. (2017). Layer-dependent ferromagnetism in a van der Waals crystal down to the monolayer limit. *Nature*, *546*(7657), 270-273.

Huang, C., Wu, S., Sanchez, A. M., Peters, J. J., Beanland, R., Ross, J. S., … Xu, X. (2014). Lateral heterojunctions within monolayer $MoSe_2$-WSe_2 semiconductors. *Nature materials*, *13*(12), 1096-1101.

Huang, Y. L., Chen, Y., Zhang, W., Quek, S. Y., Chen, C.-H., Li, L.-J., … Chen, W. (2015). Bandgap tunability at single-layer molybdenum disulphide grain boundaries. *Nature communications*, *6*(1), 6298.

Hummel, R. E. (2011). *Electronic properties of materials*. Springer Science & Business Media.

Iqbal, M., Elahi, E., Amin, A., Hussain, G., & Aftab, S. (2020). Chemical doping of transition metal dichalcogenides (TMDCs) based field effect transistors: A review. *Superlattices and Microstructures*, *137*, 106350.

Island, J. O., Buscema, M., Barawi, M., Clamagirand, J. M., Ares, J. R., Sánchez, C., … Castellanos-Gomez, A. (2014). Ultrahigh photoresponse of few-layer TiS_3 nanoribbon transistors. *arXiv preprint arXiv:1406.5003*.

Israelachvili, J., & Tabor, D. (1973). van der Waals forces: theory and experiment. In *Progress in surface and membrane science* (Vol. 7, pp. 1-55). Elsevier.

Izyumov, Y. A. (1995). Hubbard model of strong correlations. *Physics-Uspekhi*, *38*(4), 385.

Jariwala, D., Sangwan, V. K., Lauhon, L. J., Marks, T. J., & Hersam, M. C. (2014). Emerging device applications for semiconducting two-dimensional transition metal dichalcogenides. *ACS nano*, *8*(2), 1102-1120.

Jing, Y., Liu, B., Zhu, X., Ouyang, F., Sun, J., & Zhou, Y. (2020). Tunable electronic structure of two-dimensional transition metal chalcogenides for optoelectronic applications. *Nanophotonics*, *9*(7), 1675-1694.

Johannes, M., Mazin, I., & Howells, C. (2006). Fermi-surface nesting and the origin of the charge-density wave in $NbSe_2$. *Physical Review B-Condensed Matter and Materials Physics*, *73*(20), 205102.

Kam, K., & Parkinson, B. (1982). Detailed photocurrent spectroscopy of the semiconducting group vib transition metal dichalcogenides. *The Journal of Physical Chemistry*, *86*(4), 463-467.

Kandemir, A., Yapicioglu, H., Kinaci, A., Çağın, T., & Sevik, C. (2016). Thermal transport properties of MoS_2 and $MoSe_2$ monolayers. *Nanotechnology*, *27*(5), 055703.

Kang, J., Tongay, S., Zhou, J., Li, J., & Wu, J. (2013). Band offsets and heterostructures of two-dimensional semiconductors. *Applied Physics Letters*, *102*(1).

Kappera, R., Voiry, D., Yalcin, S. E., Branch, B., Gupta, G., Mohite, A. D., & Chhowalla, M. (2014). Phase-engineered low-resistance contacts for ultrathin MoS_2 transistors. *Nature materials*, *13*(12), 1128-1134.

Kassa, M. D., Woldemariam, M. M., Debelo, N. G., Gebremeskel, D. K., & Habura, K. H. (2024). A computational exploration of structural, electronic, and optical properties of Hf substituted $CaZr_{1-x}Hf_xS_3$ (x = 0.25, 0.50, and 0.75) for photovoltaic applications. *Physica Scripta*, *100*(1), 015974.

Katre, A., Togo, A., Tanaka, I., & Madsen, G. K. (2015). First principles study of thermal conductivity cross-over in nanostructured zinc-chalcogenides. *Journal of Applied Physics*, *117*(4).

Khalid, S., Ma, Y., Sun, X., Zhou, G., Wu, H., Lu, G., ... Bouhemadou, A. (2020). Electronic and optical properties of Tl_4GeX_3 (X = S, Se, and Te) compounds for optoelectronics applications: insights from DFT-computations. *Journal of Materials Research and Technology*, *9*(1), 413-420.

Khan, M. J. I., Liu, J., Latif, A., Majeed, I., Ullah, H., Asghar, M., & Ahmad, J. (2022). Investigating structural, electronic, magnetic, and optical properties of Co-doped and Co-X (X = Fe, Mn) Co-doped MoS_2 for optoelectronic applications. *Journal of Molecular Modeling*, *28*(10), 310.

Kim, Y., Huang, J.-L., & Lieber, C. M. (1991). Characterization of nanometer scale wear and oxidation of transition metal dichalcogenide lubricants by atomic force microscopy. *Applied physics letters*, *59*(26), 3404-3406.

Kittel, C. (2005). *Int. to solid state physics, 8th edn., maruzen.* John Wiley & Sons, Inc., New York.

Ko, T.-S., Huang, C.-C., Lin, D.-Y., Ruan, Y.-J., & Huang, Y. S. (2016). Electrical and optical properties of Co-doped and undoped MoS_2. *Japanese Journal of Applied Physics*, *55*(4S), 04EP06.

Kohn, W., & Sham, L. (1996). Density functional theory. In *Conference proceedings-italian physical society* (Vol. 49, pp. 561-572).

Kokalj, A. (1999). Xcrysden a new program for displaying crystalline structures and electron densities. *Journal of Molecular Graphics and Modelling*, *17*(3-4), 176-179.

Komsa, H.-P., & Krasheninnikov, A. V. (2012). Two-dimensional transition metal dichalcogenide alloys: stability and electronic properties. *The journal of physical chemistry letters*, *3*(23), 3652-3656.

Koós, A. A., Vancsó, P., Szendro, M., Dobrik, G., Antognini Silva, D., Popov, Z. I., … Biró, L. P. (2019). Influence of native defects on the electronic and magnetic properties of cvd grown $MoSe_2$ single layers. *The Journal of Physical Chemistry C*, *123*(40), 24855-24864.

Kresse, G., Furthmüller, J., & Hafner, J. (1995). Ab initio force constant approach to phonon dispersion relations of diamond and graphite. *Europhysics Letters*, *32*(9), 729.

Kroemer, H. (1963). A proposed class of hetero-junction injection lasers. *Proceedings of the IEEE*, *51*(12), 1782-1783.

Kroemer, H. (2001). Nobel lecture: Quasielectric fields and band offsets: teaching electrons new tricks. *Reviews of modern physics*, *73*(3), 783.

Kuball, M., Kelly, M., Cardona, M., Köhler, K., & Wagner, J. (1994). Doping dependence of the e1 and e1+δ1 critical points in highly doped n-and p-type gaas: Importance of surface band bending and depletion. *Physical Review B*, *49*(23), 16569.

Kuc, A., Heine, T., & Kis, A. (2015). Electronic properties of transition-metal dichalcogenides. *MRS bulletin*, *40*(7), 577-584.

Kumar, A., Singh, P., & Harbola, M. K. (2024). Density functional theory of material design: fundamentals and applications-II. *Oxford Open Materials Science*, *4*(1), itae002.

Kumar, J., & Shrivastava, M. (2023). Role of chalcogen defect introducing metal-induced gap states and its implications for metal-TMDs' interface chemistry. *ACS omega*, *8*(11), 10176-10184.

Kumar, S., & Schwingenschlogl, U. (2015). Thermoelectric response of bulk and monolayer $MoSe_2$ and WSe_2. *Chemistry of Materials*, *27*(4), 1278-1284.

Lahourpour, F., Boochani, A., Parhizgar, S., & Elahi, S. (2019). Structural, electronic and optical properties of graphene like nano layers MoX_2 (X: S, Se, Te): DFT study. *Journal of Theoretical and Applied Physics*, *13*, 191-201.

Lee, C., & Gonze, X. (1995). Ab initio calculation of the thermodynamic properties and atomic temperature factors of $SiO_2\alpha$ quartz and stishovite. *Physical Review B*, *51*(13), 8610.

Lee, C., Hong, J., Lee, W. R., Kim, D. Y., & Shim, J. H. (2014). Density functional theory investigation of the electronic structure and thermoelectric properties of layered MoS_2, $MoSe_2$ and their mixed layer compound. *Journal of Solid State Chemistry*, *211*, 113-119.

Lee, C., Yan, H., Brus, L. E., Heinz, T. F., Hone, J., & Ryu, S. (2010). Anomalous lattice vibrations of single and few layer MoS_2. *ACS nano*, *4*(5), 2695-2700.

Lee, M. L., Fitzgerald, E. A., Bulsara, M. T., Currie, M. T., & Lochtefeld, A. (2005). Strained Si, SiGe, and Ge channels for high-mobility metal-oxide-semiconductor field-effect transistors. *Journal of applied physics*, *97*(1).

Lehtinen, O., Komsa, H.-P., Pulkin, A., Whitwick, M. B., Chen, M.-W., Lehnert, T., ... Kaiser, U. (2015). Atomic scale microstructure and properties of se deficient two dimensional $MoSe_2$. *ACS nano*, *9*(3), 3274-3283.

Lei, S., Ge, L., Liu, Z., Najmaei, S., Shi, G., You, G., ... Ajayan, P. M. (2013). Synthesis and photoresponse of large GaSe atomic layers. *Nano letters*, *13*(6), 2777-2781.

Li, C.-Y., Le, J.-B., Wang, Y.-H., Chen, S., Yang, Z.-L., Li, J.-F., ... Tian, Z.-Q. (2019). In situ probing electrified interfacial water structures at atomically flat surfaces. *Nature materials*, *18*(7), 697-701.

Li, D., Xu, J.-R., Ba, K., Xuan, N., Chen, M., Sun, Z., ... Zhang, Z. (2017). Tunable bandgap in few-layer black phosphorus by electrical field. *2D Materials*, *4*(3), 031009.

Li, J., Li, J., Tang, J., Tao, Z., Xue, S., Liu, J., ... Zhu, X. (2023). Direct observation of topological phonons in graphene. *Physical Review Letters*, *131*(11), 116602.

Li, J., Yan, W., Lv, Y., Leng, J., Zhang, D., Coileáin, C. Ó., ... Cho, J. (2020). Sub millimeter size high mobility single crystal $MoSe_2$ monolayers synthesized by NaCl assisted chemical vapor deposition. *RSC advances*, *10*(3), 1580-1587.

Li, L., Chen, Z., Hu, Y., Wang, X., Zhang, T., Chen, W., & Wang, Q. (2013). Single-layer single-crystalline SnSe nanosheets. *Journal of the American Chemical Society*, *135*(4), 1213-1216.

Li, L., Kim, J., Jin, C., Ye, G. J., Qiu, D. Y., Da Jornada, F. H., ... Yang, F. (2017). Direct observation of the layer-dependent electronic structure in phosphorene. *Nature nanotechnology*, *12*(1), 21-25.

Li, M.-Y., Chen, C.-H., Shi, Y., & Li, L.-J. (2016). Heterostructures based on two-dimensional layered materials and their potential applications. *Materials Today*, *19*(6), 322-335.

Li, X., Lin, M.-W., Basile, L., Hus, S. M., Puretzky, A. A., Lee, J., ... Idrobo, J. C. (2016). Isoelectronic tungsten doping in monolayer $MoSe_2$ for carrier type modulation. *Advanced Materials*, *28*(37), 8240-8247.

Li, X., & Zhu, H. (2015). Two dimensional MoS_2: Properties, preparation, and applications. *Journal of Materiomics*, *1*(1), 33-44.

Li, Y., Chernikov, A., Zhang, X., Rigosi, A., Hill, H. M., Van Der Zande, A. M., ... Heinz, T. F. (2014). Measurement of the optical dielectric function of monolayer transition metal dichalcogenides: MoS_2, $MoSe_2$, WS_2, and WSe_2. *Physical Review B*, *90*(20), 205422.

Li, Y., Rao, Y., Mak, K. F., You, Y., Wang, S., Dean, C. R., & Heinz, T. F. (2013). Probing symmetry properties of few layer MoS_2 and h-BN by optical second harmonic generation. *Nano letters*, *13*(7), 3329-3333.

Li, Y., Wang, M., & Sun, J. (2022). Molecular engineering strategies toward molybdenum diselenide design for energy storage and conversion. *Advanced Energy Materials*, *12*(45), 2202600.

Liang, W. (1971). Reflectivity of MoS_2 and $NbSe_2$ (interband transitions). *Journal of Physics C: Solid State Physics*, *4*(18), L378.

Lin, Z., Carvalho, B. R., Kahn, E., Lv, R., Rao, R., Terrones, H., ... Terrones, M. (2016). Defect engineering of two-dimensional transition metal dichalcogenides. *2D Materials*, *3*(2), 022002.

Lin, Z., Fu, B., & An, Y. (2020). Effects of defects and anions on the geometry, electronic structures and exchange interaction of Fe doped 2H-$MoSe_2$ monolayer. *Applied Surface Science*, *528*, 146960.

Liu, B., Köpf, M., Abbas, A. A., Wang, X., Guo, Q., Jia, Y., ... Pielnhofer, F. (2015). Black arsenic-phosphorus: layered anisotropic infrared semiconductors with highly tunable compositions and properties. *arXiv preprint arXiv:1505.07061*.

Liu, H., Neal, A. T., Zhu, Z., Luo, Z., Xu, X., Tománek, D., & Ye, P. D. (2014). Phosphorene: an unexplored 2D semiconductor with a high hole mobility. *ACS nano*, *8*(4), 4033-4041.

Liu, H.-L., Yang, T., Chen, J.-H., Chen, H.-W., Guo, H., Saito, R., ... Li, L.-J. (2020). Temperature dependent optical constants of monolayer MoS_2, $MoSe_2$, WS_2, and WSe_2: spectroscopic ellipsometry and first principles calculations. *Scientific reports*, *10*(1), 15282.

Liu, M., Johnston, M. B., & Snaith, H. J. (2013). Efficient planar heterojunction perovskite solar cells by vapour deposition. *Nature*, *501*(7467), 395-398.

Lodesani, A., Picone, A., Brambilla, A., Giannotti, D., Jagadeesh, M. S., Calloni, A., ... Finazzi, M. (2019). Graphene as an ideal buffer layer for the growth of high quality ultrathin Cr_2O_3 layers on Ni (111). *ACS nano*, *13*(4), 4361-4367.

Loh, L., Zhang, Z., Bosman, M., & Eda, G. (2021). Substitutional doping in 2D transition metal dichalcogenides. *Nano Research*, *14*(6), 1668-1681.

Lu, X., & Yang, L. (2017). Stark effect of doped two-dimensional transition metal dichalcogenides. *Applied Physics Letters*, *111*(19).

Luo, S., Hao, G., Fan, Y., Kou, L., He, C., Qi, X., … Zhong, J. (2015). Formation of ripples in atomically thin MoS_2 and local strain engineering of electrostatic properties. *Nanotechnology*, *26*(10), 105705.

Luo, Z., Hao, J., & Li, J. (2022). The optical properties of $MoSe_2$ in bulk and monolayer with different crystal orientation based on first principles calculations. *Academic Journal of Materials & Chemistry*, *3*(1), 51-57.

Ma, W., Alonso-González, P., Li, S., Nikitin, A. Y., Yuan, J., Martín-Sánchez, J., … Vélez, S. (2018). In-plane anisotropic and ultra low loss polaritons in a natural van der waals crystal. *Nature*, *562*(7728), 557-562.

Mak, K. F., Lee, C., Hone, J., Shan, J., & Heinz, T. F. (2010). Atomically thin MoS_2: a new direct gap semiconductor. *Physical review letters*, *105*(13), 136805.

Manzeli, S., Ovchinnikov, D., Pasquier, D., Yazyev, O. V., & Kis, A. (2017). 2D transition metal dichalcogenides. *Nature Reviews Materials*, *2*(8), 1-15.

Markov, M., Rezaei, S. E., Sadeghi, S. N., Esfarjani, K., & Zebarjadi, M. (2019). Thermoelectric properties of semimetals. *Physical Review Materials*, *3*(9), 095401.

Mashmool, A., Saeidi, P., Yalameha, S., & Nourbakhsh, Z. (2020). First principles calculations of structural, electronic and optical properties MoX_2 (X = S, Se) metal dichalcogenides and their nano-layers. *Journal of Magnetism and Magnetic Materials*, *503*, 166572.

McDonnell, S., Addou, R., Buie, C., Wallace, R. M., & Hinkle, C. L. (2014). Defect dominated doping and contact resistance in MoS_2. *ACS nano*, *8*(3), 2880-2888.

Mimura, T., Hiyamizu, S., Fujii, T., & Nanbu, K. (1980). A new field effect transistor with selectively doped GaAs/$Al_xGa_{1-x}As$ heterojunctions. *Japanese journal of applied physics*, *19*(5), L225.

Mirabella, D., Aldao, C., & Deza, R. (1994). Orbital nonorthogonality effects in band structure calculations within the tight-binding scheme. *American Journal of Physics*, *62*(2), 162-165.

Mitterreiter, E., Schuler, B., Micevic, A., Hernangómez-Pérez, D., Barthelmi, K., Cochrane, K. A., … Wong, E. (2021). The role of chalcogen vacancies for atomic defect emission in MoS_2. *Nature communications*, *12*(1), 3822.

Molas, M. R., Nogajewski, K., Slobodeniuk, A. O., Binder, J., Bartos, M., & Potemski, M. (2017). The optical response of monolayer, few-layer and bulk tungsten disulfide. *Nanoscale*, *9*(35), 13128-13141.

Molina-Sanchez, A., & Wirtz, L. (2011). Phonons in single layer and few layer MoS_2 and WS_2. *Physical Review B-Condensed Matter and Materials Physics*, *84*(15), 155413.

Monkhorst, H. J., & Pack, J. D. (1976). Special points for brillouin-zone integrations. *Physical review B*, *13*(12), 5188.

Muhammad, I. Y. (2021). Structural and electronic properties of 2D chalcogenides. In *Journal of physics: Conference series* (Vol. 1719, p. 012029).

Narimani, M., & Nourbakhsh, Z. (2016). Electronic, topological phase and optical properties of XPdBi (X = Lu, Sc) nano layers. *Thin Solid Films*, *616*, 287-296.

Nasir, M., Hadi, M., Rayhan, M., Ali, M., Hossain, M., Roknuzzaman, M., … Ostrikov, K. (2017). First principles study of superconducting ScIrP and ScIrP pnictides. *Physica status solidi (b)*, *254*(11), 1700336.

Nazir, G., Tariq, S., Afaq, A., Mahmood, Q., Saad, S., Mahmood, A., & Tariq, S. (2018). Under pressure dft investigations on optical and electronic properties of $PbZrO_3$. *Acta Physica Polonica A*, *133*(1), 105-113.

Nieminen, R., & Ashcroft, N. (1981). Theory of inhomogeneous fluids. *Physical Review A*, *24*(1), 560.

Ning, C.-Z., Dou, L., & Yang, P. (2017). Bandgap engineering in semiconductor alloy nanomaterials with widely tunable compositions. *Nature Reviews Materials*, *2*(12), 1-14.

Nolen, J. R., Runnerstrom, E. L., Kelley, K. P., Luk, T. S., Folland, T. G., Cleri, A., … Caldwell, J. D. (2020). Ultraviolet to far-infrared dielectric function of n-doped cadmium oxide thin films. *Physical review materials*, *4*(2), 025202.

Noman, M., Sherwani, T., Jan, S. T., & Ismail, M. (2023). Exploring the impact of kesterite charge transport layers on the photovoltaic properties of $MAPbI_3$ perovskite solar cells. *Physica Scripta*, *98*(12), 125507.

Nourbakhsh, Z. (2010). Structural, electronic and optical properties of ZnX and CdX compounds (X = Se, Te and S) under hydrostatic pressure. *Journal of Alloys and Compounds*, *505*(2), 698-711.

Novoselov, K. S., Geim, A. K., Morozov, S. V., Jiang, D., Zhang, Y., Dubonos, S. V., … Firsov, A. A. (2004). Electric field effect in atomically thin carbon films. *science*, *306*(5696), 666-669.

Oliva, R., Laurien, M., Dybala, F., Kopaczek, J., Qin, Y., Tongay, S., … Kudrawiec, R. (2019). Pressure dependence of direct optical transitions in ReS_2 and $ReSe_2$. *npj 2D Materials and Applications*, *3*(1), 20.

Ong, S. P., Richards, W. D., Jain, A., Hautier, G., Kocher, M., Cholia, S., … Ceder, G. (2013). Python materials genomics (pymatgen): A robust, open-source python library for materials analysis. *Computational Materials Science*, *68*, 314-319.

Onga, M., Zhang, Y., Suzuki, R., & Iwasa, Y. (2016). High circular polarization in electroluminescence from $MoSe_2$. *Applied Physics Letters*, *108*(7).

Pandey, S. K., Das, R., & Mahadevan, P. (2020). Layer-dependent electronic structure changes in transition metal dichalcogenides: the microscopic origin. *ACS omega*, *5*(25), 15169-15176.

Parlinski, K., Li, Z., & Kawazoe, Y. (1997). First principles determination of the soft mode in cubic ZrO_2. *Physical Review Letters*, *78*(21), 4063.

Pavone, P., & Baroni, S. (1991). Ab initio calculation of phonon dispersions in semiconductors. *Phys. Rev. B*, *43*, 7231-7242.

Penn, D. R. (1962). Wave-number-dependent dielectric function of semiconductors. *Physical review*, *128*(5), 2093.

Perdew, J. P. (1991). Generalized gradient approximations for exchange and correlation: A look backward and forward. *Physica B: Condensed Matter*, *172*(1-2), 1-6.

Perdew, J. P., Burke, K., & Ernzerhof, M. (1996). Generalized gradient approximation made simple. *Physical review letters*, *77*(18), 3865.

Perdew, J. P., Burke, K., & Ernzerhof, M. (1998). Perdew, burke, and ernzerhof reply. *Physical Review Letters*, *80*(4), 891.

Petrik, P. (2014). Parameterization of the dielectric function of semiconductor nanocrystals. *Physica B: Condensed Matter*, *453*, 2-7.

Pfrommer, B. G., Côté, M., Louie, S. G., & Cohen, M. L. (1997). Relaxation of crystals with the quasi-newton method. *Journal of Computational Physics*, *131*(1), 233-240.

Pike, N. A., Dewandre, A., Van Troeye, B., Gonze, X., & Verstraete, M. J. (2018). Vibrational and dielectric properties of the bulk transition metal dichalcogenides. *Physical Review Materials*, *2*(6), 063608.

Qiu, H., Xu, T., Wang, Z., Ren, W., Nan, H., Ni, Z., … Song, F. (2013). Hopping transport through defect-induced localized states in molybdenum disulphide. *Nature communications*, *4*(1), 2642.

Rasmussen, F. A., & Thygesen, K. S. (2015). Computational 2D materials database: electronic structure of transition-metal dichalcogenides and oxides. *The Journal of Physical Chemistry C*, *119*(23), 13169-13183.

Rassay, S. S., Tang, W., & Ravindra, N. M. (2016). Optical properties and temperature dependence of energy gap of transition-metal dichalcogenides. *Proceedings MS&T, Salt Lake City, Utah*, 23-27.

Redaelli, L., Mukhtarova, A., Valdueza-Felip, S., Ajay, A., Bougerol, C., Himwas, C., … Monroy, E. (2014). Effect of the quantum well thickness on the performance of InGan photovoltaic cells. *Applied Physics Letters*, *105*(13).

Reshak, A. H., & Auluck, S. (2003). Electronic and optical properties of the 1 T phases of TiS_2, $TiSe_2$, and $TiTe_2$. *Physical Review B*, *68*(24), 245113.

Rhodes, D., Chae, S. H., Ribeiro-Palau, R., & Hone, J. (2019). Disorder in van der waals heterostructures of 2D materials. *Nature materials*, *18*(6), 541-549.

Ribeiro-Soares, J., Almeida, R., Barros, E. B., Araujo, P. T., Dresselhaus, M. S., Cançado, L. G., & Jorio, A. (2014). Group theory analysis of phonons in two-dimensional transition metal dichalcogenides. *Physical Review B*, *90*(11), 115438.

Rudnev, V., Loveless, D., & Cook, R. L. (2017). *Handbook of induction heating*. CRC press.

Sadasivam, S., Waghmare, U. V., & Fisher, T. S. (2015). Electron-phonon coupling and thermal conductance at a metal-semiconductor interface: First-principles analysis. *Journal of Applied Physics*, *117*(13).

Sahni, V., & Sahni, V. (2004). The Hohenberg-Kohn theorems and Kohn-Sham density functional theory. *Quantal Density Functional Theory*, 99-123.

Sahoo, P. K., Memaran, S., Nugera, F. A., Xin, Y., Diaz Marquez, T., Lu, Z., … Balicas, L. (2019). Bilayer lateral heterostructures of transition-metal dichalcogenides and their optoelectronic response. *ACS nano*, *13*(11), 12372-12384.

Sangwan, V. K., & Hersam, M. C. (2018). Electronic transport in two-dimensional materials. *Annual review of physical chemistry*, *69*(1), 299-325.

Santosh, K., Longo, R. C., Addou, R., Wallace, R. M., & Cho, K. (2014). Impact of intrinsic atomic defects on the electronic structure of mos2 monolayers. *Nanotechnology*, *25*(37), 375703.

Schmidt, K., & Kalos, M. (1987). Few-and many-fermion problems. In *Applications of the monte carlo method in statistical physics* (pp. 125-143). Springer.

Schneemeyer, L. F., & Sienko, M. J. (1980). Crystal data for mixed-anion molybdenum dichalcogenides. *Inorganic Chemistry*, *19*(3), 789-791.

Schutte, W., De Boer, J., & Jellinek, F. (1987). Crystal structures of tungsten disulfide and diselenide. *Journal of Solid State Chemistry*, *70*(2), 207-209.

Sedhain, R. P., & Kaphle, G. C. (2017). Structural and electronic properties of transition metal di-chalcogenides MoX_2, (M = (Mo, W) and X = (S, Se) in bulk state: a first-principles study. *Journal of Institute of Science and Technology*, *22*(1), 41-50.

Shafqat, A., Iqbal, T., & Majid, A. (2017). A DFT study of intrinsic point defects in monolayer $MoSe_2$. *Aip Advances*, *7*(10).

Sharma, A., Khan, M. S., Khan, M. S., & Husain, M. (2021). Ab initio study of molybdenum sulfo-selenides alloy as a flexible anode for sodium-ion batteries. *Applied Surface Science*, *536*, 147973.

Shawahni, A. M., Abu-Jafar, M. S., Jaradat, R. T., Ouahrani, T., Khenata, R., Mousa, A. A., & Ilaiwi, K. F. (2018). Structural, elastic, electronic and optical properties of $SrTMO_3$ (TM = Rh, Zr) compounds: insights from FP-LAPW study. *Materials*, *11*(10), 2057.

Shen, D., Zhao, B., Zhang, Z., Zhang, H., Yang, X., Huang, Z., … Wu, R. (2022). Synthesis of group VIII magnetic transition metal doped monolayer $MoSe_2$. *ACS nano*, *16*(7), 10623-10631.

Shen, J., Wu, J., Wang, M., Dong, P., Xu, J., Li, X., … Ye, M. (2016). Surface tension components based selection of cosolvents for efficient liquid phase exfoliation of 2D materials. *Small*, *12*(20), 2741-2749.

Shrivastava, A., Saini, S., & Singh, S. (2022). Ab initio investigations of electronic and optical properties of Sn-hBN hetero-structure. *Physica B: Condensed Matter*, *624*, 413390.

Shu, H., Zhou, D., Li, F., Cao, D., & Chen, X. (2017). Defect engineering in $MoSe_2$ for the hydrogen evolution reaction: from point defects to edges. *ACS applied materials & interfaces*, *9*(49), 42688-42698.

Singh, A. K., Kumar, P., Late, D., Kumar, A., Patel, S., & Singh, J. (2018). 2D layered transition metal dichalcogenides (MoS_2): synthesis, applications and theoretical aspects. *Applied Materials Today*, *13*, 242-270.

Sofer, Z., Sedmidubskỳ, D., Luxa, J., Bouša, D., Huber, Š., Lazar, P., … Pumera, M. (2017). Universal method for large-scale synthesis of layered transition metal dichalcogenides. *Chemistry-A European Journal*, *23*(42), 10177-10186.

Splendiani, A., Sun, L., Zhang, Y., Li, T., Kim, J., Chim, C.-Y., … Wang, F. (2010). Emerging photoluminescence in monolayer $MoSe_2$. *Nano letters*, *10*(4), 1271-1275.

Su, D., Liu, G., Ma, M., Wei, R., Mu, Y., Yang, Z., & Zhang, G. (2024). First principles study of the effect of doping on the optoelectronic properties of defective monolayers of $MoSe_2$. *Journal of Molecular Modeling*, *30*(2), 29.

Su, S.-H., Hsu, W.-T., Hsu, C.-L., Chen, C.-H., Chiu, M.-H., Lin, Y.-C., … Li, L.-J. (2014). Controllable synthesis of band-gap-tunable and monolayer transition-metal dichalcogenide alloys. *Frontiers in Energy Research*, *2*, 27.

Suh, J., Park, T.-E., Lin, D.-Y., Fu, D., Park, J., Jung, H. J., … Sun, Y. (2014). Doping against the native propensity of MoS_2: degenerate hole doping by cation substitution. *Nano letters*, *14*(12), 6976-6982.

Sukanya, R., Karthik, R., Al Mahmud, A., Kumar, D. R., Kamaraj, E., Breslin, C. B., & Shim, J.-J. (2025). Vanadium doped $MoSe_2$ nanosheets: Induced lattice contraction and enhanced conductivity for superior hydrogen evolution reaction. *Electrochemistry Communications*, *175*, 107916.

Sun, L., Li, Q., Ren, H., Su, H., Shi, Q., & Yang, J. (2008). Strain effect on electronic structures of graphene nanoribbons: A first-principles study. *The Journal of chemical physics*, *129*(7).

Susarla, S., Kutana, A., Hachtel, J. A., Kochat, V., Apte, A., Vajtai, R., … Ajayan, P. M. (2017). Quaternary 2D transition metal dichalcogenides (TMDs) with tunable bandgap. *Advanced Materials*, *29*(35), 1702457.

Sutton, A. P. (1993). *Electronic structure of materials*. Clarendon Press.

Tan, C., Luo, Z., Chaturvedi, A., Cai, Y., Du, Y., Gong, Y., … Zheng, L. (2018). Preparation of high-percentage 1T-phase transition metal dichalcogenide nanodots for electrochemical hydrogen evolution. *Advanced Materials*, *30*(9), 1705509.

Terrones, H., López-Urías, F., & Terrones, M. (2013). Novel hetero-layered materials with tunable direct band gaps by sandwiching different metal disulfides and diselenides. *Scientific reports*, *3*(1), 1549.

Thijs, P. J., Tiemeijer, L. F., Kuindersma, P., Binsma, J., & Van Dongen, T. (1991). High-performance 1.5 μ wavelength InGaAs-InGaAsP strained quantum well lasers and amplifiers. *IEEE journal of quantum electronics*, *27*(6), 1426-1439.

Tian, D., Zeng, C., Fu, Y., Wang, H., Luo, H., Xiang, C., ... Zhu, X. (2016). A DFT study of the structural, electronic and optical properties of transition metal doped fluorite oxides: $Ce_{0.75}M_{0.25}O_2$ (M = Fe, Co, Ni). *Solid State Communications*, *231*, 68-79.

Tian, J., Zhao, Y., Wang, B., Hou, H., & Zhang, Y. (2018). The structural, mechanical and thermodynamic properties of Ti-B compounds under the influence of temperature and pressure: First principles study. *Materials Chemistry and Physics*, *209*, 200-207.

Tian, Y., Zhu, Z., Ge, Z., Sun, A., Zhang, Q., Huang, S., ... Meng, J. (2020). Electronic and magnetic properties of 3d transition metal doped $MoSe_2$ monolayer. *Physica E: Low-Dimensional Systems and Nanostructures*, *116*, 113745.

Timrov, I., Marzari, N., & Cococcioni, M. (2018). Hubbard parameters from density-functional perturbation theory. *Physical Review B*, *98*(8), 085127.

Togo, A., Oba, F., & Tanaka, I. (2008). Transition pathway of CO_2 crystals under high pressures. *Physical Review B-Condensed Matter and Materials Physics*, *77*(18), 184101.

Togo, A., & Tanaka, I. (2015). First principles phonon calculations in materials science. *Scripta Materialia*, *108*, 1-5.

Tongay, S., Narang, D. S., Kang, J., Fan, W., Ko, C., Luce, A. V., ... Pathak, V. (2014). Two dimensional semiconductor alloys: Monolayer $Mo_{1-x}W_xSe_2$. *Applied Physics Letters*, *104*(1).

Tongay, S., Zhou, J., Ataca, C., Lo, K., Matthews, T. S., Li, J., ... Wu, J. (2012). Thermally driven crossover from indirect toward direct bandgap in 2D semiconductors: $MoSe_2$ versus MoS_2. *Nano letters*, *12*(11), 5576-5580.

Tonndorf, P., Schmidt, R., Böttger, P., Zhang, X., Börner, J., Liebig, A., ... Zahn, D. R. (2013). Photoluminescence emission and raman response of monolayer MoS_2, $MoSe_2$, and WSe_2. *Optics express*, *21*(4), 4908-4916.

Tsai, J.-Y., Pan, J., Lin, H., Bansil, A., & Yan, Q. (2022). Antisite defect qubits in monolayer transition metal dichalcogenides. *Nature communications*, *13*(1), 492.

Tsui, D. C., Stormer, H. L., & Gossard, A. C. (1982). Two-dimensional magnetotransport in the extreme quantum limit. *Physical Review Letters*, *48*(22), 1559.

Tyagi, P., & Choudhary, S. (2022). Modulating the optical and electrical properties of $MoSe_2$ (molybdenum diselenide) and WS_2 (tungsten disulfide) monolayer by the adsorption of halogen (F, Cl, Br, I and At) atoms. *Optical and Quantum Electronics*, *54*(12), 869.

Ugeda, M. M., Bradley, A. J., Shi, S.-F., Da Jornada, F. H., Zhang, Y., Qiu, D. Y., ... Shen, Z.-X. (2014). Giant bandgap renormalization and excitonic effects in a monolayer transition metal dichalcogenide semiconductor. *Nature materials*, *13*(12), 1091-1095.

van de Walle, A., Asta, M., & Ceder, G. (2002). The alloy theoretic automated toolkit: A user guide. *Calphad*, *26*(4), 539-553.

Van Hove, L. (1953). The occurrence of singularities in the elastic frequency distribution of a crystal. *Physical Review*, *89*(6), 1189.

Verble, J., & Wieting, T. (1970). Lattice mode degeneracy in MoS_2 and other layer compounds. *Physical review letters*, *25*(6), 362.

Vikraman, D., Hussain, S., Akbar, K., Karuppasamy, K., Chun, S.-H., Jung, J., & Kim, H.-S. (2018). Design of basal plane edges in metal doped nanostripes structured $MoSe_2$ atomic layers to enhance hydrogen evolution reaction activity. *ACS Sustainable Chemistry & Engineering*, *7*(1), 458-469.

Vinturaj, V., Yadav, A. K., Jasil, T., Kiran, G., Singh, R., Singh, A. K., ... Pandey, S. K. (2023). Theoretical investigation of electronic and optical properties of doped and defective $MoSe_2$ monolayers. *Bulletin of Materials Science*, *46*(3), 121.

Vogt, P., De Padova, P., Quaresima, C., Avila, J., Frantzeskakis, E., Asensio, M. C., ... Le Lay, G. (2012). Silicene: compelling experimental evidence for graphenelike two-dimensional silicon. *Physical review letters*, *108*(15), 155501.

Wakabayashi, N., Smith, H., & Nicklow, R. (1975). Lattice dynamics of hexagonal MoS_2 studied by neutron scattering. *Physical Review B*, *12*(2), 659.

Wang, D., Zhang, X., Li, B., Liu, L., & Shen, D. (2014). Dynamical properties and their strain dependence of ZnSe (ZnSe: N): Zinc blende and wurtzite. *Aip Advances*, *4*(6).

Wang, G., Chernikov, A., Glazov, M. M., Heinz, T. F., Marie, X., Amand, T., & Urbaszek, B. (2018). Colloquium: Excitons in atomically thin transition metal dichalcogenides. *Reviews of Modern Physics*, *90*(2), 021001.

Wang, Q., & Kalantar-Zadeh, K. (2012). A.. kis, jn coleman, and ms strano. *Nat. Nanotechnol*, *7*, 699.

Wang, Q., Wu, P., Cao, G., & Huang, M. (2013). First principles study of the structural and electronic properties of MoS_2-WS_2 and MoS_2-$MoTe_2$ monolayer heterostructures. *Journal of Physics D: Applied Physics*, *46*(50), 505308.

Wang, Q. H. (2020). Controlled doping and electrical transport in layered transition metal dichalcogenides. *Advanced Materials*, *32*(18), 1904649.

Wang, Q. H., Kalantar-Zadeh, K., Kis, A., Coleman, J. N., & Strano, M. S. (2012). Electronics and optoelectronics of two-dimensional transition metal dichalcogenides. *Nature nanotechnology*, *7*(11), 699-712.

Wang, S., Robertson, A., & Warner, J. H. (2018). Atomic structure of defects and dopants in 2D layered transition metal dichalcogenides. *Chemical Society Reviews*, *47*(17), 6764-6794.

Wang, S. Y., Ko, T. S., Huang, C. C., & Huang, Y. S. (2014). Optical and electrical properties of MoS_2 and Fe doped $MoSe_2$. *Japanese Journal of Applied Physics*, *53*(4S), 04EH07.

Wang, Y., Li, S., & Yi, J. (2016). Electronic and magnetic properties of Co doped MoS_2 monolayer. *Scientific reports*, *6*(1), 24153.

Wang, Y., Shang, S.-L., Fang, H., Liu, Z.-K., & Chen, L.-Q. (2016). First-principles calculations of lattice dynamics and thermal properties of polar solids. *npj Computational Materials*, *2*(1), 1-10.

Wang, Z., Liu, P., Ito, Y., Ning, S., Tan, Y., Fujita, T., ... Chen, M. (2016). Chemical vapor deposition of monolayer $Mo_{1-x}W_xS_2$ crystals with tunable band gaps. *Scientific reports*, *6*(1), 21536.

Wehling, T., Novoselov, K., Morozov, S., Vdovin, E., Katsnelson, M., Geim, A., & Lichtenstein, A. (2008). Molecular doping of graphene. *Nano letters*, *8*(1), 173-177.

Wei, W., Dai, Y., Sun, Q., Yin, N., Han, S., Huang, B., & Jacob, T. (2015). Electronic structures of in-plane two-dimensional transition-metal dichalcogenide heterostructures. *Physical Chemistry Chemical Physics*, *17*(43), 29380-29386.

Wells, A. F. (2012). *Structural inorganic chemistry*. OUP Oxford.

Wen, Z., Zhao, Y., Hou, H., Wang, B., & Han, P. (2017). The mechanical and thermodynamic properties of heusler compounds Ni_2XAl (X = Sc, Ti, V) under pressure and temperature: A first principles study. *Materials & Design*, *114*, 398-403.

Wickramaratne, D., Zahid, F., & Lake, R. K. (2014). Electronic and thermoelectric properties of few-layer transition metal dichalcogenides. *The Journal of chemical physics*, *140*(12).

Wilson, J. A., & Yoffe, A. (1969). The transition metal dichalcogenides discussion and interpretation of the observed optical, electrical and structural properties. *Advances in Physics*, *18*(73), 193-335.

Wu, R., Drozdov, I. K., Eltinge, S., Zahl, P., Ismail-Beigi, S., Božović, I., & Gozar, A. (2019). Large area single crystal sheets of borophene on Cu (111) surfaces. *Nature Nanotechnology*, *14*(1), 44-49.

Wu, T.-m., Xu, R.-x., Zheng, X., & Zhuang, W. (2016). Electronic structures and thermoelectric properties of two dimensional MoS_2/$MoSe_2$ heterostructures. *Chinese Journal of Chemical Physics*, *29*(4), 445-452.

Xi, X., Wang, Z., Zhao, W., Park, J.-H., Law, K. T., Berger, H., … Mak, K. F. (2016). Ising pairing in superconducting $NbSe_2$ atomic layers. *Nature Physics*, *12*(2), 139-143.

Xie, L.-Y., & Zhang, J.-M. (2017). The structure, electronic, magnetic and optical properties of the Mn-doped and Mn-X (X = F, Cl, Br, I and At) Co-doped monolayer WS_2: a first-principles study. *Journal of Alloys and Compounds*, *702*, 138-145.

Xu, H., Zhu, J., Ma, Q., Ma, J., Bai, H., Chen, L., & Mu, S. (2021). Two-dimensional MoS_2: Structural properties, synthesis methods, and regulation strategies toward oxygen reduction. *Micromachines*, *12*(3), 240.

Xu, W.-b., Huang, B.-j., Li, P., Li, F., Zhang, C.-w., & Wang, P.-j. (2014). The electronic structure and optical properties of Mn and B, C, N co-doped MoS_2 monolayers. *Nanoscale research letters*, *9*(1), 554.

Yamcicier, C., Merdan, Z., & Kurkcu, C. (2018). Investigation of the structural and electronic properties of CdS under high pressure: an ab initio study. *Canadian Journal of Physics*, *96*(2), 216-224.

Yamusa, S. A., Shaari, A., & Isah, I. (2022). Structural stability, electronic and optical properties of bulk MoS_2 transition metal dichalcogenides: A dft approach. *J. Appl. Phys*, *14*, 40.

Yan, Z., Yoon, M., & Kumar, S. (2018). Influence of defects and doping on phonon transport properties of monolayer MoS_2. *2D Materials*, *5*(3), 031008.

Yang, C.-H., & Chang, S.-T. (2022). First principles study of the optical properties of TMDc/graphene heterostructures. In *Photonics* (Vol. 9, p. 387).

Yang, X., Liu, J., & Koster, L. J. A. (2025). The exceptionally high dielectric constant of doped organic semiconductors. *Advanced Electronic Materials*, *11*(3), 2400413.

Yaseen, M. S., Sun, J., Fang, H., Murtaza, G., & Sholl, D. S. (2021). First principles study of electronic and optical properties of ternary compounds $AuBX_2$ (X = S, Se, Te) and $AuMTe_2$ (M = Al, In, Ga). *Solid State Sciences*, *111*, 106508.

Yoffe, A. (1973). Layer compounds. *Annu. Rev. Mater. Sci., v. 3, pp. 147-170.*

Yu, J., Wu, S., Zhao, X., Li, Z., Yang, X., Shen, Q., … Yan, J. (2023). Progress on two-dimensional transitional metal dichalcogenides alloy materials: growth, characterisation, and optoelectronic applications. *Nanomaterials*, *13*(21), 2843.

Yu, P., Lin, J., Sun, L., Le, Q. L., Yu, X., Gao, G., … Zeng, Q. (2017). Metal semiconductor phase transition in $WSe_{2(1-x)}Te_{2x}$ monolayer. *Advanced Materials*, *29*(4), 1603991.

Yu, S. H., Lee, Y., Jang, S. K., Kang, J., Jeon, J., Lee, C., … Lee, S. (2014). Dye-sensitized MoS_2 photodetector with enhanced spectral photoresponse. *ACS nano*, *8*(8), 8285-8291.

Yue, Q., Chang, S., Qin, S., & Li, J. (2013). Functionalization of monolayer MoS_2 by substitutional doping: a first principles study. *Physics Letters A*, *377*(19-20), 1362-1367.

Yun, W. S., Han, S., Hong, S. C., Kim, I. G., & Lee, J. (2012). Thickness and strain effects on electronic structures of transition metal dichalcogenides: 2H-MX_2 semiconductors (M = Mo, W; X = S, Se, Te). *Physical Review B-Condensed Matter and Materials Physics*, *85*(3), 033305.

Yun, W. S., & Lee, J. (2014). Unexpected strong magnetism of Cu doped single layer MoS_2 and its origin. *Physical Chemistry Chemical Physics*, *16*(19), 8990-8996.

Zhang, G., & Yong-Wei. (2017). Thermoelectric properties of two-dimensional transition metal dichalcogenides. *Journal of Materials Chemistry C*, *5*(31), 7684-7698.

Zhang, K. (2023). Thermal and thermoelectric properties of two-dimensional transition metal dichalcogenides: a review. *Materials Today Physics*, *32*, 100952.

Zhang, S., Guo, S., Chen, Z., Wang, Y., Gao, H., Gómez-Herrero, J., … Zeng, H. (2018). Recent progress in 2D group-VA semiconductors: from theory to experiment. *Chemical Society Reviews*, *47*(3), 982-1021.

Zhang, X., Qiao, X.-F., Shi, W., Wu, J.-B., Jiang, D.-S., & Tan, P.-H. (2015). Phonon and raman scattering of two-dimensional transition metal dichalcogenides from monolayer, multilayer to bulk material. *Chemical Society Reviews*, *44*(9), 2757-2785.

Zhang, X., Tan, Q.-H., Wu, J.-B., Shi, W., & Tan, P.-H. (2016). Review on the raman spectroscopy of different types of layered materials. *Nanoscale*, *8*(12), 6435-6450.

Zhang, Y., & Yang, W. (1998). “Generalized gradient approximation made simple”. *Physical Review Letters*, *80*(4), 890.

Zhang, Z., Xie, J., Yang, D., Wang, Y., Si, M., & Xue, D. (2015). Manifestation of unexpected semiconducting properties in few-layer orthorhombic arsenene. *Applied Physics Express*, *8*(5), 055201.

Zhao, M., Hao, Y., Zhang, C., Zhai, R., Liu, B., Liu, W., … Papadakis, R. (2022). Advances in two-dimensional materials for optoelectronics applications. *Crystals*, *12*(8), 1087.

Zhao, M., Zhang, W., Liu, M., Zou, C., Yang, K., Yang, Y., … Huang, S. (2016). Interlayer coupling in anisotropic/isotropic van der Waals heterostructures of ReS_2 and MoS_2 monolayers. *Nano Research*, *9*, 3772-3780.

Zhao, W. (2015). Continuously tunable bandgap in transition metal dichalcogenide alloys. *Nano Letters*, *15*(7), 4830-4836.

Zhao, X., Zhang, X., Wang, T., Wei, S., & Yang, L. (2017). Effective n-type F doped $MoSe_2$ monolayers. *RSC Advances*, *7*(43), 26673-26679.

Zhao, Y., Luo, X., Li, H., Zhang, J., Araujo, P. T., Gan, C. K., … Dresselhaus, M. S. (2013). Interlayer breathing and shear modes in few trilayer MoS_2 and WSe_2. *Nano letters*, *13*(3), 1007-1015.

Zhao, Y., Ren, Y., Coileáin, C. Ó., Li, J., Zhang, D., Arora, S. K., … Wu, H.-C. (2021). High response and broadband photodetection by monolayer $MoSe_2$ with vanadium doping and mo vacancies. *Applied Surface Science*, *564*, 150399.

Zhao, Y., Wang, W., Li, C., & He, L. (2017). First-principles study of nonmetal doped monolayer $MoSe_2$ for tunable electronic and photocatalytic properties. *Scientific Reports*, *7*(1), 17088.

Zhou, J., Lin, J., Huang, X., Zhou, Y., Chen, Y., Xia, J., … Lei, J. (2018). A library of atomically thin metal chalcogenides. *Nature*, *556*(7701), 355-359.

Zhou, L., Yu, S., Yang, Y., Li, Q., Li, T., & Zhang, D. (2021). Adsorption of gas molecules (NH_3, C_2H_6O, C_3H_6O, CO, H_2S) on a noble metal (Ag, Au, Pt, Pd, Ru) doped $MoSe_2$ monolayer: a first principles study. *New Journal of Chemistry*, *45*(28), 12367-12376.

Zhou, W., Zou, X., Najmaei, S., Liu, Z., Shi, Y., Kong, J., … Idrobo, J.-C. (2013). Intrinsic structural defects in monolayer molybdenum disulfide. *Nano letters*, *13*(6), 2615-2622.